Strong-field processes in Atoms and Polyatomic Molecules

By

Noslen Suárez Rojas

A Dissertation submitted in partial fulfillment
of the requirements for the degree of
Doctor of Philosophy

ICFO - Institut de Ciències Fotòniques
UPC - Universitat Politècnica de Catalunya

Thesis Advisors:

Prof. Dr. Maciej Lewenstein
Prof. Dr. Jens Biegert
Dr. Marco Bellini

Barcelona, September 2017

ABSTRACT

High-Order-Harmonic Generation (HHG) and Above-Threshold Ionization (ATI) result from the interaction of ultrashort laser pulses with matter. HHG, for instance, is nowadays the workhorse to produce attosecond pulses. ATI, moreover, constitutes an invaluable tool to extract electron structural and dynamical information of the target, i.e., atoms, molecules, and solids. However, since theoretical *ab-initio* treatments of even the simplest diatomic systems are beyond today's computational capabilities, approximate qualitative descriptions are demanded.

In this thesis, we develop a general theory to describe the dynamics of electrons that are ionized when an atom or molecule is exposed to a strong low frequency laser field. Our approach extends and improves the well-established theoretical strong-field approximation (SFA). Additionally, our modified strong field approximation (MSFA) can be extended in a natural way from atomic systems to a more complex molecules and multielectron systems. Our scheme involves two innovative aspects: (i) First, the bound-continuum and rescattering matrix elements can be analytically computed for both atomic and multicenter molecular systems, using a nonlocal short range (SR), but separable, potential. When compared with the standard models, these analytical derivations make possible to directly examine how the ATI and HHG spectra depend on the driven media and laser-pulse features. Furthermore, our model allows us to disentangle the different processes contributing to the total spectra, amongst other capabilities, and it allows us to adjust both the internuclear separation and atomic or molecular potential in a direct and simple way. Furthermore, we can turn on and off contributions having distinct physical origins or corresponding to different mechanisms that correspond to (1) direct tunneling ionization; (2) electron rescattering/recombining on the center of origin; and, finally, (3) electron rescattering/recombining on a different center. (ii) Second, the multicenter matrix elements in our theory are free from nonphysical coordinate-system-dependent terms; this is accomplished by adapting the coordinate system to the center from which the corresponding time-dependent wave function originates.

Having established the basic formalism, we then study the HHG and ATI processes for a variety of atomic and molecular systems. We compare the SFA results with the full numerical solutions of the time-dependent Schrödinger equation (TDSE), when available, within the few-cycle pulse regime. We show how our MSFA can be used to look inside the underlying physics of those phenomena. With our tool it is

possible to investigate the interference features, ubiquitously present in every strong-field phenomenon involving a multicenter target, or to describe laser-induced electron diffraction (LIED) measurements retrieving molecular structural information from the photoelectron spectra.

Our approach paves the way to study the HHG and ATI processes in much more complex molecular targets. Additionally, it potentially can be extended to study these kind of recombination and rescattering scenarios in solid targets.

RESUMEN

Durante las últimas dos décadas, el estudio de las interacciones de los pulsos de luz con la materia, ya sean átomos, moléculas o sólidos ha generado un gran interés científico. Fenómenos tales como la generación de armónicos de orden superior (HHG) y la ionización por encima del umbral (ATI), originados por la interacción de pulsos láser ultracortos con la materia, han captado la atención de la comunidad científica. Los procesos de HHG y ATI representan una herramienta invaluable para la producción de pulsos de luz con duración de attosegundos, además de para extraer información dinámica y estructural de los átomos, moléculas y sólidos. Desde el punto de vista teórico la descripción de este tipo de interacciones requiere la utilización de métodos aproximados, dado que un tratamiento *ab-initio*, incluso de los sistemas diatómicos más simples, está más allá de las capacidades computacionales actuales.

En esta tesis, desarrollamos una teoría general para describir la dinámica de ionización de electrones cuando un átomo o molécula está expuesto a un campo externo fuerte y de longitud de onda larga. Nuestro modelo está basado en la bien establecida aproximación de campo fuerte (SFA). Nuestra teoría: la aproximación de campo fuerte modificada (MSFA), es capaz de describir la interacción de un pulso de luz, no sólo con átomos sino también con moléculas y sólidos. La MSFA está construida como una extensión natural y consecuente del modelo atómico, describiendo desde los sistemas más simples hasta las moléculas más complejas, incluyendo sistemas de muchos electrones. Nuestro enfoque abarca dos aspectos innovadores: (i) En primer lugar, los elementos de matriz que describen la dispersión e interacciones de electrones en el continuo se calculan analíticamente, tanto para sistemas atómicos como moleculares. Esto se logra utilizando un tipo de potencial de corto alcance (SR), no local y separable. En comparación con los modelos estándares, estas derivaciones analíticas permiten examinar directamente cómo los espectros ATI y HHG dependen de las características del pulso láser. Nuestra derivación analítica permite diferenciar los diferentes procesos que contribuyen al espectro total, además de que nos permite fijar la distancia internuclear y el potencial atómico o molecular de una manera directa y sencilla. También es posible activar y desactivar las contribuciones que tienen diferentes orígenes físicos o que corresponden a diferentes mecanismos como, (1) ionización directa por túnel; (2) dispersión/recombinación de electrones en el átomo de ionización; y, por último, (3) dispersión/recombinación de electrones en un átomo distinto al de ionización. (ii) En segundo lugar, en nuestra

teoría los elementos matriciales de los sistemas multi-atómicos se encuentran libres de calibraciones no físicas y son independientes del sistema de coordenadas. Esto se consigue adaptando el sistema de coordenadas al átomo del que se origina la correspondiente función de onda dependiente del tiempo. Una vez establecido el formalismo básico del MSFA, estudiamos los procesos de HHG y ATI para una gran variedad de sistemas atómicos y moleculares. Comparamos los resultados del MSFA con las soluciones numéricas de la ecuación de Schrödinger dependiente del tiempo (TDSE), cuando sea posible. Demostramos que nuestro modelo de MSFA puede ser utilizado para estudiar la física de los procesos fundamentales que están detrás de HHG y ATI. Con esta herramienta es posible investigar los procesos de interferencia, inherentes a todos los fenómenos de campo fuerte, en sistemas multi-céntricos. Tambíen es posible describir mediciones experimentales de difracción de electrones inducida por láser (LIED), permitiendo recuperar información estructural mediante el análisis de los espectros de fotoelectrones.

Nuestro modelo abre el camino para estudiar los procesos de HHG y ATI en sistemas de moléculas complejas. Además tiene la potencialidad de poder ser fácilmente extendido para estudiar procesos de recombinación y dispersión, no sólo en moléculas grandes, sino tambíen en sólidos.

So please ask your self:
What would I do if I were not afraid?
and then go do it.

—**Sheryl Sandberg**

Por todo lo que aún nos queda, a ti, mi ALBE...

ACKNOWLEDGMENTS

This thesis has been quite a long journey, of happy and not so happy moments, which helped me to grow up from both the personal and professional sides. This work would not have been possible without the help of some key people who have been surrounding me throughout the whole Phd.

First, I would like to thank my supervisor Prof. Dr Jens Biegert for give me the opportunity to start at ICFO and then to establish the collaboration with the QOT group.

Second, I would like to take the opportunity to thank my supervisor Prof. Maciej Lewenstein for his competent supervision during the last three years. I am thankful to his advices throughout the years, the opportunity of presenting our work at numerous conferences and for the culmination of this thesis. Thanks Maciej for make me enjoy the science again!!

I also would like to acknowledge Dr. Marco Bellini and his group, in particular Chiara Corsi, for their warm welcome at LENS; Grazie mille for making me feel as one of you since the moment I arrived in Florence.

Another key person during my PhD has been Marcelo. His capability of analysis and scientific thinking are really admirable to me. From him I have learned the beauty of the strong field physics. His guidance through these years has been decisive for the success of this thesis. We have not only shared congresses but also beers, meals and good moments that make me see him as a friend rather than as a colleague.

I also would like to acknowledge Dr. Alexis Chacón who guided me through the art of C++ programing and my first ATI simulations. He took my programming skills from zero to the level that I needed. Thanks Alexis for the discussions and all the learning process.

My special thanks to the people at the UPC, in special to Prof. Ramón Vilaseca for his support.

CONTENTS

Part I

THEORETICAL TOOLS

1

GENERAL THEORY FOR STRONG-FIELD IONIZATION OF ATOMS DRIVEN BY STRONG LASER FIELDS

In this chapter, we start revisiting the Strong-Field Approximation (SFA) or Lewenstein model for High-Order-Harmonic Generation (HHG) and Above-Threshold Ionization (ATI) driven by few-cycle infrared (IR) laser pulses. We aim to compare this approach with the numerical solution of the TDSE. We compute HHG spectra for two atomic species in different conditions [1, 2]. In the case of ATI we present results in one (1D) and two (2D) spatial dimensions for an atomic system [3, 4]. For simplicity, our analytical atomic model is based on a nonlocal, but separable, potential, which can be considered a short-range (SR) potential. In order to verify the validity of our analytical SR model and to understand how its predictions compare with a true Coulomb potential, we numerically integrate the time-dependent Schrödinger equation (TDSE) for the hydrogen atom and compute both harmonic spectra and photoelectron energy and momentum distributions.

In the course of our calculations we have to face with various kinds of singular expressions. All of them have to be treated in the distribution sense [5]; some are even apparently nonintegrable. Obviously, such expressions cannot be used efficiently in numerical calculations, so we have to regularize them. We stress, however, that the used regularization approach is not an artificial mathematical trick; it has its physical origin in the finite size of the propagating wave packets. We illustrate these points with more detail in Appendix 5. Furthermore, in Appendix 6 we discuss general properties of the rescattering matrix element in the framework of scattering theory [6].

The main original results of this chapter are:

- The comprehensive development of the mathematical foundations to calculate the HHG and ATI spectra in atomic systems using the SFA approach.
- The identification of the two main terms contributing to the ATI spectra: the direct and rescattering transition amplitudes.
- The analytical formulation of the rescattering matrix element by using a nonlocal SR potential; this reinforce us to demonstrate the strong influence the atomic target features have in the rescattering process.

- The validation of the our semiclassical approach over the basis of the excellent agreement between our calculations and the exact solution of the full dimensionality TDSE.
- The capability of our model to capture the carrier-to-envelope-phase (CEP) asymmetries and the clear confirmation that the photoelectron spectra contain structural information.

1.1 SFA: TRANSITION PROBABILITY AMPLITUDE

The interaction of a strong electric field with an atomic or molecular system is described within quantum mechanics by the TDSE. It captures both the evolution of the (electronic) wave function and the time evolution of the physical observables. The numerical solution of the TDSE offers a full quantum mechanical description of the laser-matter interaction processes and has been extensively used to study several phenomena, such as HHG [7–9] and ATI [10–14] in atomic and molecular systems. However, the full numerical integration of the TDSE in all the degrees of freedom of the system is often a laborious and sometimes impossible task to perform from numerical and computational points of view. Moreover, a physical interpretation of the numerical TDSE results and the extraction of information from the time-evolved wave function is highly nontrivial for such an *ab initio* technique.

Hence, from a purely theoretical point of view, it would be desirable to solve the TDSE analytically for the ionization process. This is one of the main steps in all laser-matter interaction phenomena, and it represents a formidable and challenging assignment. Here we discuss an alternative method to calculate both the harmonic and photoelectron spectra from atomic systems by analytically solving the TDSE under the so-called SFA. This approach dates back to Keldysh [15] and has since then been employed by many other authors [1, 3, 16–21]. It is worth noting that SFA provides a quantum framework and extension of what has been called the "Simpleman" or "three-step" or "recollision" model, usually attributed to Corkum [22], Kulander [23, 24], and van Linden van den Heuvell and Muller [25, 26] (cf. [27] for an extensive review; for earlier quantum formulation of "Atomic Antennas" see Ref. [28]; for other pioneering contributions see Refs. [29–31]).

1.1.1 *Ionization driven by strong fields*

Let us consider an atom under the influence of an ultraintense laser field. In the limit when the wavelength of the laser, λ_0, is large compared with the Bohr radius, a_0 (5.29×10^{-11} m), the electric field of the laser beam around the interaction region can be considered spatially homogeneous. Consequentially, the interacting atoms will not experi-

ence the spatial dependence of the laser electric field and, hence, only its time variation is taken into account. This is the so-called dipole approximation. In this approximation, the laser electric field can be written as

$$\mathbf{E}(t) = \mathcal{E}_0 \, f(t) \sin(\omega_0 \, t + \phi_0) \, \mathbf{e}_z. \tag{1}$$

The field of Eq. (1) has a carrier frequency $\omega_0 = \frac{2\pi c}{\lambda_0}$, where c is the speed of light, $\mathcal{E}_0$ the field peak amplitude or strength, and we consider that the laser field is linearly polarized along the z direction. $f(t)$ denotes the envelope of the laser pulse and the parameter ϕ_0 defines the CEP.

The TDSE is defined (atomic units are used throughout this thesis unless otherwise stated) by

$$i\frac{\partial}{\partial t}|\Psi(t)\rangle = \hat{H}|\Psi(t)\rangle, \tag{2}$$

where the Hamiltonian operator, $\hat{H}$, describes the laser-atom system and is the sum of two terms, i.e.,

$$\hat{H}(\mathbf{r}, t) = \hat{H}_0 + \hat{U}(\mathbf{r}, t), \tag{3}$$

where $\hat{H}_0$ is the so-called laser-free Hamiltonian of the atomic or molecular system

$$\hat{H}_0 = -\frac{\nabla^2}{2} + \hat{V}(\mathbf{r}), \tag{4}$$

where $\hat{V}(\mathbf{r})$ the atomic or molecular potential and $\hat{U}(\mathbf{r}, t) = -q_e \mathbf{E}(t) \cdot \mathbf{r}$ is the dipole coupling which describes the interaction of the atomic or molecular system with the laser radiation, written in the length gauge and under the dipole approximation. Note that in atomic units, the electron charge, denoted by q_e, is $q_e = -1$ a.u.

We restrict our model to the low-ionization regime, where the assumption (ii) of SFA is valid (see Sec. **??**).

So, based directly on the SFA statement (i) of Sec. **??**, we propose a state, $|\Psi(t)\rangle$, that describes the time evolution of the system by a coherent superposition of the ground, $|0\rangle$, and the continuum states, $|\mathbf{v}\rangle$ [1, 3]:

$$|\Psi(t)\rangle = e^{iI_p t}\left[a(t)|0\rangle + \int d^3\mathbf{v} \, b(\mathbf{v}, t)|\mathbf{v}\rangle\right]. \tag{5}$$

The factor $a(t)$ represents the amplitude of the ground state that will be considered constant in time, i.e. $a(t) \approx 1$, under the assumption that there is no depletion of the ground state. The last hypothesis follows directly from statement (ii) of Sec. **??**. The prefactor, $e^{iI_p t}$, represents the phase oscillations that describes the accumulated electron energy in the ground state ($I_p = -E_0$ is the ionization potential of the atomic system, with E_0 the ground-state energy of the atomic system). Furthermore, the transition amplitude to the continuum states

is denoted by $b(\mathbf{v},t)$ and it depends both on the kinetic momentum of the outgoing electron and the laser pulse characteristics. Therefore, our main task will be to derive a general expression for the amplitude $b(\mathbf{v},t)$. In order to do so, we substitute Eq. (5) in Eq. (2) both in left,

$$i\frac{\partial}{\partial t}|\Psi(t)\rangle = i\frac{\partial}{\partial t}\left(e^{iI_p t}\left[|0\rangle + \int d^3\mathbf{v}\, b(\mathbf{v},t)|\mathbf{v}\rangle\right]\right), \tag{6}$$

and right sides,

$$\begin{aligned}\left[\hat{H}_0 + \mathbf{E}(t)\cdot\mathbf{r}\right]|\Psi(t)\rangle &= \hat{H}_0\, e^{iI_p t}\left[|0\rangle + \int d^3\mathbf{v}\, b(\mathbf{v},t)|\mathbf{v}\rangle\right] \\ &\quad + \mathbf{E}(t)\cdot\mathbf{r}\, e^{iI_p t}\left[|0\rangle + \int d^3\mathbf{v}\, b(\mathbf{v},t)|\mathbf{v}\rangle\right]. \end{aligned}\tag{7}$$

In the above equations we need to consider that the free Hamiltonian acting on $|0\rangle$ gives

$$\hat{H}_0|0\rangle = -I_p|0\rangle, \tag{8}$$

and the free Hamiltonian over the continuum states defines an asymptotically free (outgoing) electron wave packet

$$\left[-\frac{1}{2}\nabla^2 + V(\mathbf{r})\right]|\mathbf{v}\rangle = \frac{\mathbf{v}^2}{2}|\mathbf{v}\rangle. \tag{9}$$

The time-evolution of the transition amplitude then results:

$$\begin{aligned} i\int d^3\mathbf{v}\,\dot{b}(\mathbf{v},t)\,|\mathbf{v}\rangle &= \int d^3\mathbf{v}\left(\frac{\mathbf{v}^2}{2} + I_p\right)b(\mathbf{v},t)|\mathbf{v}\rangle + \mathbf{E}(t)\cdot\mathbf{r}|0\rangle \\ &\quad + \mathbf{E}(t)\cdot\,\mathbf{r}\int d^3\mathbf{v} b(\mathbf{v},t)|\mathbf{v}\rangle. \end{aligned}\tag{10}$$

Note that we have assumed that the electron-nucleus interaction is neglected once the electron appears at the continuum, i.e., $V(\mathbf{r})|\mathbf{v}\rangle = 0$, which corresponds to the statement (iii) of Sec. **??**. Therefore, by multiplying Eq. (10) by $\langle\mathbf{v}'|$ and after some algebra,

$$\begin{aligned}\dot{b}(\mathbf{v},t) &= -i\left(\frac{\mathbf{v}^2}{2} + I_p\right)b(\mathbf{v},t) - i\mathbf{E}(t)\cdot\langle\mathbf{v}|\mathbf{r}|0\rangle \\ &\quad -i\,\mathbf{E}(t)\cdot\int d^3\mathbf{v}'\,\langle\mathbf{v}|\mathbf{r}\,b(\mathbf{v}',t)|\mathbf{v}'\rangle. \end{aligned}\tag{11}$$

The first term on the right-hand side of Eq. (11) represents the phase evolution of the electron in the oscillating laser field. In the second term we have defined the bound-free transition dipole matrix element as

$$\mathbf{d}(\mathbf{v}) = -\langle\mathbf{v}|\mathbf{r}|0\rangle, \tag{12}$$

and, finally, the last terms describe the continuum-continuum (C-C) processes,

$$\mathbf{G}(\mathbf{v},\mathbf{v}') = \langle\mathbf{v}|\mathbf{r}|\mathbf{v}'\rangle. \tag{13}$$

The processes in the continuum are fully determined by the scattering states, $\langle \mathbf{v}|/\langle \mathbf{v}'|$, constructed as a plane wave plus a correction. Working with the C-C matrix element and neglecting all the quadratic terms,

$$\langle \mathbf{v}|\mathbf{r}|\mathbf{v}'\rangle = \langle \mathbf{v}_p|\mathbf{r}|\mathbf{v}'_p\rangle + \langle \mathbf{v}_p|\mathbf{r}|\delta\mathbf{v}'\rangle + \langle \delta\mathbf{v}|\mathbf{r}|\mathbf{v}'_p\rangle. \tag{14}$$

This matrix element can be written in terms of two factors, it most singular part plus the rest, as:

$$\mathbf{G}(\mathbf{v},\mathbf{v}') = i\nabla_{\mathbf{v}}\delta(\mathbf{v}-\mathbf{v}') + \mathbf{g}(\mathbf{v},\mathbf{v}'). \tag{15}$$

The first term in Eq. (15) describes the continuum-continuum transition, $\nabla_{\mathbf{v}} b(\mathbf{v},t)$, without the influence of the scattering center and it governs the motion of a free electron in the laser field.

The second term, $\mathbf{g}(\mathbf{v},\mathbf{v}')$, includes all the rescattering processes and is called the rescattering transition matrix element. This is the matrix element where the potential core plays an essential role; it is related with the potential, $V(\mathbf{r})$, responsible for the elastic scattering of the electron with the ion-core.

Considering the above definitions the time variation of the transition amplitude $b(\mathbf{v},t)$ reads

$$\begin{aligned} \dot{b}(\mathbf{v},t) &= -i\left(\frac{\mathbf{v}^2}{2} + I_p\right) b(\mathbf{v},t) + i\,\mathbf{E}(t)\cdot\mathbf{d}(\mathbf{v}) \\ &\quad + \mathbf{E}(t)\cdot\nabla_{\mathbf{v}} b(\mathbf{v},t) - i\,\mathbf{E}(t)\cdot\int d^3\mathbf{v}'\, b(\mathbf{v}',t)\,\mathbf{g}(\mathbf{v},\mathbf{v}'). \end{aligned} \tag{16}$$

In the following we describe how it is possible to compute the transition amplitude, $b(\mathbf{v},t)$, by applying the zeroth- and first-order perturbation theory to the solution of the partial differential equation, Eq. (16). Therefore, according to this perturbation theory, we split the solution of the transition amplitude, $b(\mathbf{v},t)$, into two parts, $b_0(\mathbf{v},t)$ and $b_1(\mathbf{v},t)$; i.e., $b(\mathbf{v},t) = b_0(\mathbf{v},t) + b_1(\mathbf{v},t)$.

The zeroth order solution of our perturbation theory $b_0(\mathbf{v},t)$ is called the direct term. It describes the transition amplitude for a laser-ionized electron. This term, associated to the direct ionization processes, is directly related with the HHG process and also with those electrons contributing to the total ATI spectra that, once in the continuum, will never rescatter with the remaining ion core.

On the other hand, the first-order correction, named rescattered term, $b_1(\mathbf{v},t)$, is referred to electrons that, once ionized, have a certain probability of rescattering with the potential ion core. It is directly related with the high-energy region of the ATI spectra and essential to complete the HHG picture.

1.1.2 *Direct transition amplitude*

Let us consider the process where the electron is ionized without probability to return to the vicinity of its parent ion. This process is

modeled by the direct photoelectron transition amplitude $b_0(\mathbf{v}, t)$. As the direct ionization process should have a larger probability compared with the rescattering one [3], one can neglect the last term in Eq. (16). This is what we refer to as a zeroth-order solution:

$$\begin{aligned} \partial_t b_0(\mathbf{v}, t) &= -i\left(\frac{\mathbf{v}^2}{2} + I_p\right) b_0(\mathbf{v}, t) + i\,\mathbf{E}(t)\cdot\mathbf{d}(\mathbf{v}) \\ &\quad + \mathbf{E}(t)\cdot\nabla_{\mathbf{v}} b_0(\mathbf{v}, t). \end{aligned} \tag{17}$$

The above equation is a first-order inhomogeneous differential equation, which is easily solved by conventional integration methods (see, e.g., [32]). Therefore, the solution can be written as

$$\begin{aligned} b_0(\mathbf{v}, t) &= i\int_0^t dt'\,\mathbf{E}(t')\cdot\mathbf{d}\left[\mathbf{v} - \mathbf{A}(t) + \mathbf{A}(t')\right] \\ &\quad \times \exp\left(-i\int_{t'}^t d\tilde{t}\{[\mathbf{v} - \mathbf{A}(t) + \mathbf{A}(\tilde{t})]^2/2 + I_p\}\right). \end{aligned} \tag{18}$$

Here we have considered that the electron appears in the continuum with kinetic momentum $\mathbf{v}(t') = \mathbf{v} - \mathbf{A}(t) + \mathbf{A}(t')$ at the time t', where $\mathbf{v}$ is the final kinetic momentum (note that by virtue of using atomic units, where the electron mass $m = 1$, the kinetic electron momentum $\mathbf{p}_e$ and the electron velocity $\mathbf{v}$ have the same magnitude and direction), and $\mathbf{A}(t) = -\int^t \mathbf{E}(t')dt'$ is the vector potential of the electromagnetic field.

Introducing a new variable in the above equation, which is the canonical momentum $\mathbf{p} = \mathbf{v} - \mathbf{A}(t)$, is possible then to write Eq. (18) as a function of the canonical momentum as [1],

$$\begin{aligned} b_0(\mathbf{p}, t) &= i\int_0^t dt'\,\mathbf{E}(t')\cdot\mathbf{d}\left[\mathbf{p} + \mathbf{A}(t')\right] \\ &\quad \times \exp\left(-i\int_{t'}^t d\tilde{t}\,\{[\mathbf{p} + \mathbf{A}(\tilde{t})]^2/2 + I_p\}\right). \end{aligned} \tag{19}$$

This last expression is understood as the sum of all the ionization events which occur from the time t' to t. Then the instantaneous transition probability amplitude of an electron at a time t', at which it appears into the continuum with momentum $\mathbf{v}(t') = \mathbf{p} + \mathbf{A}(t')$, is defined by the argument of the integral in Eq. (19). Furthermore, the exponent phase factor in Eq. (19) denotes the "semiclassical action", $S(\mathbf{p}, t, t')$:

$$S(\mathbf{p}, t, t') = \int_{t'}^t d\tilde{t}\,\left\{[\mathbf{p} + \mathbf{A}(\tilde{t})]^2/2 + I_p\right\}. \tag{20}$$

This phase factor defines a possible electron trajectory from the birth time t' until the "recombination", in the case of HHG [1], or "detection" time t, for ATI [3].

1.1.3 *Rescattering transition amplitude*

In order to find a solution for the transition amplitude of the rescattered photoelectrons, $b_1(\mathbf{v},t)$, we have considered the rescattering core matrix element term of Eq. (16) different than zero; i.e., $\mathbf{g}(\mathbf{v},\mathbf{v}') \neq \mathbf{0}$. In addition, the first-order perturbation theory is applied to obtain $b_1(\mathbf{v},t)$ by inserting the zeroth-order solution $b_0(\mathbf{v},t)$ in the right-hand side of Eq. (18),

$$\begin{aligned} \dot{b}_1(\mathbf{v},t) &= -i\left(\frac{\mathbf{v}^2}{2}+I_p\right) b_1(\mathbf{v},t) \\ &\quad -i\,\mathbf{E}(t)\cdot\int d^3\mathbf{v}'\, b_0(\mathbf{v}',t)\,\mathbf{g}(\mathbf{v},\mathbf{v}'). \end{aligned} \tag{21}$$

Then we obtain $b_1(\mathbf{p},t)$ as a function of the canonical momentum $\mathbf{p}$ as follows:

$$\begin{aligned} b_1(\mathbf{p},t) &= -\int_0^t dt' \int_0^{t'} dt'' \int d^3\mathbf{p}'\, \exp\left[-iS(\mathbf{p}',t',t'')\right] \\ &\quad \times \mathbf{E}(t'')\cdot\mathbf{d}\left[\mathbf{p}'+\mathbf{A}(t'')\right] \\ &\quad \times \mathbf{E}(t')\cdot\,\mathbf{g}\left[\mathbf{p}+\mathbf{A}(t'),\mathbf{p}'+\mathbf{A}(t')\right]\,\exp\left[-iS(\mathbf{p},t,t')\right]. \end{aligned} \tag{22}$$

This last equation contains all the information about the rescattering process. In particular, it is referred to the probability amplitude of an emitted electron at the time t'', with an amplitude given by $\mathbf{E}(t'')\cdot\mathbf{d}\,[\mathbf{p}'+\mathbf{A}(t'')]$. In this step the electron has a kinetic momentum of $\mathbf{v}'(t'')=\mathbf{p}'+\mathbf{A}(t'')$. The last factor, $\exp[-iS(\mathbf{p}',t',t'')]$, is the accumulated phase of an electron born at the time t'' until it rescatters at time t'. It is a "semiclassical action" defined as,

$$S(\mathbf{p}',t',t'') = \int_{t''}^{t'} d\tilde{t}\,\left\{[\mathbf{p}+\mathbf{A}(\tilde{t})]^2/2+I_p\right\}. \tag{23}$$

The term, $\mathbf{g}[\mathbf{p}+\mathbf{A}(t'),\ \mathbf{p}'+\mathbf{A}(t')]$, contains the structural matrix element of the transition continuum-continuum at the rescattering time t'. At this particular moment in time, the electron changes its momentum from $\mathbf{p}'+\mathbf{A}(t')$ to $\mathbf{p}+\mathbf{A}(t')$. We stress, however, that the term $\mathbf{g}(\mathbf{v},\mathbf{v}')$ does not necessarily imply that the electron returns to the ion core. In addition, $\exp[-iS(\mathbf{p},t,t')]$ defines the accumulated phase of the electron after the rescattering from the time t' to the "final" one t when the electron is "measured" at the detector with momentum $\mathbf{p}$.

1.2 THEORY OF HHG AND ATI WITHIN THE SFA

So far we have formulated a model to analytically obtain the direct and the rescattering transition amplitudes for an atom exposed to a strong laser field. In the following section we develop a quantum mechanical approach for HHG and ATI using the generalized SFA model described previously [1–4].

1.2.1 *Time-dependent dipole moment*

The source of the additional frequencies that are generated during the interaction of a strong laser pulse with an atomic or molecular target, is the nonlinear dipole oscillation of the medium. Therefore, the aim is to calculate this dipole response by means of the solution of the TDSE. The time-dependent dipole moment can be written as:

$$\vec{\mu}(t) = -\langle \Psi(t)|\mathbf{r}_e|\Psi(t)\rangle, \tag{24}$$

where $|\Psi(t)\rangle$, is the state describing the time evolution of the atomic or molecular system under study and $\mathbf{r}_e = q_e\mathbf{r}$. In general, within the SFA statement, we can write the wave function of the whole system as a superposition of the ground, $|0\rangle$, and continuum states, $|\mathbf{v}\rangle$, as in Eq. (5), where the transition amplitude of the continuum states is denoted by $b(\mathbf{v}, t)$.

After some algebra with the above equations and only considering transitions from the bound to the continuum states, we have:

$$\begin{aligned}\langle \Psi(t)|\mathbf{r}_e|\Psi(t)\rangle &= \langle 0|\mathbf{r}_e|0\rangle + \int d^3\mathbf{v}\, \langle 0|\mathbf{r}_e b(\mathbf{v}, t)|\mathbf{v}\rangle + \int d^3\mathbf{v}\, b^*(\mathbf{v}, t)\langle \mathbf{v}|\mathbf{r}_e|0\rangle \\ &\quad + \int d^3\mathbf{v}' \int d^3\mathbf{v}\, b^*(\mathbf{v}', t)\langle \mathbf{v}'|\mathbf{r}_e b(\mathbf{v}, t)|\mathbf{v}\rangle. \end{aligned} \tag{25}$$

Note that the first term vanishes since $\langle 0|\mathbf{r}_e|0\rangle = 0$. Moreover, the last term contains the information of continuum-continuum events. Here we apply an additional approximation, neglecting this term, which doest not contribute to the recombination process of HHG.

We are left, then, with the time-dependent dipole moment as

$$\begin{aligned}\vec{\mu}(t) &= \int d^3\mathbf{v}\, b(\mathbf{v}, t)\langle 0|\mathbf{r}_e|\mathbf{v}\rangle + \int d^3\mathbf{v}\, b^*(\mathbf{v}, t)\langle \mathbf{v}|\mathbf{r}_e|0\rangle, \\ &= \int d^3\mathbf{v}\, b(\mathbf{v}, t)\, \mathbf{d}^*(\mathbf{v}) + c.c., \end{aligned} \tag{26}$$

where $\langle \mathbf{v}|\mathbf{r}_e|0\rangle$ is the the bound-continuum transition dipole matrix element defined in Eq. (12). In the above equation we have neglected the contribution from the rescattering part of the total transition amplitude and we are considering transitions from the continuum to the ground state. Moreover the transition amplitude contributing to the time-dependent dipole is the direct transition amplitude, called before $b_0(\mathbf{v}, t)$.

The radiation emitted by a single atom is then proportional to the time-dependent dipole moment $\vec{\mu}(t)$. The HHG spectrum, $\mathcal{I}(\omega)$, with polarization along a direction $\mathbf{e}_i$ can be calculated from the time-dependent induced dipole moment

$$\vec{\mu}_{\mathbf{e}_i}(t) = \mathbf{e}_i \cdot \int d^3\mathbf{v}\, b(\mathbf{v}, t)\, \mathbf{d}^*(\mathbf{v}) + c.c.. \tag{27}$$

In this way, the harmonic spectrum is calculated as the modulus squared of the Fourier-transformed dipole acceleration $\mathbf{a}(t)$ related to the defined time-dependent dipole matrix element [Eq. (26)] by the Ehrenfest theorem as $|\tilde{\mathbf{a}}(\omega)| = |\omega^2\,\tilde{\mu}(\omega)|$. Finally, we can compute the HHG spectra as

$$\mathcal{I}(\omega) \propto \left| \int_{-\infty}^{\infty} dt\, e^{i\omega t}\, \vec{\mu}(t) \right|^2 . \tag{28}$$

Notice that the harmonic spectra depend directly on the time-dependent dipole moment. The latter in turn depends on the form of the bound-continuum matrix element and the continuum states transition amplitude, that are different for each of atomic system under study.

1.2.1.1 *Calculation of the time-dependent dipole moment*

The transition amplitude for the continuum states, the zeroth-order solution, is defined in Eq. (19), where the "semiclassical action" defines all the possible electron trajectories from the "birth" time t' until the "recombination" one t.

Inserting Eq. (19) in the time-dependent dipole moment, Eq. (26), we get

$$\vec{\mu}(t) = i \int_0^t dt' \int d^3\mathbf{p}\, \mathbf{E}(t') \cdot \mathbf{d}\left[\mathbf{p} + \mathbf{A}(t')\right] e^{-i\,S(\mathbf{p},t,t')} \times \mathbf{d}^*[\mathbf{p} + \mathbf{A}(t)] + c.c.. \tag{29}$$

Equation (29) has to be understood as follows: the electron is ionized at time t' with a certain probability defined by $\mathbf{E}(t') \cdot \mathbf{d}[\mathbf{p} + \mathbf{A}(t')]$. During its excursion in the continuum the electronic wave function is then propagated until the time t, acquiring a classical phase $S(\mathbf{p}, t, t')$, to finally recombine with the ion core at time t with a rate given by $\mathbf{d}^*[\mathbf{p} + \mathbf{A}(t)]$. All possible combinations of birth time and momenta must be considered and therefore a multidimensional integration is required, where their contributions are coherently added up.

1.2.1.2 *Saddle-point method*

Equation (29) configures a highly oscillatory integral, both in the momentum $\mathbf{p}$ and t' variables. As a consequence, to reduce the computational time and obtain a physical meaning of the HHG process, we employ the stationary-phase or saddle-point method to evaluate it.

The fast oscillations of the momentum $\mathbf{p}$ integral, suggests to use the saddle-point method to solve Eq. (29). The dipole matrix element in Eq. (29) changes typically on a scale of the order of $p^2 \simeq I_p$. The quasiclasical action, on the other hand, changes on the scale of $p^2 \simeq 1/(t - t')$; so for $(t - t')$ of the order of one period of the laser field the quasiclassical action varies thus much faster than the other factors

in Eq. (29). Then, the integral over the momentum of Eq. (29) tends towards zero except near the extremal points of the phase; i.e.,

$$\nabla_{\mathbf{p}} S(\mathbf{p}, t, t') = \mathbf{0}. \tag{30}$$

Thus, the main contributions to the momentum integral are dominated by momenta, $\mathbf{p}_s$, which satisfy the solution of the equation: $\nabla_{\mathbf{p}} S(\mathbf{p})|_{\mathbf{p}_s} = \mathbf{0}$. These saddle-point momenta read:

$$\mathbf{p}_s = -\frac{1}{\tau}\int_{t'}^{t} \mathbf{A}(\tilde{t})\mathbf{d}\tilde{t}. \tag{31}$$

Here $\tau = t - t'$ is the excursion time of the electron in the continuum. The statement in Eq. (30) can be read as a return condition, i.e. given any two arbitrary ionization and recollision times t' and t, there will always exist a unique canonical momentum $\mathbf{p}_s$ such that an electron ionized at t' will recollide with the ion at time t. Equation (30) is nothing else but the difference between the position of the free electron at the respective ionization and recombination times,

$$\nabla_{\mathbf{p}} S(\mathbf{p}, t, t') = \mathbf{r}(t) - \mathbf{r}(t'). \tag{32}$$

In terms of classical mechanics, these momenta roots $\mathbf{p}_s$ are those corresponding to the classical electron trajectories because the momentum gradient of the action can be understood as the displacement of a particle [33]. As the momentum gradient of the action is null $\Delta\mathbf{r} = \nabla_{\mathbf{p}} S(\mathbf{p}, t, t') = \mathbf{0}$, the considered electron trajectories, $\mathbf{r}(t)$, are for an electron that is born at the time t' at a certain position $\mathbf{r}(t') = \mathbf{r}_0$. Then, after some time t the electron returns to the initial position $\mathbf{r}(t) = \mathbf{r}_0$ with an average momentum $\mathbf{p}_s$.

Therefore, the function $S(\mathbf{p}, t, t')$ can be expanded in Taylor series around the roots $\mathbf{p}_s$ and we can then apply the standard saddle-point method to the 3D momentum integral over $\mathbf{p}$ as:

$$\begin{aligned}
&\int d^3\mathbf{p}\, f(\mathbf{p}) \exp\left[-iS(\mathbf{p})\right] \\
&= \int d^3\mathbf{p}\, f(\mathbf{p}_s) \exp\left\{-i\left[S(\mathbf{p}_s) + \frac{1}{2}\nabla_{\mathbf{p}}^2 S(\mathbf{p})\Big|_{\mathbf{p}_s} \cdot (\mathbf{p} - \mathbf{p}_s)^2\right]\right\} \\
&\approx \left[\frac{\pi}{\varepsilon + \frac{i(t-t')}{2}}\right]^{\frac{3}{2}} \exp\left[-iS(\mathbf{p}_s)\right] f(\mathbf{p}_s).
\end{aligned} \tag{33}$$

Here we have introduced an infinitesimal parameter, ε, to avoid the divergence at $t = t'$. Still, the singularity is not integrable and practically impossible to be treated numerically. One should stress, however, that it is the result of the saddle-point approximation restricted exclusively to the classical action. We have regarded in the calculation that the function $f(\mathbf{p})$ is localized at a certain scale and consequently

the singularity would simply disappear. This observation and the simple method to handle it has been pioneered in Ref. [1]; we sketch the arguments to support this hypothesis in Appendix 5.

Finally, the time-dependent dipole moment for the atomic system results:

$$\begin{aligned}\vec{\mu}(t) &= i\int_0^t dt' \left[\frac{\pi}{\varepsilon + \frac{i(t-t')}{2}}\right]^{\frac{3}{2}} \mathbf{E}(t')\cdot\mathbf{d}\left[\mathbf{p}_s + \mathbf{A}(t')\right] \\ &\quad \times e^{-iS(\mathbf{p}_s,t,t')}\ \mathbf{d}^*[\mathbf{p}_s + \mathbf{A}(t)] + c.c.. \end{aligned} \tag{34}$$

The HHG spectrum $\mathcal{I}(\omega)$ is then numerically computed inserting Eq. (34) in Eq. (28).

In this section, we have defined how to compute the HHG spectra for an atomic system. In order to have all the ingredients to compute $\mathcal{I}(\omega)$ using the Eq. (28), we need to know the exact dependency of the bound-continuum matrix element and the transition amplitude for the continuum states. The method to find these quantities for an atom under the influence of an intense laser pulse will be described later in Sec. 1.3.

1.2.2 *Photoelectron spectra: Total transition amplitude*

The ATI process accounts for direct tunneling ionization, $b_0(\mathbf{p}, t)$, and rescattering, $b_1(\mathbf{v}, t)$, events. The total ATI spectra is related with the total transition amplitude, $b(\mathbf{v}, t) = b_0(\mathbf{v}, t) + b_1(\mathbf{v}, t)$ and includes both the zeroth- and first-order correction of our perturbation theory.

In particular, the photoelectron spectra, $|b(\mathbf{p}, t_F)|^2$, is a coherent superposition of both solutions, i.e. $b_0(\mathbf{p}, t_F)$ and $b_1(\mathbf{p}, t_F)$:

$$\begin{aligned}|b(\mathbf{p}, t_F)|^2 &= |b_0(\mathbf{p}, t_F) + b_1(\mathbf{p}, t_F)|^2, \\ &= |b_0(\mathbf{p}, t_F)|^2 + |b_1(\mathbf{p}, t_F)|^2 + b_0(\mathbf{p}, t_F)b_1^*(\mathbf{p}, t_F) + c.c.\end{aligned} \tag{35}$$

In the case of ATI the zeroth order solution, $b_0(\mathbf{p}, t)$, describes the transition amplitude for an electron going into the continuum at time t' that will never rescatter off with the remaining ion core and is defined in Eq. (19).

As our purpose is to obtain the final transition amplitude $b_0(\mathbf{p}, t)$, the time t will be fixed at the end of the laser field, $t = t_F$. For our calculations, we then define the integration time window as t: $[0, t_F]$. Therefore, we set $\mathbf{E}(0) = \mathbf{E}(t_F) = \mathbf{0}$ in such a way to make sure that the electromagnetic field is a time oscillating wave and does not contain static components. The same arguments are applied to the vector potential $\mathbf{A}(t)$. Additionally, we define the laser pulse envelope as $f(t) = \sin^2(\frac{\omega_0 t}{2N_c})$ where N_c denotes the number of total cycles.

On the other hand, the rescattered term $b_1(\mathbf{p}, t)$, Eq. (22), is referred to the electron that, once ionized, will have a certain probability of rescattering with the potential ion core.

The complex transition amplitude, Eq. (19), is a "single time integral" and it can be integrated numerically without major problems. However, the multiple time ("2D") and momentum ("3D") integrals of the rescattering term [Eq. (22)] present a very difficult and demanding task from a computational perspective. In order to reduce the computational difficulties and to obtain a physical meaning of the ATI process, we employ the saddle-point method to evaluate these highly oscillatory integrals, in a similar way as we did before for HHG (see Sec. 1.2.1.2).

The fast oscillations of the momentum $\mathbf{p}'$ integral for the electron rescattering transition amplitude, $b_1(\mathbf{p}, t)$, suggests indeed to use the saddle-point method to solve Eq. (22) as well. This method is expected to be accurate when both the U_p and the I_p, as well as the involved momentum $\mathbf{v}$ and $\mathbf{v}'$, are large. As the quasiclassical action $S(\mathbf{p}', t', t'')$ is proportional to I_p, U_p and $\mathbf{v}'^2$, the phase factor $\exp[-iS(\mathbf{p}', t', t'')]$ oscillates very rapidly. Then, the integral over the momentum $\mathbf{p}'$ of Eq. (22) tends towards zero except near the extremal points of the phase. The main contributions to the momentum integral are dominated by the saddle-point momenta $\mathbf{p}'_s = -\frac{1}{\tau}\int_{t''}^{t'} \mathbf{A}(\tilde{t})d\tilde{t}$ that are similar to the ones defined in Eq. (31). Here $\tau = t' - t''$ is the excursion time of the electron in the continuum. Similar to the HHG case, in terms of classical mechanics, $\mathbf{p}'_s$ are those momenta roots corresponding to the classical electron trajectories; an electron that is born at the time t'', at a certain position $\mathbf{r}(t'') = \mathbf{r}_0$, that, after some time t' in the continuum, returns to the initial position $\mathbf{r}(t') = \mathbf{r}_0$ with an average momentum $\mathbf{p}'_s$.

Therefore, we can apply the standard saddle-point method to the 3D momentum integral over $\mathbf{p}'$. Following the same reasoning as in Eq. (33) the transition amplitude for the rescattering electrons becomes:

$$\begin{aligned} b_1(\mathbf{p}, t) \;=\; & -\int_0^t dt' e^{-i\int_{t'}^{t} d\tilde{t}\left\{[\mathbf{p}+\mathbf{A}(\tilde{t})]^2/2+I_p\right\}}\, \mathbf{E}(t') \\ & \cdot \int_0^{t'} dt'' \times \mathbf{g}\left[\mathbf{p}+\mathbf{A}(t'), \mathbf{p}'_s+\mathbf{A}(t')\right] \\ & \times \left[\frac{\pi}{\varepsilon + \frac{i(t'-t'')}{2}}\right]^{\frac{3}{2}} \mathbf{E}(t'') \cdot \mathbf{d}\left[\mathbf{p}'_s+\mathbf{A}(t'')\right] \\ & \times e^{-i\int_{t''}^{t'} d\tilde{t}\left\{[\mathbf{p}'_s+\mathbf{A}(\tilde{t})]^2/2+I_p\right\}}. \end{aligned} \tag{36}$$

Here we have introduced other infinitesimal parameter, ε, to avoid now the divergence at $t' = t''$. As before, the singularity is not integrable and practically impossible to be treated numerically. The simplest way to avoid the problem is to set ε small, but nonzero; for more details see the Appendix 5.

With the last equation we have substantially reduced the dimensionality of the problem from a 5D integral to a 2D one. As the com-

puting time depends on the dimensionality of the integration problem, this reduction is extremely advantageous from a computational viewpoint. Moreover, with the saddle-point method a quasiclassical picture for the rescattering transition amplitude is obtained similar to the approach described in Refs. [3, 22].

The main problem in calculating the HHG and ATI spectrum is then the computation of the bound-free transition dipole matrix element, $\mathbf{d}(\mathbf{v})$, and the continuum-continuum transition rescattering matrix element $\mathbf{g}(\mathbf{v}, \mathbf{v}')$ for a given atomic system. In the next section, we introduce a SR potential model in order to compute both the transition matrix elements and the final photoelectron momentum distribution analytically.

1.3 MODEL ATOM

In this section, as a test case for our model, we choose a nonlocal, but separable, atomic SR potential with the purpose of computing both the direct and the rescattering transition amplitudes. These terms involve the dipole and the C-C matrix elements defined by Eqs. (12) and (15). Then our main task will be devoted to analytically finding the wave functions for the ground and scattering states of our SR potential. The Hamiltonian, $\hat{H}(\mathbf{p}, \mathbf{p}')$, of the atomic system in the momentum representation can be written as

$$\hat{H}(\mathbf{p}, \mathbf{p}') = \frac{\mathbf{p}^2}{2}\delta(\mathbf{p} - \mathbf{p}') + \hat{V}(\mathbf{p}, \mathbf{p}'), \tag{37}$$

where the first term on the right-hand side is the kinetic energy operator, and the second one is the interacting nonlocal SR potential $\hat{V}(\mathbf{p}, \mathbf{p}')$. The nonlocal SR potential can be written as follows,

$$\hat{V}(\mathbf{p}, \mathbf{p}') = -\gamma\, U(\mathbf{p})\, U(\mathbf{p}'), \tag{38}$$

and describes the attraction between the electron and the nucleus [3]. The auxiliary function $U(\mathbf{p})$ is defined by

$$U(\mathbf{p}) = \frac{1}{\sqrt{\mathbf{p}^2 + \Gamma^2}}. \tag{39}$$

This SR potential has been chosen such that it assures analytical solutions for the continuum or scattering states, i.e. , for states with energies $E > 0$. Note that the ground state can also be calculated analytically. γ is understood as a screening parameter and the parameter Γ is a constant related with the shape of the ground state.

By using such a Hamiltonian, we write the stationary Schrödinger equation, $E\,\Psi(\mathbf{p}) = \hat{H}(\mathbf{p})\Psi(\mathbf{p})$, as:

$$\begin{aligned} \hat{H}(\mathbf{p})\Psi(\mathbf{p}) &= \int d^3\mathbf{p}'\hat{H}(\mathbf{p},\mathbf{p}')\Psi(\mathbf{p}'), \\ E\,\Psi(\mathbf{p}) &= \frac{p^2}{2}\int d^3\mathbf{p}'\delta(\mathbf{p}-\mathbf{p}')\Psi(\mathbf{p}') \\ &\quad -\gamma U(\mathbf{p})\int d^3\mathbf{p}' U(\mathbf{p}')\Psi(\mathbf{p}'), \end{aligned} \tag{40}$$

where E denotes the energy of the wave function $\Psi(\mathbf{p})$.

In the following chapters we use this nonlocal SR potential to describe the interaction of the tunnel-ionized electron with the remaining ion core. This potential, Eq. (38), defined in the momentum space, is related with the space coordinates through a Fourier transform, $\hat{V}(\mathbf{x}) = FT\{\hat{V}(\mathbf{p})\}$. The auxiliary function defined in Eq. (39) turns in a modified Bessel function of the second kind (Macdonald function) in the space representation.

1.3.1 *Ground state and bound-continuum dipole matrix elements*

1.3.1.1 *Ground state*

In order to analytically obtain the ground state, $\Psi_0(\mathbf{p})$, we solve the stationary Schrödinger equation, Eq. (40), in the momentum representation

$$\frac{p^2}{2}\Psi_0(\mathbf{p}) - \frac{\gamma}{\sqrt{p^2+\Gamma^2}}\int\frac{d^3\mathbf{p}'\Psi_0(\mathbf{p}')}{\sqrt{p'^2+\Gamma^2}} = E_0\,\Psi_0(\mathbf{p}), \tag{41}$$

where the parameter γ is related to the ionization potential, I_p, of the atomic species under study. To solve Eq. (41) we consider a new variable as,

$$\breve{\varphi} = \int\frac{d^3\mathbf{p}'\Psi_0(\mathbf{p}')}{\sqrt{p'^2+\Gamma^2}}, \tag{42}$$

so the Schrödinger equation reduces to a purely algebraic equation,

$$\left(\frac{p^2}{2}+I_p\right)\Psi_0(\mathbf{p}) = \frac{\gamma}{\sqrt{p^2+\Gamma^2}}\breve{\varphi}, \tag{43}$$

where we have written the eigenenergy $E_0 = -I_p$. Therefore, the final solution reads:

$$\Psi_0(\mathbf{p}) = \frac{\mathcal{N}}{\sqrt{(p^2+\Gamma^2)(\frac{p^2}{2}+I_p)}} \tag{44}$$

where $\mathcal{N} = \gamma\,\breve{\varphi}$ denotes a normalization constant. By dividing the last formula by $\sqrt{p^2+\Gamma^2}$ and taking the volume integral on $\mathbf{p}$, we finally obtain

$$\breve{\varphi} = \gamma\breve{\varphi}\int\frac{d^3\mathbf{p}}{(p^2+\Gamma^2)(\frac{p^2}{2}+I_p)}. \tag{45}$$

The solution of the last integral in Eq. (45) gives us the relationship between the parameters I_p, Γ and γ:

$$\begin{aligned} \gamma \int_0^{2\pi} d\theta \int_0^{\pi} d\varphi \, \sin\varphi \int_0^{\infty} \frac{dp\, p^2}{(p^2+\Gamma^2)(\frac{p^2}{2}+I_p)} &= 1, \\ \frac{4\pi^2\gamma}{\Gamma+\sqrt{2I_p}} &= 1. \end{aligned} \tag{46}$$

This last equation allows us to control the parameters Γ or γ, in such a way as to match the I_p of the atomic system under scrutiny. Furthermore, by using the normalization condition for the bound states, $\int d^3\mathbf{p}\, \Psi_0^*(\mathbf{p})\Psi_0(\mathbf{p}) = 1$, we have:

$$\begin{aligned} \mathcal{N}^2 \int_0^{2\pi} d\theta \int_0^{\pi} d\varphi \, \sin\varphi \int_0^{\infty} \frac{dp\, p^2}{(p^2+\Gamma^2)(\frac{p^2}{2}+I_p)^2} &= 1, \\ 4\pi\mathcal{N}^2 \int_0^{\infty} \frac{dp\, p^2}{(p^2+\Gamma^2)(\frac{p^2}{2}+I_p)^2} &= 1. \end{aligned} \tag{47}$$

In this way the normalization constant is defined as,

$$\mathcal{N} = [1/I_{1N}]^{1/2}, \tag{48}$$

where solving the normalization integral as,

$$I_{1N} = 4\cdot 4\pi \int_0^{\infty} \frac{dp\, p^2}{(p^2+\Gamma^2)(p^2+2I_p)^2} = \frac{4\pi^2}{\sqrt{2I_p}(\Gamma+\sqrt{2I_p})^2}, \tag{49}$$

we calculate the normalization constant, as well as the analytical ground wave function $\Psi_0(\mathbf{p})$. Explicitly, the normalization factor reads

$$\mathcal{N}^2 = \frac{\sqrt{2I_p}\left(\Gamma+\sqrt{2I_p}\right)^2}{4\pi^2}. \tag{50}$$

1.3.1.2 *Bound-continuum transition matrix element*

So far we have obtained, analytically, the ground state supported by our nonlocal SR potential model. This ground state allow us to calculate the bound-free transition dipole matrix element by using Eq. (12). The free or continuum state is approximated as a plane wave of a given momentum, $\mathbf{p}_0$, and therefore the bound-free transition dipole matrix in the momentum representation reads:

$$\begin{aligned} \mathbf{d}(\mathbf{p}_0) &= i\int \delta(\mathbf{p}'-\mathbf{p}_0)\nabla_{\mathbf{p}'}\Psi_0(\mathbf{p}')\, d^3\mathbf{p}', \\ &= -i\nabla_{\mathbf{p}'}\Psi_0(\mathbf{p}')\big|_{\mathbf{p}_0}. \end{aligned} \tag{51}$$

Inserting Eq. (44) in the above equation and after some elementary algebra, we obtain the transition dipole matrix:

$$\begin{aligned} \mathbf{d}(\mathbf{p}_0) &= -i\mathcal{N}\nabla_{\mathbf{p}'}\left[\frac{1}{(p'^2+\Gamma^2)^{\frac{1}{2}}\left(\frac{p'^2}{2}+I_p\right)}\right]\Bigg|_{\mathbf{p}_0}, \\ &= -i\mathcal{N}\mathcal{A}(\mathbf{p}_0), \end{aligned} \tag{52}$$

where, $\mathcal{A}(\mathbf{p}_0)$ is defined as

$$\mathcal{A}(\mathbf{p}_0) = \frac{-2\mathbf{p}_0\,(3p_0^2 + 2I_p + 2\Gamma^2)}{(p_0^2+\Gamma^2)^{\frac{3}{2}}(p_0^2+2I_p)^2}. \tag{53}$$

Now we have all the ingredients to calculate the HHG spectra of any atom by Eqs. (34) and (28). So far we have obtained the general form of the atomic bound-free dipole matrix element. Moreover, depending on the atomic system that we want to study, we need to particularize and find the values of the corresponding Γ and γ parameters.

The second important quantity to be calculated before evaluating the whole transition amplitude $b(\mathbf{p}, t)$ is the rescattering transition matrix element, $\mathbf{g}(\mathbf{p}, \mathbf{p}')$. Hence, we need to find the scattering or continuum wave functions of our model potential. These states are obtained by analytically solving the time-independent Schrödinger equation in the momentum representation for positive energies.

1.3.2 *Scattering waves and continuum-continuum transition matrix element*

Let us consider the scattering wave, $\Psi_{\mathbf{p}_0}(\mathbf{p})$, with asymptotic momentum, $\mathbf{p}_0$, as a coherent superposition of a plane wave and an extra correction $\delta\Psi_{\mathbf{p}_0}(\mathbf{p})$:

$$\Psi_{\mathbf{p}_0}(\mathbf{p}) = \delta(\mathbf{p}-\mathbf{p}_0) + \delta\Psi_{\mathbf{p}_0}(\mathbf{p}). \tag{54}$$

This state has an energy $E = \mathbf{p}_0^2/2$. Then the Schrödinger equation in momentum representation, Eq. (40), for $\Psi_{\mathbf{p}_0}(\mathbf{p})$ reads

$$\begin{aligned}
\frac{p_0^2}{2}\,\Psi_{\mathbf{p}_0}(\mathbf{p}) &= \frac{p^2}{2}\,\Psi_{\mathbf{p}_0}(\mathbf{p}) - \frac{\gamma}{\sqrt{p^2+\Gamma^2}}\int \frac{d^3\mathbf{p}'\,\Psi_{\mathbf{p}_0}(\mathbf{p}')}{\sqrt{p'^2+\Gamma^2}}, \\
\left(\frac{p^2}{2} - \frac{p_0^2}{2}\right)\delta\Psi_{\mathbf{p}_0}(\mathbf{p}) &= \frac{\gamma}{\sqrt{p^2+\Gamma^2}\sqrt{p_0^2+\Gamma^2}} \\
&\quad + \frac{\gamma}{\sqrt{p^2+\Gamma^2}}\int \frac{d^3\mathbf{p}'\,\delta\Psi_{\mathbf{p}_0}(\mathbf{p}')}{\sqrt{p'^2+\Gamma^2}}.
\end{aligned} \tag{55}$$

In the last equation, we had applied elementary algebra and the following Dirac δ distribution properties: $(\frac{p^2}{2} - \frac{p_0^2}{2})\,\delta(\mathbf{p}-\mathbf{p}_0) = 0$ and $\int \frac{d^3\mathbf{p}'\,\delta(\mathbf{p}'-\mathbf{p}_0)}{\sqrt{p'^2+\Gamma^2}} = \frac{1}{\sqrt{p_0^2+\Gamma^2}}$.

We proceed analogously to the ground state case. Lets define a new variable as in Eq. (42), $\breve{\varphi}' = \int \frac{d^3\mathbf{p}'\,\delta\Psi(\mathbf{p}')}{\sqrt{p'^2+\Gamma^2}}$. After this, the correction $\delta\Psi_{\mathbf{p}_0}$ results:

$$\delta\Psi_{\mathbf{p}_0}(\mathbf{p}) = \frac{\mathcal{B}(\mathbf{p}_0)}{\sqrt{p^2+\Gamma^2}\,(p_0^2 - p^2 + i\epsilon)}, \tag{56}$$

where $\mathcal{B}(\mathbf{p}_0)$ is a constant quantity with respect to $\mathbf{p}$, which depends on the asymptotic momentum $\mathbf{p}_0$ and is defined as:

$$\mathcal{B}(\mathbf{p}_0) = -2\gamma\left[\frac{1}{\sqrt{p_0^2+\Gamma^2}} + \breve{\varphi}'\right]. \tag{57}$$

In Eq. (56), ϵ is another infinitesimal parameter introduced to avoid the divergence at the "energy shell" $p^2 = p_0^2$ and . The singularity at the "energy shell" is avoided due to the finite spread of the involved wave packets. In all our atomic numerical calculations we set $\epsilon = 0.2$ a.u. $= 0.4 I_p$. A detailed discussion about this point is contained in the Appendix 5 and in the following sections.

$\mathcal{B}(\mathbf{p}_0)$ is obtained by integrating Eq. (56) multiplied by $\frac{1}{\sqrt{p^2+\Gamma^2}}$. In this way we get $\breve{\varphi}'$ as a function of $\mathcal{B}(\mathbf{p}_0)$ and insert it in Eq. (57) getting that,

$$\mathcal{B}(\mathbf{p}_0) = \frac{-2\gamma}{(p_0^2+\Gamma^2)^{\frac{1}{2}}}\left(1 - \frac{4\pi^2 i\gamma}{|p_0| + i\Gamma}\right)^{-1}. \tag{58}$$

Finally, the scattering wave functions can be written as

$$\Psi_{\mathbf{p}_0}(\mathbf{p}) = \delta(\mathbf{p}-\mathbf{p}_0) + \frac{\mathcal{B}(\mathbf{p}_0)}{\sqrt{p^2+\Gamma^2}\left(p_0^2 - p^2 + i\epsilon\right)}. \tag{59}$$

The later equation tells us that the correction $\delta\Psi_{\mathbf{p}_0}(\mathbf{p})$ to the plane wave is a function of the parameters of the atomic potential, Γ and γ. Therefore, the rescattering process will depend on the shape of the potential. However, in the limit when the momentum $\mathbf{p}_0$ goes to infinity this correction term vanishes, i.e., $\lim_{\mathbf{p}_0\to\infty} \delta\Psi_{\mathbf{p}_0}(\mathbf{p}) = 0$, and then the atomic potential does not play any role in the rescattering process.

1.3.2.1 *Continuum-continuum transition matrix element*

Let us consider the scattering waves obtained in Eq. (59) and use them to evaluate the rescattering transition matrix element presented in Eq. (15), i.e.,

$$\mathbf{g}(\mathbf{p}_1, \mathbf{p}_2) \;=\; \langle \delta_{\mathbf{p}_1} | \mathbf{r} | \delta\Psi_{\mathbf{p}_2} \rangle + \langle \delta\Psi_{\mathbf{p}_1} | \mathbf{r} | \delta_{\mathbf{p}_2} \rangle. \tag{60}$$

In here notice that $\langle \delta\Psi_{\mathbf{p}_1} | \mathbf{r} | \delta\Psi_{\mathbf{p}_2} \rangle$ is not considered. In the present case this term, proportional to $\mathcal{B}^*(\mathbf{p}_1)\mathcal{B}(\mathbf{p}_2)$, vanishes due to the rotational symmetry [in fact, $\mathcal{B}(\mathbf{p}_1)$ depends on p_1^2 only, while the scattering parts of the wave functions depend only on p^2]. In general, we can restrict ourselves to the first order perturbation theory, and neglect all quadratic or superior terms in γ. So, the rescattering matrix element is,

$$\begin{aligned} \mathbf{g}(\mathbf{p}_1, \mathbf{p}_2) \;=\; & \int \delta(\mathbf{p}-\mathbf{p}_1)\, i\nabla_{\mathbf{p}}\, \delta\Psi_{\mathbf{p}_2}(\mathbf{p}) d^3\mathbf{p} \\ & + \int \delta\Psi^*_{\mathbf{p}_1}(\mathbf{p})\, i\nabla_{\mathbf{p}}\, \delta(\mathbf{p}-\mathbf{p}_2) d^3\mathbf{p}, \end{aligned} \tag{61}$$

where,

$$\begin{aligned}\mathbf{g}(\mathbf{p}_1,\mathbf{p}_2) &= \int_{-\infty}^{+\infty}\delta(\mathbf{p}-\mathbf{p}_1)\,\nabla_{\mathbf{p}}\frac{i\mathcal{B}(\mathbf{p}_2)}{(p^2+\Gamma^2)^{\frac{1}{2}}(p_2^2-p^2+i\epsilon)}d^3\mathbf{p}\\ &+\int_{-\infty}^{+\infty}\frac{i\mathcal{B}^*(\mathbf{p}_1)}{(p^2+\Gamma^2)^{\frac{1}{2}}(p_1^2-p^2-i\epsilon)}\nabla_{\mathbf{p}}\delta(\mathbf{p}-\mathbf{p}_2)d^3\mathbf{p}.\end{aligned} \tag{62}$$

The last momentum integrals are evaluated by applying the same Dirac δ distribution property used in Eq. (52) and, after some algebra, the transition matrix continuum-continuum element for our model SR potential reads:

$$\begin{aligned}\mathbf{g}(\mathbf{p}_1,\mathbf{p}_2) &= i\nabla_{\mathbf{p}}\delta\Psi_{\mathbf{p}_2}(\mathbf{p})\Big|_{\mathbf{p}_1}-i\nabla_{\mathbf{p}}\delta\Psi^*_{\mathbf{p}_1}(\mathbf{p})\Big|_{\mathbf{p}_2},\\ &= iB(\mathbf{p}_2)\,\nabla_{\mathbf{p}}\left[\frac{1}{(p^2+\Gamma^2)^{\frac{1}{2}}(p_2^2-p^2+i\epsilon)}\right]\Bigg|_{\mathbf{p}_1}\\ &\quad -iB^*(\mathbf{p}_1)\,\nabla_{\mathbf{p}}\left[\frac{1}{(p^2+\Gamma^2)^{\frac{1}{2}}(p_1^2-p^2-i\epsilon)}\right]\Bigg|_{\mathbf{p}_2}.\end{aligned} \tag{63}$$

The derivative is solved as,

$$\nabla_x\left[\frac{1}{(x^2+\Gamma^2)^{\frac{1}{2}}(a^2-x^2+i\epsilon)}\right]=\frac{x(3x^2-a^2+2\Gamma-i\epsilon)}{(x^2+\Gamma^2)^{\frac{3}{2}}(a^2-x^2+i\epsilon)^2}. \tag{64}$$

In this way the rescattering matrix element reads as:

$$\mathbf{g}(\mathbf{p}_1,\mathbf{p}_2) = iB(\mathbf{p}_2)\,\mathcal{C}_1(\mathbf{p}_1,\mathbf{p}_2)-iB^*(\mathbf{p}_1)\,\mathcal{C}_2(\mathbf{p}_1,\mathbf{p}_2), \tag{65}$$

where

$$\begin{aligned}\mathcal{C}_1(\mathbf{p}_1,\mathbf{p}_2)&=\left[\frac{\mathbf{p}_1(3p_1^2-p_2^2+2\Gamma^2)}{(p_1^2+\Gamma^2)^{\frac{3}{2}}(p_2^2-p_1^2+i\epsilon)^2}\right],\\ \mathcal{C}_2(\mathbf{p}_1,\mathbf{p}_2)&=\left[\frac{\mathbf{p}_2(3p_2^2-p_1^2+2\Gamma^2)}{(p_2^2+\Gamma^2)^{\frac{3}{2}}(p_1^2-p_2^2-i\epsilon)^2}\right].\end{aligned} \tag{66}$$

The above expression, Eq. (65), clearly contains a nonintegrable singularity at the "energy shell" of the form: $1/(p_1^2-p_2^2+i\epsilon)^2$. In contrast to the singularity appearing in Eqs. (34) and (36), the present one is not a result of any saddle-point approximation, etc.; it is intrinsic in the scattering theory (see Appendix 5 and [6]). Still, in more realistic calculations and taking into account, for instance, the finite size of the focal region of the laser, this singularity becomes smoothed and ceases to exist. We argue in Appendix 5 that in the present calculation the smoothing occurs actually on a scale related to the size of the wave packets involved, which motivates us to use in practical numerical approaches a finite, nonzero value of $\epsilon = 0.2$ a.u. The results do

not depend significantly on the particular value of this regularization parameter.

So far we have formulated a model, which describes the photoionization process leading to two main terms, namely, the direct $b_0(\mathbf{p}, t_F)$ and the rescattering $b_1(\mathbf{p}, t_F)$ one.

The developed model is an alternative way to describe both the HHG and ATI processes driven by a strong laser pulse. The method is physically intuitive and can be understood on the basis of a quasiclassical picture, i.e. , electron trajectories. This is the main difference of our approach in comparison to the full numerical solution of the TDSE, whose physical interpretation is, in spite of its accuracy, frequently challenging. The main advantage of the proposed model is that Eqs. (19) and (36) give a clear physical understanding of the HHG and ATI process and provide a rich information about both the laser field and the atomic target which are encoded into the complex transition amplitude $b(\mathbf{p}, t) = b_0(\mathbf{p}, t) + b_1(\mathbf{p}, t)$. The exact analytical solutions of those direct and rescattering transition amplitudes are, however, nontrivial to obtain if no approximations are considered. In particular, for the rescattering photoelectrons, the solution is even more complex and depends, generally, on the laser electric field shape.

1.4 NUMERICAL RESULTS AND DISCUSSION

In this section, we calculate HHG and ATI spectra for different atomic systems using the approach presented the previous sections. In addition, we compare the HHG spectra from hydrogen and argon atoms computed with our model with those obtained using the exact numerical solution of the three-dimensional (3D)-TDSE. A scan over different laser wavelengths and peak intensities is performed in order to verify and validate our approach. In a second stage, we compute a set of ATI spectra. For this we numerically integrate both terms, i.e., $b_0(\mathbf{p}, t)$ and $b_1(\mathbf{p}, t)$, for the nonlocal SR potential and compare those results to the numerical solution of the 3D-TDSE.

1.4.1 *HHG: Comparison between SFA and 3D-TDSE models*

The HHG spectra of an hydrogen atom is performed by Fourier transforming the time-dependent dipole moment presented in Eq. (34). The parameters of the nonlocal potential are fixed to $\Gamma = 1$ and $\gamma = 38$ a.u., in such a way as to match the ionization potential of the H atom, $I_p = 0.5$ a.u. Note that several values of Γ and γ can be employed to obtain the same I_p. Therefore, these parameters are chosen to match the ground-state wave function, Eq. (44), of our SR potential model with the shape of the ground-state wave function of an actual hydrogen atom.

The HHG spectra at different laser wavelengths and using our quasiclassical SFA model are shown in Fig. 1(a). In addition, in Fig. 1(b) we show the HHG spectra obtained by using the numerical solution of the 3D-TDSE.

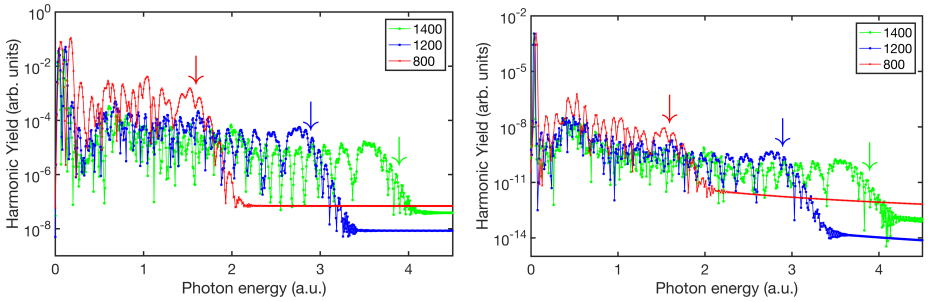

Figure 1: HHG spectra $\mathcal{I}(\omega)$ (in logarithmic scale) of hydrogen driven by a strong few-cycle pulse at different wavelengths. $\lambda_1 = 800$ nm (red asterisk line), $\lambda_2 = 1200$ nm (blue square line) and $\lambda_3 = 1400$ nm (green circle line). (a) Quasiclassical SFA model; (b) 3D-TDSE. The arrows in all the panels indicate the position of the classical HHG cutoff.

In order to compute the HHG spectra displayed in Fig. 1 we consider the laser pulse described by Eq. (1), with a $\sin^2$ envelope shape. The laser peak intensity is set to $I_0 = 1.58 \times 10^{14}$ W $\cdot$ cm^{-2} and different laser wavelengths (see the panels labels for details) are used. Additionally we fix $N_c = 4$ and $\phi_0 = 0$ rad. A total of 131072 points in the time window $t \in [0, t_F]$, where $t_F = N_c T_0$ and $T_0 = 2\pi/\omega_0$, are used during the numerical integration. The HHG spectra of Fig. 1(b) are obtained by numerically solving the 3D-TDSE in the length gauge. Thus, by Fourier transforming the dipole acceleration, calculated from the time-propagated electronic wave function, the HHG spectra are extracted. We have used our code, which is based on an expansion in spherical harmonics, Y_{lm} considering only the $m = 0$ terms due to the cylindrical symmetry of the problem. The numerical technique to solve the 3D-TDSE is based on a Crank-Nicolson scheme implemented on a splitting of the time-evolution operator that preserves the norm of the electronic wave function.

Both panels of Fig. 1 reveal the typical HHG behavior, namely, (i) a rapidly decreasing of the harmonic yield for the lower energies (< 0.5a.u. $\approx 10^{\text{th}}$), (ii) a plateau with almost constant yield, and (iii) an abrupt end at the so-called HHG cutoff. The cutoff energy is one of the most important features of any HHG spectrum. It can be defined as the maximum photon energy that can be released at recollision. Classically it is possible to prove that [1, 22]

$$\omega_{\text{cutoff}} = I_p + 3.17\, U_p, \tag{67}$$

where ω_{cutoff} is the maximum photon energy. As can we see from Fig. 1, both the SFA and 3D-TDSE calculations show the expected classical cutoff defined by Eq. (67), noted with an arrow at $\omega_{cutoff-800} = 1.59$ a.u. (43.26 eV), $\omega_{cutoff-1200} = 2.97$ a.u. (80.8 eV) and $\omega_{cutoff-1400} = 3.87$ a.u. (105.3 eV), respectively. From Eq. (67) we should notice that $\omega_{cutoff} \propto I\lambda^2$ and this behavior can also be observed in Fig. 1. For instance, the spectra at $\lambda_3 = 1400$ nm have a cutoff energy about four times higher than the one calculated using a wavelength of $\lambda_1 = 800$ nm.

A natural next step would be to test our model with a more complex atom. In order to do so, in Fig. 2 we show HHG spectra for an argon atom, calculated both with (i) our quasiclassical SFA [Fig. 2(a)] and (ii) using the numerical solution of the 3D-TDSE under the single active electron (SAE) approximation [Fig. 2(b)]. We employ two different laser peak intensities and using a laser pulse with a central frequency of $\omega_0 = 0.057$ a.u., that corresponds to a wavelength of about 800 nm. The nonlocal SR potential parameters are fixed to $\Gamma = 1$ and $\gamma = 35$ a.u. As in the previous case, we confirm that our model is capable to capture not only the dependency of the harmonic spectra with the wavelength, but also with the laser peak intensity. As we can observe, and considering that $I_2 > I_1$, a clear cutoff extension in the HHG spectra for I_2 is observed. A remarkable good agreement between both methods is clearly seen in Fig. 2 and for both laser peak intensities.

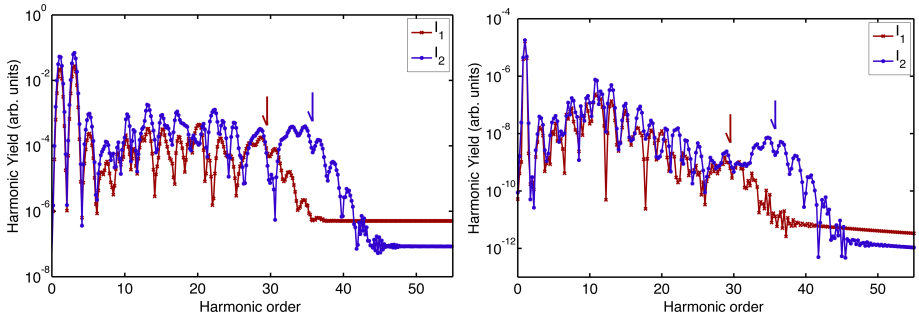

Figure 2: HHG spectra $\mathcal{I}(\omega)$ (in logarithmic scale) of Ar driven by a strong few-cycle pulse with $\lambda = 800$ nm, at different laser peak intensities. (a) Our quasiclassical SFA at $I_1 = 1.58 \times 10^{14}$ W $\cdot$ cm^{-2} (red square line) and $I_2 = 2.08 \times 10^{14}$ W $\cdot$ cm^{-2} (blue cross line), (b) same as in (a) but solving the 3D-TDSE. Note that in this case the minimum in the efficiency around the 27th harmonic is the Cooper minimum in Ar. The arrows in all the panels indicate the position of the classical HHG cutoff.

The HHG spectra presented both for a single electron system (H, Fig. 1) and a complex target (Ar, Fig. 2) reveal the very good agree-

ment between our quasiclassical SFA model and the numerical solution of the 3D-TDSE.

1.4.2 *ATI: Capturing the CEP dependence*

The numerical integration of Eqs. (19) and (36) has been performed by employing a rectangular rule with dedicated emphasis on the convergence of the results. As the final momentum distribution, Eq. (35) is "locally" independent of the momentum $\mathbf{p}$: i.e., $|b(\mathbf{p},t)|^2$ can be computed concurrently for a given set of distinct $\mathbf{p}$ values, we have optimized the calculation of the whole transition amplitude, $|b(\mathbf{p},t)|^2$, by using the OPENMP parallel package [34]. The final momentum photoelectron distribution, $|b(\mathbf{p},t)|^2$, is computed both in a 1D-momentum line along p_z, and in a 2D-momentum plane (p_y, p_z). We compare these results with the numerical solutions of the TDSE in one (1D) and two (2D) dimensions, respectively.

In case of the 1D calculations for the ATI spectra, the momentum grid was symmetrically defined with a length of $\mathbf{L}_{p_z} = 4.0$ a.u. and a step size of $\delta p_z = 0.02$ a.u. We use in our simulations an ultrashort laser pulse with central wavelength $\lambda = 800$ nm (photon energy, 1.55 eV) and peak intensity $I_0 = 1 \times 10^{14}$ W $\cdot$ cm^{-2}, being the rest of the parameters as in the HHG case. The time step is fixed to $\delta t = 0.2$ a.u. Figure 3 shows the final photoelectron distribution or ATI spectra, in logarithmic scale, as a function of the ponderomotive energy, U_p, for electrons with positive momenta along the p_z direction. Figure 3(a) depicts the total contribution, Eq. (35); meanwhile, Fig. 3(b) shows the contribution of both the direct $|b_0(\mathbf{p},t)|^2$ and rescattering terms $|b_1(\mathbf{p},t)|^2$. For completeness, the interference term, $b_{Int}(\mathbf{p},t) = b_0^*(\mathbf{p},t)\, b_1(\mathbf{p},t) + b_0(\mathbf{p},t)\, b_1^*(\mathbf{p},t)$ is included as an inset of Fig. 3(a). The first clear observation is that each term contributes to different regions of the ATI spectra; i.e., for electron energies $E_{p_z} \lesssim 3U_p$ the direct term $|b_0(\mathbf{p},t)|^2$ dominates the spectrum and, on the contrary, it is the rescattering term, $|b_1(\mathbf{p},t)|^2$ the one that prevails in the high-energy electron region. In addition, we observe that the interference term follows the trend of the direct one [see the inset of Fig. 3(a)] and does not play any role for electron energies $E_{p_z} \gtrsim 5U_p$. We shall see next that both direct and rescattering terms are needed in order to adequately describe the ATI process.

To confirm that our model is able to capture the left-right asymmetry [35], in Fig. 4 we compute ATI spectra for electrons with positive and negative momenta along the p_z direction. Fig. 4(a) shows the results of our quasiclassical model; meanwhile, in Fig. 4(b) the 1D-TDSE is used. The photoelectrons with negative (*positive*) momentum are conventionally named *left* (*right*) electrons and, correspondingly, the photoelectron spectra associated are labeled by $|b_{\mathbf{L}}(p_z,\phi_0)|^2$ and $|b_{\mathbf{R}}(p_z,\phi_0)|^2$, respectively.

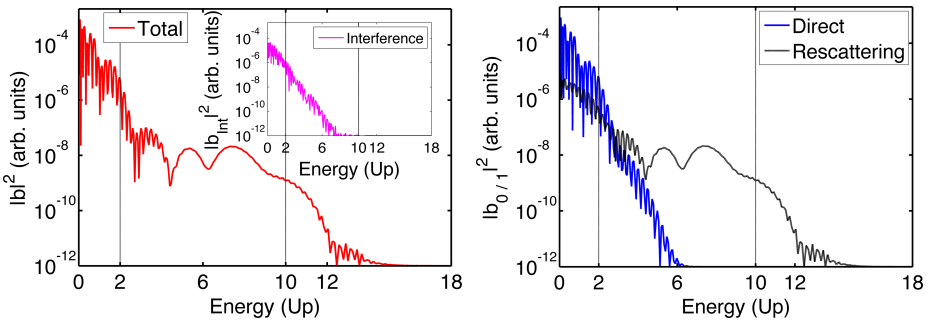

Figure 3: Photoelectron ATI spectra (in logarithmic scale) as a function of the ponderomotive electron energy U_p computed by using our quasiclassical model and for each one of the transition terms. (a) Total photoelectron spectrum, Eq. (35) (red line), with the interference term in the inset (magenta line). (b) Direct photoelectron spectrum $|b_0(p_z, t_F)|^2$ and rescattering photoelectron spectrum $|b_1(p_z, t_F)|^2$ are depicted in blue solid and black dashed lines, respectively. The vertical dashed lines correspond to the classical $2U_p$ and $10U_p$ cutoffs.

The photoelectron spectra computed by using the numerical solution of the 1D-TDSE, Fig. 4(b), allow us to evaluate the accuracy of our quasiclassical ATI model. The numerical integration of the 1D-TDSE is performed by using the split-spectral operator algorithm [36] and we use FFTW [37] to evaluate the kinetic energy operator of our Hamiltonian $\hat{H} = \frac{\hat{p}_z^2}{2} + \hat{V}(z) + zE(t)$. For the present numerical solution of the 1D-TDSE, we have fixed the position grid step to $\delta z = 0.2$ a.u., with a total number of points $N_z = 17000$. The ground state is computed via imaginary time propagation with a time step of $\delta t = -0.02\,i$ and the soft-core Coulomb potential is given by $V(z) = -\frac{1}{\sqrt{z^2+a}}$. The parameter $a = 2$ a.u. is chosen in such a way that the ground state yields the ionization potential of the hydrogen atom; i.e., $I_p = 0.5$ a.u.

The strong-field laser-matter interaction is simulated by evolving the ground-state wave function in real time, with a time step of $\delta t = 0.02$ a.u., and under the action of both the atomic potential and the laser field. The laser pulse parameters are the same as those used to compute the results of Fig. 3. At the end of the laser field t_F, when the electric field is zero, we compute the final photoelectron energy-momentum distribution $|b_{TDSE}(p_z, t_F)|^2$, by projecting the "free" electron wave packet, $\Psi_c(z, t_F)$, over plane waves. The wave packet $\Psi_c(z, t_F)$ is computed by smoothly masking the bound states from the entire wave function function $\Psi(z, t_F)$ via $\Psi_c(z, t_F) = h(z)\Psi(z, t_F)$, where $h(z) = \exp(-(\frac{z-z_0}{\sigma})^2)$ is a Gaussian filter.

Figure 4 demonstrates good qualitative agreement between the photoelectron spectra calculated with our quasiclassical model and those

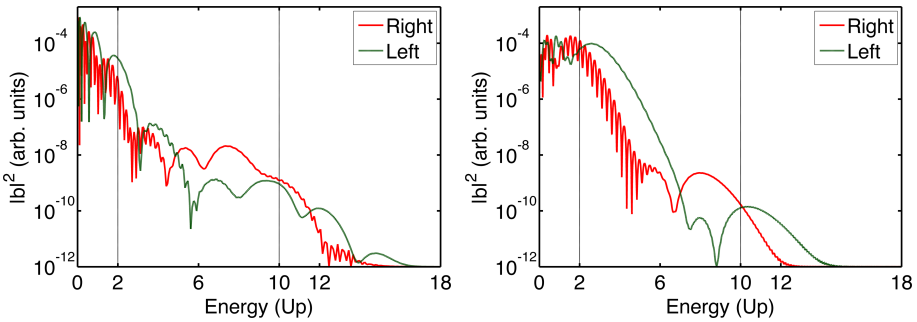

Figure 4: Comparison of the ATI spectra for an hydrogen atom. (a) Photoelectron energy distribution (in logarithmic scale) for the emitted electrons with negative (green dashed line) and positive (red solid line) momentum obtained by the integration of our derived full transition amplitude $|b(p_z, t_F)|^2$ (SFA). (b) The same as in (a) but computed by the numerical solution of the 1D-TDSE. The vertical dashed lines correspond to the classical $2U_p$ and $10U_p$ cutoffs.

obtained by the numerical solution of the 1D-TDSE. The left-right photoelectron spectra show the expected two cutoffs defined by $2U_p$ and $10U_p$ (black dashed lines) which are present in the ATI process [3, 35]. This shows that our approach is a reliable alternative for the calculation of ATI spectra. Our model furthermore captures the left-right dependence of the emitted photoelectrons as shown in Fig. 4(a), and in comparison with the 1D-TDSE shown in Fig. 4(b). The ability to capture this dependence and its features is especially important for applications to methods such as Laser-induced electron diffraction (LIED), which relies on large momentum transfers and backscattered electron distributions. For instance, photoelectrons ejected towards the left differ substantially from those emitted to the right for the case when a few-cycle driving pulse is used. According to the quasiclassical analysis of Sec. 1.1, one can then infer that electron trajectories emitted towards the right have larger probability to perform backward rescattering with the ionic core than the electrons emitted towards the left [35, 38]. This behavior is clearly reproduced by both models shown in Fig. 4 and it is the basis for the stereo ATI technique developed by Paulus *et al.* [38].

Since our model is capable of capturing the general CEP dependence, we turn to a more detailed investigation on whether our model can reproduce detailed CEP dependence by computing the ATI spectra as a function of the absolute CEP phase ϕ_0. Henceforth, we define the left-right asymmetry $\mathcal{A}(p_z, \phi_0)$ as visibility:

$$\mathcal{A}(p_z, \phi_0) = \frac{|b_L(p_z, \phi_0)|^2 - |b_R(p_z, \phi_0)|^2}{|b_R(p_z, \phi_0)|^2 + |b_L(p_z, \phi_0)|^2}. \tag{68}$$

We compute the ATI spectra for a set of CEP values between $\phi_0 = \mp 180°$ and evaluate the asymmetry $\mathcal{A}(p_z, \phi_0)$ of Eq. (68). The results

are shown in Fig. 5. Our calculated asymmetry $A(p_z, \phi_0)$ shows a clear dependence on the absolute CEP phase ϕ_0 of the laser pulse. For instance, when the CEP is $\phi_0 = \mp 90°$, the photoelectron spectra show a left-right symmetry, which is clearly visible in the energy region between 0 and $4U_p$ (see Fig. 5). This symmetry can be attributed to the direct term b_0, which dominates the photoelectron spectra at lower energies and is a consequence of the symmetry of the electric field with respect to the envelope maximum. On the other hand, and as we shall see later, the high-energy rescattered electrons do not follow this symmetry.

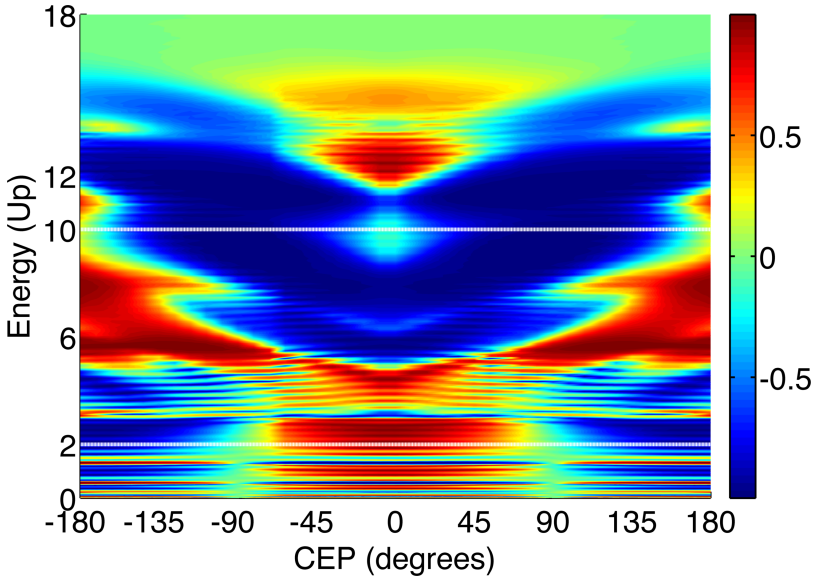

Figure 5: Asymmetry of the photoelectron energy distribution $A(p_z, \phi_0)$ as a function of the CEP. The horizontal dashed white lines denote the $2U_p$ and $10U_p$ cutoffs rule for the direct and rescattering photoelectrons, respectively. The laser pulse and the atomic parameters are the same that those used in Fig. 4.

For the energy range $5U_p \lesssim E_{p_z} \lesssim 12U_p$, the term $|b_L|^2$ is much less important than $|b_R|^2$ around $\phi_0 = 0°$. This implies that left electron trajectories have less probability to perform backward rescattering than those trajectories emitted to the right. Note that this process changes if the CEP of the laser pulse is larger than 90°; thereby the change is for energies between $5U_p \lesssim E_{p_z} \lesssim 8U_p$. In this energy interval the electron trajectories emitted to the left have a larger probability than the ones towards the right. For low-energy photoelectrons $E_{p_z} < 5U_p$, the asymmetry oscillates between positive and negative values, which means that its value for direct photoelectrons is more difficult to evaluate compared to using rescattered ones. Thus, the results depicted in Fig. 5 clearly show that our model describes the typical dependence of the ATI spectra on the CEP [35, 38] and, in particular, the backward rescattering events. Our model therefore can be used to describe the absolute phase of the driving IR laser pulse.

With the purpose to understand the left-right symmetry (or asymmetry) presented in Fig. 5, we compute both the direct and the rescattering terms for two different CEP values, namely $\phi_0 = 0°$ and $\phi_0 = 90°$. The results are depicted in Fig. 6. In the case of $\phi_0 = 0°$ the laser pulse is asymmetric with respect to the pulse envelope maximum; i.e., it has a $\sin(\omega_0 t)$ carrier wave. Consequently, from the phase contribution in Eq. (19) of the direct term, one can expect that the phase as a function of time is asymmetric as well. It is a consequence of the Fourier relation that a temporal asymmetry leads to an asymmetric spectral phase. In analogy, the temporal asymmetry of the phase of the direct photoelectron term leads to the final photoelectron momentum distribution $|b_0(p_z, t_F)|^2$ being asymmetric with respect to the momentum zero axis. This dependence is the origin of the asymmetric shape of the left-right emitted photoelectrons shown in Fig. 6(a). On the other hand, when the phase of Eq. (19) is time symmetric, which is the case of $\phi_0 = 90°$, i.e. the phase is proportional to $\cos(\omega_0 t)$, we infer that the photoelectron spectrum for the direct term should be symmetric. This is exactly what we observe in the direct term which is depicted in Fig. 6(b). Moreover, in both cases, the rescattering term $|b_1(p_z, t_F)|^2$ is asymmetric with respect to the $p_z = 0$ momentum. Hence, from the quasiclassical analysis addressed in Eq. (36) and due to the few-cycle electric field wave form, the electron trajectories strongly depend on the CEP and the left-right momentum asymmetry is visible due to the occurrence and interference of only a few emission and rescattering events.

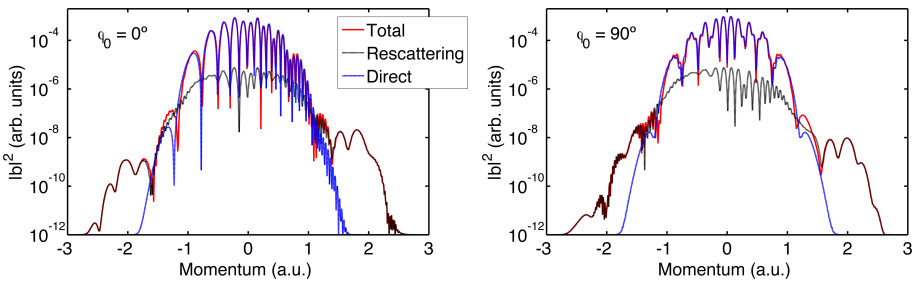

Figure 6: Left-right photoelectron momentum distributions (in logarithm scale) for the different contributions to the total ATI. Direct term $|b_0(p_z, t_F)|^2$ (blue dashed line), rescattering term $|b_1(p_z, t_F)|^2$ (black dashed with points line), and "total" term, $|b(p_z, t_F)|^2 = |b_0(p_z, t_F) + b_1(p_z, t_F)|^2$ (red solid line) of the ATI spectra for two different CEP values. (a) $\phi_0 = 0°$and (b) $\phi_0 = 90°$, respectively. The laser pulse and the atomic parameters are the same than those used in Fig. 4.

In order to complete the analysis, we have extended our numerical calculations of the photoelectron momentum distribution for the ATI process from a 1D-momentum line to a 2D-momentum plane. In

Fig. 7 we depict results for both models: our analytical quasiclassical ATI model [Fig. 7(a)] and the exact numerical solution of the 2D-TDSE [Fig. 7(b)]. We find qualitative good agreement between the results of our model and the full numerical solution of the 2D-TDSE. We also find that the distribution is symmetric with respect to the p_y axis. Note that these observations are in good agreement with calculations and measurements presented in Refs. [39–41].

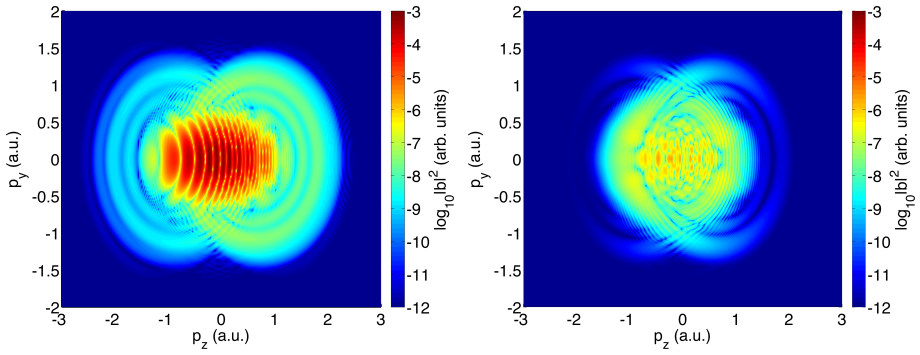

Figure 7: Comparison between our semiclassical model and the 2D-TDSE for an hydrogen atom. Photoelectron ATI spectra $|b(p_z, p_y, t_F)|^2$ (in logarithmic scale) computed by employing our SFA model (a) and the 2D-TDSE (b), respectively. The laser-pulse parameters used in these calculations are the same as those employed in Fig 4. Note that the laser field is polarized along the z direction.

The comparison shows that our quasiclassical approach can be used to model 2D-momentum distributions and even 3D-momentum distributions. However, from the contrast between the two models, we infer that our semianalytical model is limited to photoelectrons with high energies. The origin of this discrepancy arises from the approximation made in the model with regard to the atomic potential. Statement (iii) (see Sec. **??**) relates to the fact that the atomic potential is neglected when the electron is born in the continuum. Hence, we expect that electrons with lower final energies are not well described by our quasiclassical approach.

Finally, the main advantage of the analytical model is shown in Fig. 8 which depicts the individual contributions to the 2D ATI spectrum, namely, the direct [Fig. 8(a)], rescattering [Fig. 8(b)], and interference term [Fig. 8(c)], respectively. The resulting total and experimentally accessible ATI momentum spectrum $|b(p_z, p_y, t_F)|^2$ is shown in Fig. 8(d).

The atomic potential and the laser parameters used in these simulations are identical to those employed in the calculations for Figs. 3-6. Analogously to the 1D case, the computed photoelectron momentum spectrum for the direct term [Fig. 8(a)] shows contributions for electron energies less than $2U_p$. We find that the contribution of the rescat-

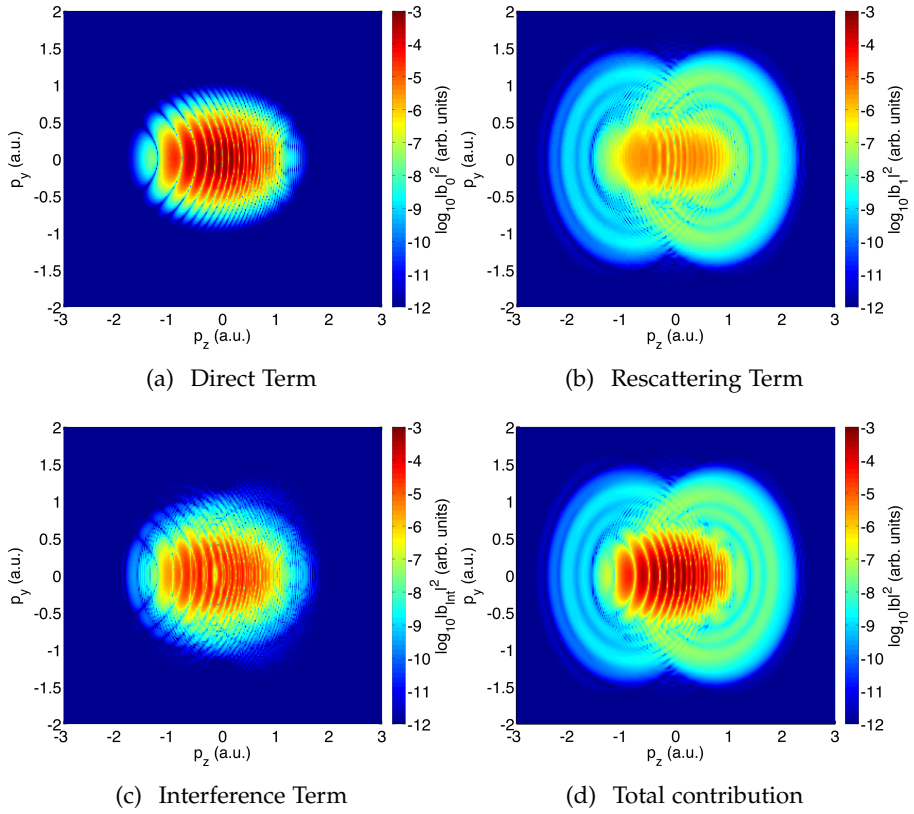

(a) Direct Term (b) Rescattering Term

(c) Interference Term (d) Total contribution

Figure 8: Different contributions to the photoelectron spectra for a 2D-momentum plane (p_z, p_y). ATI photoelectron spectra (in logarithmic scale) as a function of the momentum (p_z, p_y) computed by our quasiclassical model for each term. (a) Direct term; (b) rescattering term; (c) interference term; (d) total contribution.

tering term [Fig. 8(b)] extends to higher momentum values. Clearly visible is the symmetry of the structures about the p_y axis for all the terms and a left-right asymmetric shape for electrons with $p_z < 0$ or $p_z > 0$.

We want to emphasize the importance of Eqs. (22) and (65), from which we conclude that the form of the calculated ATI spectra strongly depends on the parameters Γ and γ of our SR potential model. These parameters have a large influence on the rescattering term, which could get mostly suppressed for a particular choice of them. This strong dependence suggests that the rescattering process substantially depends on the atomic target, which means that particular structural information is encoded in the ATI photoelectron spectra. Consequently, the proposed semianalytical model can be used to extract target structure and electron dynamics from measured photoelectron spectra.

1.5 CONCLUSIONS AND OUTLOOK

We presented a quasiclassical approach that deals with atomic HHG and ATI within the SAE. We have studied the ionization and rescattering processes mediated by a strong laser field interacting with an atomic system. We analyzed in detail approximate analytical solutions of the TDSE, obtained under the assumption of the SFA; i.e., once an electron is tunnel ionized, its dynamics is solely governed by the driving laser, which leads to rescattering or recollision events. First, we have validated our formalism comparing the atomic HHG and ATI spectra with results extracted from the 3D-TDSE. We have used a large set of laser intensities and wavelengths and two different atomic species, hydrogen and argon.

Based on this approach, we have identified and calculated the two main contributing terms in the ATI process: the direct and the rescattering transition probability amplitudes. In addition, the bound-free dipole and the rescattering transition matrix elements were *analytically computed* for a nonlocal SR potential. We stressed that this is one of the main differences between our developed model and those traditionally found in the literature for the ATI process. These *analytical derivations* of the rescattering matrix element allowed us to demonstrate that the rescattering process strongly depends on the atomic target features. A quasiclassical analysis of the time-dependent dipole moment and for the rescattering transition amplitude was performed in terms of the saddle-point approximation, that permits linking the dynamics to relevant quasiclassical information, i.e., classical electron trajectories.

Our model provides a simple framework for both the HHG and ATI understanding, which is in agreement with the available experimental observations. Additionally, our approach predictions are borne out by numerical calculations.

Our analytical results suggest that the main contributions to the rescattering transition amplitude correspond to electron trajectories, with the significant probability of backward scattering off the ionic core. Our model was used to demonstrate that both contributions, the direct and the rescattering terms, showed left-right asymmetry depending on the CEP of the laser pulse. This behavior has been confirmed by a comparison with the exact numerical solution of the TDSE and we found very good qualitative agreement, particularly in the high-energy region of the photoelectron spectra. Apart from testing the validity of our model, we stress out that it presents important advantages, such as the possibility to disentangle the effects of both the direct and the rescattered terms.

We also showed that the model is sensitive to the CEP, and by using the fact that we can investigate individual contributions to the photoelectron spectrum, we identified that the rescattering term plays a

dominant role by varying its influence based on the atomic parameters. These findings confirm that the photoelectron spectra contain structural information about the rescattering process, i.e., about the shape of the ground-state wave function, as well as the bound-free and continuum-continuum matrix transition elements. This dependence implies that atomic structural information can be efficiently extracted with our model for methods such as LIED, that grounds on the ATI process.

While our aim was to set the foundation of a basic semianalytical theoretical framework based on the SFA, we note that our approach is applicable to more complex, and thus more interesting, systems such as molecules. So, could our method be extended to, for instance, diatomic molecules? Which kind of information could be extracted? Can our model include molecular dynamics such as vibrations or dissociation? Is possible to include the ground-state molecular orbital information? We address these and similar questions in the next chapters.

2

MODIFIED STRONG-FIELD APPROXIMATION IN DIATOMIC MOLECULES

The study of molecular systems under the influence of a strong laser field has attracted a lot of attention recently. Some efforts have been already made in the study and development of new theoretical tools to investigate the structure of complex systems such as molecules. The *ab initio* numerical treatment of the molecular ionization is much more demanding than that of the atomic case. Therefore, simple theories, such as the Strong-Field Approximation (SFA) are even more desirable than in the atomic case. In this chapter we present a Modified Strong-Field Approximation model (MSFA) to address the problem of a diatomic molecule under the influence of a strong laser field. In the present contribution we build on the theory presented in the Chapter 1, namely (a) extending the approach to two-center molecular systems and (b) including a more accurate description of the molecular ground state. For (b) a linear combination of atomic orbitals (LCAO), obtained from chemical software suites, is used to model the high-occupied molecular orbital (HOMO). In principle, our approach is capable to manage any basis set, but in order to keep the formulation as analytical as possible, we employ throughout the thesis a STO-3G basis set.

The main original results are:

- The presentation of a MSFA model to study High-Order-Harmonic Generation (HHG) and Above-Threshold Ionization (ATI) processes in two-center molecules, which is free of any artificial and nonphysical effect.
- The calculation and possibility to disentangle the different terms, direct, local and nonlocal and cross, that contribute to the total HHG and ATI spectra.
- The appearance of intramolecular interferences. These are found in the dependence of the HHG spectra with the molecular orientation. We could recognize the origin of the deep minima in the spectra; it is product of the destructive interference between electronic wave packets recombining at the same center.
- The finding that for molecules short and long trajectories are present whereas for atoms the short trajectories are dominant. This was extracted from the time-analysis of the HHG spectra.

- The feasibility to extract the internuclear distance of a H_2^+ molecule using the information encoded in its ATI spectra via a simple interference formula.
- The inclusion of the HOMO shape in the bound-continuum transition matrix element using a LCAO. This correction on the bound-continuum matrix element allows us to correctly describe heteronuclear molecules.
- The comparison and good agreement of our theoretical calculations with experimental measurements obtained at ICFO for the O_2^+ molecule.

2.1 OVERCOMING THE DRAWBACKS OF SFA

The standard SFA method, however, has severe drawbacks, namely, the electronic states in the continuum are described in their simplest approximation by Volkov states (a plane wave in the presence of the laser field) or, in a slightly more sophisticated version, by Coulomb-Volkov states or similar ones which take into account Coulomb corrections [42–44]. These states are typically not orthogonal to the target bound states and, as such, this introduces spurious contributions. For instance, when we compute the transition dipole matrix element $\mathbf{d}(\mathbf{v})$ between the bound $|0\rangle$ and continuum $|\phi_{\mathbf{v}}\rangle$ states, the result depends linearly on the choice of the center of the coordinate system: $\mathbf{d}(\mathbf{v}) = q_e\langle\phi_{\mathbf{v}}|\hat{\mathbf{r}}|0\rangle \neq q_e\langle\phi_{\mathbf{v}}|(\hat{\mathbf{r}}-\mathbf{R})|0\rangle$, where $\mathbf{R}$ is a constant coordinate shift, typically corresponding to the distance between the nuclei (the so-called internuclear distance) in a two-center molecule. This is an artificial and nonphysical effect, particularly problematic when $\mathbf{R} \to \infty$ in the dipole matrix elements. Most authors handle this problem by neglecting the linear terms in $\mathbf{R}$ in the dipole matrix elements [45–47]. Nevertheless, this is not a systematic approach since it does not solve adequately problems related with various phase factors appearing on the molecular dipole matrix elements. In addition, they present a strong dependence on the choice of the gauge, or complications with the correct asymptotic behavior for $\mathbf{R} \to \infty$ and yet to $\mathbf{R} \to 0$ (cf. [45]). Furthermore, the agreement with the time-dependent Schrödinger equation (TDSE) results is typically poor. Aside from the mentioned weaknesses, we should note that these previous studies have led to a relatively good description of the HHG and ATI process in diatomic molecules.

In this chapter, we propose a natural and systematic solution of all the above-mentioned problems by extending the SFA to complex molecules of two centers without ambiguities. Our version of the MSFA for HHG and ATI has the following appealing properties:

(a) It analytically reproduces the results for $\mathbf{R} \to \infty$; for the particular case of diatomic molecules, this corresponds to two identical

atoms (sources) generating electronic (photonic) states with a phase difference corresponding to the distance $\mathbf{R}$ between them.

(b) It reproduces analytically the asymptotic limit for $\mathbf{R} \to 0$; for the case of a diatomic molecule, we end up with the usual single-atom formulation.

(c) Statements (a) and (b) agree well with their counterpart solutions obtained using the 3D-TDSE.

(d) It allows us to interpret the results in terms of quantum orbits, e.g., we could disentangle contributions for electrons originating at a given center $\mathbf{R}_j$ that rescatters at another one $\mathbf{R}_{j'}$, etc.

(e) It is free of nonphysical dependencies on $\mathbf{R}_j$.

(f) It agrees well with experimental results at ICFO concerning O_2^+ molecules.

Our approach is based on the following observation: both in the HHG and ATI cases the molecular response, which is determined by the probability amplitude of an electron in the continuum with a given energy and velocity, depends linearly on the wave functions of the initial (ground) state. More generally, the solution of the *linear* TDSE depends *linearly* on the wave function of the initial state. Commonly, for a molecule it is natural to write this function as a summation of the contributions corresponding to different nuclei: for a diatomic molecule it is a sum of two terms, for triatomic molecules a sum of three, etc. Following this reasoning, our modified SFA consists in the following steps:

- Decompose the initial ground state of the molecule into a superposition of terms centered at $\mathbf{R}_j$, $j = 1, 2, \ldots$, i.e., at the position where the heavy nuclei are located.
- Solve independently a TDSE, exactly or using the SFA for each term, using a coordinate system centered at each $\mathbf{R}_j$.
- Transform at the end all terms to the same coordinate system and coherently add them up.

Further, this approach is formally exact, as the exact numerical solutions of the TDSE are used; in fact it might even has some numerical advantages. On the other hand, the formulation is approximated if the SFA is used to solve the TDSE, but this approach seems to give particularly robust outcomes which agreed very well with the exact ones.

We illustrate our point with the simplest possible example: a two-center molecule with two identical atoms separated at certain distance R driven by a strong ultrashort laser field linearly polarized

along the z direction, but nothing prevents to apply our formalism to more complex molecular targets (see next chapter). To model the electron-heavy ion interactions we take advantage of the short-range (SR) potential model developed by Becker *et al*. [48]. Considering the ATI spectra are sensitive to the internuclear distance and the orientation between the molecular axis and the polarization direction of the laser field z, we aim to generalize the SFA for atomic systems presented in Chapter 1 to the above-mentioned diatomic molecular targets. Furthermore, we put particular emphasis to all the possible scenarios: tunneling ionization from both centers and propagation in the continuum until the measurement process; tunneling ionization from one particular center, electron propagation in the continuum, and rescattering on the same parent center; tunneling ionization from one center, electron propagation in the continuum, and rescattering with its neighbouring parent center; and (perhaps the most peculiar one) tunneling ionization from one center, electron propagation in the continuum, and rescattering on the same center, causing electron rescattering from the parent neighbouring center.

2.2 GENERALIZED SFA: TRANSITION PROBABILITY AMPLITUDES

We aim to extend the SFA for atomic systems presented in Chapter 1 to molecular targets. In particular, we focus ourselves on calculating the HHG and the final photoelectron ATI spectrum by means of solving the TDSE. We consider a molecule with two identical centers (see Fig. 9) separated by a distance R and driven by a short and intense linearly polarized laser pulse.

We define the relative vector position $\mathbf{R} = \mathbf{R}_2 - \mathbf{R}_1$ where $\mathbf{R}_1 = -\frac{\mathbf{R}}{2}(\mathbf{R}_2 = +\frac{\mathbf{R}}{2})$ is the position of one atom placed at the *left*(*right*).

2.2.1 *Basics of SFA: A remainder*

To find the transition probability amplitude in the two-center molecule we first take the Born-Oppenheimer approximation. Considering the mass ratio of electrons to nuclei is $\frac{M_n}{m_e} \lesssim 1836$, the electrons thus move much faster than the nuclei. One can therefore, at every moment in time, view the electrons in a molecule to move in the quasi-static potential of the slow nuclei. In general, as the molecular nuclei are much heavier than the electrons and the laser pulse duration is shorter than the nuclei vibration and rotational dynamics, we fix the nuclei positions and neglect the repulsive interaction between them. Further, throughout the formulation, we consider both the the single active electron (SAE) and dipole approximations. The TDSE that de-

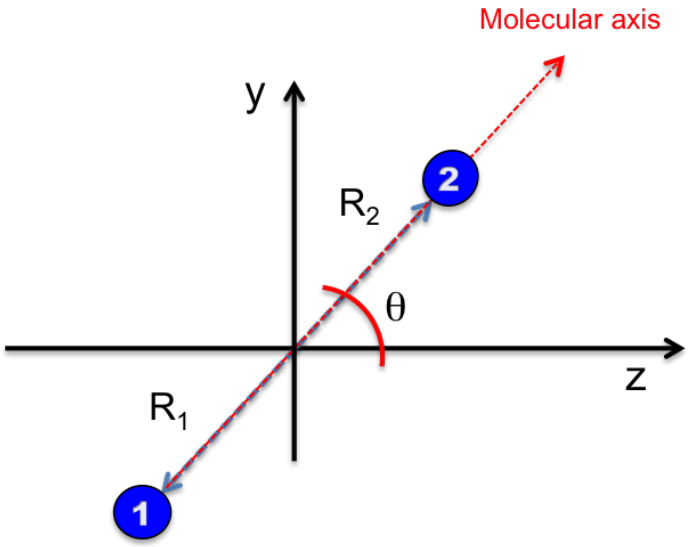

Figure 9: Two-center molecular system aligned a θ angle with respect to the laser electric field polarization. The red line represents the molecular axis that forms an angle of α between $\mathbf{R}_1 = [0, -\frac{R}{2}\sin(\theta), -\frac{R}{2}\cos(\theta)]$ and $\mathbf{R}_2 = [0, \frac{R}{2}\sin(\theta), \frac{R}{2}\cos(\theta)]$.

scribes the whole laser-molecule interaction in the length gauge can be written as:

$$i\frac{\partial}{\partial t}|\Psi(t)\rangle = \left[\frac{\hat{\mathbf{p}}^2}{2} + \hat{V}(\mathbf{r}) + \hat{\mathbf{E}}(t)\cdot\hat{\mathbf{r}}\right]|\Psi(t)\rangle, \tag{69}$$

with $\hat{\mathbf{p}} = -i\nabla$ the canonical momentum operator and $\hat{V}(\mathbf{r})$ is the potential operator that describes the interaction of the nuclei with the active electron. In the following we will restrict our model to the low ionization regime, where the SFA is valid [1, 3, 15, 17–19].

In addition, we assume that $V(\mathbf{r})$ does not play an important role in the electron dynamics once the electron appears in the continuum following the basic three SFA statements defined in the Sec. **??** [1, 3, 4].

2.2.2 *SFA: An appropriate treatment of two-center systems*

Based on the first statement (i) of the SFA and the linearity of the Schrödinger equation, we propose a general state for the system as:

$$|\Psi(t)\rangle = |\Psi_1(t)\rangle + |\Psi_2(t)\rangle, \tag{70}$$

which is the coherent superposition of two states $|\Psi_1(t)\rangle$ and $|\Psi_2(t)\rangle$. The subindices '1' and '2' refer to the contributions of the spatially localized *left* and *right* nuclei, respectively. We note that these *left-right* states are not orthogonal between them. Following the same

assumption that in Refs. [3, 4], each single state can be written as the coherent superposition of ground *left-right* and continuum states

$$|\Psi_1(t)\rangle = e^{iI_p t}\left[a(t)|0_1\rangle + \int d^3\mathbf{v}\, b_1(\mathbf{v},t)|\mathbf{v}\rangle\right], \tag{71}$$

$$|\Psi_2(t)\rangle = e^{iI_p t}\left[a(t)|0_2\rangle + \int d^3\mathbf{v}\, b_2(\mathbf{v},t)|\mathbf{v}\rangle\right]. \tag{72}$$

Note that the whole ground state, i.e., $|0\rangle = |0_1\rangle + |0_2\rangle$, is a composition of *left* $|0_1\rangle$ and *right* $|0_2\rangle$ contributions. In this way we are able to separate the whole state $|\Psi(t)\rangle$ both as the *left-right* states described in Eq. (70) and the two above ones (Eqs. (71) and (72)).

The amplitude of the state $|0\rangle$ is considered constant in time, i.e. $a(t) \approx 1$, under the assumptions of the statement (ii) of SFA (see Sec. **??**). The prefactor $e^{iI_p t}$ describes the accumulated electron energy in the ground state where $I_p = -E_0$ (E_0 is the molecular ground-state energy. Furthermore, the continuum states transition amplitudes $b_1(\mathbf{v},t)$ and $b_2(\mathbf{v},t)$ are referring to the electron wave function ionized from the *left* and *right* nuclei, respectively.

Our main task will be thereby to derive general expressions, by means of the Eq. (69) and the definitions of Eqs. (71) and (72), for the transition amplitudes $b_1(\mathbf{v},t)$ and $b_2(\mathbf{v},t)$.

As in the atomic case, we shall consider that $\hat{H}_0|0_{1,2}\rangle = -I_p|0_{1,2}\rangle$ and $\hat{H}_0|\mathbf{v}\rangle = \frac{\mathbf{v}^2}{2}|\mathbf{v}\rangle$ fulfill for the bound and continuum states, respectively. Consequently, the evolution of the transition amplitude $b_1(\mathbf{v},t)$ becomes

$$\begin{aligned} i\int d^3\mathbf{v}\, \dot{b}_1(\mathbf{v},t)\,|\mathbf{v}\rangle \;=\; & \int d^3\mathbf{v}\left(\frac{\mathbf{v}^2}{2}+I_p\right) b_1(\mathbf{v},t)|\mathbf{v}\rangle + \mathbf{E}(t)\cdot\mathbf{r}\,|0_1\rangle \\ & + \mathbf{E}(t)\cdot\mathbf{r}\int d^3\mathbf{v}\, b_1(\mathbf{v},t)|\mathbf{v}\rangle. \end{aligned} \tag{73}$$

On the above equation we have assumed that the electron-nuclei interactions are neglected once the electron appears in the continuum, based on the statement (iii) of the SFA (see Sec. **??**). Therefore, by multiplying Eq. (73) by $\langle\mathbf{v}'|$ and after some algebra, the time variation of the transition amplitude reads as

$$\begin{aligned} \dot{b}_1(\mathbf{v},t) \;=\; & -i\left(\frac{\mathbf{v}^2}{2}+I_p\right) b_1(\mathbf{v},t) + i\,\mathbf{E}(t)\cdot\mathbf{d}_1(\mathbf{v}) \\ & -i\,\mathbf{E}(t)\cdot\int d^3\mathbf{v}'\, b_1(\mathbf{v}',t)\langle\mathbf{v}|\mathbf{r}|\mathbf{v}'\rangle. \end{aligned} \tag{74}$$

The first two terms on the right-hand side of Eq. (74) represent the phase evolution of the electron within the oscillating laser field. In the last term, we have defined the bound-free transition dipole matrix element as

$$\mathbf{d}_1(\mathbf{v}) = -\langle\mathbf{v}|\mathbf{r}|0_1\rangle. \tag{75}$$

Here, $|\mathbf{v}\rangle$ represents in general a scattering state built up as the superposition of a plane wave $|\mathbf{v}_p\rangle$ and corrections on the *left*, $|\delta\mathbf{v}_1\rangle$ and *right* $|\delta\mathbf{v}_2\rangle$

$$|\mathbf{v}\rangle = |\mathbf{v}_p\rangle + |\delta\mathbf{v}_1\rangle + |\delta\mathbf{v}_2\rangle. \tag{76}$$

Based on last SFA statement (iii) (see Sec. **??**), our formulation only considers the continuum state as a plane wave $|\mathbf{v}_p\rangle$ for the calculation of the bound-free dipole matrix element. We shall pay special attention to the computation of Eq. (75). Firstly, let us stress the fact that plane waves are not orthogonal to the bound states. Secondly, notice also that our bound state is defined depending on the relative position of one the atoms $\mathbf{R}_1$ with respect to the origin of coordinates. In this sense, we need to introduce a "position correction" on the dipole transition matrix in order to avoid nonphysical terms with linear dependence on R (see Sec. 2.1 for more details). So, for the *left* contribution we introduce a correction to the dipole matrix element as

$$\begin{aligned} \mathbf{d}_1(\mathbf{v}) &= -\langle\mathbf{v}_p|(\mathbf{r}-\mathbf{R}_1)|0_1\rangle, \\ &= -\langle\mathbf{v}_p|\mathbf{r}|0_1\rangle + \mathbf{R}_1\langle\mathbf{v}_p|0_1\rangle. \end{aligned} \tag{77}$$

Similarly for $b_2(\mathbf{v},t)$ we define a bound-free transition dipole matrix as:

$$\mathbf{d}_2(\mathbf{v}) = -\langle\mathbf{v}_p|(\mathbf{r}-\mathbf{R}_2)|0_2\rangle, \tag{78}$$

and the total bound-free transition dipole matrix is thus:

$$\mathbf{d}(\mathbf{v}) = \mathbf{d}_1(\mathbf{v}) + \mathbf{d}_2(\mathbf{v}). \tag{79}$$

For atomic systems, the above analysis is not necessary since the atom is placed at the origin of the coordinate system. Furthermore, in the second term of Eq. (77) the continuum state $|\mathbf{v}\rangle$ is an eigenstate of the full atomic Hamiltonian H_0, therefore, this extra term $\mathbf{R}_1\langle\mathbf{v}_p|0_1\rangle$ disappears.

On the third term of Eq. (74) we define the continuum-continuum transition matrix element, $\mathbf{G}(\mathbf{v},\mathbf{v}') = \langle\mathbf{v}|\mathbf{r}|\mathbf{v}'\rangle$ Eq. (13), that relies upon on the scattering states $|\mathbf{v}\rangle$ and $|\mathbf{v}'\rangle$.

Working with the last term of Eq (74), where the scattering states are defined as in Eq. (76), and similarly with $|\mathbf{v}'\rangle = |\mathbf{v}'_p\rangle + |\delta\mathbf{v}'_1\rangle + |\delta\mathbf{v}'_2\rangle$, we get:

$$\begin{aligned} &\int d^3\mathbf{v}'\,\langle\mathbf{v}|\mathbf{r}|\mathbf{v}'\rangle\, b_1(\mathbf{v}',t) \\ &= \int d^3\mathbf{v}'\,\langle\mathbf{v}_p|\mathbf{r}|\mathbf{v}'_p\rangle\, b_1(\mathbf{v}',t) + \int d^3\mathbf{v}'\,\langle\mathbf{v}_p|\mathbf{r}|\delta\mathbf{v}'_1\rangle\, b_1(\mathbf{v}',t) \\ &+ \int d^3\mathbf{v}'\,\langle\mathbf{v}_p|\mathbf{r}|\delta\mathbf{v}'_2\rangle\, b_1(\mathbf{v}',t) + \int d^3\mathbf{v}'\,\langle\delta\mathbf{v}_1|\mathbf{r}|\mathbf{v}'_p\rangle\, b_1(\mathbf{v}',t) \\ &+ \int d^3\mathbf{v}'\,\langle\delta\mathbf{v}_2|\mathbf{r}|\mathbf{v}'_p\rangle\, b_1(\mathbf{v}',t). \end{aligned} \tag{80}$$

Similarly to the atomic case we neglect all the quadratic and superior terms considering only the first order contributions, i.e. we have dropped off all the terms as $\langle \delta\mathbf{v}_j|\mathbf{r}|\delta\mathbf{v}_j'\rangle/\langle \delta\mathbf{v}_j'|\mathbf{r}|\delta\mathbf{v}_j\rangle$ in the above equation.

Appealing to the non-orthogonality of the bound states, at this moment we need to introduce a correction on the $\mathbf{R}_1$ and $\mathbf{R}_2$ states depending on the projections:

$$\begin{aligned}
&\int d^3\mathbf{v}'\,\langle \mathbf{v}|(\mathbf{r}-\mathbf{R}_j)|\mathbf{v}'\rangle\, b_1(\mathbf{v}',t)\\
&=\int d^3\mathbf{v}'\,\langle \mathbf{v}_p|(\mathbf{r}-\mathbf{R}_1)|\mathbf{v}_p'\rangle\, b_1(\mathbf{v}',t)+\int d^3\mathbf{v}'\,\langle \mathbf{v}_p|(\mathbf{r}-\mathbf{R}_1)|\delta\mathbf{v}_1'\rangle\, b_1(\mathbf{v}',t)\\
&+\int d^3\mathbf{v}'\,\langle \mathbf{v}_p|(\mathbf{r}-\mathbf{R}_2)|\delta\mathbf{v}_2'\rangle\, b_1(\mathbf{v}',t)+\int d^3\mathbf{v}'\,\langle \delta\mathbf{v}_1|(\mathbf{r}-\mathbf{R}_1)|\mathbf{v}_p'\rangle\, b_1(\mathbf{v}',t)\\
&+\int d^3\mathbf{v}'\,\langle \delta\mathbf{v}_2|(\mathbf{r}-\mathbf{R}_2)|\mathbf{v}_p'\rangle\, b_1(\mathbf{v}',t). \qquad (81)
\end{aligned}$$

Working with the first term on the right-hand side the above equation,

$$\begin{aligned}
&\int d^3\mathbf{v}'\,\langle \mathbf{v}_p|(\mathbf{r}-\mathbf{R}_1)|\mathbf{v}_p'\rangle\, b_1(\mathbf{v}',t) \qquad (82)\\
&=\int d^3\mathbf{v}'\,\langle \mathbf{v}_p|\mathbf{r}|\mathbf{v}_p'\rangle\, b_1(\mathbf{v}',t)-\mathbf{R}_1\int d^3\mathbf{v}'\langle \mathbf{v}_p|\mathbf{v}_p'\rangle\, b_1(\mathbf{v}',t)\\
&=\int d^3\mathbf{v}'\, i\,\nabla_{\mathbf{v}}\,\delta(\mathbf{v}-\mathbf{v}')\, b_1(\mathbf{v}',t)-\mathbf{R}_1\int d^3\mathbf{v}'\,\delta(\mathbf{v}-\mathbf{v}')\, b_1(\mathbf{v}',t),
\end{aligned}$$

and considering Eqs. (81) and (82) we have

$$\begin{aligned}
&\int d^3\mathbf{v}'\langle \mathbf{v}|(\mathbf{r}-\mathbf{R}_j)|\mathbf{v}'\rangle\, b_1(\mathbf{v}',t) \qquad (83)\\
&=\int d^3\mathbf{v}'\,\Big\{ i\,\nabla_{\mathbf{v}}\delta(\mathbf{v}-\mathbf{v}')-\mathbf{R}_1\delta(\mathbf{v}-\mathbf{v}')+\langle \mathbf{v}_p|(\mathbf{r}-\mathbf{R}_1)|\delta\mathbf{v}_1'\rangle\\
&+\langle \mathbf{v}_p|(\mathbf{r}-\mathbf{R}_2)|\delta\mathbf{v}_2'\rangle+\langle \delta\mathbf{v}_1|(\mathbf{r}-\mathbf{R}_1)|\mathbf{v}_p'\rangle+\langle \delta\mathbf{v}_2|(\mathbf{r}-\mathbf{R}_2)|\mathbf{v}_p'\rangle\Big\}\, b_1(\mathbf{v}',t).
\end{aligned}$$

From here we can see that introducing adequately the correction depending on the atomic position we can define the continuum-continuum matrix element similarly to the atomic case as,

$$\mathbf{G}(\mathbf{v},\mathbf{v}')=i\,\nabla_{\mathbf{v}}\delta(\mathbf{v}-\mathbf{v}')-\mathbf{R}_j\delta(\mathbf{v}-\mathbf{v}')+\mathbf{g}(\mathbf{v},\mathbf{v}'), \qquad (84)$$

where in the less singular part, $\mathbf{g}(\mathbf{v},\mathbf{v}')$, we have all the information about the rescattering processes depending on the correction to the continuum states $\langle \delta\mathbf{v}_j|$. Notice that this equation is similar to the one obtained in the atomic case, Eq. (15), but with an extra term due to the position correction.

The first two terms on the right-hand side of Eq. (84) describe the motion of a free electron in the continuum. They are associated to events where the laser-ionized electron is accelerated by the laser electric field without any probability of rescattering. The last one,

the rescattering transition matrix element $\mathbf{g}(\mathbf{v},\mathbf{v}')$, accounts for all the rescattering processes concerning the entire molecule. For $\mathbf{g}(\mathbf{v},\mathbf{v}')$ the residual Coulomb potential has to be taken into account. In this sense, it can be written as a sum of components representing each rescattering channel on the molecule. The third term of Eq. (84) then reads as

$$\mathbf{g}(\mathbf{v},\mathbf{v}') = \mathbf{g}_{11}(\mathbf{v},\mathbf{v}') + \mathbf{g}_{22}(\mathbf{v},\mathbf{v}') + \mathbf{g}_{21}(\mathbf{v},\mathbf{v}') + \mathbf{g}_{12}(\mathbf{v},\mathbf{v}'). \quad (85)$$

The first two terms in the above equation contain information about spatially local processes involving only one of the atoms: the so-called local terms. On the contrary, the last two ones, describe processes involving both atomic centers, henceforth, we refer to them as nonlocal and cross terms, respectively.

So, after the above definitions, the transition amplitude for the *left* states, now depending directly from the position of the atom, reads as

$$\begin{aligned}\dot{b}_1(\mathbf{v},t) &= -i\left[\frac{\mathbf{v}^2}{2} + I_p - \mathbf{R}_1\cdot\mathbf{E}(t)\right] b_1(\mathbf{v},t) + i\mathbf{E}(t)\cdot\mathbf{d}_1(\mathbf{v}) \quad (86)\\ &\quad + \mathbf{E}(t)\cdot\nabla_{\mathbf{v}} b_1(\mathbf{v},t) - i\mathbf{E}(t)\cdot\int d^3\mathbf{v}'\, b_1(\mathbf{v}',t)\,\mathbf{g}(\mathbf{v},\mathbf{v}').\end{aligned}$$

The transition amplitude for the processes related to the nucleus in the *right* can be found following exactly the same procedure, namely, (i) projecting the entire Hamiltonian of the system on the *right* wave function Eq. (72) to get an equation similar to Eq. (73); (ii) multiplying it by a scattering state $\langle\mathbf{v}'|$, and (iii) defining the bound-continuum and continuum-continuum transition matrix elements including their respective corrections.

A general equation containing both of the processes mentioned before reads as:

$$\begin{aligned}\dot{b}_j(\mathbf{v},t) &= -i\left[\frac{\mathbf{v}^2}{2} + I_p - \mathbf{R}_j\cdot\mathbf{E}(t)\right] b_j(\mathbf{v},t) + i\mathbf{E}(t)\cdot\mathbf{d}_j(\mathbf{v}) \quad (87)\\ &\quad + \mathbf{E}(t)\cdot\nabla_{\mathbf{v}} b_j(\mathbf{v},t) - i\mathbf{E}(t)\cdot\int d^3\mathbf{v}'\, b_j(\mathbf{v}',t)\,\mathbf{g}(\mathbf{v},\mathbf{v}'),\end{aligned}$$

where the subscript j, taking the value *left* $j = 1$ or *right* $j = 2$, represents the position of each atom. For instance, to obtain the transition amplitude for the *left* states, [Eq. (86)], we need to set $j = 1$ in the above equation.

In the following, we shall describe how it is possible to compute the transition amplitude $b_j(\mathbf{v},t)$ by applying the zeroth- and first-order perturbation theory to the solution of the partial differential equation [Eq. (87)].

According to the perturbation theory, the transition amplitude solution $b_j(\mathbf{v},t)$,

$$b_j(\mathbf{v},t) = b_{0,j}(\mathbf{v},t) + b_{1,j}(\mathbf{v},t), \quad (88)$$

can be split into two parts, i.e. the zeroth-order solution $b_{0,j}(\mathbf{v},t)$ and the first-order solution $b_{1,j}(\mathbf{v},t)$. These terms correspond to the direct and rescattering terms, respectively. As is known, the direct term describes the transition amplitude for a laser-ionized electron that goes to the continuum and never rescatters with the remaining molecular ions. This term is related not only with the HHG processes but also with the ATI problem. On the other hand, the rescattering term $b_{1,j}(\mathbf{v},t)$ is referred to an electron that, once ionized in a particular center, has a certain probability of rescattering with each of the molecular ions; this is only related with the ATI processes.

2.2.3 *Direct transition amplitude*

Let us consider the process where the electron is ionized from one of the atoms of the molecule. For this, as in the case of an atom, we are going to apply perturbation theory on $\mathbf{g}(\mathbf{v},\mathbf{v}')$. Henceforth, we are only considering the most singular part, $i\nabla_{\mathbf{v}}\delta(\mathbf{v}-\mathbf{v}')-\mathbf{R}_j\delta(\mathbf{v}-\mathbf{v}')$, of the continuum-continuum matrix element Eq. (84). This mean that we only consider the terms until $\nabla_{\mathbf{v}}b_{0,j}(\mathbf{v},t)$, in Eq. (87) [3, 4]. This is what we refer as zeroth-order solution:

$$\begin{aligned}\partial_t b_{0,j}(\mathbf{v},t) &= -i\left[\frac{\mathbf{v}^2}{2}+I_p-\mathbf{R}_j\cdot\mathbf{E}(t)\right]b_{0,j}(\mathbf{v},t)\\ &\quad +i\,\mathbf{E}(t)\cdot\mathbf{d}_j(\mathbf{v})+\mathbf{E}(t)\cdot\nabla_{\mathbf{v}}b_{0,j}(\mathbf{v},t).\end{aligned}\tag{89}$$

The latter Schrödinger equation can be solved exactly and $b_{0,j}$ can be written in terms of the new variable $\mathbf{p}=\mathbf{v}-\mathbf{A}(t)$ [1], the canonical momentum, as:

$$\begin{aligned}b_{0,j}(\mathbf{p},t) &= i\int_0^t dt'\,\mathbf{E}(t')\cdot\mathbf{d}_j\left[\mathbf{p}+\mathbf{A}(t')\right]\\ &\quad\times\exp\left(-i\int_{t'}^t d\tilde{t}\,\{[\mathbf{p}+\mathbf{A}(\tilde{t})]^2/2+I_p-\mathbf{R}_j\cdot\mathbf{E}(\tilde{t})\}\right).\end{aligned}\tag{90}$$

This last equation is understood in terms of the final kinetic momentum $\mathbf{v}$ (note that in atomic units $\mathbf{p}=\mathbf{v}$). Equation (90) has a direct physical interpretation, it represents the sum of all the ionization events that occur from the time t' to t. Then, the instantaneous transition probability amplitude of an electron at a time t', at which it appears into the continuum with momentum $\mathbf{v}(t')=\mathbf{p}+\mathbf{A}(t')$, is defined by the argument of the $[0,t]$ integral in Eq. (90)

For the diatomic molecule we observe that the exponent phase factor, denoting the "semiclassical action" $S_j(\mathbf{p},t,t')$, depends on the atom position $\mathbf{R}_j$,

$$S_j(\mathbf{p},t,t')=\int_{t'}^t d\tilde{t}\,\left\{[\mathbf{p}+\mathbf{A}(\tilde{t})]^2/2+I_p-\mathbf{R}_j\cdot\mathbf{E}(\tilde{t})\right\}.\tag{91}$$

Note that the transition amplitude equations obtained so far differ from the atomic case and now depend on the position from which

the electron is tunnel ionized to the continuum. The semiclassical action $S_j(\mathbf{p}, t, t')$ explicitly contains this dependency. This phase factor defines a possible electron trajectory from the birth time t', at position $\mathbf{R}_j$, until the "detection" one t in the case of ATI. For the case of HHG processes this phase factor is understood as the trajectories from the ionization atom at $\mathbf{R}_j$, until the "recombination" one at time t.

Finally, the total transition amplitude for the direct process taking place on our two-center molecular system reads as:

$$b_0(\mathbf{p}, t) = b_{0,1}(\mathbf{p}, t) + b_{0,2}(\mathbf{p}, t). \tag{92}$$

The above equation give us information about the direct processes in the entire molecule, but it is written as the sum of two independent terms that can be understood as follows:

(1) The first term, $b_{0,1}(\mathbf{p}, t)$, accounts for electrons that tunnel from an atom located at $\mathbf{R}_1$. These electrons can go back to the parent ion and recombine with the same parent ion in a HHG processes. Moreover in the case of ATI this tunnel-ionized electrons stay in the continuum until the detection time.

(2) The process described by $b_{0,2}(\mathbf{p}, t)$ is similar to (1) but now the ionization is from the atom located at $\mathbf{R}_2$.

2.2.4 *Rescattering transition amplitude*

The first order correction, the transition amplitude of the rescattered photoelectrons $b_1(\mathbf{v}, t)$, is obtained considering $\mathbf{g}(\mathbf{v}, \mathbf{v}') \neq \mathbf{0}$ and the zeroth-order solution $b_{0,j}(\mathbf{p}, t)$ in the Eq. (87). Thereby we obtain a general equation to describe the rescattering process as

$$\begin{aligned} \dot{b}_{1,jj'}(\mathbf{v}, t) &= -i\left[\frac{\mathbf{v}^2}{2} + I_p - \mathbf{R}_j \cdot \mathbf{E}(t)\right] b_{1,j'j}(\mathbf{v}, t) \\ &\quad -i\,\mathbf{E}(t) \cdot \int d^3\mathbf{v}'\, b_{0,j}(\mathbf{v}', t)\, \mathbf{g}_{jj'}(\mathbf{v}, \mathbf{v}'), \end{aligned} \tag{93}$$

where j denotes the atom from where the electron is released and j' the one where the electron is rescattered. This equation is solved as:

$$\begin{aligned} b_{1,jj'}(\mathbf{p}, t) &= -\int_0^t dt' \int_0^{t'} dt'' \int d^3\mathbf{p}' \\ &\quad \times \mathbf{E}(t'') \cdot \mathbf{d}_j\left[\mathbf{p}' + \mathbf{A}(t'')\right] \exp\left[-iS_j(\mathbf{p}', t', t'')\right] \\ &\quad \times \mathbf{E}(t') \cdot \mathbf{g}_{jj'}\left[\mathbf{p} + \mathbf{A}(t'), \mathbf{p}' + \mathbf{A}(t')\right] \exp\left[-iS_{j'}(\mathbf{p}, t, t')\right]. \end{aligned} \tag{94}$$

The last equation is written in terms of the canonical momentum and depends on the ionization t'' and rescattering t' times. To interpret Eq. (94) let us start from the ionization time. The second line

represents the probability that certain electron makes a transition to the continuum with amplitude $\mathbf{E}(t'')\cdot\mathbf{d}_j\left[\mathbf{p}'+\mathbf{A}(t'')\right]$. The phase factor, $\exp\left[-iS_j(\mathbf{p}',t',t'')\right]$, defines all the possibles trajectories of this electron born at the time t'' in $\mathbf{R}_j$ until it rescatters at time t'. In the same way the last line is related with the rescattering processes. In here $\mathbf{E}(t')\cdot\mathbf{g}_{jj'}\left[\mathbf{p}+\mathbf{A}(t'),\mathbf{p}'+\mathbf{A}(t')\right]$ denotes the probability that one electron with momentum $\mathbf{p}'+\mathbf{A}(t')$ makes an elastic rescattering with the ion core t'. During this interaction the electron accumulates certain phase $S_{j'}(\mathbf{p},t,t')$ that now depends on the rescattering center $\mathbf{R}_{j'}$.

Additionally, Eq. (94) depends directly on the ionization and recombination atom because the continuum-continuum rescattering matrix element can be written depending on the atoms positions. Furthermore, Eq. (94) is split then in four terms [see Eq. (85)], that are associated to the continuum-continuum matrix element. Finally, the rescattering transition amplitude contains four terms as well, i.e.,

$$b_1(\mathbf{p},t)=b_{1,11}(\mathbf{p},t)+b_{1,22}(\mathbf{p},t)+b_{1,12}(\mathbf{p},t)+b_{1,21}(\mathbf{p},t). \tag{95}$$

The above equation includes information about all the possible rescattering scenarios which take place in our two-center molecular system. We are going to dig deeper in this general equation in the next sections.

2.3 THEORY OF HHG AND ATI IN DIATOMIC MOLECULES

In this section we are going to treat the HHG and ATI problems giving explicit expressions to compute each processes and shall follow a similar procedure as in the atomic case. We do not only write the final equations, since in here there are a lot of more processes, but we split the final HHG and ATI spectra en several contributions in a way of having a detailed analysis of the different recombination and rescattering scenarios.

2.3.1 *Time-dependent dipole moment*

In order to calculate the HHG spectrum generated by a diatomic molecule we use the results obtained in the section before. As we define in Eq. (70) the time-evolution of a two-center molecule is written as a coherent superposition of two states $|\Psi_1(t)\rangle$ and $|\Psi_2(t)\rangle$. Each contribution, in turn, is written as a composition of bound, $|0\rangle = |0_1\rangle+|0_2\rangle$, and continuum states. The time-dependent dipole for the two-center system is defined as in the atomic case, Eq. (24), and reads:

$$\begin{aligned}\vec{\mu}(t) \;=\; & -\langle\Psi_1(t)\rangle|\mathbf{r}_e|\Psi_1(t)\rangle-\langle\Psi_1(t)\rangle|\mathbf{r}_e|\Psi_2(t)\rangle \\ & -\langle\Psi_2(t)\rangle|\mathbf{r}_e|\Psi_1(t)\rangle-\langle\Psi_2(t)\rangle|\mathbf{r}_e|\Psi_2(t)\rangle.\end{aligned} \tag{96}$$

Manipulating the above equation, as we did with Eq. (25), we have:

$$\begin{aligned}\vec{\mu}(t) &= -\int d^3\mathbf{v}\, b_{0,1}(\mathbf{v},t)\langle 0|\mathbf{r}|\mathbf{v}\rangle - \int d^3\mathbf{v}\, b_{0,2}(\mathbf{v},t)\langle 0|\mathbf{r}|\mathbf{v}\rangle \\ &\quad -\int d^3\mathbf{v}\, b^*_{0,1}(\mathbf{v},t)\langle \mathbf{v}|\mathbf{r}|0\rangle - \int d^3\mathbf{v}\, b^*_{0,2}(\mathbf{v},t)\langle \mathbf{v}|\mathbf{r}|0\rangle. \quad (97)\end{aligned}$$

In the above equation we need to introduce the respective correction depending on the atoms positions: $\langle 0|(\mathbf{r}-\mathbf{R}_j)|\mathbf{v}\rangle$ and $\langle \mathbf{v}|(\mathbf{r}-\mathbf{R}_j)|0\rangle$. In this way we can identify the total bound-continuum dipole matrix elements defined in Eq. (79). So, working with the terms we have:

$$\begin{aligned}\vec{\mu}(t) &= \int d^3\mathbf{v}\, \mathbf{d}^*(\mathbf{v}) b_{0,1}(\mathbf{v},t) + \int d^3\mathbf{v}\, b^*_{0,1}(\mathbf{v},t)\mathbf{d}(\mathbf{v}) \\ &\quad + \int d^3\mathbf{v}\, \mathbf{d}^*(\mathbf{v}) b_{0,2}(\mathbf{v},t) + \int d^3\mathbf{v}\, b^*_{0,2}(\mathbf{v},t)\mathbf{d}(\mathbf{v}), \quad (98)\end{aligned}$$

from which the total time-dependent dipole moment for the diatomic system $\vec{\mu}(t)$ is easily obtained and has the following form:

$$\begin{aligned}\vec{\mu}(t) &= \int d^3\mathbf{v}\, \mathbf{d}^*_1(\mathbf{v}) b_{0,1}(\mathbf{v},t) + \int d^3\mathbf{v}\, \mathbf{d}^*_2(\mathbf{v}) b_{0,1}(\mathbf{v},t) \\ &\quad + \int d^3\mathbf{v}\, \mathbf{d}^*_1(\mathbf{v}) b_{0,2}(\mathbf{v},t) + \int d^3\mathbf{v}\, \mathbf{d}^*_2(\mathbf{v}) b_{0,2}(\mathbf{v},t) + c.c. \quad (99)\end{aligned}$$

In the last equation we require to insert the explicit expression for the continuum states transition amplitude $b_{0,j}(\mathbf{p},t)$ and the bound-continuum matrix element $\mathbf{d}_j(\mathbf{p})$. Notice that Eq. (99) depends on the atoms positions, so we can define the molecular time-dependent dipoles as a function of these quantities, for both the ionization and recombination events. The time-dependent dipole moment $\vec{\mu}_{jj'}(t)$ thus reads as

$$\begin{aligned}\vec{\mu}_{jj'}(t) &= i\int_0^t dt' \int d^3\mathbf{p}\, \mathbf{E}(t')\cdot \mathbf{d}_j\left[\mathbf{p}+\mathbf{A}(t')\right] \\ &\quad \times e^{-i\left\{S(\mathbf{p},t,t')+\mathbf{R}_j\cdot[\mathbf{A}(t)-\mathbf{A}(t')]\right\}} \mathbf{d}^*_{j'}[\mathbf{p}+\mathbf{A}(t)], \quad (100)\end{aligned}$$

where the subscripts j and j' represent the ionization and the recombination atoms positions, respectively.

The total time-dependent dipole moment can then be written as a sum of components,

$$\vec{\mu}(t) = \vec{\mu}_{11}(t) + \vec{\mu}_{22}(t) + \vec{\mu}_{12}(t) + \vec{\mu}_{21}(t). \quad (101)$$

Equation (101) contains information about all the recombination processes occurring in the entire molecule during the HHG phenomenon. The four terms in the above equation encode all the individual molecular recombination processes. Our physical interpretation of those contributions is as follows:

(i) An electron is ionized from the atom placed at the *left* with respect to the coordinate origin at time t' with certain probability: $\mathbf{E}(t')\cdot\mathbf{d}_1\,[\mathbf{p}+\mathbf{A}(t')]$. During its excursion in the continuum, this electron accumulates a phase which depends on the position from where it was detached, in this case $\mathbf{R}_1$. Finally, because the electric field changes its sign and the electron returns to the vicinity of the parent ion, the probability of recombination results $\mathbf{d}_1^*[\mathbf{p}+\mathbf{A}(t)]$. In this step, the excess energy acquired from the laser electric field is converted into a high-energy photon. The whole process is then described by

$$\begin{aligned}\vec{\mu}_{11}(t) &= i\int_0^t dt'\int d^3\mathbf{p}\,\mathbf{E}(t')\cdot\mathbf{d}_1\,\left[\mathbf{p}+\mathbf{A}(t')\right]\\ &\quad\times e^{-i\{S(\mathbf{p},t,t')+\mathbf{R}_1\cdot[\mathbf{A}(t)-\mathbf{A}(t')]\}}\,\mathbf{d}_1^*[\mathbf{p}+\mathbf{A}(t)].\end{aligned}\tag{102}$$

(ii) The second term is understood in a similar way. In this case, the ionization and recombination processes occur in the core placed at the *right*. The equation describing this process, $\vec{\mu}_{22}(t)$, is similar to Eq. (102) but now considering the matrix element $\mathbf{d}_2(\mathbf{v})$: the electron is detached from and recombines at the position $\mathbf{R}_2$. The two processes described before are spatially localized (involving only one core placed at a fixed position $\mathbf{R}_1$ or $\mathbf{R}_2$) and we then refer to them as *local* processes.

(iii) The last two terms, $\vec{\mu}_{21}(t)$ and $\vec{\mu}_{12}(t)$, describe events involving two atoms at two different positions $\mathbf{R}_1$ and $\mathbf{R}_2$. Here, $\vec{\mu}_{21}$ can be understood as follows: the electron is tunnel ionized from the atom on the *right* with certain probability given by: $\mathbf{E}(t')\cdot\mathbf{d}_2\,[\mathbf{p}+\mathbf{A}(t')]$. After this ionization event the electron starts to move under the laser electric field influence accumulating energy and acquiring a phase: $e^{-i\{S(\mathbf{p},t,t')+\mathbf{R}_2\cdot[\mathbf{A}(t)-\mathbf{A}(t')]\}}$. Finally, the electron returns back to the other core (located at the *left*) at the time t to end up its journey in a recombination process that has an amplitude proportional to: $\mathbf{d}_1^*[\mathbf{p}+\mathbf{A}(t)]$. As in previous cases, the excess energy is converted and emitted in a form of a high-energy photon. Considering that both centers are involved in the HHG process, we call these terms as *cross* processes.

Note from the above description that we have to account four different possible processes corresponding to four different time-dependent dipole moments. Two of them are *local* where ($j = j'$) and the other two *cross* ($j \neq j'$) representing all the possible recombination scenarios in our diatomic molecule.

Similarly to the atomic case (see Sec. 1.2.1.2) and in order to drop the integral over the momentum variable $\mathbf{p}$ to reduce the numerical complexity of the above equations we apply the saddle-point method.

In this way the the time-dependent dipole moment for the diatomic molecule then reads as

$$\vec{\mu}_{jj'}(t) = i\int_0^t dt' \left[\frac{\pi}{\varepsilon + \frac{i(t-t')}{2}}\right]^{\frac{3}{2}} \mathbf{E}(t')\cdot\mathbf{d}_j\left[\mathbf{p}_s + \mathbf{A}(t')\right] \times e^{-i\left\{S(\mathbf{p}_s,t,t')+\mathbf{R}_j\cdot[\mathbf{A}(t)-\mathbf{A}(t')]\right\}} \mathbf{d}^*_{j'}[\mathbf{p}_s + \mathbf{A}(t)]. \quad (103)$$

Finally, the total HHG spectrum is calculated using Eq. (28), similarly to the atomic case, but using the time-dependent dipole moment obtained in Eq. (103). As it was discussed, four terms are needed to compute the total diatomic molecular HHG spectrum. Each term represents a different process, and this is equivalent to the split made in the time-dependent dipole moment [see Eq. (101)]. We label each contribution depending on the position of the atoms, e.g., from the *left − left* term we obtain the $\mathcal{I}_{11}(\omega)$ spectrum. Similarly, we write the other three terms as $\mathcal{I}_{22}(\omega)$, $\mathcal{I}_{12}(\omega)$, and $\mathcal{I}_{21}(\omega)$, respectively.

It is convenient to identify two main contributions in the total HHG spectrum [Eq. (103)], namely, (i) the ones generated for the *local* processes and (ii) the ones developed by the *cross* processes. In this way, we can write the total HHG spectrum as

$$\mathcal{I}(\omega) = \mathcal{I}_{Local}(\omega) + \mathcal{I}_{Cross}(\omega), \quad (104)$$

where $\mathcal{I}_{Local}(\omega) = \mathcal{I}_{11}(\omega) + \mathcal{I}_{22}(\omega)$ and $\mathcal{I}_{Cross}(\omega) = \mathcal{I}_{12}(\omega) + \mathcal{I}_{21}(\omega)$ denote the *local* and *cross* terms, respectively.

2.3.2 *ATI in diatomic systems*

In the case of the two-center system the total ATI photoelectron spectra, $|b(\mathbf{p}, t_F)|^2$, is computed as a coherent superposition of both the direct $b_0(\mathbf{p}, t_F)$ and rescattered $b_1(\mathbf{p}, t_F)$ transition amplitudes, see Eq. (35).

As we established from the previous sections, in the diatomic case the direct term is a composition of two terms, each of them giving information about the direct ionization processes that take place in each of the molecular centers. To calculate the ATI spectra we need then the transition amplitude $b_{0,j}(\mathbf{p}, t)$ at the end of the laser pulse, i.e. at the $t = t_F$. Consequently, we shall define the integration time window as t: $[0, t_F]$. Furthermore, we set $\mathbf{E}(0) = \mathbf{E}(t_F) = \mathbf{0}$, in such a way to make sure that the laser electric field is a time oscillating wave and does not contain static components [the same arguments apply to the vector potential $\mathbf{A}(t)$].

In the case of the rescattering transition amplitude we have fourth terms, as we define in Eq. (95). In addition, a direct physical interpretation of each term can be inferred as following;

(1) The first term, $b_{1,11}(\mathbf{v}, t)$, denotes electron-tunneling ionization from an atom located at $\mathbf{R}_1$ and rescattering with the same parent ion. We refer this process as "spatially localized" since the

electron performs a local rescattering with the same atomic core $j = j'$ from which it was born.

(2) The process described by $b_{1,12}(\mathbf{v}, t)$ considers both atoms of the molecule. It represents an event where the electron is tunnel ionized from an atom at $\mathbf{R}_1$ and rescatters with the other atom at $\mathbf{R}_2$. We call this process as "cross process". In fact, there exists another process involving both atoms. It occurs when the electron is detached from an atom located at $\mathbf{R}_1$ and rescatters with the same parent ion, but there is certain probability of electron emission from the other ion core, placed at $\mathbf{R}_2$. We label the latter as "nonlocal process".

(3) The other "local" term, $b_{1,22}(\mathbf{v}, t)$ describes the same process as (1), but now for an atom located at $\mathbf{R}_2$.

(4) Finally, $b_{1,21}(\mathbf{v}, t)$ represents the same process as in (2), but now the tunnel-ionization process takes place at $\mathbf{R}_2$.

The differential equation describing the local rescattering processes is constructed considering $j = j'$ in Eq. (94). For processes localized at the *left* we need to set $j = j' = 1$ and for the ones at the *right* $j = j' = 2$, respectively. In this way, the transition amplitude for the local processes on $\mathbf{R}_1$ reads as

$$\begin{aligned} b_{1,11}(\mathbf{p}, t) \;=\; & -\int_0^t dt' \int_0^{t'} dt'' \int d^3\mathbf{p}'\, \mathbf{E}(t') \cdot \\ & \times \exp\left[-iS_1(\mathbf{p}', t', t'')\right] \mathbf{E}(t'') \cdot \mathbf{d}_1\left[\mathbf{p}' + \mathbf{A}(t'')\right] \\ & \times \mathbf{g}_{11}\left[\mathbf{p} + \mathbf{A}(t'), \mathbf{p}' + \mathbf{A}(t')\right] \exp\left[-iS_1(\mathbf{p}, t, t')\right]. \end{aligned} \tag{105}$$

As we expect, the rescattering transition amplitude contains two exponential factors, each representing the excursion of the electron in the continuum: before and after the rescattering event. In the above equation, both phase factors need to be evaluated with the same subscript, i.e., $S_1(\mathbf{p}, t, t') - S_1(\mathbf{p}', t', t'')$ or $S_2(\mathbf{p}, t, t') - S_2(\mathbf{p}', t', t'')$ since they are local processes.

The cross and nonlocal processes are formulated by considering $j \neq j'$ in the following way: $j = 1, 2$, $j' = 2, 1$ in Eq. (94). The phase factors have to be set now in different atomic positions: it means $S_1(\mathbf{p}, t, t') - S_2(\mathbf{p}', t', t'')$ or $S_2(\mathbf{p}, t, t') - S_1(\mathbf{p}', t', t'')$. For instance, the transition amplitude for the *left-right* process reads as

$$\begin{aligned} b_{1,12}(\mathbf{p}, t) \;=\; & -\int_0^t dt' \int_0^{t'} dt'' \int d^3\mathbf{p}'\, \mathbf{E}(t') \cdot \\ & \times \mathbf{E}(t'') \cdot \mathbf{d}_1\left[\mathbf{p}' + \mathbf{A}(t'')\right] \exp\left[-iS_1(\mathbf{p}', t', t'')\right] \\ & \times \mathbf{g}_{12}\left[\mathbf{p} + \mathbf{A}(t'), \mathbf{p}' + \mathbf{A}(t')\right] \exp\left[-iS_2(\mathbf{p}, t, t')\right]. \end{aligned} \tag{106}$$

Here, we notice that the above equation describes the atomic system presented in Ref. [4] when the internuclear distance goes to zero,

$\mathbf{R} \to 0$. The verification of this limit for the direct process is straightforward. The phase factor in Eq. (91) then becomes the well-known semiclassical action $S(\mathbf{p}, t, t')$ and the transition amplitude exactly has the same dependency as for an atom, if we replace the atomic matrix elements on it. For the rescattering events, we have to neglect in Eq. (95) the contribution of the nonlocal and cross terms (the last two terms) and follow the same procedure as before. In the following sections, we obtain the exact dependency of the rescattered matrix elements and demonstrate that the atomic limit can also be recovered when $\mathbf{R} \to 0$.

In the total rescattering transition amplitude, Eq. (95), we can identify two main contributions, namely, one generated for the local processes and the other one for the nonlocal and cross processes. In this way, we define the rescattering transition amplitude as

$$b_1(\mathbf{p}, t) = b_{Local}(\mathbf{p}, t) + b_{NL+Cross}(\mathbf{p}, t), \tag{107}$$

where

$$b_{Local}(\mathbf{p}, t) = b_{1,11}(\mathbf{p}, t) + b_{1,22}(\mathbf{p}, t), \tag{108}$$

and

$$b_{NL+Cross}(\mathbf{p}, t) = b_{1,12}(\mathbf{p}, t) + b_{1,21}(\mathbf{p}, t). \tag{109}$$

The direct transition amplitude, Eq. (90), is computed straightforwardly. For the rescattering one, Eq. (94) we shall employ the saddle-point method in order to reduce the integral over momentum (see Sec. 1.2.1.2). The quasiclassical action for the two-center molecule model, Eq. (94), can be rewritten as

$$S_j(\mathbf{p}', t', t'') = \mathbf{R}_j \cdot [\mathbf{A}(t') - \mathbf{A}(t'')] + S(\mathbf{p}', t', t''), \tag{110}$$

where $S(\mathbf{p}', t', t'') = \int_{t''}^{t'} d\tilde{t} \left\{ [\mathbf{p}' + \mathbf{A}(\tilde{t})]^2/2 + I_p \right\}$ is the same phase factor as in the atomic case Eq. (23). Thus, we proceed by applying the standard saddle-point method to the Eq. (94), in the same way as we did in Section. 1.2.1.2.

$$\begin{aligned} b_{1,jj'}(\mathbf{p}, t) \quad = \quad & -\int_0^t dt' \int_0^{t'} dt'' \left[\frac{\pi}{\varepsilon + \frac{i(t'-t'')}{2}} \right]^{\frac{3}{2}} \\ & \times \mathbf{E}(t'') \cdot \mathbf{d}_j \left[\mathbf{p}_s + \mathbf{A}(t'') \right] \exp \left[-iS_j(\mathbf{p}_s, t', t'') \right] \\ & \times \mathbf{E}(t') \cdot \mathbf{g}_{jj'} \left[\mathbf{p} + \mathbf{A}(t'), \mathbf{p}_s + \mathbf{A}(t') \right] \exp \left[-iS_{j'}(\mathbf{p}, t, t') \right]. \end{aligned} \tag{111}$$

As in the atomic case, ε is a non-zero parameter introduced to avoid the divergence at $t' = t''$.

So, in the last equation [Eq. (111)], we have substantially reduced the dimensionality of the problem, i.e., from a 5D integral to a 2D one. This reduction is extremely advantageous from a computational

viewpoint. Moreover, with the saddle-point method a quasiclassical picture for the rescattering transition amplitude is obtained for molecular systems, similarly to the atomic approach described in [3, 4, 22].

In order to calculate the total photoelectron spectra for the two-center molecular system, we first need to define the ground and the continuum states. After having found them, we then compute the bound-free transition dipole matrix elements $\mathbf{d}_1(\mathbf{p})$ and $\mathbf{d}_2(\mathbf{p})$ and the continuum-continuum transition rescattering matrix element $\mathbf{g}_{jj'}(\mathbf{p}, \mathbf{p}')$. In the next section, we shall introduce a SR potential model in order to analytically compute both the transition matrix elements and the final photoelectron momentum distribution.

In the derivation of the length-gauge flavor of the SFA for HHG in diatomic molecules, and in particular for the computation of the total bound-continuum matrix element, an unphysical term is neglected, without giving a consistent reason or argument (see [45–47] for more details). This term, that is a linear function of the internuclear distance $\mathbf{R}$, immediately introduces convergence problems as $\mathbf{R} \to \infty$. Clearly, this behavior enters in conflict between the length and velocity gauges predictions. This controversy is observed in the case of ATI as well. The root of the problem relies in the degree of approximation to handle the continuum states, considered as a set of plane waves for the molecular system, without considering the relative position of each atomic core. This creates an unphysical treatment and therefore the appearance of such undesired term. In our approach, we solve this issue by computing $\mathbf{d}_j(\mathbf{v}) = -\langle \mathbf{v}|(\hat{\mathbf{r}} - \mathbf{R}_j)|0_j\rangle$, where the bound-continuum matrix element is calculated with respect to each atomic center located at $\mathbf{R}_j$. Note that if no approximations are done, i.e., if we consider the case where $\langle \mathbf{v}|$ is a scattering wave of the field-free Hamiltonian H_0, the above-mentioned problem will not arise: the scattering waves are orthonormal to the ground states $|0_j\rangle$. However, as the main core of the SFA is to handle the continuum states as Volkov states, i.e., neglecting the influence of the residual molecular potential once the electron is in the continuum, the convergence problems would remain if we do not correct the bound-continuum matrix element.

2.4 TRANSITION MATRIX AMPLITUDES CALCULATION

We aim to employ two different models to calculate the total photoelectron spectra of molecular systems. In the first model we use a nonlocal SR potential $\hat{V}_{\mathbf{M}}(\mathbf{p}, \mathbf{p}')$ to describe the interaction of the electron with the multi-ionic center. Using this potential we are going to compute the bound, $\Psi_0(\mathbf{p})$, and scattering states, $\Psi_{\mathbf{p}_0}(\mathbf{p})$, as well as the corresponding dipole $\mathbf{d}(\mathbf{p})$, and rescattering, $\mathbf{g}(\mathbf{p}, \mathbf{p}')$ transition matrix elements.

For the second model we are going to obtain the molecular bound states $\Psi_{0_{LCAO}}(\mathbf{p})$ using a LCAO. This description appears to be more accurate than the one based on the SR potential. For instance, it is able to model not only *s*-states, as is the case of the SR model, but also p and more complex ones. Additionally it gives a more precise characterization of the bound-free dipole matrix element $\mathbf{d}_{LCAO}(\mathbf{p})$. In order to maintain the model as analytical as possible, we compute the scattering states and the continuum-continuum transition matrix elements using the nonlocal SR potential.

2.4.1 *A simplified molecular model: Nonlocal SR potential*

In this section, we define a simplified molecular model to validate the general above-described formulation and to compute both HHG and ATI photoelectron spectra. Let us consider a diatomic molecule constructed as two fixed nuclei centers under the single active electron (SAE) approximation. We describe the interaction of the electron with each molecular nuclei by a nonlocal SR potential. The Hamiltonian of the system in the momentum representation can be written as

$$\hat{H}_{\mathbf{M}}(\mathbf{p},\mathbf{p}') = \frac{\mathbf{p}^2}{2}\delta(\mathbf{p}-\mathbf{p}') + \hat{V}_{\mathbf{M}}(\mathbf{p},\mathbf{p}'). \tag{112}$$

The first term on the right-hand side is the kinetic energy operator, and the second one is the interacting nonlocal SR potential defined according to

$$\begin{aligned}\hat{V}_{\mathbf{M}}(\mathbf{p},\mathbf{p}') &= -\gamma'\,U(\mathbf{p})\,U(\mathbf{p}')\,e^{-i\mathbf{R}_2\cdot(\mathbf{p}-\mathbf{p}')} \\ &\quad -\gamma'\,U(\mathbf{p})\,U(\mathbf{p}')\,e^{-i\mathbf{R}_1\cdot(\mathbf{p}-\mathbf{p}')}.\end{aligned} \tag{113}$$

This potential describes the interaction between the active electron and each of the nuclei of the molecule, and depends on the internuclear relative vector position $\mathbf{R} = \mathbf{R}_2 - \mathbf{R}_1$. The function $U(\mathbf{p})$ is the same auxiliary function used in Chapter 1, Eq. (39) [3, 4]. The parameters $\gamma' = \frac{\gamma}{2}$ and Γ are constants related with the shape of the ground state (for more details see [4]).

To obtain the ground state and calculate the bound-free dipole matrix element we need to solve the stationary Schrödinger equation as follows:

$$\hat{H}_{\mathbf{M}}(\mathbf{p})\Psi_0(\mathbf{p}) = \int d^3\mathbf{p}'\hat{H}_{\mathbf{M}}(\mathbf{p},\mathbf{p}')\Psi_0(\mathbf{p}') = E_0\,\Psi_0(\mathbf{p}). \tag{114}$$

In the next chapter we develop a MSFA model for molecules with more than two centers. For this we use an extended version of the nonlocal SR potential, defined in Eq. (113), that inherits the same properties.

2.4.1.1 *Ground states and bound-continuum dipole matrix element*

By using $\hat{H}_{\mathbf{M}}(\mathbf{p},\mathbf{p}')$ from Eq. (112), and inserting it in the Schrödinger equation we have,

$$\begin{aligned}\hat{H}_{\mathbf{M}}(\mathbf{p})\Psi_0(\mathbf{p}) &= \int d^3\mathbf{p}'\hat{H}_{\mathbf{M}}(\mathbf{p},\mathbf{p}')\Psi(\mathbf{p}'), \qquad (115)\\ E_0\,\Psi_0(\mathbf{p}) &= \frac{p^2}{2}\int d^3\mathbf{p}'\delta(\mathbf{p}-\mathbf{p}')\Psi_0(\mathbf{p}')\\ &\quad -\gamma' U(\mathbf{p})\int d^3\mathbf{p}'\Psi_0(\mathbf{p}')U(\mathbf{p}')e^{-i\mathbf{R}_2\cdot(\mathbf{p}-\mathbf{p}')}\\ &\quad -\gamma' U(\mathbf{p})\int d^3\mathbf{p}'\Psi_0(\mathbf{p}')U(\mathbf{p}')e^{-i\mathbf{R}_1\cdot(\mathbf{p}-\mathbf{p}')}.\end{aligned}$$

Similar to the atomic case (see the Sec. 1.3), to analytically solve Eq. (115), in the momentum representation, we consider a new set of variables as,

$$\breve{\varphi}_1 = \int d^3\mathbf{p}'\Psi_0(\mathbf{p}')U(\mathbf{p}')e^{i\mathbf{R}_2\cdot\mathbf{p}'} = \int \frac{d^3\mathbf{p}'\Psi_0(\mathbf{p}')e^{i\mathbf{R}_2\cdot\mathbf{p}'}}{\sqrt{p'^2+\Gamma^2}}, \qquad (116)$$

$$\breve{\varphi}_2 = \int d^3\mathbf{p}'\,\Psi_0(\mathbf{p}')U(\mathbf{p}')e^{i\mathbf{R}_1\cdot\mathbf{p}'} = \int \frac{d^3\mathbf{p}'\Psi_0(\mathbf{p}')e^{i\mathbf{R}_1\cdot\mathbf{p}'}}{\sqrt{p'^2+\Gamma^2}}. \qquad (117)$$

To directly obtain the molecular ground state analytically, $\Psi_0(\mathbf{p})$, we solve,

$$\left(\frac{p^2}{2}+I_p\right)\Psi_0(\mathbf{p}) = \gamma' U(\mathbf{p})\,e^{-i\mathbf{R}_2\cdot\mathbf{p}}\,\breve{\varphi}_1 + \gamma' U(\mathbf{p})\,e^{-i\mathbf{R}_1\cdot\mathbf{p}}\,\breve{\varphi}_2, \qquad (118)$$

where I_p denotes the ionization potential energy of the wave function $\Psi_0(\mathbf{p})$ which is related to the ground potential energy by $E_0 = -I_p$. The ground state wave function in momentum space is defined by

$$\Psi_0(\mathbf{p}) = \frac{\gamma'\,\breve{\varphi}_1\,e^{-i\mathbf{R}_2\cdot\mathbf{p}}}{\sqrt{(p^2+\Gamma^2)(\frac{p^2}{2}+I_p)}} + \frac{\gamma'\,\breve{\varphi}_2\,e^{-i\mathbf{R}_1\cdot\mathbf{p}}}{\sqrt{(p^2+\Gamma^2)(\frac{p^2}{2}+I_p)}}. \qquad (119)$$

To find the variables defined in Eqs. (116) and (117), we need to solve an eigenvalues problem that looks like

$$\begin{pmatrix}\breve{\varphi}_1\\ \breve{\varphi}_2\end{pmatrix} = \begin{pmatrix}I_1 & I_2\\ I_2 & I_1\end{pmatrix}\times\begin{pmatrix}\breve{\varphi}_1\\ \breve{\varphi}_2\end{pmatrix}, \qquad (120)$$

where I_1 and I_2 are integrals as,

$$I_1 = \gamma'\int \frac{d^3\mathbf{p}\,U^2(\mathbf{p})}{(\frac{p^2}{2}+I_p)} = \frac{4\pi^2\gamma'}{\Gamma+\sqrt{2I_p}}, \qquad (121)$$

and

$$\begin{aligned} I_2 &= \gamma' \int \frac{d^3\mathbf{p}\, U^2(\mathbf{p})}{(\frac{p^2}{2}+I_p)} e^{\pm i(\mathbf{R}_1-\mathbf{R}_2)\cdot\mathbf{p}} \\ &= \frac{8\pi^2\gamma'}{|R_1-R_2|}\left\{\frac{e^{-|R_1-R_2|\Gamma}-e^{-|R_1-R_2|\sqrt{2I_p}}}{2\,(2I_p-\Gamma^2)}\right\} \\ &= \frac{4\pi^2\gamma'}{R}\left\{\frac{e^{-R\Gamma}-e^{-R\sqrt{2I_p}}}{2I_p-\Gamma^2}\right\}. \end{aligned} \tag{122}$$

The solution of this eigenvalues problem let us two possible solutions,

$$\breve{\varphi}_1 = \breve{\varphi}_2 \;\text{ and }\; \breve{\varphi}_1 = -\breve{\varphi}_2, \tag{123}$$

and the energy relation,

$$1 - I_1 = I_2. \tag{124}$$

Those two possible solutions in Eq. (123) correspond to symmetric and antisymmetric wave functions for the ground state: $\Psi_0(\mathbf{p})$. Throughout this paper, we shall only consider the symmetric wave function as follows:

$$\Psi_0(\mathbf{p}) = \frac{\mathcal{M}}{\sqrt{(p^2+\Gamma^2)}(\frac{p^2}{2}+I_p)}\left[2\cos\left(\frac{\mathbf{R}\cdot\mathbf{p}}{2}\right)\right], \tag{125}$$

where $\mathcal{M} = \gamma'\,\breve{\varphi}_1 = \frac{\gamma}{2}\,\breve{\varphi}_1$ is a normalization constant. This constant is obtained by employing the conventional normalization condition for the bound states. In this way we can define,

$$\mathcal{M} = \gamma'\,\breve{\varphi}_1 = [1/I_{2N}]^{1/2}, \tag{126}$$

where,

$$\begin{aligned} I_{2N} &= \int \frac{d^3\mathbf{p}}{(p^2+\Gamma^2)(\frac{p^2}{2}+I_p)^2}\left[2\cos\left(\frac{\mathbf{R}\cdot\mathbf{p}}{2}\right)\right]^2, \\ &= 2\int \frac{d^3\mathbf{p}\, e^{\pm i\mathbf{R}\cdot\mathbf{p}}}{(p^2+\Gamma^2)(\frac{p^2}{2}+I_p)^2} + 2\int \frac{d^3\mathbf{p}}{(p^2+\Gamma^2)(\frac{p^2}{2}+I_p)^2}, \\ &= 2\,I_R + 2\,I_{1N}. \end{aligned} \tag{127}$$

In here I_{1N} is the normalization constant for the atomic case presented in Eq. (49), see Chapter 1. The other integral I_R is solved in a similar way as,

$$I_R = \int \frac{d^3\mathbf{p}\, e^{\pm i\mathbf{R}\cdot\mathbf{p}}}{(p^2+\Gamma^2)(\frac{p^2}{2}+I_p)^2} = \frac{4(2\pi^2)}{(2I_p-\Gamma^2)^2}\left\{\frac{e^{-|R|\Gamma}}{|R|} - \frac{e^{-|R|\sqrt{2I_p}}}{|R|} - \frac{e^{-|R|\sqrt{2I_p}}(2I_p-\Gamma^2)}{2\sqrt{2I_p}}\right\}. \tag{128}$$

Consequently, the $\mathcal{M}$ factor thereby reads as

$$\mathcal{M} = \frac{1}{2}\left[\frac{2\pi^2}{(2I_p-\Gamma^2)^2}\left\{\frac{2\,e^{-R\Gamma}}{R}-\frac{2\,e^{-R\sqrt{2I_p}}}{R} -\frac{(2I_p-\Gamma^2)e^{-R\sqrt{2I_p}}}{\sqrt{2I_p}}+\frac{(\sqrt{2I_p}-\Gamma)^2}{\sqrt{2I_p}}\right\}\right]^{-1/2}. \quad (129)$$

With the exact dependency of $\mathcal{M}$ we have well defined the bound state for our two-center molecular system. The wave function for the bound state can then be written as a combination of two *left* and *right* functions, $\Psi_0(\mathbf{p}) = \Psi_{0,1}(\mathbf{p}) + \Psi_{0,2}(\mathbf{p})$, in agreement with the photoelectron transition amplitude derivation. $\Psi_0(\mathbf{p})$ thus reads as:

$$\Psi_0(\mathbf{p}) = \frac{\mathcal{M}\,e^{-i\mathbf{R}_1\cdot\mathbf{p}}}{\sqrt{(p^2+\Gamma^2)}(\frac{p^2}{2}+I_p)}+\frac{\mathcal{M}\,e^{-i\mathbf{R}_2\cdot\mathbf{p}}}{\sqrt{(p^2+\Gamma^2)}(\frac{p^2}{2}+I_p)}. \quad (130)$$

In the above wave function we can clearly see that each term contains information about only one of the nuclei. The first term corresponds to the electron wavefunction portion located at the atom on the *left* at $\mathbf{R}_1 = -\frac{\mathbf{R}}{2}$, meanwhile the second one to the electron wavefunction portion placed on the *right* atom of the molecule at $\mathbf{R}_2 = +\frac{\mathbf{R}}{2}$, respectively.

Equation (124) gives us a relationship between the electronic energy E_e of the two-center molecular system and the internuclear distance R as follows:

$$\frac{2\pi^2\gamma}{R(\Gamma^2-2E_e)}\left[e^{-\sqrt{2E_e}R}-e^{-\Gamma R}+R(\Gamma-\sqrt{2E_e})\right]=1. \quad (131)$$

In order to test the validity of the latter formulas, in Fig. 10 we show the potential energy surface (PES) of the simplest diatomic molecule: H_2^+, as a function of internuclear distance. We depict the different energy contributions, electronic and nuclear, of the H_2^+ molecular system obtained using the SFA model (left panel) and the exact solution of the TDSE (right panel). While the electron-nuclei interaction is described by a kind of nonlocal SR potential for our test molecular model, we choose as a repulsive potential between the nuclei a Yukawa one.

We stress that Fig. 10 is in very good agreement with the PES reported in the literature [49]: it shows the minimum of equilibrium for an interatomic distance at $R_0 = 2$ a.u. This value is a clear signal of the good description offered by our SFA model. When R is large, the two atoms are weakly interacting and the energy of the system is equal to the energy of the atomic hydrogen, -0.5 a.u. As R becomes smaller, the interaction results stronger and the energy is large and negative. In this case, we say that a bond is formed between the atoms. At even smaller values of R, the internuclear repulsion is

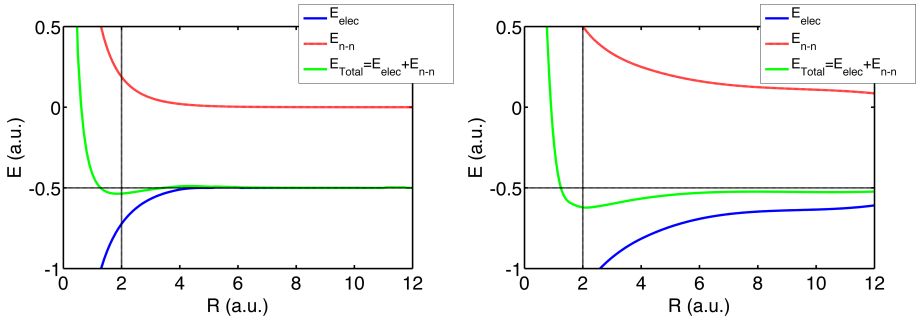

(a) (b)

Figure 10: Potential Energy Surface (PES) for the diatomic molecule H_2^+ as a function of the internuclear distance. (a) Electronic energy (blue line) calculated using Eq. (124), nuclear-nuclear energy (red line) and total energy of the system (green line) obtained with the SFA model. (b) The same as in (a) but computed by the numerical solution of the TDSE. The vertical dashed lines shows the energy minimum corresponding to the equilibrium distance of the system.

very large (red line), therefore, the energy is large and positive. It is a standard approach to use zero-range potentials as a caricature of the true Coulomb ones in SFA. In fact, this choice is perfectly legitimate within the SFA framework, where the atomic or molecular potential is neglected when the electron is moving in the continuum, but if we consequently take, for instance, delta potentials between the two protons in the H_2^+ molecule, we would not have the possibility of stabilizing it for $R \neq 0$. For this reason, we employ a Yukawa potential, that is also a short-range caricature of the Coulomb potential, but it has a finite-range repulsive core, which combined with attractive electronic energy allows to reach the stabilization of our molecule for finite values of R in the Born-Oppenheimer approximation. By comparing our results with the TDSE, we could argue that our approximation appears to work perfectly well.

2.4.1.2 *Bound-continuum transition matrix element*

So far we have analytically obtained the ground state of our two-center molecular system. It allows us to compute the bound-free transition dipole matrix element $\mathbf{d}_1(\mathbf{p}_0)$ and $\mathbf{d}_2(\mathbf{p}_0)$ by using Eqs. (77) and (78). By approximating the free or continuum state as a plane wave with a given momentum $\mathbf{p}_0$, the bound-free transition dipole matrix in the momentum representation reads as

$$\begin{aligned} \mathbf{d}_1(\mathbf{p}_0) &= -i\nabla_{\mathbf{p}}\Psi_{0,1}(\mathbf{p})\big|_{\mathbf{p}_0} + \mathbf{R}_1\Psi_{0,1}(\mathbf{p}_0), \\ &= -i\,\mathcal{MA}(\mathbf{p}_0)\,e^{-i\mathbf{R}_1\cdot\mathbf{p}_0}, \end{aligned} \tag{132}$$

for the atom on the *left*, meanwhile that for the one on the *right* it results:

$$\mathbf{d}_2(\mathbf{v}) = -2i\,\mathcal{MA}(\mathbf{p}_0)\,e^{-i\mathbf{R}_2\cdot\mathbf{p}_0}. \tag{133}$$

In both cases, $\mathcal{A}(\mathbf{p}_0)$ is the quantity defined in Sec. 1.3.1, Eq. (53).

The total bound continuum matrix element for the whole two-center system is defined as:

$$\mathbf{d}(\mathbf{p}_0) = -2i\,\mathcal{MA}(\mathbf{p}_0)\left\{e^{-i\mathbf{R}_1\cdot\mathbf{p}_0} + e^{-i\mathbf{R}_2\cdot\mathbf{p}_0}\right\}. \tag{134}$$

With the definition of the ionization dipole we are able to calculate the time-dependent dipole moment for each of the molecular centers defined in Sec. [**ch:3.3.1**] Eq. (100). In this equation we need to evaluate in the saddle-point moment $\mathbf{p}_s$ for each of the *local* and *cross* terms. In fact, the phases of the *local* contributions in Eq. (100), function on the relative positions $\mathbf{R}_{1/2}$ of the atoms, cancel each other defining a saddle-point momentum $\mathbf{p}_s$ equivalent to the one found for the atomic case [see Sec. 1.2.1.2, Eq. (31)]. On the other hand, the *cross* processes present more complex phases, that directly depend on the position variables. For instance, in $\vec{\mu}_{21}(t)$ $(\vec{\mu}_{12}(t))$ the saddle-point momentum is described by: $\mathbf{p}_{s_2} = -\frac{1}{\tau}\left[\mathbf{R}_2 + \int_{t'}^{t}\mathbf{A}(\tilde{t})\mathbf{d}\tilde{t}\right]$ $\left(\mathbf{p}_{s_1} = -\frac{1}{\tau}\left[-\mathbf{R}_1 + \int_{t'}^{t}\mathbf{A}(\tilde{t})\mathbf{d}\tilde{t}\right]\right)$. In all our cases the model is employed to small internuclear distances, where the condition: $R < \mathcal{E}_0/\omega^2$ is fulfilled, with $\mathcal{E}_0$ and ω_0 being the laser electric field peak amplitude and carrier frequency, respectively. As a consequence, it is not necessary to consider these saddle-point momentum definitions (for more details about the validity of this approximation see [46]). Thus, we proceed by applying the standard saddle-point momentum to both the *local* and *cross* contributions.

The second important quantity to be calculated before evaluating the whole transition amplitude $b(\mathbf{p}, t)$ is the rescattering transition matrix element $\mathbf{g}(\mathbf{p}, \mathbf{p}')$. Hence, we need to find the scattering or continuum wave functions of our model potential. Next, we shall calculate them by analytically solving the time-independent Schrödinger equation in the momentum representation for positive energies.

2.4.1.3 *Scattering waves and the continuum-continuum transition matrix element*

Let us consider a scattering wave $\Psi_{\mathbf{p}_0}(\mathbf{p})$, with asymptotic momentum $\mathbf{p}_0$, as a coherent superposition of a plane wave and an extra correction $\delta\Psi_{\mathbf{p}_0}(\mathbf{p})$ as in Eq. (54). In this case we are considering a two-center molecule so the correction is also a superposition of corrections as,

$$\begin{aligned}\Psi_{\mathbf{p}_0}(\mathbf{p}) &= \delta(\mathbf{p}-\mathbf{p}_0) + \delta\Psi_{\mathbf{p}_0}(\mathbf{p}) \\ &= \delta(\mathbf{p}-\mathbf{p}_0) + \delta\Psi_{\mathbf{p}_0,1}(\mathbf{p}) + \delta\Psi_{\mathbf{p}_0,2}(\mathbf{p}).\end{aligned} \tag{135}$$

This state has an energy $E = \mathbf{p}_0^2/2$. Then, the Schrödinger equation in momentum representation reads as

$$\left(\frac{p^2}{2} - \frac{p_0^2}{2}\right)\delta\Psi_{\mathbf{p}_0}(\mathbf{p}) = -\hat{V}_{\mathbf{M}}(\mathbf{p},\mathbf{p}_0) - \int d^3\mathbf{p}'\hat{V}_{\mathbf{M}}(\mathbf{p},\mathbf{p}')\delta\Psi_{\mathbf{p}_0}(\mathbf{p}'). \quad (136)$$

Inserting the nonlocal SR potential, Eq (113), in Eq. (136) and after some algebra, we obtain:

$$\begin{aligned}&\left(\frac{p^2}{2} - \frac{p_0^2}{2}\right)\delta\Psi_{\mathbf{p}_0}(\mathbf{p}) \quad (137)\\ &= \gamma' U(\mathbf{p})U(\mathbf{p}_0)\left[e^{-i\mathbf{R}_2\cdot(\mathbf{p}-\mathbf{p}_0)} + e^{-i\mathbf{R}_1\cdot(\mathbf{p}-\mathbf{p}_0)}\right]\\ &+\gamma' U(\mathbf{p})\int U(\mathbf{p}')\left[e^{-i\mathbf{R}_2\cdot(\mathbf{p}-\mathbf{p}')} + e^{-i\mathbf{R}_1\cdot(\mathbf{p}-\mathbf{p}')}\right]\delta\Psi_{\mathbf{p}_0}(\mathbf{p}')d^3\mathbf{p}'.\end{aligned}$$

Now introducing the new variables $\breve{\varphi}_1'$ and $\breve{\varphi}_2'$ as

$$\breve{\varphi}_1' = \int d^3\mathbf{p}'\delta\Psi_{\mathbf{p}_0}(\mathbf{p}')U(\mathbf{p}')e^{i\mathbf{R}_1\cdot\mathbf{p}'} = \int \frac{d^3\mathbf{p}'\delta\Psi_{\mathbf{p}_0}(\mathbf{p}')e^{i\mathbf{R}_1\cdot\mathbf{p}'}}{\sqrt{p'^2+\Gamma^2}}, \quad (138)$$

$$\breve{\varphi}_2' = \int d^3\mathbf{p}'\delta\Psi_{\mathbf{p}_0}(\mathbf{p}')U(\mathbf{p}')e^{i\mathbf{R}_2\cdot\mathbf{p}'} = \int \frac{d^3\mathbf{p}'\delta\Psi_{\mathbf{p}_0}(\mathbf{p}')e^{i\mathbf{R}_2\cdot\mathbf{p}'}}{\sqrt{p'^2+\Gamma^2}}, \quad (139)$$

we have,

$$\begin{aligned}(p^2 - p_0^2)\delta\Psi_{\mathbf{p}_0}(\mathbf{p}) &= 2\gamma' U(\mathbf{p})U(\mathbf{p}_0)\left[e^{-i\mathbf{R}_2\cdot(\mathbf{p}-\mathbf{p}_0)} + e^{-i\mathbf{R}_1\cdot(\mathbf{p}-\mathbf{p}_0)}\right]\\ &+ 2\gamma'\breve{\varphi}_1' U(\mathbf{p})e^{-i\mathbf{R}_1\cdot\mathbf{p}} + 2\gamma'\breve{\varphi}_2' U(\mathbf{p})e^{-i\mathbf{R}_2\cdot\mathbf{p}},\end{aligned} \quad (140)$$

Finally, for $\delta\Psi_{\mathbf{p}_0}$ we write

$$\begin{aligned}\delta\Psi_{\mathbf{p}_0}(\mathbf{p}) &= \frac{\mathcal{D}_1(\mathbf{p}_0)\, e^{-i\mathbf{R}_2\cdot(\mathbf{p}-\mathbf{p}_0)} - \mathcal{D}_2(\mathbf{p}_0)\, e^{-i\mathbf{R}_2\cdot(\mathbf{p}+\mathbf{p}_0)}}{\sqrt{p^2+\Gamma^2}\,(p_0^2 - p^2 + i\epsilon)}\\ &+\frac{\mathcal{D}_1(\mathbf{p}_0)\, e^{-i\mathbf{R}_1\cdot(\mathbf{p}-\mathbf{p}_0)} - \mathcal{D}_2(\mathbf{p}_0)\, e^{-i\mathbf{R}_1\cdot(\mathbf{p}+\mathbf{p}_0)}}{\sqrt{p^2+\Gamma^2}\,(p_0^2 - p^2 + i\epsilon)},\end{aligned} \quad (141)$$

where ϵ is another infinitesimal parameter to avoid the divergence at the "energy shell", $p^2 = p_0^2$. The singularity at the "energy shell" is avoided due to the finite spread of the involved wave packets. In numerical calculations we set throughout this chapter $\epsilon = 0.4$ a.u. (for more details, see [4]). The integration "constants" for the scattering states in Eq. (141) have the following dependency:

$$\mathcal{D}_1(\mathbf{p}_0) = \frac{\gamma}{\sqrt{p_0^2+\Gamma^2}}\left\{\frac{1+I_1'}{I_2'^2 - (1+I_1')^2}\right\}; \quad (142)$$

$$\mathcal{D}_2(\mathbf{p}_0) = \frac{\gamma}{\sqrt{p_0^2+\Gamma^2}}\left\{\frac{I_2'}{I_2'^2-(1+I_1')^2}\right\}, \tag{143}$$

where

$$\begin{aligned} I_1' &= 2\gamma' \int \frac{d^3\mathbf{p}}{(p^2+\Gamma^2)(p_0^2-p^2+i\epsilon)}, \\ &= \frac{-4\pi^2\gamma'}{\Gamma - i\sqrt{|p_0^2+i\,\epsilon|}}, \end{aligned} \tag{144}$$

$$\begin{aligned} I_2' &= 2\gamma' \int \frac{d^3\mathbf{p}\, e^{\pm i(\mathbf{R}_1-\mathbf{R}_2)\cdot\mathbf{p}}}{(p^2+\Gamma^2)(p_0^2-p^2+i\epsilon)}, \\ &= \frac{-2\pi^2\gamma'}{|R_1-R_2|}\left\{\frac{e^{i|R_1-R_2|\sqrt{p_0^2+i\epsilon}}-e^{-|R_1-R_2|\,\Gamma}}{(p_0^2+\Gamma^2+i\epsilon)}\right\}, \\ &= \frac{-4\pi^2\gamma'}{R\,(p_0^2+\Gamma^2+i\epsilon)}\left[e^{iR\sqrt{p_0^2+i\epsilon}}-e^{-R\,\Gamma}\right]. \end{aligned} \tag{145}$$

Finally, the correction to the scattering states for each of the atoms reads as,

$$\delta\Psi_{1\mathbf{p}_0}(\mathbf{p}) = \frac{\mathcal{D}_1(\mathbf{p}_0)\, e^{-i\mathbf{R}_1\cdot(\mathbf{p}-\mathbf{p}_0)} - \mathcal{D}_2(\mathbf{p}_0)\, e^{-i\mathbf{R}_1\cdot(\mathbf{p}+\mathbf{p}_0)}}{\sqrt{p^2+\Gamma^2}\,(p_0^2-p^2+i\epsilon)}, \tag{146}$$

$$\delta\Psi_{2\mathbf{p}_0}(\mathbf{p}) = \frac{\mathcal{D}_1(\mathbf{p}_0)\, e^{-i\mathbf{R}_2\cdot(\mathbf{p}-\mathbf{p}_0)} - \mathcal{D}_2(\mathbf{p}_0)\, e^{-i\mathbf{R}_2\cdot(\mathbf{p}+\mathbf{p}_0)}}{\sqrt{p^2+\Gamma^2}\,(p_0^2-p^2+i\epsilon)}. \tag{147}$$

Equation (146) describes electrons that have probability of scatter with the ion core placed at $\mathbf{R}_1$. Similarly, Eq. (147) represents a scattering process with the nucleus placed at $\mathbf{R}_2$.

2.4.1.4 *Continuum-continuum transition matrix element*

Let us consider the scattering waves obtained in Eqs. (146) and (147) to evaluate the rescattering transition matrix element of Eq. (85) as,

$$\begin{aligned} \mathbf{g}(\mathbf{v},\mathbf{v}') &= \langle \mathbf{v}_p|(\mathbf{r}-\mathbf{R}_1)|\delta\mathbf{v}_1'\rangle + \langle \delta\mathbf{v}_1|(\mathbf{r}-\mathbf{R}_1)|\mathbf{v}_p'\rangle \\ &\quad + \langle \mathbf{v}_p|(\mathbf{r}-\mathbf{R}_2)|\delta\mathbf{v}_2'\rangle + \langle \delta\mathbf{v}_2|(\mathbf{r}-\mathbf{R}_2)|\mathbf{v}_p'\rangle, \\ &= \mathbf{g}_1(\mathbf{v},\mathbf{v}') + \mathbf{g}_2(\mathbf{v},\mathbf{v}'). \end{aligned} \tag{148}$$

The above transition matrix element contains information over the rescattering processes in the full molecule. In this way we can split it into two main contributions related to the atoms on the *left* and the atom on the *right*. Working with the $\mathbf{g}_1(\mathbf{p}_1,\mathbf{p}_2)$ matrix element in the momentum space we have,

$$\begin{aligned} \mathbf{g}_1(\mathbf{p}_1,\mathbf{p}_2) &= i\nabla_{\mathbf{p}}\delta\Psi_{1\mathbf{p}_2}(\mathbf{p})\Big|_{\mathbf{p}_1} - \mathbf{R}_1\delta\Psi_{1\mathbf{p}_2}(\mathbf{p}_1) \\ &\quad -i\nabla_{\mathbf{p}}\delta\Psi^*_{1\mathbf{p}_1}(\mathbf{p})\Big|_{\mathbf{p}_2} - \mathbf{R}_1\delta\Psi^*_{1\mathbf{p}_1}(\mathbf{p}_2), \end{aligned} \tag{149}$$

where,

$$\begin{aligned}\mathbf{g}_1(\mathbf{p}_1,\mathbf{p}_2) &= -i^2\mathbf{R}_1\delta\Psi_{1_{\mathbf{p}_2}}(\mathbf{p}_1) + i\mathcal{D}_1(\mathbf{p}_2)\mathcal{C}_1(\mathbf{p}_1,\mathbf{p}_2)\, e^{-i\mathbf{R}_1\cdot(\mathbf{p}_1-\mathbf{p}_2)} \\ &\quad -i\mathcal{D}_2(\mathbf{p}_2)\mathcal{C}_1(\mathbf{p}_1,\mathbf{p}_2)\, e^{-i\mathbf{R}_1\cdot(\mathbf{p}_1+\mathbf{p}_2)} - \mathbf{R}_1\delta\Psi_{1_{\mathbf{p}_2}}(\mathbf{p}_1) \\ &\quad -i^2\mathbf{R}_1\delta\Psi^*_{1_{\mathbf{p}_1}}(\mathbf{p}_2) - i\mathcal{D}_1^*(\mathbf{p}_1)\mathcal{C}_2(\mathbf{p}_1,\mathbf{p}_2)\, e^{i\mathbf{R}_1\cdot(\mathbf{p}_2-\mathbf{p}_1)} \\ &\quad +i\mathcal{D}_2^*(\mathbf{p}_1)\mathcal{C}_2(\mathbf{p}_1,\mathbf{p}_2)\, e^{i\mathbf{R}_1\cdot(\mathbf{p}_1+\mathbf{p}_2)} - \mathbf{R}_1\delta\Psi^*_{1_{\mathbf{p}_1}}(\mathbf{p}_2). \end{aligned} \tag{150}$$

Notice that all the unphysical terms depending directly of the internuclear distance $\mathbf{R}_1$ cancel each others. In this way, after some algebra we get:

$$\begin{aligned}\mathbf{g}_1(\mathbf{p}_1,\mathbf{p}_2) &= \mathrm{i}\Big[\mathcal{D}_1(\mathbf{p}_2)\mathcal{C}_1(\mathbf{p}_1,\mathbf{p}_2) - \mathcal{D}_1^*(\mathbf{p}_1)\mathcal{C}_2(\mathbf{p}_1,\mathbf{p}_2)\Big]\, e^{-i\mathbf{R}_1\cdot(\mathbf{p}_1-\mathbf{p}_2)} \\ &\quad -i\mathcal{D}_2(\mathbf{p}_2)\mathcal{C}_1(\mathbf{p}_1,\mathbf{p}_2)\, e^{-i\mathbf{R}_1\cdot(\mathbf{p}_1+\mathbf{p}_2)} \\ &\quad +i\mathcal{D}_2^*(\mathbf{p}_1)\mathcal{C}_2(\mathbf{p}_1,\mathbf{p}_2)\, e^{i\mathbf{R}_1\cdot(\mathbf{p}_1+\mathbf{p}_2)}. \end{aligned} \tag{151}$$

In this last equation we can directly identify the rescattering term associated to the direct processes in the atom on the *left* in the first line. The other two terms are related to the cross and nonlocal processes involving the atom at $\mathbf{R}_1$. Working in the same way with the term $\mathbf{g}_2(\mathbf{p}_1,\mathbf{p}_2)$ we obtain,

$$\begin{aligned}\mathbf{g}_2(\mathbf{p}_1,\mathbf{p}_2) &= i\Big[\mathcal{D}_1(\mathbf{p}_2)\mathcal{C}_1(\mathbf{p}_1,\mathbf{p}_2) - \mathcal{D}_1^*(\mathbf{p}_1)\mathcal{C}_2(\mathbf{p}_1,\mathbf{p}_2)\Big]\, e^{-i\mathbf{R}_2\cdot(\mathbf{p}_1-\mathbf{p}_2)} \\ &\quad -i\mathcal{D}_2(\mathbf{p}_2)\mathcal{C}_1(\mathbf{p}_1,\mathbf{p}_2)\, e^{-i\mathbf{R}_2\cdot(\mathbf{p}_1+\mathbf{p}_2)} \\ &\quad +i\mathcal{D}_2^*(\mathbf{p}_1)\mathcal{C}_2(\mathbf{p}_1,\mathbf{p}_2)\, e^{i\mathbf{R}_2\cdot(\mathbf{p}_1+\mathbf{p}_2)}. \end{aligned} \tag{152}$$

In the above equation we can also identify the rescattering matrix element related to the local processes in the atom on the *right* in the first line. Those two rescattering matrix elements, that we call $\mathbf{g}_{11}(\mathbf{p}_1,\mathbf{p}_2)$ and $\mathbf{g}_{22}(\mathbf{p}_1,\mathbf{p}_2)$, can be understood looking at the phase factor $e^{-i\mathbf{R}_{1/2}\cdot(\mathbf{p}_1-\mathbf{p}_2)}$. Moreover we can identify trajectories as: one electron with momentum $\mathbf{p}_2$ is going back to the parent ion at $\mathbf{R}_{1/2}$ making an elastic rescattering leaving the ion on $\mathbf{R}_{1/2}$ going to the continuum again with momentum $\mathbf{p}_1$. In the same logic and taking into account the symmetries of the molecule $\mathbf{R}_1 = -\mathbf{R}_2$, we can identify the term related to the cross and nonlocal processes from the total rescattering matrix element as:

$$\begin{aligned}\mathbf{g}(\mathbf{p}_1,\mathbf{p}_2) &= \mathcal{Q}_1(\mathbf{p}_1,\mathbf{p}_2)\left[e^{-i\mathbf{R}_1\cdot(\mathbf{p}_1-\mathbf{p}_2)} + e^{-i\mathbf{R}_2\cdot(\mathbf{p}_1-\mathbf{p}_2)}\right] \\ &\quad + \mathcal{Q}_2(\mathbf{p}_1,\mathbf{p}_2\left[e^{i\mathbf{R}_1\cdot\mathbf{p}_2-i\mathbf{R}_2\cdot\mathbf{p}_1} + e^{i\mathbf{R}_2\cdot\mathbf{p}_2-i\mathbf{R}_1\cdot\mathbf{p}_1}\right]. \end{aligned} \tag{153}$$

The new variables are defined as:

$$\mathcal{Q}_1(\mathbf{p}_1,\mathbf{p}_2) = i\Big[\mathcal{D}_1(\mathbf{p}_2)\mathcal{C}_1(\mathbf{p}_1,\mathbf{p}_2) - \mathcal{D}_1^*(\mathbf{p}_1)\mathcal{C}_2(\mathbf{p}_1,\mathbf{p}_2)\Big], \tag{154}$$

$$\mathcal{Q}_2(\mathbf{p}_1,\mathbf{p}_2) = -i\Big[\mathcal{D}_2(\mathbf{p}_2)\mathcal{C}_1(\mathbf{p}_1,\mathbf{p}_2) - \mathcal{D}_2^*(\mathbf{p}_1)\mathcal{C}_2(\mathbf{p}_1,\mathbf{p}_2)\Big], \quad (155)$$

where the terms, $\mathcal{C}_1(\mathbf{p}_1,\mathbf{p}_2)$ and $\mathcal{C}_2(\mathbf{p}_1,\mathbf{p}_2)$ are the same as the ones defined in Eq. (66). From these last equations we can identify all the contributions, i.e., local, $\mathbf{g}_{11/22}(\mathbf{p}_1,\mathbf{p}_2)$ and nonlocal and cross, $\mathbf{g}_{12/21}(\mathbf{p}_1,\mathbf{p}_2)$, respectively. The cross terms look like,

$$\mathbf{g}_{12}(\mathbf{p}_1,\mathbf{p}_2) = \mathcal{Q}_2(\mathbf{p}_1,\mathbf{p}_2)\, e^{i\mathbf{R}_1\cdot\mathbf{p}_2 - i\mathbf{R}_2\cdot\mathbf{p}_1}, \quad (156)$$

$$\mathbf{g}_{21}(\mathbf{p}_1,\mathbf{p}_2) = \mathcal{Q}_2(\mathbf{p}_1,\mathbf{p}_2)\, e^{i\mathbf{R}_2\cdot\mathbf{p}_2 - i\mathbf{R}_1\cdot\mathbf{p}_1}. \quad (157)$$

This equation have a similar interpretation as the local one; an electron in the continuum change from momentum $\mathbf{p}_2$ to momentum $\mathbf{p}_1$ in a rescattering process that involves two atoms at different positions.

After obtaining both the bound-free and rescattering transition matrix elements, it is possible to compute Eqs. (90) and (111) to obtain the direct, the rescattering and the total photoelectron transition amplitudes. The presented model is an alternative way to describe the ATI process mediated by a strong laser pulse. Our two-center molecular model is an extension to the one presented in Ref.[4] and renders to the same atomic equations when $\mathbf{R} \to 0$ (see Appendix 9 for more details and proofs).

2.4.2 *Molecular orbital as a LCAO*

In this section we are going to calculate the molecular bound states as a LCAO of Gaussian-like functions. Our formulation takes full advantage of the GAMESS package [50, 51]. For simplicity we use a STO-3G basis set, but note that our approach is quite general and other basis sets could be employed.

Let us define the bound state of the molecular system as:

$$\Psi_{0_{LCAO}}(\mathbf{p}) = \sum_{j=1}^{2}\sum_{i=1}^{5} G_{j(i)}\Phi_{j(i)}(\mathbf{p}), \quad (158)$$

where the index j represents the number of the atoms in the molecule. Furthermore, the index i accounts for the different atomic orbitals (AOs) (throughout our contribution we model molecular systems using only 1s, 2s and 2p states, but states with other quantum numbers could be implemented), i.e.

$$\begin{aligned} i &= 1 \to 1s, \\ i &= 2 \to 2s, \\ i &= 3 \to 2p_x, \\ i &= 4 \to 2p_y, \\ i &= 5 \to 2p_z. \end{aligned} \quad (159)$$

Furthermore, $G_{j(i)}$ is a constant defining the *weight* of each atomic orbital. In our case we consider the HOMO and the particular values are obtained using GAMESS. Finally, the functions $\Phi_{j(i)}(\mathbf{p})$ define the atomic orbitals. For instance, an atomic orbital based on s states can be written as:

$$\Phi_{j(s)}(\mathbf{p}) \;=\; e^{-i\mathbf{R}_j\cdot\mathbf{p}}\,\frac{1}{2^{3/2}}\sum_{n=1}^{3}\frac{C_{n;j(s)}}{\zeta_{n;j(s)}^{3/2}}\,e^{\frac{-\mathbf{p}^2}{4\zeta_{n;j(s)}}}, \tag{160}$$

meanwhile that for 2p states are:

$$\Phi_{j(2p_r)}(\mathbf{p}) = -i\,p_r\,e^{-i\mathbf{R}_j\cdot\mathbf{p}}\,\frac{1}{2^{5/2}}\sum_{n=1}^{3}\frac{C_{n;j(p_r)}}{\zeta_{n;j(p_r)}^{5/2}}\,e^{\frac{-\mathbf{p}^2}{4\zeta_{n;j(p_r)}}}. \tag{161}$$

Here the index r can take the values x, y, or z. The coefficients $C_{n;j(s,p_r)}$ and $\zeta_{n;j(s,p_r)}$ are obtained using, for example, a Roothaan-Hartree-Fock optimization scheme (see [50, 51] for more details).

The dipole transition matrix element within this model, that describes the transition of the electron from the bound to the continuum state, then reads as:

$$\mathbf{d}_{LCAO}(\mathbf{v}) = -\langle\mathbf{v}|(\mathbf{r}-\mathbf{R}_j)|\Psi_{0_{LCAO}}\rangle = -\langle\mathbf{v}|\mathbf{r}|\Psi_{0_{LCAO}}\rangle + \mathbf{R}_j\langle\mathbf{v}|\Psi_{0_{LCAO}}\rangle. \tag{162}$$

More explicitly,

$$\mathbf{d}_{LCAO}(\mathbf{p}_0) = -\sum_{j=1}^{2}\sum_{i=1}^{5}G_{j(i)}\Big\{i\nabla_{\mathbf{p}}\,\Phi_{j(i)}(\mathbf{p})\Big|_{\mathbf{p}_0} - \mathbf{R}_j\,\Phi_{j(i)}(\mathbf{p}_0)\Big\}, \tag{163}$$

where depending on the states character the gradient results

$$i\nabla_{\mathbf{p}}\,\Phi_{j(1s)}(\mathbf{p})\Big|_{\mathbf{p}_0} = \mathbf{R}_j\,\Phi_{j(1s)}(\mathbf{p}_0) - \frac{i\,\mathbf{p}_0}{2\,\zeta_{j;n(s)}}\,\Phi_{j(1s)}(\mathbf{p}_0), \tag{164}$$

for the s states and

$$\begin{aligned} i\nabla_{\mathbf{p}}\,\Phi_{j(2p_r)}(\mathbf{p})\Big|_{\mathbf{p}_0} \;&=\; \mathbf{R}_j\,\Phi_{j(2p_r)}(\mathbf{p}_0) - \frac{i\,\mathbf{p}_0\Phi_{j(2p_r)}(\mathbf{p}_0)}{2\,\zeta_{n;j(2p_r)}} \\ &\quad + \delta\Phi_{j(2p_r)}(\mathbf{p}_0)\,\hat{\mathbf{r}}, \end{aligned} \tag{165}$$

where

$$\delta\Phi_{j(2p_r)}(\mathbf{p}_0) = e^{-i\mathbf{R}_j\cdot\mathbf{p}_0}\,\frac{1}{2^{5/2}}\sum_{n=1}^{3}\frac{C_{n;j(2p_z)}}{\zeta_{n;j(2p_z)}^{5/2}}\,e^{\frac{-\mathbf{p}_0^2}{4\zeta_{n;j(2p_z)}}}, \tag{166}$$

for the p states.

Using the above equations we are able to obtain analytical expressions for the molecular dipole transition matrix elements of the different molecular systems that we want to study. In this chapter we are going to calculate the ATI spectra for two prototypical two-center molecules: O_2 and CO using both the SR and the LCAO model.

2.4.2.1 *Bound-continuum dipole matrix: O_2 molecule*

The bound state (HOMO) for the O_2 molecule oriented on the y-axis, written as a LCAO, reads as:

$$\Psi_{0-O_2}(\mathbf{p}) = G_{1(2p_z)}\Phi_{1(2p_z)}(\mathbf{p}) + G_{2(2p_z)}\Phi_{2(2p_z)}(\mathbf{p}). \quad (167)$$

Furthermore, the dipole transition matrix element can be computed from

$$\begin{aligned}\mathbf{d}_{O_2}(\mathbf{p}_0) = &-G_{1(2p_z)}\left\{i\nabla_{\mathbf{p}}\,\Phi_{1(2p_z)}(\mathbf{p})\Big|_{\mathbf{p}_0} - \mathbf{R}_1\,\Phi_{1(2p_z)}(\mathbf{p}_0)\right\}\\ &-G_{2(2p_z)}\left\{i\nabla_{\mathbf{p}}\,\Phi_{2(2p_z)}(\mathbf{p})\Big|_{\mathbf{p}_0} - \mathbf{R}_2\,\Phi_{2(2p_z)}(\mathbf{p}_0)\right\},\end{aligned} \quad (168)$$

where inserting the Eqs. (161) and (165) into the above equation we explicit have,

$$\begin{aligned}\mathbf{d}_{O_2}(\mathbf{p}_0) = &\; G_{1(2p_z)}\left\{i\,\mathbf{p}_0\frac{\Phi_{1(2p_z)}(\mathbf{p}_0)}{2\,\zeta_{1;n(2p_z)}} - \delta\Phi_{1(2p_z)}(\mathbf{p}_0)\,\hat{\mathbf{j}}\right\}\\ &+ G_{2(2p_z)}\left\{i\,\mathbf{p}_0\frac{\Phi_{2(2p_z)}(\mathbf{p}_0)}{2\,\zeta_{2;n(2p_z)}} - \delta\Phi_{2(2p_z)}(\mathbf{p}_0)\,\hat{\mathbf{j}}\right\}.\end{aligned} \quad (169)$$

The parameters $G_{(1,2)(2p_z)}$ and $\zeta_{n;1/2(2p_z)}$ are obtained setting the molecule in its equilibrium position via an optimization procedure using GAMESS [50, 51].

2.4.2.2 *Bound-continuum dipole matrix: CO molecule*

For the case of CO the bound state is a composition of 1s, 2s and 2p states. It can then be written as:

$$\begin{aligned}\Psi_{0-CO}(\mathbf{p}) = &\; G_{1(1s)}\Phi_{1(1s)}(\mathbf{p}) + G_{1(2s)}\Phi_{1(2s)}(\mathbf{p}) + G_{1(2p_z)}\Phi_{1(2p_z)}(\mathbf{p})\\ &+ G_{2(1s)}\Phi_{2(1s)}(\mathbf{r}) + G_{2(2s)}\Phi_{2(2s)}(\mathbf{p}) + G_{2(2p_z)}\Phi_{2(2p_z)}(\mathbf{p}).\end{aligned} \quad (170)$$

The dipole transition matrix element reads as:

$$\begin{aligned}\mathbf{d}_{CO}(\mathbf{p}_0) = &-G_{1(1s)}\left\{i\nabla_{\mathbf{p}}\,\Phi_{1(1s)}(\mathbf{p})\Big|_{\mathbf{p}_0} - \mathbf{R}_1\,\Phi_{1(1s)}(\mathbf{p}_0)\right\}\\ &-G_{1(2s)}\left\{i\nabla_{\mathbf{p}}\,\Phi_{1(2s)}(\mathbf{p})\Big|_{\mathbf{p}_0} - \mathbf{R}_1\,\Phi_{1(2s)}(\mathbf{p}_0)\right\}\\ &-G_{1(2p_z)}\left\{i\nabla_{\mathbf{p}}\,\Phi_{1(2p_z)}(\mathbf{p})\Big|_{\mathbf{p}_0} - \mathbf{R}_1\,\Phi_{1(2p_z)}(\mathbf{p}_0)\right\}\\ &-G_{2(1s)}\left\{i\nabla_{\mathbf{p}}\,\Phi_{2(1s)}(\mathbf{p})\Big|_{\mathbf{p}_0} - \mathbf{R}_2\,\Phi_{2(1s)}(\mathbf{p}_0)\right\}\\ &-G_{2(2s)}\left\{i\nabla_{\mathbf{p}}\,\Phi_{2(2s)}(\mathbf{p})\Big|_{\mathbf{p}_0} - \mathbf{R}_2\,\Phi_{2(2s)}(\mathbf{p}_0)\right\}\\ &-G_{2(2p_z)}\left\{i\nabla_{\mathbf{p}}\,\Phi_{2(2p_z)}(\mathbf{p})\Big|_{\mathbf{p}_0} - \mathbf{R}_2\,\Phi_{2(2p_z)}(\mathbf{p}_0)\right\},\end{aligned} \quad (171)$$

where, more explicitly, we then have:

$$\begin{aligned}\mathbf{d}_{CO}(\mathbf{p}_0) = & G_{1(1s)}\left\{i\,\mathbf{p}_0\frac{\Phi_{1(1s)}(\mathbf{p}_0)}{2\,\zeta_{1;n(1s)}}\right\} + G_{1(2s)}\left\{i\,\mathbf{p}_0\frac{\Phi_{1(2s)}(\mathbf{p}_0)}{2\,\zeta_{1;n(2s)}}\right\} \\ & + G_{1(2p_z)}\left\{i\,\mathbf{p}_0\frac{\Phi_{1(2p_z)}(\mathbf{p}_0)}{2\,\zeta_{1;n(2p_z)}} - \delta\Phi_{1(2p_z)}(\mathbf{p}_0)\,\hat{\mathbf{k}}\right\} \\ & + G_{2(1s)}\left\{i\,\mathbf{p}_0\frac{\Phi_{2(1s)}(\mathbf{p}_0)}{2\,\zeta_{2;n(1s)}}\right\} + G_{2(2s)}\left\{i\,\mathbf{p}_0\frac{\Phi_{2(2s)}(\mathbf{p}_0)}{2\,\zeta_{2;n(2s)}}\right\} \\ & + G_{2(2p_z)}\left\{i\,\mathbf{p}_0\frac{\Phi_{2(2p_z)}(\mathbf{p}_0)}{2\,\zeta_{2;n(2p_z)}} - \delta\Phi_{2(2p_z)}(\mathbf{p}_0)\,\hat{\mathbf{k}}\right\}. \quad (172)\end{aligned}$$

We stress that the method is physically intuitive, and can be understood on the basis of a quasiclassical picture, i.e. ,electron trajectories. This is the main difference of our approach in comparison to the numerical solution of the TDSE, whose physical interpretation is, in spite of its accuracy, frequently challenging. The main advantage of the proposed model is that Eqs. (90) and (112) give a clear physical understanding of the ATI process and provide rich and useful information about both the laser field and the diatomic molecular target, which are encoded into the complex transition amplitude $b(\mathbf{p}, t) = b_0(\mathbf{p}, t) + b_1(\mathbf{p}, t)$. The exact analytical solutions of both the direct and rescattering transition amplitudes are, however, not trivial to obtain if no approximations are considered. In particular, for the rescattering photoelectrons, the solution is even more complex and depends, generally, of the laser electric field shape.

2.5 RESULTS AND DISCUSSION

Throughout this section we apply the molecular version of our model to four prototypical diatomic systems: H_2^+, H_2, O_2 and CO. We then calculate the HHG and ATI spectra for those systems.

For the HHG section, we analyze two systems: H_2^+ and H_2. Furthermore, we display and study the contributions coming from the *local* and *cross* recombination processes. This analysis helps us to distinguish which contributions interfere constructively or destructively to the total HHG spectra. The basic analysis of the interference minima of the harmonic spectra with respect to the alignment for H_2^+ is discussed. In addition, the contribution of the different processes to the total spectra is assessed. A time analysis of the HHG spectra using a Gabor transformation is performed and the influence of the short and long trajectories is investigated. A comparison of the time-frequency distribution of an hydrogen atom and a dihydrogen molecule is presented.

In a second stage, we shall compare the outcomes of our model for the ATI spectra emitted from a H_2^+ system to the exact numerical solution of the 3D-TDSE. A scan on different internuclear distances

of the ionization probability and the whole momentum distribution along the laser polarization and molecular orientation axis shows that our model works reasonably well. Furthermore, the splitting of contributions coming from the *left* and *right* nuclei and *local*, *cross*, and *nonlocal* rescattering processes helps to distinguish which part of the photoelectron spectra is relevant for each kind of event. The molecular internuclear distance is retrieved probing that our model is capable to capture the structural information encoded on the photoelectron spectra.

In here we use two different methods to analytically obtain the bound-free transition matrix element, a key piece in the total photoelectron spectra calculation. First, we use a nonlocal SR potential to describe the interaction between the active electron and the ionic centers. Note that such SR only supports s states. Second, we use a LCAO, to correctly describe the molecular orbital; the LCAO supports both s and p states. We compare the results from the two models and the effect of the shape of the molecular orbital on the ATI spectra.

Finally, a comparison with the experimental photoelectron spectra on the O_2^+ molecule driven by a mid-IR source (3.1 μm) demonstrates that our simplified model is able to render the main physics behind the rescattering process in a more "complex" symmetric diatomic molecule.

2.5.1 *Diatomic molecular systems: HHG*

In this section, we calculate HHG spectra for two prototypical diatomic molecules: H_2^+ and H_2.

2.5.1.1 *H_2^+ molecule*

Figure 11 shows the numerically computed HHG spectra for an H_2^+ molecule by using the quasiclassical SFA model presented before. The H_2^+ system is modelled by two identical centers separated by an internuclear distance $R = 2.2$ a.u. (1.16 Å) and the molecular axis forms a θ angle with respect to the incident laser electric field polarization, i.e., $\mathbf{R} = (0, 0, R\cos\theta)$.

The parameters of our nonlocal SR potential are set to $\Gamma = 1.0$ and $\gamma = 0.1$ a.u. in order to reproduce the minimum at the equilibrium internuclear distance, $R_0 = 2.0$ a.u. (1.06 Å), in the PES (see Fig. 10). The total ionization potential extracted from the potential energy surface in our model yields $I_p = 0.68$ a.u. (18.50 eV). This electronic ground-state energy allows us to fix the correct asymptotic behavior of the H_2^+ PES. Note that this last value differs from the one obtained with a real Coulomb potential that leads a pure electronic energy of 1.1 a.u. (30 eV) approximately.

The incident laser field shape is identical to the one used in the atomic case and has a central frequency $\omega_0 = 0.057$ a.u. with a total

number of cycles is $N_c = 4$ and $\phi_0 = 0$ rad. The time step is set to $\delta t = 0.032$ a.u. and this corresponds to a total of $N_t = 20000$ points for the numerical integration. Finally, the laser peak intensity is set to $I_0 = 5 \times 10^{14}$ W $\cdot$ cm^{-2}.

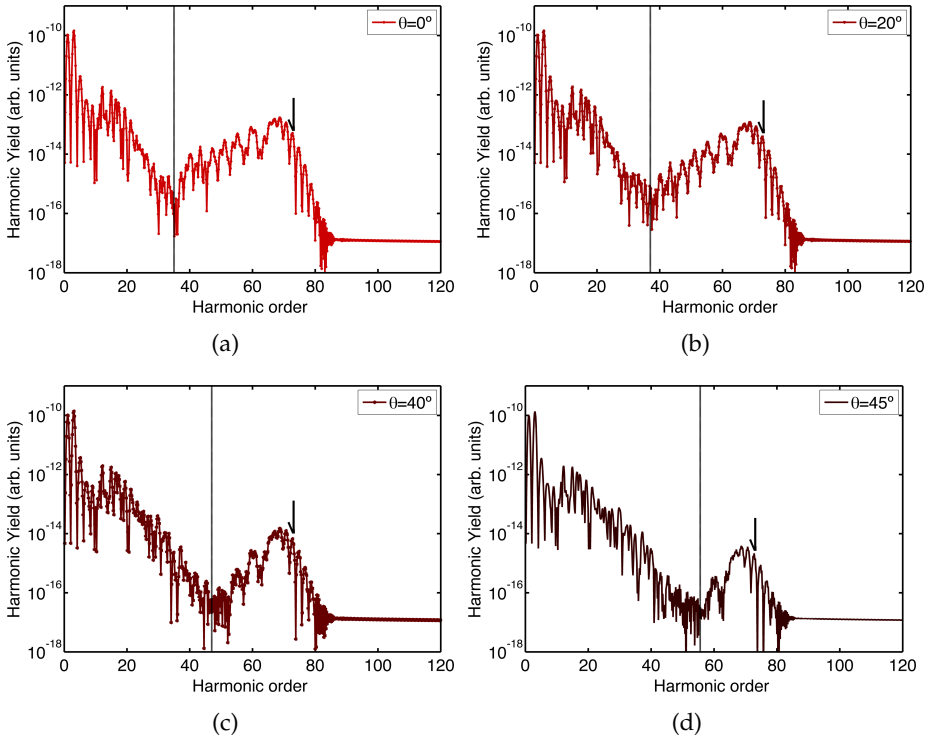

Figure 11: Total HHG spectra $\mathcal{I}(\omega)$ (in logarithmic scale), Eq. (104), of an H_2^+ molecule driven by a strong few-cycle pulse as a function of the harmonic order computed using our quasiclassical SFA. (a) HHG for an H_2^+ molecule aligned with the laser pulse polarization axis, i.e., $\theta = 0°$; (b) the same as (a) but for $\theta = 20°$; (c) the same as (a) but for $\theta = 40°$; (d) the same as (a) but for $\theta = 45°$. The vertical lines indicate the position of the interference minima of our quasiclassical SFA model and the arrows in all the panels the position of the classical HHG cutoff, respectively.

In Fig. 11, we display results for a scan of four different molecular orientations, namely Fig. 11(a) $\theta = 0°$ (this value corresponds to the so-called parallel alignment), Fig. 11(b) 20°, Fig. 11(c) 40° and Fig. 11(d) 45°, respectively. As we can see in all the panels an absolute minimum over the total HHG spectra is clearly visible and the harmonic order where these minima is located increases with the orientation angle. The existence of those minima and their dependency with the alignment angle can be explained by invoking an interference phenomenon as we will see below. In the most simplest picture the minima appears as a consequence of the harmonic emission of two radiant points (see, e.g., [52] for more details).

According to the equation describing the destructive interference of two radiant sources, $R\cos\theta = (2m+1)\lambda_k/2$, where λ_k is the de Broglie wavelength of the returning electron and considering the "fundamental" instance $m = 0$, the minima should be located at the 18^{th}, 20^{th}, 30^{th}, and 36^{th} harmonic order for $\theta = 0°$, $\theta = 20°$, $\theta = 40°$, and $\theta = 45°$, respectively. The positions of the minima in our SFA calculation are $\approx 35^{th}$, $\approx 37^{th}$, $\approx 45^{th}$ and $\approx 54^{th}$, respectively (see the vertical lines in all the panels of Fig. 11). We speculate that the shifts in harmonic frequency are related with the kind of potential used in our calculations; the nonlocal SR potential does not correctly describe the low energy part of the HHG spectra, where the Coulomb potential plays an important role [53]. We note, however, that our SFA calculation for $\theta = 40°$ is in excellent agreement with the numerical solution of the 2D-TDSE and 3D-TDSE for the H_2^+ molecule [52, 54]. Lastly, we observe that in all the HHG spectra of Fig. 11 the position of the classical cutoff is in excellent agreement with Eq. (67) (see the arrows in all the panels of Fig. 11). Particularly, for our H_2^+ molecular system and the laser parameters used in our simulations, the cutoff frequency is $\omega_{cutoff} = 4.15$ a.u. (112.92 eV), corresponding to the 72^{th} harmonic order.

Clearly, our quasiclassical molecular SFA model has drawbacks and advantages. The first advantage is from the computational viewpoint; the numerical calculations using our SFA approach are much faster than the numerical solution of the 3D-TDSE. The computation of one single HHG spectrum for a set of fixed parameters takes few seconds. The second, and might be the most important one, is the possibility to disentangle the different processes contributing to the final HHG spectra (see Sec. 2.3.1). In order to do so in the Fig. 12, left panel, we plot the different contributions for an H_2^+ molecule aligned $\theta = 20°$ with respect to the laser field polarization. Figure 12(a) shows the total $\mathcal{I}(\omega)$ (red circle line), the *local* $\mathcal{I}_{local}(\omega)$ (blue line) and the *cross* $\mathcal{I}_{cross}(\omega)$ (dark brown asterisk line) contributions (for details see Sec. 2.3.1).

As we can see from this picture, the two-center destructive interference is not present either in the *local* or in the *cross* contributions. The latter have a deep minimum but at a different position, about the 60^{th} harmonic order, while the former remains almost constant in yield for all the harmonic frequencies. In order to trace out the origin of the two-center destructive interference present in the total HHG spectra in Fig. 12(b)-(c) we plot the independent local and cross terms. The deep minimum does not exist in the harmonic spectra from the independent atoms, neither in the cross. This suggested that this feature is related to processes starting and ending in the same atomic site. To follow the analysis in Fig. 13 we plot the contributions for processes ending, i.e. $|\vec{\mu}_{11} + \vec{\mu}_{21}|^2 \propto \left|\int_{-\infty}^{\infty} dt\, e^{i\omega t}\,[\vec{\mu}_{11}(t) + \vec{\mu}_{21}(t)]\right|^2$, and start-

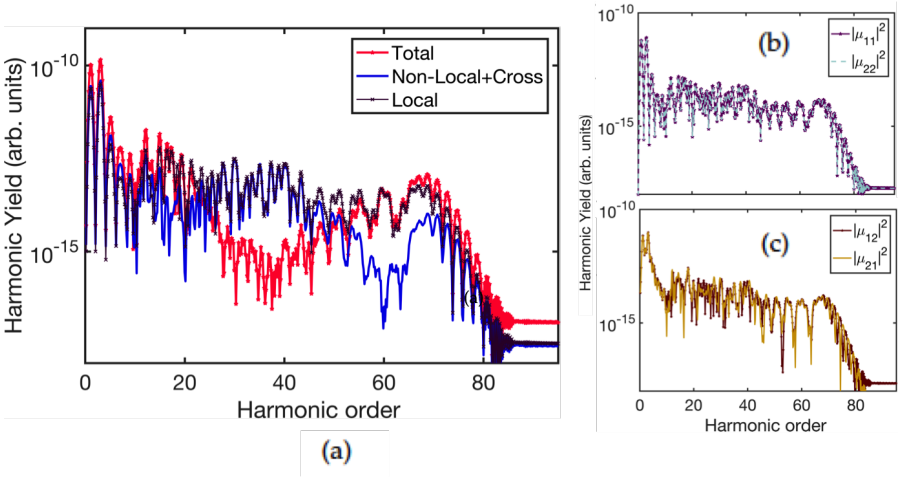

Figure 12: HHG spectra $\mathcal{I}(\omega)$ (in logarithmic scale) of an H_2^+ molecule, Eq. (104), as a function of the harmonic order calculated using our quasiclassical SFA and for an orientation angle $\theta = 20°$. (a) local, cross and total contributions to the HHG spectrum. (b) Local contributions; purple circle line: ionization and recombination at $\mathbf{R}_1$ and light blue dashed line: ionization and recombination at $\mathbf{R}_2$. (c) Cross contributions: dark brown circle line: ionization at $\mathbf{R}_1$ and recombination at $\mathbf{R}_2$, light brown line: ionization at $\mathbf{R}_2$ and recombination at $\mathbf{R}_1$.

ing, i.e. $|\vec{\mu}_{11} + \vec{\mu}_{12}|^2 \propto \left|\int_{-\infty}^{\infty} dt\, e^{i\omega t}\, [\vec{\mu}_{11}(t) + \vec{\mu}_{12}(t)]\right|^2$, on the same site.

As we can see all of this terms leads to a strong suppression of a relatively broad band of consecutive harmonics, leading to a global minimum in the harmonic spectrum. It means that, for the case of the recombination on $\mathbf{R}_1$ (dark green circle line), the electron wave packet ionized at $\mathbf{R}_1$ interferes with the one coming from $\mathbf{R}_2$ and the other way around. And similar for the case where the ionization processes take place in the same atom (dark red circle line). These minima are generated by the interference between electronic orbits starting/ending at the same center.

This features are a direct consequence of the symmetries in the molecular system that is captured in the MSFA model by the correct treatment of the coordinate system. The use of the standard SFA model for molecules without include the correction based on the position of the atoms may leave suspicious results. This is the case for the work presented in Faria 2007 [55] where a linear term on R is included in the saddle-point equations or in the recombination matrix elements. This linear term on R in the matrix element naturally vanish out when the exact position of the atomic centers is taken into account; the same for the phase factor in the local terms.

The artificial addition of R in the modified saddle-point equations give differences in the magnitud between the different local and cross

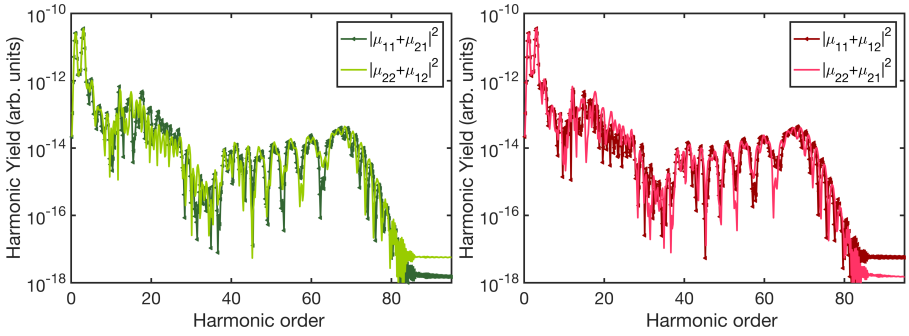

Figure 13: Different contributions depending on the, (a) recombination atom. Green circle line: recombination at $\mathbf{R}_1$ and light green line: recombination at $\mathbf{R}_2$. (b) Ionization atom; red circle line: ionization at $\mathbf{R}_1$ and light red line: ionization at $\mathbf{R}_2$.

terms. This dependency is also leading an incorrect asymptotic condition when $\mathbf{R} \to \infty$. Our model offer a new alternative to avoid this kind of unphysical result. The differences between our results and those presented in previous works, e.g. [55], are directly related to the coordinate system used and the linear terms on the matrix elements phases. Our modification of the SFA uses a SR potential that allows us to compute exactly both the continuum and ground states (note that the continuum states of this potential differ from the plane waves). Using a separable SR potential one has a lot freedom to adjust its parameters and adequately scrutinize the "centers" effects.

From the drawbacks side, we have seen that our nonlocal SR potential is unable to accurately reproduce the interference minima positions for some of the molecular orientation angles. We note, however, that these minima are typically washed out when an average over the molecular orientation is considered, configuration that is commonly used in molecular HHG experiments.

2.5.1.2 *Time-frequency analysis for H_2^+*

We have seen in Fig. 12 that the independent processes $\vec{\mu}_{11}(t)/\vec{\mu}_{22}(t)$ and $\vec{\mu}_{21}(t)/\vec{\mu}_{12}(t)$, are the ones interfering and creating the deep minimum in the total HHG spectra. In order to dig deeper about the existence of this distinctive feature a Gabor analysis [56, 57] over the different contributions is displayed in Fig. 14. The Gabor transformation was performed upon the time-dependent dipole moment calculated using our quasiclassical SFA model. The laser parameters are the same as in Fig. 12.

This time-frequency analysis allows us to reveal the half-cycle bursts of radiation from which the HHG spectrum is formed and the main trajectories contributing. In Figs. 14(a) and 14(b), we show the *local* and *cross* processes at $\mathbf{R}_1$, $\vec{\mu}_{11}(t)$, and $\vec{\mu}_{21}(t)$, respectively (note that

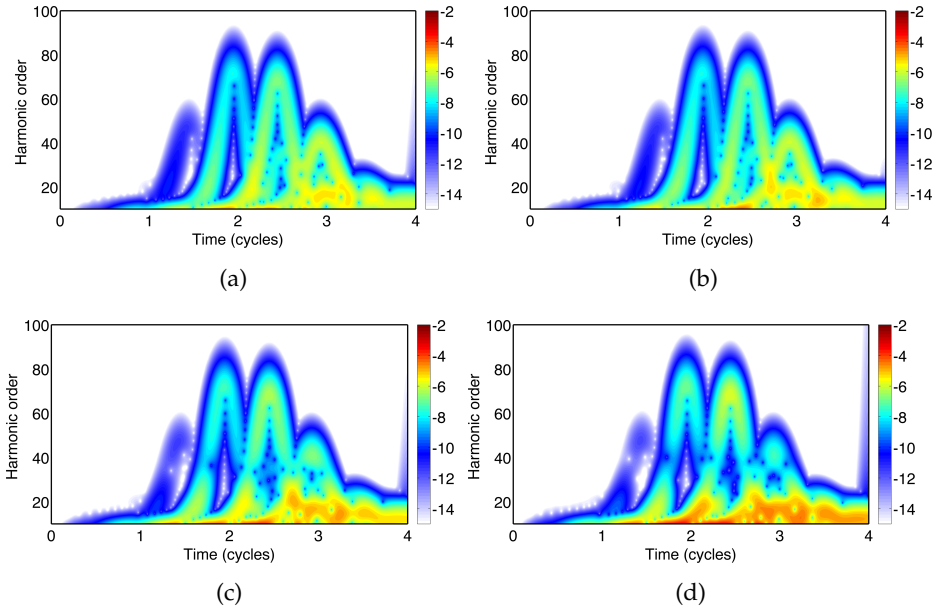

Figure 14: Gabor transformation of the time-dependent dipole moment of an H_2^+ diatomic molecule oriented $\theta = 20°$ with the laser field. (a) *local* processes at $\mathbf{R}_1$ using the time-dependent dipole moment $\vec{\mu_{11}}(t)$; (b) the same as (a) but for the *cross* processes $\vec{\mu_{21}}(t)$; (c) the same as (a) but for all the recombination processes at $\mathbf{R}_1$, i.e., $\vec{\mu_{11}}(t) + \vec{\mu_{21}}(t)$; (d) Gabor transformation for the total time-dependent dipole moment $\vec{\mu}_{2N}(t)$.

identical plots can be obtained by changing $\mathbf{R}_1$ by $\mathbf{R}_2$). As we can observe from these figures, they both look almost equal and similar to the atomic case. In both cases, we have the contribution of the short and long trajectories. For the earlier cycles, the first and second ones, the short trajectory contributions dominate while for the latest cycles both long and short trajectories have the same weight. The main differences between these two contributions are in the low-energy region around the end of the laser pulse, the third optical cycle, where the contribution of the *cross* processes $\vec{\mu}_{21}(t)$ is slightly higher than the *local* ones.

Finally, we plot in Fig. 14(c) all the recombination processes contributions at $\mathbf{R}_1$, i.e., $\vec{\mu_{11}}(t) + \vec{\mu_{21}}(t)$ and in Fig. 14(d) the total contributions. From these figures is evident the presence of an interference minimum for the whole temporal window. This means that the, $\vec{\mu}_{11}(t)$ and $\vec{\mu}_{21}(t)$ processes, that describe electrons arriving at the same point $\mathbf{R}_1$ from two different atomic sources, $\mathbf{R}_1$ and $\mathbf{R}_2$, respectively, cancel each other and an interference zone is seen for an harmonic order of around 35^{th}. These two contributions are dominated by the short trajectories, therefore, both incoming electron wave packets arrive at the same time and as a consequence a destructive interference is observed. This feature is inherited to the total time-dependent dipole moment [see Fig. 14(d)].

2.5.1.3 H_2 *molecule*

The next simplest diatomic molecule is H_2. In order to investigate the behavior and versatility of our semiclassical SFA model, we compute HHG spectra using the time-dependent dipole moment presented in Sec. 2.3.1. We consider an H_2 molecule in equilibrium where the two H atoms are separated a distance of $R = 1.4$ a.u. (0.74 Å). The ionization potential of the outer electron predicted by our nonlocal SR potential is $I_p = 1.5$ a.u. (40.82 eV) and it was calculated by setting $\Gamma = 1.0$ and $\gamma = 0.12$ a.u. With these parameters our model reproduces the PES of H_2 with a minimum at the equilibrium internuclear distance [58]. The driven laser pulse has the same parameters as for the case of H_2^+.

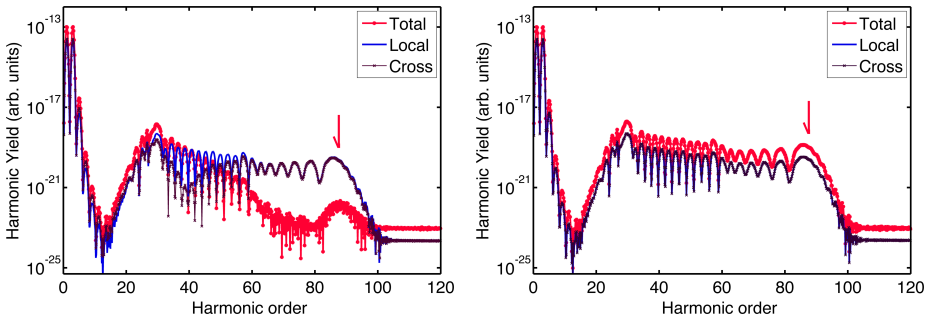

Figure 15: Different contributions to the molecular HHG spectrum (in logarithmic scale) for an H_2 molecule. (a) *Total*, *local*, and *cross* contributions for a molecule oriented parallel ($\theta = 0°$) to the laser field polarization; (b) the same as in (a) but for $\theta = 90°$ (perpendicular orientation).

Figure 15 shows the different contributions to the total HHG spectrum by considering two different molecular orientations: parallel, $\theta = 0°$ [Fig. 15(a)] and perpendicular, $\theta = 90°$ [Fig. 15(b)] with respect to the incident laser pulse polarization. The total HHG spectrum (in red) is computed as the sum of all possible processes Eq. (101). In both panels, we have grouped two main contributions: (i) the *local* and (ii) the *cross* ones. The *local* contributions (blue line) are processes related with only one atom or position, i.e., they involve the sum of processes involving only one single atom, meaning ionization from the $\mathbf{R}_1/\mathbf{R}_2$ and recombination at the same atom. On the other hand, the *cross* contributions (in dark brown) include processes involving both of the atoms in the molecule, i.e., ionization from the atom located at $\mathbf{R}_1$ and recombination on the atom located at $\mathbf{R}_2$ and the other way around.

The first observation regarding Fig. 15 is that for the case of parallel orientation [Fig. 15(a)], the total HHG spectrum starts to gradually decrease for harmonic orders higher than the $\approx 30^{\text{th}}$. This behavior is

due to a destructive interference of the *local* and the *cross* processes. The latter shows a deep minimum around the $\approx 40^{th}$ harmonic order. In the case of the molecule perpendicularly oriented, Fig. 15(b), an extended plateau with a cutoff around the 90^{th} harmonic order is clearly visible. In both cases, parallel and perpendicular, the molecular HHG spectra shows a deep minimum around the 12^{th} harmonic order. As in the case of H_2^+ previously presented, the utilization of a nonlocal SR potential restricts our results to the higher harmonics order, where the influence of the molecular potential details is less relevant.

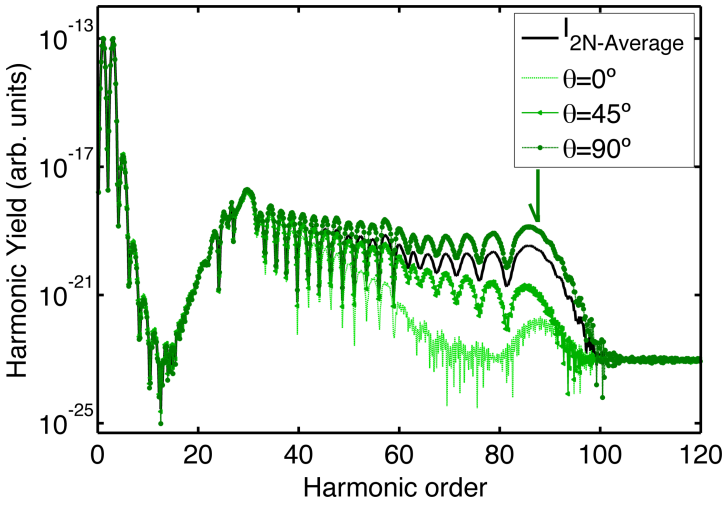

Figure 16: Total H_2 molecular HHG spectra (in logarithmic scale) for $\theta = 0°$, $\theta = 45°$, $\theta = 90°$ and averaged over nine different molecular orientations.

It is interesting to note that for the case of perpendicular orientation, $\theta = 90°$ [Fig. 15(b)], both the *local* and *cross* processes contribute evenly in the plateau region of the HHG spectra, while for the parallel orientation $\theta = 0°$ [Fig. 15(a)] both present a different behavior. We can then infer that for the $\theta = 90°$ case, the total HHG spectrum reaches a maximum yield at the cutoff region. This is due to the fact that, for this favorable orientation, the contribution of each of the processes, *local* and *cross*, is comparable.

Finally, in Fig. 16, we show the total HHG spectra for three different molecular orientations, $\theta = 0°$, $\theta = 45°$, and $\theta = 90°$ and an averaged case over nine values of θ in the range $[0° - 360°]$. Our diatomic molecule is symmetrical with respect to the origin, i.e., $\mathbf{R}_1 = -\mathbf{R}/2$ and $\mathbf{R}_2 = \mathbf{R}/2$ and, consequently, the total HHG spectra for $\theta = 0°$ and $\theta = 180°$ are identical. The same behavior is observed for the spectra at 45°, 135°, 225°, and 315° or for 90° and 270°. We can observe in Fig. 16 how different molecular configurations contribute to the total HHG spectra. As we can see, the difference in the total HHG spectra for different orientation angles is hardly to notice for lower harmonic orders ($< 30^{th}$). Differences start to be noticeable in the

mid-plateau and cutoff regions. In these zones the highest HHG yield is reached for the perpendicular orientation ($\theta = 90°$), thus confirming the results presented in Fig. 15. Two final remarks are in order, namely, (i) the averaged total HHG spectrum is about one order of magnitude lower than the one at perpendicular orientation; (ii) the average procedure washes out any two-slit interference fingerprint.

2.5.1.4 *Time-frequency analysis for H_2*

In Fig. 17, we perform a Gabor transformation upon the time-dependent dipole moment for both an H atom and our diatomic H_2 molecule. Our aim with this time-energy analysis is to investigate the influence of the short and long trajectories for the molecular system and highlight the differences with the atomic case. In Fig. 17(a), we show the calculation for the H atom, while in Fig. 17(b) we depict the same analysis for the molecular system randomly oriented. In both cases we have considered a laser peak intensity $I_0 = 5 \times 10^{14}$ W $\cdot$ cm^{-2}.

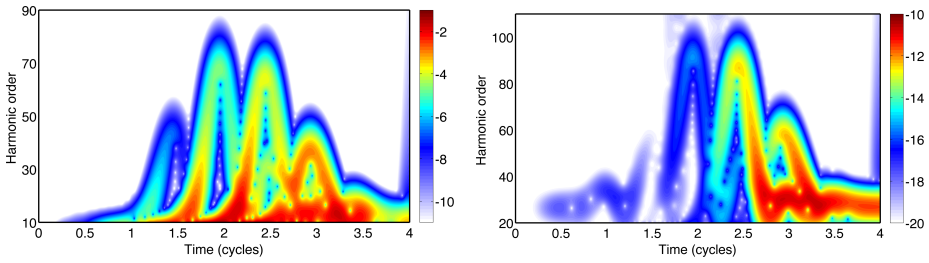

(a) (b)

Figure 17: Gabor transformation of the time-dependent dipole. (a) An hydrogen atom (H) driven by a laser pulse with a peak intensity of $I_0 = 5 \times 10^{14}$ W $\cdot$ cm^{-2}; (b) same as (a) but for a molecule of hydrogen (H_2) randomly oriented.

In general, both figures look quite different. The atomic system [Fig. 17(a)] is mostly dominated by the short trajectories while the molecular system [Fig. 17(b)] have a prevailing contribution from the long ones. This is so because the orientation average procedure removes every fingerprint of two-center interferences.

From a detailed comparison between the atomic and molecular cases we observe that for the former, even when the short trajectories are dominant at the beginning of the laser pulse (first two optical cycles), some contribution of the long ones survives for the later optical cycles, where long and short trajectories contributions are similar (three optical cycles). On the contrary, in the molecular system, short and long trajectories contribute to different optical cycles. For instance, in the first and second optical cycles the main contribution is from the short trajectories while for the third and fourth optical cycles a big contribution of the long trajectories appears. In the molecular system, the contributions of the long trajectories start to increase, be-

ing paramount for the later optical cycles where the contribution of the short ones is less significant.

2.5.2 *ATI: Comparison between SFA and 3D-TDSE*

The numerical integration for the photoelectron spectra computation by means of Eqs. (90),(111) and (35) has been performed via a rectangular rule with particular emphasis on the convergence of the results. As the final momentum distribution, Eq. (35), is "locally" independent of the momentum $\mathbf{p}$, $|b(\mathbf{p},t)|^2$ can be computed concurrently for a given set of $\mathbf{p}$ values. We have optimized the calculation of the whole transition amplitude $|b(\mathbf{p},t)|^2$, by using the OPENMP parallel package [34] and the MPI paradigm [59]. The final momentum photoelectron distribution $|b(\mathbf{p},t)|^2$ is computed both in a 1D momentum line along p_z, and in a 2D momentum plane (p_z, p_y). We shall compare these results with the numerical solution of the 3D-TDSE. We use in our simulations an ultrashort laser pulse with the same characteristics as for the HHG calculations. The time step is fixed to $\delta t = 0.02$ a.u., and the numerical integration time window of ≈ 11 fs.

In addition, we perform the numerical integration of the 3D-TDSE by using the Crank-Nicolson algorithm in cylindrical coordinates (ρ, z) where the polar angle φ is neglected. This is well justified by considering the laser field is linearly polarized along the molecular z axis and the fact that the magnetic momentum electron quantum number m remains as a conserved quantity during the whole evolution of the system. Thereby, the electronic Hamiltonian of our system is $\hat{H} = \frac{\hat{p}_\rho^2}{2} + \frac{\hat{p}_z^2}{2} + \hat{V}(\rho,z) + zE(t)$. For the present numerical solution of the TDSE, we have fixed the position grid step to $\delta\rho = \delta z = 0.2$ a.u., with a total number of points for the $\rho-$axis of $\mathbf{N}_\rho = 6000$ and the $z-$axis of $\mathbf{N}_z = 12000$, respectively. The ground state is computed via imaginary time propagation with a time step of $\delta t = -0.02\,i$ and the Coulomb potential for our two-center molecule is given by: $V(\rho,z) = -\frac{1}{\sqrt{\rho^2+(z+R/2)^2}} - \frac{1}{\sqrt{\rho^2+(z-R/2)^2}}$. The strong field laser molecule interaction is simulated by evolving the electronic ground state wave function in real time, with a time step of $\delta t = 0.02$ a.u., and under the action of both the molecular potential and the laser electric field. At the end of the laser pulse t_F, when the laser electric field is zero, we compute the final photoelectron energy-momentum distribution $|b_{TDSE}(p_\rho, p_z, t_F)|^2$, by projecting the "free"-electron wave packet, $\Psi_c(\rho,z,t_F)$, over plane waves. The wave packet $\Psi_c(\rho,z,t_F)$, is calculated by smoothly masking the bound states from the entire wave function $\Psi(\rho,z,t_F)$.

First, and in order to test if our model is capable to capture the final photoelectron spectrum of the ATI processes, we compare our SFA model to the numerical solution of the 3D-TDSE for the simplified case of H_2^+. Figure 18 depicts such comparison. In Fig. 18(a), we cal-

culate a scan of the ionization probability over a set of 15 interatomic distances. Note that by ionization probability the reader should understand the final-time integral momentum distribution of the whole transition probability amplitude, Eq. (35). Here, we set the molecular axis parallel to the laser electric field polarization. Those results show a reasonable agreement between the SFA and 3D-TDSE models, particularly for larger internuclear distances, when the details of the potential are not so relevant. In both calculations we can observe that for shorter distances the ionization probability is strongly dependent on the relative position of the atoms inside the molecule. The ionization probability scales almost exponentially (note that the scale is logarithmic) and increases rapidly, when the atoms are close to each other, at $R \lesssim 4$ a.u. Both models present the same trend, namely, a low-ionization probability for shorter distances, followed by a rapid increasing, and a sort of "stabilization" for larger internuclear distances. The physical picture of this behavior is as follows: the electron is tightly (loosely) bounded for small (larger) internuclear distances. According to the Keldysh-Faisal-Reiss model, the electrons have less probability to be ionized by tunneling effect [15, 17, 18] for potentials with larger I_p, which of course in this molecular case corresponds to small internuclear distances. Note that we mean small or large internuclear distances R in comparison to the equilibrium one R_0 ($R_0 = 2.0$ a.u. for our H_2^+ molecule). Furthermore, the same tendency of both the SFA and the 3D-TDSE in the whole internuclear distances range is observed, except a constant factor, which clearly indicates the difference between the SR (SFA) and long-range (3D-TDSE) potentials. Further, the ionization probability shows a stabilization value (around 10^{-3} arb. units for both cases) from which it remains constant regardless the value of R.

The previous comparison only describes the final photoelectron spectra dependence on the internuclear distance. A better scenario to evaluate the quality of our model, however, can be employed, namely, a one-to-one analysis of the ATI momentum distributions. The aim is to confirm if our model is able to capture both the interference nature of the ATI spectra for molecules and the underlying electron dynamics. In Fig. 18(b), we show results of the photoelectron momentum spectra computed by our quasiclassical model and the 3D-TDSE along the momentum line $\mathbf{p} = (0, 0, p_z)$, at $R = 3.8$ a.u. As in Fig. 18(a), we observe an excellent agreement between both models. It means that our quasiclassical approach is able to provide a reasonable good description of the whole ATI processes. We can argue that the two models are describing the same physics: stronger oscillations for small values of momentum followed by a rapid decrease of the ATI yield (at $|p_z| \lesssim 2.5$ a.u.), a plateau, where the amplitude remains almost constant, and both approaches end up with an abrupt cutoff around the same value of $|p_z| \lesssim 4$ a.u.

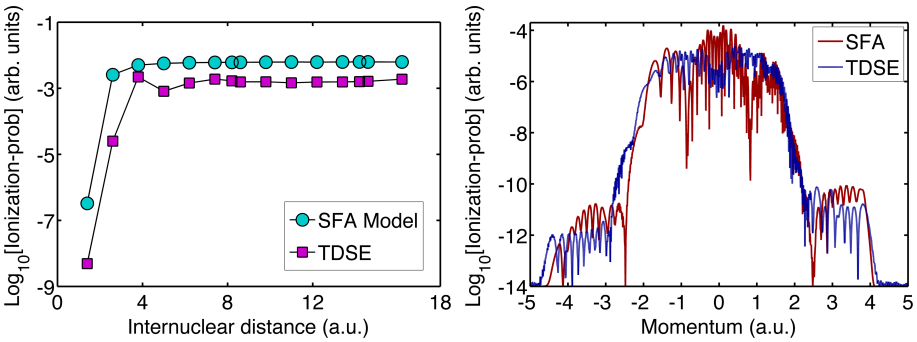

Figure 18: (a) Ionization probability (in logarithmic scale) as a function of the internuclear distance R calculated using the SFA (circle magenta) and the TDSE (square light blue) for $I_0 = 4 \times 10^{14}$ W · cm^{-2}. (b) Full transition amplitude $|b(p_z, t_F)|^2$ as a function of the photoelectron final momentum, calculated using the SFA model (red line) and ATI computed by the numerical solution of the TDSE (blue line) in all the cases the molecule is oriented along the laser field polarization.

2.5.2.1 *Disentangling the different contributions to the final ATI spectra*

One of the main advantages of our SFA model is the possibility to disentangle the different contributions to the final ATI spectra (for details, see previous sections). In Fig. 19, we show the different contributions, in logarithmic scale, as a function of the ponderomotive energy U_p for electrons with negative momenta along the p_z direction and for a fixed value of R, close to the equilibrium distance $R_0 = 2.0$ a.u. Figure 19(a) shows the main contributions to the full final photoelectron spectra: the total $|b(\mathbf{p}, t)|^2$ [Eq. (35)], the direct $|b_0(\mathbf{p}, t)|^2$ [Eq. (90)], and the rescattering $|b_1(\mathbf{p}, t)|^2$ [Eq. (111)] terms, respectively. In the same way in Fig. 19(b) we plot the two terms $|b_{0,1}(\mathbf{p}, t)|^2$ and $|b_{0,2}(\mathbf{p}, t)|^2$ which contribute to the direct process. The terms that play an important role in the rescattering process $|b_{Local}(\mathbf{p}, t)|^2$ [Eq. (108)] and $|b_{Nl+Cross}(\mathbf{p}, t)|^2$ [Eq. (109)] are displayed in Fig. 19(c). As we can infer from the latter figure, the main contribution to the rescattering term is from the local processes (see Sec. 2.2). Finally, in Fig. 19(d) we show the two processes contributing to the local one. For this calculation we have considered the molecule aligned in the same direction as the laser electric field polarization, i.e., the internuclear distance vector has only a z component $\mathbf{R} = (0, 0, R_z)$.

Our second clear observation in Fig. 19 is that each term contributes to different regions of the photoelectron spectra, i.e., for electron energies $E_p \lesssim 4U_p$ the direct term $|b_0(\mathbf{p}, t)|^2$ dominates the spectrum and, on the contrary, it is the rescattering term $|b_1(\mathbf{p}, t)|^2$ the one that prevails in the high-energy electron region. The photoelectron spectra show the expected two cutoffs defined by $2U_p$ and $10U_p$ (black

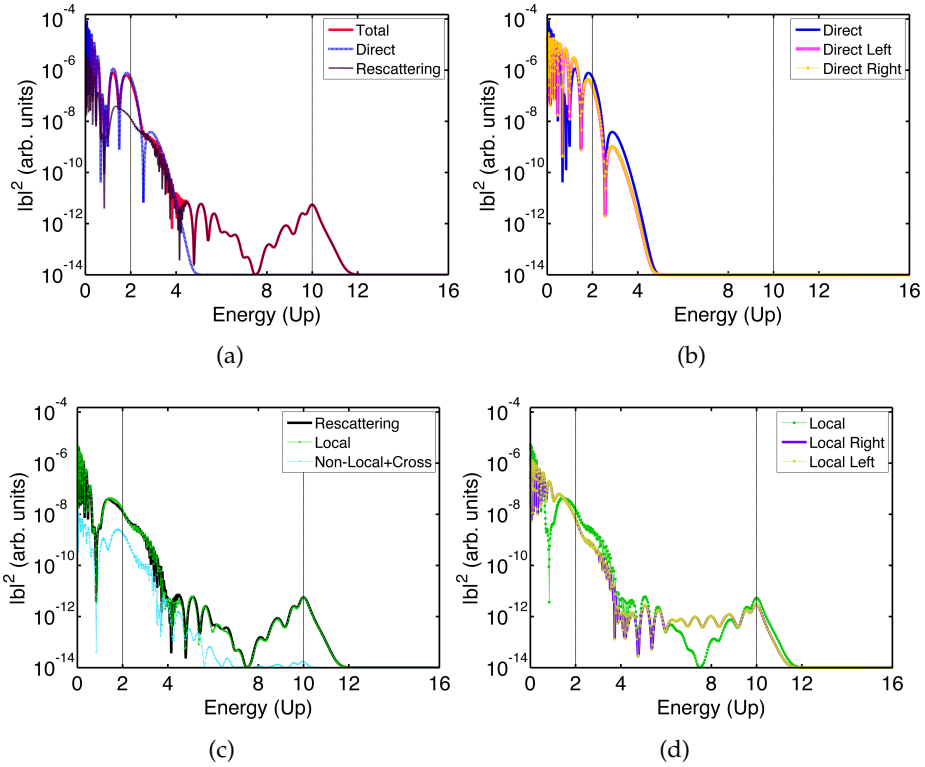

Figure 19: Total, direct and rescattering contributions of the photoelectron spectra (in logarithmic scale) as a function of the ponderomotive electron energy U_p calculated by using our quasi-classical SFA model for $R = 2.6$ a.u. We consider the molecule aligned parallel to the laser field polarization. The peak laser intensity used in this calculation is set to $I_0 = 4 \times 10^{14}$ W $\cdot$ cm^{-2}.

dashed lines) which are present in every atomic and molecular ATI process [3, 35]. As a consequence of this last observation we can safely argue that our approach is a reliable alternative for the calculation of photoelectron spectra in molecules. For the direct process, Fig. 19(b), we observe that both the direct *left* and direct *right* terms contribute within a comparable energy range. In addition, both terms show the same behavior, having exactly the same energy for the interference minimum: the coherent sum of these two terms, the total direct contribution (solid blue line), has a deeper minimum value around 1.0 a.u. In Fig. 19(c), we observe that the local term (green dotted line) contributes mostly in the low-energy region of the ATI spectrum. Furthermore, the nonlocal and cross terms do not contribute for electron energies $E_p \gtrsim 6U_p$. It is also demonstrated that the contribution of $|b_{Nl+Cross}(\mathbf{p}, t)|^2$ becomes even less important for larger internuclear distances as it is expected. Finally, in Fig. 19(d) we show that the local right and local left contributions have the same shape and contribute to the whole energy range.

2.5.2.2 *2D-momentum distributions*

Having in mind a deeper analysis of the ATI processes, we extend our numerical calculations from a 1D momentum line (Fig. 19) to a 2D momentum plane. The results of our computations are shown in Fig. 20. Here, we depict the different contributions using our analytical quasiclassical ATI model. For this calculation we use a laser field with a peak intensity of $I_0 = 1 \times 10^{14}$ W $\cdot$ cm^{-2} and the internuclear distance is set to $R = 4.2$ a.u.

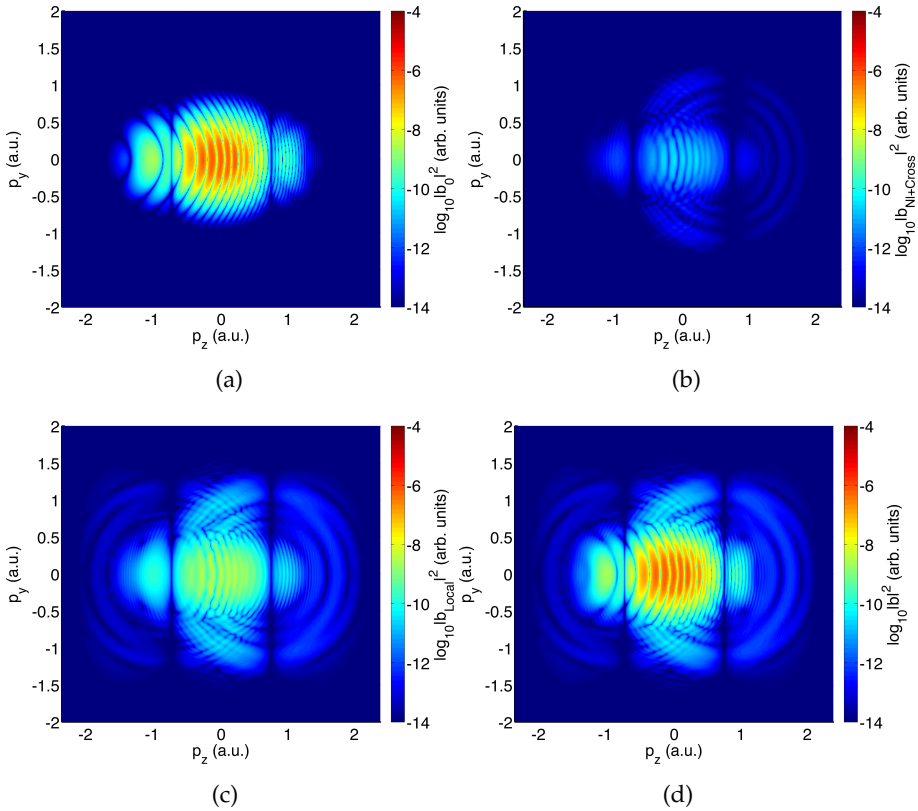

Figure 20: Different contributions to the photoelectron spectra for a 2D-momentum plane (p_z, p_y). ATI photoelectron spectra (in logarithmic scale) as a function of the momentum (p_z, p_y) computed by our quasi-classical model for each term. (a) Direct term, (b) NLocal and cross terms, (c) Local term and (d) Total contribution. We use a laser field with a peak intensity of $I_0 = 1 \times 10^{14}$ W $\cdot$ cm^{-2} and the internuclear distance is set to $R = 4.2$ a.u. The molecule is aligned parallel to the laser field polarization.

There are various features present in the 2D-ATI spectrum that we reproduce with our model. The main ones are the electron energy cutoffs and the behaviour of the spectra under inversion. Furthermore, we observe a symmetry of the structures about the p_y axis for all the terms. Additionally, a left-right asymmetric for electrons with $p_z < 0$ or $p_z > 0$ is also seen. These left-right asymmetries (see Fig. 20(b)) is a consequence of the CEP. Studying these asymmetries we can detect

changes in the CEP of the laser pulse as we did for the atomic system in Sec. 1.4.2.

The ATI spectra present footprints of molecular internal structural information. Particularly they are encoded in the features observed in the spectra and can be explained in terms of a few quantum orbits and their superposition. More precisely, by analyzing the presence or absence of ATI peaks one can extract information about the alignment angle of the molecule with respect to the laser field polarization or the internuclear distance; this last point will be addressed in the next section.

The 2D calculations resemble the features of the 1D ones: the low momenta region of the spectrum is dominated by the direct process [Fig. 20(a)], meanwhile the rescattering term, dominated by the local processes, is important for large electron momenta [Fig. 20(c)]. Furthermore, the nonlocal and cross [Fig. 20(b)] processes can be neglected when compared to the local processes. In all the figures we clearly distinguish the position of a deep minimum about an electron momentum $p = 0.74$ a.u. (the corresponding energy is $E = 1.23\ U_p$) and the well-known asymmetric rings.

2.5.2.3 *Two slit interference minima analysis*

As was already mentioned, one of the advantages of our diatomic SFA model is that it allows us to account for the individual contributions to the ATI spectrum. In addition, aside from being analytically formulated, our model is able to switch on and off each of the ionization mechanisms which build up the final total and experimentally accessible ATI momentum spectrum $|b(p_z, p_y, t_F)|^2$.

As was already mentioned, one of the main concerns with our model is to find a way to retrieve structural information of the molecular system starting from the ATI spectra. In the following we perform a detailed analysis of the interference pattern for different internuclear distances. Here, the well-known two-slit interference formula $p = \frac{(2n+1)\pi}{R\cos\theta}$, [45] is used in order to extract the internuclear distance from the interference pattern present in the photoelectron spectra.

In Figs. 21 and 22 , we show the photoelectron distribution or ATI spectra [$|b(p,t)|^2$], in logarithmic scale, as a function of the final electron momentum for different internuclear distances. Figure 21 depicts the ATI spectra for a large value of the internuclear distance: $R = 14.2$ a.u., in order to see a considerable number of interference minima. Furthermore, the ATI spectra in Fig. 22 are computed varying the internuclear distance R (see the panel labels for the values). The dashed black lines represent the expected minima calculated by applying the two-slit interference formula. As it is observed, our model is able to reproduce all the interference minima and this is a clear evidence that the photoelectron spectra contains structural information of the molecular system.

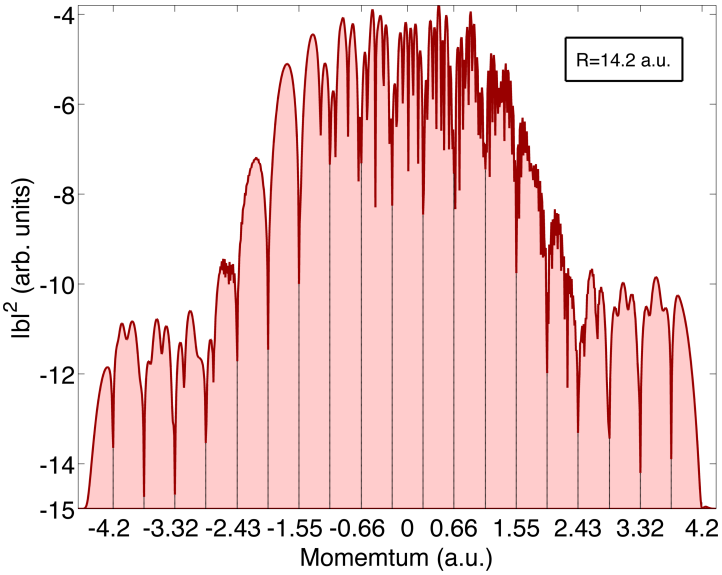

(a)

Figure 21: ATI spectra calculated using the SFA model for an intensity value of $I_0 = 4 \times 10^{14}$ W $\cdot$ cm^{-2}, as a function of the momentum. The molecule is consider aligned with the laser field polarization and with an internuclear distance of R = 14.2 a.u.

2.5.3 *The role of the initial state: O_2 and CO*

Along this section, we calculate the ATI spectra from two different diatomic molecules using the two approaches presented in Sec. 2.4, namely:

Model A: a nonlocal SR potential is used to calculate the bound and scattering states, as well the bound-continuun and continuum-continuum matrix element (see Sec. 2.4.1).

Model B: a linear combination of atomic orbitals -LCAO- is employed to get the bound states and the bound-continuun dipole matrix and a nonlocal SR potential for the scattering states and the continuum-continuum matrix element (see Sec. 2.4.2).

We compare the ATI spectra obtained from each of the models in order to highlight their similarities and differences [60].

2.5.3.1 *O_2 molecule: The role of the initial state*

The computation of the photoelectron spectra was performed by using Eqs. (35), (134) and (153) for the case of *Model A*. Here we set $\Gamma = 1$ and $\gamma = 0.08$ a.u. in our nonlocal SR potential in order to match the dioxygen ionization potential obtained with GAMESS, $I_p = 0.334$ a.u for the singlet state. Next, in the case of the calculation using the *Model B*, we use Eqs. (35), (169) and (153).

The ultrashort laser pulse used in the simulation along this section has the same characteristics as in the previous calculations, i.e. the

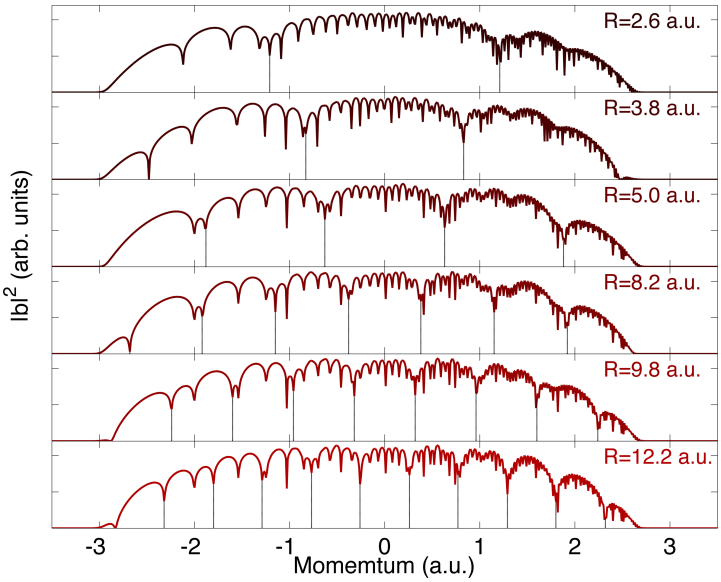

(a)

Figure 22: Photoelectron spectra of an H_2^+ molecule, aligned parallel to the laser field polarization, as a function of the momentum for an internuclear range $R = [2.6, 12.2]$ a.u. The result where obtained using the SFA model, the laser pulse intensity was set to $I_0 = 4 \times 10^{14}$ W $\cdot$ cm^{-2}.

wavelength is set to 800 nm and the peak intensity to $I_0 = 1.0 \times 10^{14}$ W$\cdot$cm^{-2}.

In Fig. 23, we display the respective molecular orbitals (right panels) and the results for the 1D photoelectron spectra (left panels) using each of the models. In this case the molecule is oriented perpendicular to the laser field polarization (z-axis).

In the upper panels of Fig. 23 we present the results using the *Model A*. Here, we use the nonlocal SR potential to obtain the ground state and the bound-free dipole matrix element. This kind of potential only support s states as we can see in Fig. 23(b). On the contrary, the *Model B* gives a more accurate description of the O_2 molecular orbital (MO) (see Fig. 23(d)). The shape of the MO introduces noticeable differences in the final total photoelectron spectra (red line) as well in the different, direct (blue line) and rescattering (black line), contributions.

Figures 23(a) and 23(c) show the main contributions to the full final photoelectron spectra, namely: the total $|b(\mathbf{p}, t)|^2$, Eq. (35), the direct $|b_0(\mathbf{p}, t)|^2$, Eq. (90) and the rescattering $|b_1(\mathbf{p}, t)|^2$, Eq. (111) terms, respectively. The black solid lines define the two cutoffs defined by $2U_p$ and $10U_p$. As we can infer from the latter figures the two models show slightly different behaviors. In the case of *Model A*, that describes the HOMO as a superposition of two one-electron 1s AOs, Fig. 23(a), we see an overestimation of the direct processes. This fact could be caused by the kind of SR potential used to get the molec-

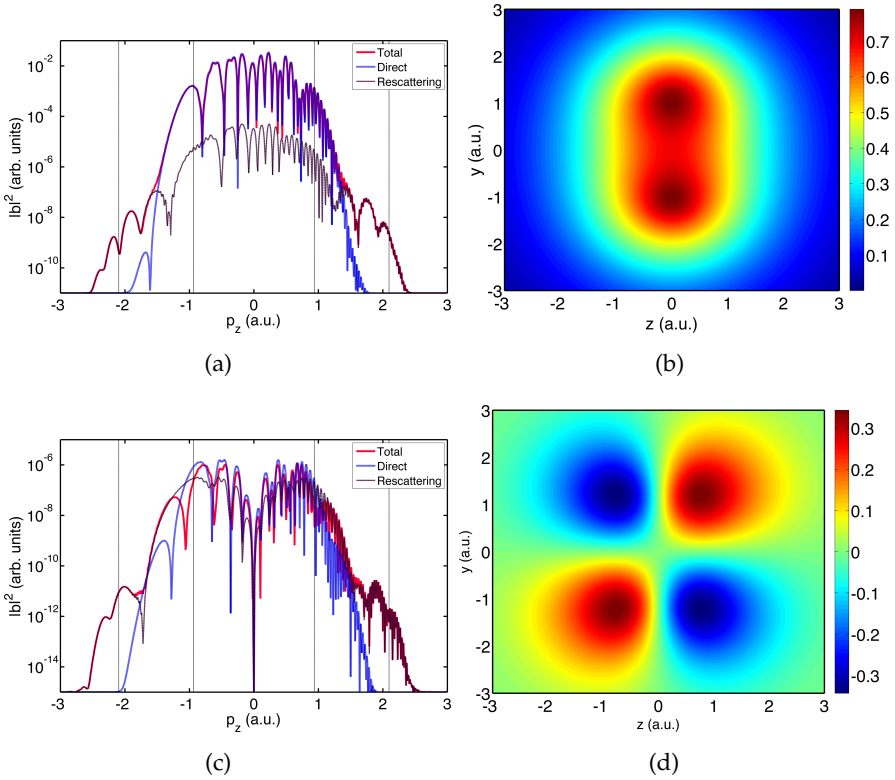

Figure 23: (a)-(b) Total, direct and rescattering contributions to the photoelectron spectra as a function of the final momentum and HOMO calculated using the nonlocal SR potential, respectively. (c)-(d) The same as in (a)-(b) but now the HOMO is modeled using a LCAO. In all the cases, we used, an O_2 molecule oriented perpendicular to the laser field polarization. The molecule is consider in equilibrium with an internuclear distance of R = 2.28 a.u (1.21 Å).

ular ground state. This SR potential does not properly describe the attraction force felt by the electron both when it is bound and in the continuum. In this way this electron could 'escape' more easily from the ionic core and becomes a 'direct electron'.

Results from the two models also show some similarities: stronger oscillations for small values of the electron momentum followed by a rapid decrease of the ATI yield (at $|p_z| \lesssim 1.0$ a.u.), a plateau, where the amplitude remains almost constant, and both approaches end up with an abrupt cutoff around the same value of $|p_z| \lesssim 2.1$ a.u. (black solid lines) [3, 35].

We can also observe from Figs. 23(a) and 23(c) that the differences start to disappear for higher electron energies, where the spectra are dominated by the rescattered electrons. This is so because the core potential plays a minor role in this energy region. Furthermore, our model captures the carrier-envelope phase (CEP) asymmetry as well: electrons with positive final momentum are more influenced by the

laser field polarization and this creates a stronger interference pattern.

2.5.3.2 *CO molecule*

In the CO calculation we set the parameters of our nonlocal SR potential to $\Gamma = 1$ and $\gamma = 0.09$ a.u., in order to match the ionization potential obtained with GAMESS, $I_p = 0.44$ a.u. As we already mentioned, this nonlocal SR potential only describe MOs as a composition of s states, see Fig. 23(b). On the other hand, the main advantage to use GAMESS is that it describes the MO much more accurately. Additionally, with GAMESS we have the possibility to easily model more complex molecules. The MO of the CO molecule obtained from GAMESS is a superposition of $1s$, $2s$ and $2p$ states and it is shown in Fig. 24. We consider the CO molecule is in equilibrium, the internuclear distance is set to $R = 2.12$ a.u. (1.127 Å), and oriented parallel to the laser field polarization.

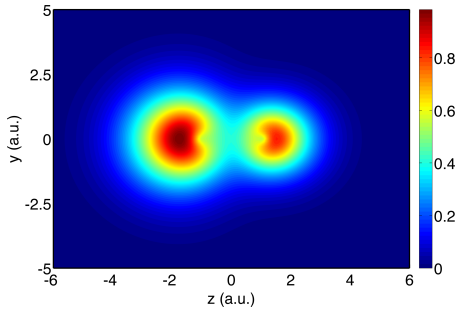

(a) HOMO of the CO molecule

Figure 24: CO HOMO presented in the $z - y$ plane calculated using GAMESS. The CO molecule is in equilibrium with an internuclear distance of $R = 2.12$ a.u. and oriented parallel to the laser field polarization.

Figure 25 shows the main contributions to the final photoelectron spectra for the CO molecule: the total $|b(\mathbf{p}, t)|^2$, Eq. (35), the direct $|b_0(\mathbf{p}, t)|^2$, Eq. (90) and the rescattering $|b_1(\mathbf{p}, t)|^2$, Eq. (111) terms, respectively. In the Fig. 25(a) we display the results using the *Model A*, meanwhile the ones from the *Model B* are shown in Fig. 25(b).

A clear observation from these plots is that each term contributes to different regions of the photoelectron spectra, i.e. for electron energies $E_p \lesssim 2U_p$ the direct term $|b_0(\mathbf{p}, t)|^2$ dominates the spectrum and, on the contrary, it is the rescattering term, $|b_1(\mathbf{p}, t)|^2$ the one that wins in the high-energy electron region. Both photoelectron spectra shows the expected two cutoffs defined by $2U_p$ and $10U_p$ (black solid lines) which are ubiquitously present in both atomic and diatomic molecular ATI [3, 35].

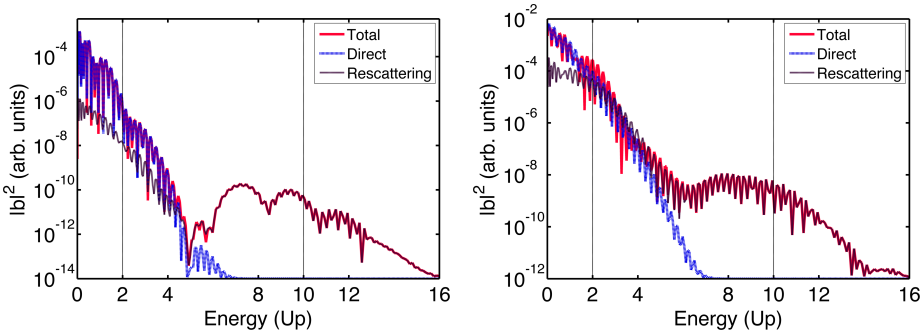

Figure 25: Total, direct and rescattering contributions of the photoelectron spectra, as a function of the electron energy in U_p units, for the CO molecule. (a) *Model A* and (b) *Model B*. The molecule is in equilibrium with an internuclear distance of $R = 2.12$ a.u. (1.127 Å) and aligned along the polarization axes z. The laser peak intensity and wavelength are $I_0 = 1 \times 10^{14}$ W $\cdot$ cm^{-2} and $\lambda = 800$nm, respectively.

One of the main differences between the two models is that the total maximum yield amplitude is two orders of magnitude higher in the case of the *Model B*, than in the *Model A*. Besides this contrast the dynamic range of both spectra is quite similar: about ten orders of magnitude until the end of the signal. In here we only show the electrons moving to the 'right', i.e. with positive momentum; but as in the above case of O_2 the total spectra show CEP asymmetries.

The two spectra show some remarkable similarities; both have a deep minimum around $5U_p$, more pronounced for the *Model A* case [Fig. 25(a)], from where the yield of the direct processes starts to decrease. The contribution of the direct processes is negligible for energies $\gtrsim 7U_p$, from where the spectra is dominated by the scattering processes. The two CO spectra show, in general, more similarities than in the O_2 case; this is due to the nature of the CO HOMO: in the CO molecule the MO is a composition of not only 2p also 1s AOs and our SR potential is able to partially include the contribution of the latter.

In order to have a more complete picture of the underlying mechanisms we present in Fig. 26 the different direct processes contributions to the total ATI spectra. In Fig. 26(a) we show the split of the direct processes obtained using the *Model A*, whereas in Fig. 26(b) we depict the results using the *Model B*. The first observation in this comparison arises from the fact that the contributions from the atom on the *left* ($|b_{0,1}(\mathbf{p}, t)|^2$), i.e. carbon, and the atom on the *right* ($|b_{0,2}(\mathbf{p}, t)|^2$), i.e. oxygen, are different in the case of the *Model B* [Fig. 26(b)]. The amount of photoelectrons ionized from the carbon atom (pink dotted line) is much larger than the one from the oxygen (yellow dotted line). This is in agreement with the shape of the CO HOMO, see Fig. 24,

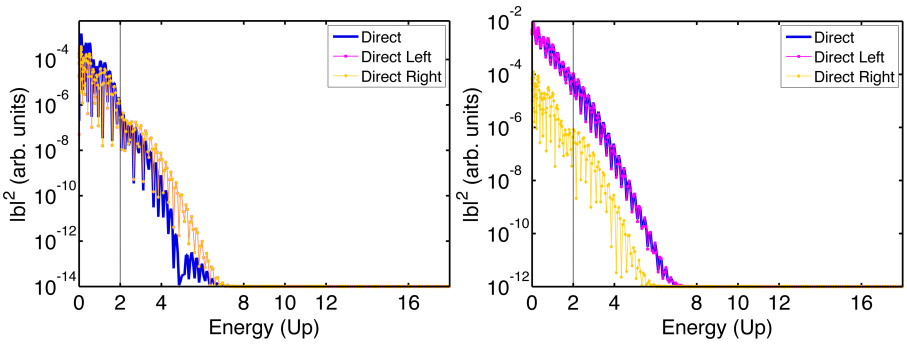

Figure 26: Direct contributions to the CO photoelectron spectra (in logarithmic scale) as a function of the electron energy, in U_p units, calculated by using *Model A* (a) and *Model B* (b).The molecule is in equilibrium with an internuclear distance of $R = 2.12$ a.u. (1.127 Å) and aligned along the polarization axes z. The laser peak intensity and wavelength are $I_0 = 1 \times 10^{14}$ W · cm^{-2} and $\lambda = 800$nm, respectively.

where the electronic cloud around the carbon atom is much bigger. The same effect is observed for the recattering terms (not shown), where the total local term is dominated by the local processes coming from the carbon atom.

In the case of the calculations using *Model A* those differences are not so pronounced, see Fig. 26(a): we can observe that the contributions of both atoms are equal in amplitude and shape. This is so because the bound state obtained from the SR potential does not properly describe the CO HOMO: this potential is unable to take into account the heteronuclear character of the CO molecule and describes its HOMO similar to the one shown in Fig. 23(b).

Considering the nuclear asymmetry features discussed before we next study the differences in the ATI spectra for the molecule aligned parallel (0°) or antiparallel (180°) with respect to the laser field polarization. The results of a 2D calculation, for both orientations and using the LCAO within the *Model B* is presented in Fig. 27. Figures 27(a) and 27(c) show a sketch of the molecular orientation, superimposed over the MO. Here we can see that for the case of the CO molecule aligned parallel (antiparallel) the carbon atom is on the 'left' ('right'), meanwhile the oxygen atom is on the 'right' ('left'). Furthermore, Figs. 27(b) and 27(d) depict the total ATI spectra for both the parallel and antiparallel cases, respectively.

The total ATI spectra presented in Figs 27(b)-(d) show the typical CEP asymmetry, but surprisingly any features related to the heteronuclear character of the CO molecule appear to be missing: the two ATI spectra, the one obtained for the molecule at 0° (Fig. 27(b)) and the one for 180° (Fig. 27(d)), look almost identical.

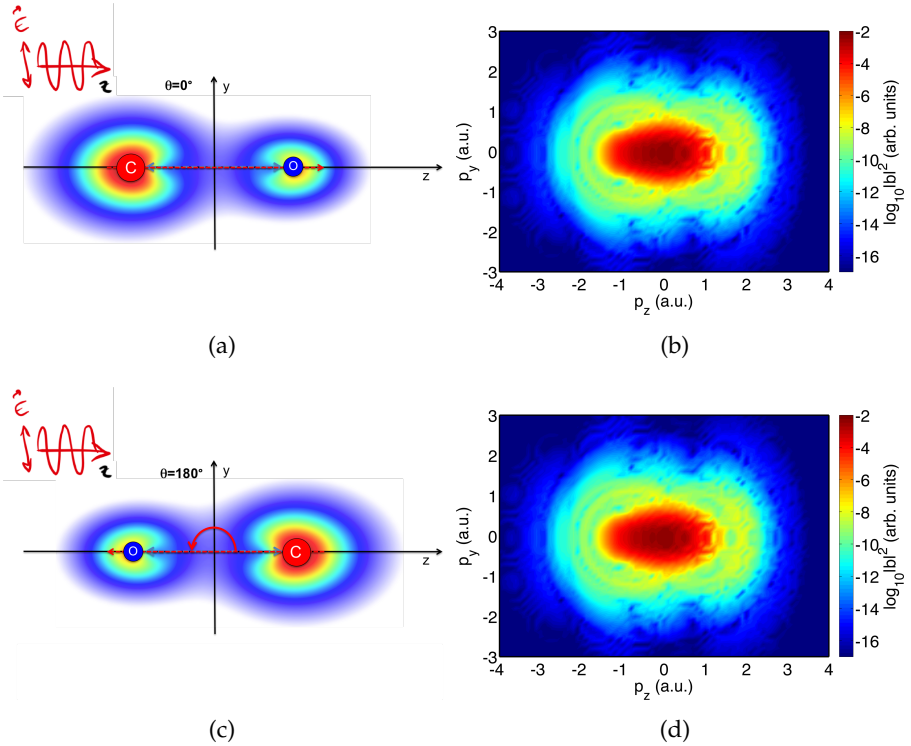

Figure 27: Total photoelectron spectra for a 2D-momentum plane (p_z, p_y) computed by our quasiclassical model. (a) Representation of the CO molecule aligned at 0° with respect to the laser field polarization; (b) total ATI photoelectron spectra; (c)-(d) the same as in (a)-(b) but for the molecule aligned at 180° with the laser field polarization. The molecule was consider in equilibrium with an internuclear distance of $R = 2.12$ a.u. (1.127 Å). The laser peak intensity and wavelength are $I_0 = 1 \times 10^{14}$ W $\cdot$ cm^{-2} and $\lambda = 800$nm, respectively.

In order to get a more detailed description of the CO ATI spectra presented in Figs 27(b)-(d) in Fig. 28 we plot the contribution of the rescattering processes to the total ATI. On the other hand, the direct contributions show the expected behavior: a symmetry inversion. In this case the major contribution also comes from the carbon atom on the *right* ($|b_{0,2}(\mathbf{p}, t)|^2$), whereas the direct ionization from the oxygen atom, on the *left* ($|b_{0,1}(\mathbf{p}, t)|^2$), is much more smaller.

In Figs. 28(a) and 28(b) we present the local processes contributions $|b_{1,11}(\mathbf{p}, t)|^2$ and $|b_{1,22}(\mathbf{p}, t)|^2$, respectively. On the other hand, Figs. 28(c) and 28(d) depict the cross and nonlocal contributions, namely $|b_{1,12}(\mathbf{p}, t)|^2$ and $|b_{1,21}(\mathbf{p}, t)|^2$. In all the cases the molecule is aligned 180° with the laser field polarization, i.e. the oxygen atom is on the left, meanwhile the carbon atom is on the right. Interestingly, for the case of 0° we obtain the same plots, but with the terms interchanged, i.e. now the higher contribution comes from the carbon atom now located in the *left* at the position R_1. This is the same asymmetry feature observed in the direct terms, see Fig. 26(b). The heteronuclear

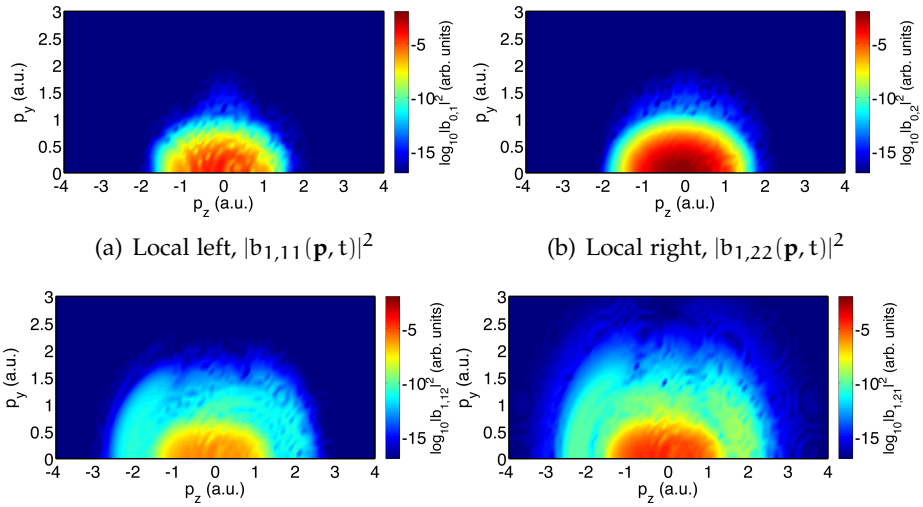

(a) Local left, $|b_{1,11}(\mathbf{p},t)|^2$

(b) Local right, $|b_{1,22}(\mathbf{p},t)|^2$

(c) Nlocal+Cross left, $|b_{1,12}(\mathbf{p},t)|^2$

(d) Nlocal+Cross right, $|b_{1,21}(\mathbf{p},t)|^2$

Figure 28: Rescattering contributions to the photoelectron spectra for a 2D-momentum plane (p_z, p_y). ATI photoelectron spectra (in logarithmic scale) calculated by using the *Model B* for a CO molecule at equilibrium $R = 2.12$ a.u. and oriented antiparallel ($\theta = 180°$) to the laser field polarization. (a) Local term of the atom on the left; (b) local term of the atom on the right; (c) nonlocal and cross term with ionization from the left; (d) nonlocal and cross term with ionization from the right. The laser peak intensity was set to $I_0 = 1 \times 10^{14}$ W · cm^{-2}.

character of the molecule can now be seen in the local and rescattering components but, as we observed, not in the total photoelectron spectra. This fact could be related to the compensation of the MO differences when the direct and rescattering terms are coherently added.

2.5.4 *Theory versus experimental results*

In order to conclude our analysis, and as an additional validation of our model, we compare the results computed using the SFA approach with experimental data obtained at ICFO for O_2^+ molecules [61]. The experimental data were taken for randomly oriented molecules and the laser pulse was CEP randomized, i.e., an average of the theoretical results over both the molecular orientations and different CEP values is required for an accurate theoretical description. The reported laser peak intensity and wavelength are $I_0 = 8.5 \times 10^{13}$ W · cm^{-2} and $\lambda = 3.1$ μm, respectively. The laser pulse has a duration of 75 fs full-width at half-maximum at a repetition rate of 160 kHz. Furthermore, the O–O bond length is retrieved from the photoelectron spectra and set to a value $R = 1.17$ Å (2.21 a.u.) [61]. This value of R corresponds to an ionization potential energy of $I_p = 0.93$ a.u and, in order to reproduce this value, in our model we set the parameters of

the nonlocal potential $\Gamma = 0.75$ and $\gamma = 0.097$ a.u. With these values we obtain a very good fit to the dissociation energy $E_d = 18.5$ eV, and the equilibrium internuclear distance $R = 1.116$ Å (2.11 a.u.), reported in the literature [62].

In order to accurately compare with the experimental measurements, the calculated ATI spectra are averaged over the orientation of the molecule with respect to the laser polarization axis, using eight values of the orientation angle θ in the range $[0° - 360°]$. In addition, an average over the CEP values, and for the same orientation range, is considered. For symmetry considerations, only 16 different sets of photoelectron spectra are computed. For each set a total of 8192 points in the (p_z, p_y) plane are used. Around 150 000 CPU hours were employed for the whole ATI computation. For the comparison experiment versus theory, we employ the same laser peak intensity (no focal averaging is considered in the calculations) and the internuclear distance reported in the experiment for each calculation. The result of this comparison is depicted in Fig. 29.

In Fig. 29(a) we show the calculated total ionization probability $|b(\mathbf{p}, t)|^2$ [Eq. (35)] and in Fig. 29(b) we present the experimental data. In order to make an easier comparison, the theoretical calculations are multiplied by a constant factor. The plots show that our model is in very good agreement with the experimental measurements. In fact, both panels present the same color scales, covering six orders of magnitude. Both the simulated and measured data exhibit the same regions of signal, with comparable amplitudes for all the longitudinal momentum. In addition, a similar dome structure, around $p_z = [-3; 3]$ and $p_y = [0; 0.7]$, is observed in both pictures. Note that the interference fringes are not observed either in the experimental or in the theoretical calculations. Thereby, the different recollision scenarios in terms of electron trajectories are washed out due to both the molecular orientation and CEP averages. We could trace out the theory versus experiment discrepancies considering that (i) our SFA model neglects Coulomb effects, which could be important in the low-energy region of the ATI spectrum; (ii) we are working within the SAE, i.e., our approach does not take into account any multielectron contributions, that could play a role in the photoelectron distributions, particularly for multielectronic molecules; (iii) we are not including a laser intensity focal average, i.e., in our calculations only one laser intensity is used in the simulations, contrarily with the experiment, where the atoms or molecules in the interaction region feel different laser intensities, due the intensity spatial distribution of the laser beam.

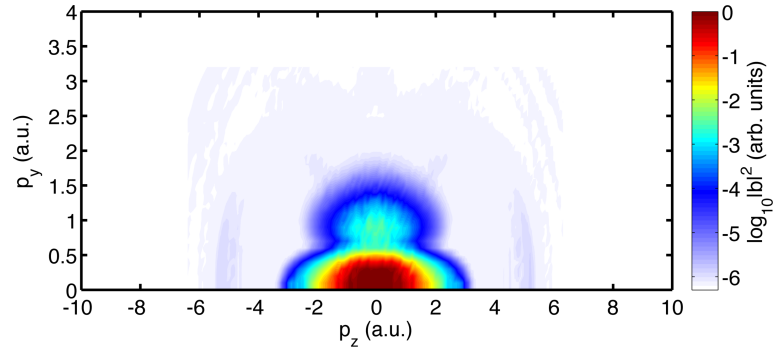

(a)

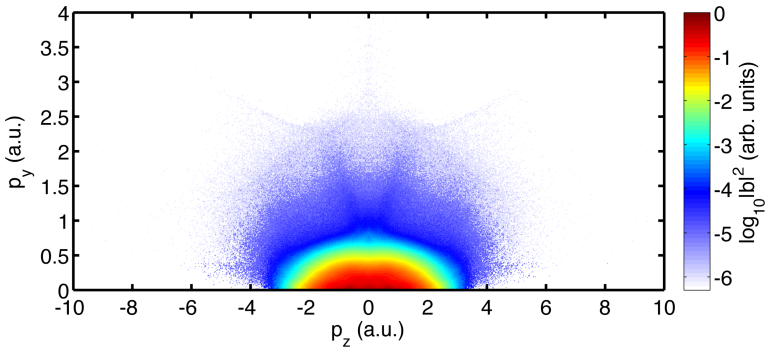

(b)

Figure 29: Photoelectron spectra for the O_2^+ molecule. (a) ATI spectra calculated using the SFA model; (b) Experimental ATI spectra obtained in the Attosecond and Ultrafast Optics group at ICFO [61]. In the theoretical calculations the laser peak intensity, wavelength and total time duration are $I_0 = 8.5 \times 10^{13}$ W $\cdot$ cm^{-2}, $\lambda = 3.1\mu$m and 52 fs (5 optical cycles), respectively. In addition, the internuclear distance is set to $R = 2.21$ a.u. (1.17 Å), the molecule is randomly oriented.

2.6 CONCLUSIONS AND OUTLOOK

We have presented a MSFA model to describe the HHG and ATI processes in small two-center molecules. This model is an extension of the previous framework developed for atomic systems. Our approach is based on the analytical solution of the TDSE with respect to each molecular center. One of the main advantages of our theoretical model, with respect to those used before, is that it gives solutions free of any artificial and nonphysical effects. In fact, a correct asymptotic behavior for $\mathbf{R} \to \infty$ and yet to $\mathbf{R} \to 0$ is obtained. In addition, the time-dependent dipole and the rescattering transition amplitude is written as a sum of components, obtained from equations which describe each recombination and rescattering processes (direct, local and nonlocal and cross) independently.

This model shows that each component contributes, in a different way, to different regions of the HHG and ATI spectra. We present results for four different diatomic systems: H_2, H_2^+, O_2 and CO.

We have investigated HHG in H_2, H_2^+ showing that our approach is able to capture the interference features, ubiquitously present in every diatomic HHG process. The HHG spectra, as well as their dependence on the molecular orientation, contain interference patterns that are due to interfering contributions emitted from the different atomic centers.

For the H_2^+ molecule the interference pattern, in the HHG spectra, generated at different orientations, predicted by the two-slit interference formula, was studied. We demonstrate that the deep interference minimum is generated by the destructive interference of electronic wave packets recombining at the same center.

We studied the effect of the molecular orientation in the total HHG spectra amplitude. We found that depending on the alignment the HHG yield changes on several orders of magnitude. The different contributions of the HHG spectra, local and cross, were presented.

We perform a time-frequency analysis that allow us to reveal the half-cycle bursts of radiation from which the HHG spectrum is composed and the main trajectories contributing to it. A comparison with atomic and diatomic system was performed. The Gabor analysis reveals that for the H atom the short trajectories are dominant whereas on the contrary, in the molecular system short and long trajectories contribute.

For the ATI processes we have validated our formalism comparing our SFA model to the numerical solution of the 3D-TDSE for the simplified case of an H_2^+ molecule using a large set of internuclear distances. The magnitude of the ionization probability for different values of R was calculated and compared with the 3D-TDSE outcomes, and indeed our results present a very good agreement. Both models exhibit the similar behavior: the ionization probability shows the same tendencies, namely, it starts to increase linearly with R reaching a saturation value from which it remains constant. The results indicate that, our version of SFA compares very well with the 3D-TDSE.

Similar as the atomic case, the different contributions of the total ATI spectra was assessed. The calculations point out, as expected, that the main contribution to the rescattering transition amplitude corresponds to local events, with the cross and nonlocal terms playing almost no role, when the internuclear distance becomes much larger than the equilibrium one. We should stress, however, that our model is by no means a simple correction to the well-established SFA. Here, we do predict physical processes which were not previously considered, e.g., those modelled by the nonlocal and cross terms, and we do provide methods to identify their contributions, which, at the end, can be quite significant for small internuclear distances compared to

the equilibrium one. On top of that, our SFA-based approach agrees well with the experimental data, which provides an even stringent argument in its favor.

In the ATI description, we used our model as a proof-of-principle confirming that photoelectron spectra contain structural information about the target system. We employ it to retrieve, satisfactorily, the internuclear distance of an H_2^+ molecule using a simple interference equation.

To complete the analysis we also performed a study about the role of the initial state in the ATI spectra. We used two models to calculate the bound-continuum dipole matrix element: one based completely on a nonlocal SR potential, *Model A*, and one that combines a LCAO description for the bound state and the SR potential for the scattering states, *Model B*. We calculate the different contributions to the photoelectron spectra for both models in two diatomic prototypical systems: O_2 and CO. We show, for instance, that the *Model A*, describing the MO only with *s*-type AOs, does not capture the molecular asymmetry of the CO system.

As was already established for atoms, one of the cores of our model is the saddle-point approximation, that was successfully applied to the present molecular case as well.

There are still open questions about how to adapt the SFA for molecules in such a ways that its level of prediction would become as good as for the atomic case. The comparison between the 3D-TDSE with our MSFA, as well as the good agreement between the experimental data and simulations, validates our theoretical model and allow us to believe that extensions to more complicated systems, such as polyatomic molecules with more than three centers, are perfectly feasible.

3

MSFA FOR N-CENTER MOLECULAR SYSTEMS

The present chapter extends the Modified Strong-Field Approximation (MSFA) approach developed in the previous chapters to more complex polyatomic molecules. The study of High-Order-Harmonic Generation (HHG) and Above-Threshold Ionization (ATI) processes in multicenter molecular systems is one of the most important challenges nowadays. We introduce an analytical description of molecular HHG and ATI, that extends the well-established theoretical Strong-Field Approximation (SFA). The direct numerical solution of the time-dependent Schrödinger equation (TDSE) for complex systems, with more than two centers, is a quite challenging and formidable task from the numerical and computational viewpoints. Even for the simplest diatomic molecule, H_2^+, one has to solve a 3D-TDSE, that typically requires the utilization of a multicore CPU and a large amount of memory. In addition, the interpretation of the results extracted from the TDSE is a not trivial subject, in particular if one wants to disentangle the underlying physical mechanisms contributing to the total HHG and ATI photoelectron spectra. Thus, approximate descriptions such as the SFA and related methods play a fundamental role in the adequate description of HHG and ATI processes.

In this chapter, we use the SFA within the framework of the Lewenstein's model to study both HHG and ATI for n-center molecular systems in the few-cycle infrared (IR) laser pulse regime. The derivation for such complex molecular systems is constructed as a consecutive extension of the model for diatomics presented in Chapter 2. As examples, we compute both HHG and ATI spectra for several molecules of three and four atoms.

Our approach involves two innovative aspects:

- First, using a model nonlocal, but separable, short-range (SR) potential we analytically calculate the bound-continuum dipole and the rescattering transition matrix elements for a molecular multicenter systems. In comparison with the standard approaches to the HHG/ATI processes, this analytic derivation of the different matrix elements gives us the possibility to study directly how the HHG/ATI spectra depend on the molecular target and laser pulse features; we can turn on and off contributions having distinct physical origins or corresponding to different physical mechanisms. This allows us to quantify their weights in the various regions of the HHG/ATI spectra.

- Second, as in Ref. [63] and Chapter 2 of this thesis, in our theory the dipole matrix elements are free from nonphysical

coordinate-system-dependent terms; this is achieved by adapting the coordinate system, in which SFA is performed, to the center from which the corresponding part of the time-dependent wave function originates.

Additionally, our model captures also the interference features, ubiquitously present in any multicenter target.

The main original results are:

- The extension of the SFA atomic model to complex molecules, formed by n centers.
- The possibility to split the different mechanisms contributing to the total HHG and ATI spectra: direct, local, nonlocal and cross.
- The finding that in the total HHG spectra the cross processes dominate over the local ones.
- From the inspection of the HHG cutoff energy dependency with the molecular alignment, we concluded that there is a preferential molecular orientation. This also depends on the molecular geometry.
- The feasibility to disentangle the three different cross contributions for the CO_2 ATI spectra. This reveals that the most probable electron trajectory is the one that involves the two closest atoms. For the total local term the outermost atoms, in this case the oxygens, contribute more.
- Using two different models we investigated the influence of the p-type orbitals in the recombination and rescattering mechanisms. These phenomena are instrumental both for HHG and ATI. We found that the spectra yield exhibits a strong dependency, showing an increase of about two orders of magnitude, when s and p-type orbitals are considered to describe the highest occupied molecular orbital (HOMO).

3.1 GENERALIZATION OF THE SFA FOR n-CENTER MOLECULAR SYSTEMS

In this section we develop an analytical model to obtain the direct probability transition amplitude, as well as the ground and scattering states, needed to calculate the HHG spectra for n-center molecular systems. We obtain the equations to calculate the different contributions to the rescattering transition probability amplitudes building up the total ATI photoelectron spectra as well. This approach can be considered an extension of the atomic and diatomic models presented in Chapters 1 and 2 (see also Refs. [2, 4, 60, 63]).

3.1.1 *Transition probability amplitude*

We consider a molecular system of n independent atoms under the influence of an intense and short IR laser field. The TDSE that describes the whole laser-molecule interaction will be solved considering the single active electron (SAE) approximation and the standard SFA approximation (see Sec. **??**).

Thus, within the SFA approach we propose a final state as a superposition of atomic orbitals as:

$$\begin{aligned} |\Psi(t)\rangle &= \sum_{j=1}^{n} |\Psi_j(t)\rangle, \\ &= e^{iI_p t}\left(\sum_{j=1}^{n} |0_j\rangle + \sum_{j=1}^{n}\int d^3\mathbf{v}\, b_j(\mathbf{v},t)|\mathbf{v}\rangle\right), \end{aligned} \tag{173}$$

to describe the time-evolution of the n-center system. In turn, each independent state, $|\Psi_j(t)\rangle$, is a coherent superposition of ground, $|0\rangle = \sum_{j=1}^{n} |0_j\rangle$, and continuum states, $|\mathbf{v}\rangle$ [1, 3], where the total transition amplitudes to the continuum states depend on the atomic position, $b(\mathbf{v},t) = \sum_{j=1}^{n} b_j(\mathbf{v},t)$. Remember that the subscript $j = 1,2,3...n$ refers to the positions $\mathbf{R}_1, \mathbf{R}_2, ..., \mathbf{R}_n$ of each of the atoms in the molecule, respectively.

Here, as in the diatomic case, we follow the same steps as in Chapter 2. The general expressions for each transition amplitude $b_0(\mathbf{v},t)$ and $b_1(\mathbf{v},t)$ are obtained from a differential equation in the form of Eq. (74). This equation contains the matrix elements defining the ionization, $\langle\mathbf{v}|\mathbf{r}|0_j\rangle$, process that explicitly depends on $|\mathbf{v}\rangle$.

The state $|\mathbf{v}\rangle$ represents a scattering state, modelled as a plane wave plus a correction over each of the centers of the molecule $\langle\delta\mathbf{v}|/\langle\delta\mathbf{v}'|$. This states are defined depending on the relative position of each of the atoms, $\mathbf{R}_j$, with respect to the origin of coordinates (see Chapter 2 and [63] for more details). They are a coherent superposition of states over all the atoms in the molecule as $|\mathbf{v}\rangle = |\mathbf{v}_p\rangle + |\delta\mathbf{v}\rangle$, where $|\delta\mathbf{v}\rangle = \sum_{j=1}^{n} |\delta\mathbf{v}_j\rangle$.

So, a bound-continuum matrix element is defined for each of the atoms in the molecule and a correction over the position, $\mathbf{R}_j$, is introduced in each contribution to keep the orthogonality to the bound states,

$$\mathbf{d}_j(\mathbf{v}) = -\langle\mathbf{v}_p|\mathbf{r}-\mathbf{R}_j|0_j\rangle = -\langle\mathbf{v}_p|\mathbf{r}|0_j\rangle + \mathbf{R}_j\langle\mathbf{v}_p|0_j\rangle. \tag{174}$$

Besides, those equation also contains the continuum-continuum (C-C) matrix element defined as, $\langle\mathbf{v}|\mathbf{r}|\mathbf{v}'\rangle = i\nabla_{\mathbf{v}}\delta(\mathbf{v}-\mathbf{v}') - i\mathbf{R}_j\delta(\mathbf{v}-\mathbf{v}') + \mathbf{g}(\mathbf{v},\mathbf{v}')$, similar to the diatomic case Eq. (84). It can be written as a singular part, $\langle\mathbf{v}_p|\mathbf{r}|\mathbf{v}'_p\rangle - \mathbf{R}_j\langle\mathbf{v}_p|\mathbf{v}'_p\rangle = i\,\nabla_{\mathbf{v}}\delta(\mathbf{v}-\mathbf{v}') - \mathbf{R}_j\delta(\mathbf{v}-\mathbf{v}')$, describing the movement of a free electron in the continuum, plus the rescattering term.

For a n-center molecule the rescattering matrix element reads then as:

$$\begin{aligned} \mathbf{g}(\mathbf{v},\mathbf{v}') &= \langle \mathbf{v}_p|(\mathbf{r}-\mathbf{R}_j)|\delta\mathbf{v}'\rangle + \langle \delta\mathbf{v}|(\mathbf{r}-\mathbf{R}_j)|\mathbf{v}'_p\rangle, \\ &= \sum_{j=1}^{n}\Big[\langle \mathbf{v}_p|(\mathbf{r}-\mathbf{R}_j)|\delta\mathbf{v}'_j\rangle + \langle \delta\mathbf{v}_j|(\mathbf{r}-\mathbf{R}_j)|\mathbf{v}'_p\rangle\Big]. \end{aligned} \quad (175)$$

The rescattering matrix element contains all the information about the rescattering events in the entire molecular system. In this way is possible also to split it depending on the correction to the continuum states $\langle\delta\mathbf{v}_j|$. Consequently, we will solve an independent equation as Eq. (74, in order to find the direct and the rescattering processes for the n-atoms system. Notice that those equation are defined depending on the atomic center j, so for the entire molecule of n-centers the total amplitude is a sum of the independent transition amplitudes in each of the atoms, i.e.

$$\dot{b}(\mathbf{v},t) = \sum_{j=1}^{n}\dot{b}_j(\mathbf{v},t). \quad (176)$$

In the next section we find the exact form of the above equation and give details about its solution. Additionally we present the formulation to calculate the direct and the rescattering transition amplitudes.

3.1.2 *Direct transition amplitude*

In the case of HHG we are interested in describing processes where the electron is ionized and goes to the continuum, never returning to the vicinity of the remaining ion core, i.e., the so-called direct processes. As the direct ionization process should have a larger probability compared with the rescattering one [3, 4], one might neglect the rescattering factor $\mathbf{g}(\mathbf{v},\mathbf{v}') \approx 0$. The direct transition amplitude, in terms of the canonical momentum $\mathbf{p} = \mathbf{v} - \mathbf{A}(t)$, can be written as:

$$b_0(\mathbf{p},t) = \sum_{j=1}^{n}\Big\{ i\int_0^t dt'\,\mathbf{E}(t')\cdot\mathbf{d}_j\left[\mathbf{p}+\mathbf{A}(t')\right]\times\exp\left[-iS_j(\mathbf{p},t,t')\right]\Big\}. \quad (177)$$

The physical interpretation of the above equation is straightforward: it is the sum of all the ionization events that occur from the time t' to t for the whole system. Then, the instantaneous transition probability amplitude of an electron at a time t', at which it appears into the continuum with momentum $\mathbf{v}(t') = \mathbf{p}+\mathbf{A}(t')$, is defined by the argument of the $[0,t]$ integral in Eq. (177). Furthermore, the "semiclassical action" $S_j(\mathbf{p},t,t')$, Eq. (91), defines a possible electron

trajectory from the birth time t', at position $\mathbf{R}_j$, until the recombination/rescattering one t. As expected, note that the obtained transition amplitude equations also depend on the position from which the electron is tunnel ionized to the continuum; the same holds for the semiclassical action $S_j(\mathbf{p}, t, t')$.

3.1.3 *Rescattering transition amplitude*

In order to find the solution for the transition amplitude of the rescattered photoelectrons, $b_1(\mathbf{v}, t)$, we have considered $\mathbf{g}(\mathbf{v}, \mathbf{v}') \neq \mathbf{0}$. The first-order correction, $b_1(\mathbf{v}, t)$, is then obtained using the zeroth-order solution, $b_{0,j}(\mathbf{p}, t)$, as:

$$\begin{aligned} b_1(\mathbf{p}, t) \;=\; & -\sum_{j=1}^{n}\sum_{j'=1}^{n}\int_0^t dt' \int_0^{t'} dt'' \int d^3\mathbf{p}' \\ & \times \mathbf{E}(t'')\cdot\mathbf{d}_j\left[\mathbf{p}' + \mathbf{A}(t'')\right]\exp\left[-iS_j(\mathbf{p}', t', t'')\right] \\ & \times \mathbf{E}(t')\cdot\mathbf{g}_{jj'}\left[\mathbf{p} + \mathbf{A}(t'), \mathbf{p}' + \mathbf{A}(t')\right]\exp\left[-iS_{j'}(\mathbf{p}, t, t')\right], \end{aligned} \tag{178}$$

where j denotes the atom from where the electron is released and j' the one where the electron is rescattered. The above equation contains information about all the possible rescattering scenarios which take place in our n-center molecular system. In addition, a direct physical interpretation of each term can be inferred considering $j = j'$ for the local rescattering processes and $j \neq j'$ for the cross and nonlocal ones (for more details see Chapter 2).

As in Chapter 2 and Ref. [60, 63], the total rescattering transition amplitude, Eq. (107), is split in two main contributions: the local and the nonlocal + cross processes. In this way we thus define the rescattering transition amplitude as:

$$b_1(\mathbf{p}, t) = b_{Local}(\mathbf{p}, t) + b_{NL+Cross}(\mathbf{p}, t), \tag{179}$$

where now

$$b_{Local}(\mathbf{p}, t) = \sum_{j=1}^{n} b_{1,jj}(\mathbf{p}, t), \tag{180}$$

and

$$b_{NL+Cross}(\mathbf{p}, t) = \sum_{j\neq j'}^{n} b_{1,jj'}(\mathbf{p}, t). \tag{181}$$

3.1.4 *Time-dependent dipole moment for n-center molecular systems*

The computation of the HHG spectrum generated by a n-center molecule using the definition in Eq. (28) involves the search of the exact bound states describing the whole system. In order to do so, in Sec. 3.2, we

calculate the ground and scattering states by applying a method similar to the one used in the chapters before, i.e. using a nonlocal SR potential [2, 4, 60, 63]. In short, we consider a n-center molecule as a set of n atoms placed at the $\mathbf{R}_j$ positions. By employing the TDSE on that system and our basic SFA approach, the total molecular time-dependent dipole moment $\vec{\mu}(t)$ reads:

$$\vec{\mu}(t) = \sum_{j}^{n}\sum_{j'}^{n}\int d^3\mathbf{p}\, \mathbf{d}^*_{j'}(\mathbf{p}) b_{0,j}(\mathbf{p},t) + c.c., \tag{182}$$

where $\mathbf{d}^*_{j'}(\mathbf{p})$ is defined in Eq. (174) and $b_{0,j}(\mathbf{p},t)$ in Eq. (177). In the computation of the $\vec{\mu}(t)$, as in the previous chapters, we use the saddle-point method to solve the integral over momentum (see Sec. 1.2.1.2).

The above equation contains information about all the possible recombination scenarios present in our n-center molecule. Its interpretation is the same as in the case of diatomic systems, see Chapter 2.

The total time-dependent dipole, Eq. (182), can be split in two main contributions: the local and the cross processes, i.e.

$$\vec{\mu}_{\text{Local}}(t) = \sum_{j=1}^{n}\vec{\mu}_{jj}(t), \tag{183}$$

and

$$\vec{\mu}_{\text{Cross}}(t) = \sum_{j\neq j'}^{n}\vec{\mu}_{jj'}(t). \tag{184}$$

3.1.5 *ATI in polyatomic molecules*

The total photoelectron spectra, $|b(\mathbf{p},t_F)|^2$, is a coherent superposition of both the direct $b_0(\mathbf{p},t_F)$ and rescattered $b_1(\mathbf{p},t_F)$ transition amplitudes, i.e., $|b(\mathbf{p},t_F)|^2 = |b_0(\mathbf{p},t_F) + b_1(\mathbf{p},t_F)|^2$, as we defined in Eq. (35). In general, the equations for the transition amplitudes for a n-center molecule are similar to the diatomic case. So, in this case we also have to apply the standard saddle-point method to the rescattering transition amplitude, Eq. (178). In this way we substantially reduce the computational cost in the numerical computation of the integrals.

To complete the calculation of the total photoelectron spectra, $|b(\mathbf{p},t_F)|^2$ we first need to define the ground and the continuum states of our n-center molecular system. After having found them we then compute the bound-free transition dipole matrix elements, $\mathbf{d}_j(\mathbf{v})$, and the continuum-continuum transition rescattering matrix elements $\mathbf{g}(\mathbf{v},\mathbf{v}')$. In the next section, we shall explain how to analytically compute both the transition matrix elements and the final photoelectron momentum distribution.

3.2 A SIMPLIFIED MODEL FOR A n-CENTER MOLECULAR SYSTEMS

To obtain the ground and continuum states for a complex n-center molecule we have chosen a nonlocal SR potential to describe the interaction of the active electron with the nuclei as,

$$\hat{V}_{\mathbf{M}}(\mathbf{p},\mathbf{p}') = -\gamma'\, U(\mathbf{p})\, U(\mathbf{p}') \sum_{j=1}^{n} e^{-i\mathbf{R}_j\cdot(\mathbf{p}-\mathbf{p}')}, \tag{185}$$

where $U(\mathbf{p})$ is defined in Eq. (39). $\gamma' = \frac{\gamma}{n}$ is a parameter related with the shape of the ground state and now depends on the total numbers of atoms. We also consider fixed nuclei under the SAE approximation.

Solving the stationary Schrödinger equation for the system we have:

$$\left(\frac{p^2}{2} + I_p\right)\Psi_0(\mathbf{p}) = \gamma'\, U(\mathbf{p}) \sum_{j=1}^{n} e^{-i\mathbf{R}_j\cdot\mathbf{p}} \times \int d^3\mathbf{p}'\Psi_0(\mathbf{p}')U(\mathbf{p}')e^{i\mathbf{R}_j\cdot\mathbf{p}'}. \tag{186}$$

Defining new variables $\breve{\varphi}_j$ as

$$\breve{\varphi}_j = \int d^3\mathbf{p}'\Psi_0(\mathbf{p}')U(\mathbf{p}')e^{i\mathbf{R}_j\cdot\mathbf{p}'} = \int \frac{d^3\mathbf{p}'\Psi_0(\mathbf{p}')e^{i\mathbf{R}_j\cdot\mathbf{p}'}}{\sqrt{p'^2+\Gamma^2}}, \tag{187}$$

we could analytically obtain the bound states by solving Eq. (186) in the momentum representation. Explicitly we can write the wave function $\Psi_0(\mathbf{p})$ for the bound state in momentum space as follow:

$$\Psi_0(\mathbf{p}) = \frac{\gamma'}{\sqrt{(p^2+\Gamma^2)}(\frac{p^2}{2}+I_p)} \sum_{j=1}^{n} \breve{\varphi}_j e^{-i\mathbf{R}_j\cdot\mathbf{p}}. \tag{188}$$

To obtain the value of the integration constants we are going to work with the above equation multiplying it by $e^{-i\mathbf{R}_j\cdot\mathbf{p}}$ and $U(\mathbf{p})$, respectively in order to complete the left-hand side, i.e.

$$\breve{\varphi}_j = \gamma' \sum_{j'} \breve{\varphi}_{j'} \int d^3\mathbf{p}\, \frac{U^2(\mathbf{p})\, e^{i(\mathbf{R}_j-\mathbf{R}_{j'})\cdot\mathbf{p}}}{(\frac{p^2}{2}+I_p)}, \tag{189}$$

$$\breve{\varphi}_j = \sum_{j'} \breve{\varphi}_{j'}\, I_{jj'}, \tag{190}$$

where

$$I_{jj'} = \gamma' \int d^3\mathbf{p}\, \frac{e^{i(\mathbf{R}_j-\mathbf{R}_{j'})\cdot\mathbf{p}}}{(p^2+\Gamma^2)(\frac{p^2}{2}+I_p)}. \tag{191}$$

From here, we finally obtain an eigenvalues problem that looks like,

$$\begin{pmatrix} \breve{\varphi}_1 \\ \breve{\varphi}_2 \\ \vdots \\ \breve{\varphi}_n \end{pmatrix} = \begin{pmatrix} I_{11} & I_{12} & \cdots & I_{1n} \\ I_{21} & I_{22} & \cdots & I_{2n} \\ \vdots & \vdots & \ddots & \vdots \\ I_{n1} & I_{n2} & \cdots & I_{nn} \end{pmatrix} \times \begin{pmatrix} \breve{\varphi}_1 \\ \breve{\varphi}_2 \\ \vdots \\ \breve{\varphi}_n \end{pmatrix} \tag{192}$$

The solution of this eigenvalues problem give us the values of $\breve{\varphi}_j$. They allow us to fully determine the bound state as in the case of Eq. (188).

The ground state defined in Eq. (188) is the total state of the full molecular system with n atoms and can be written as,

$$\Psi_0(\mathbf{p}) = \sum_j^n \Psi_{0j}(\mathbf{p}) = \sum_j^n \frac{\gamma' \, U(\mathbf{p})}{(\frac{p^2}{2} + I_p)} \breve{\varphi}_j \, e^{-i\mathbf{R}_j \cdot \mathbf{p}}, \tag{193}$$

The normalization constant $\mathcal{M} = \gamma' \breve{\varphi}_j = \frac{\gamma}{n} \breve{\varphi}_j$ is calculated using the conventional normalization condition as,

where,

$$\mathcal{M} = \frac{1}{\left[4 \sum_{j,j'}^n \int d^3\mathbf{p} \, \frac{U^2(\mathbf{p}) \, e^{-i(\mathbf{R}_j - \mathbf{R}_{j'}) \cdot \mathbf{p}}}{(p^2 + 2I_p)^2}\right]^{1/2}} = \frac{1}{[I_n N]^{1/2}}. \tag{194}$$

3.2.1 *Ground state and bound-continuum dipole matrix elements*

The full dipole matrix element for the molecular system is built as a sum over all the dipole matrix elements for each of the atoms as:

$$\mathbf{d}(\mathbf{p}) = \sum_{j=1}^n \mathbf{d}_j(\mathbf{p}), \tag{195}$$

where the individual dipole matrix element $\mathbf{d}_j(\mathbf{p})$ depends on the position of the atom $\mathbf{R}_j$ and is calculated using the definition in Eq. (174) as,

$$\mathbf{d}(\mathbf{p}_0) = \sum_{j=1}^n \left[-i\nabla_{\mathbf{p}} \Psi_{0,j}(\mathbf{p}) \Big|_{\mathbf{p}_0} + \mathbf{R}_j \Psi_{0,j}(\mathbf{p}_0) \right]. \tag{196}$$

From here, working with the derivative functions, we have:

$$\begin{aligned} \mathbf{d}(\mathbf{p}_0) = \sum_{j=1}^n \Bigg\{ & -i\mathcal{M} \, \nabla_{\mathbf{p}} \left[\frac{U(\mathbf{p}) \, e^{-i\mathbf{R}_j \cdot \mathbf{p}}}{(\frac{p^2}{2} + I_p)} \right] \Bigg|_{\mathbf{p}_0} \\ & + \mathbf{R}_j \, \mathcal{M} \, \frac{U(\mathbf{p}_0) \, e^{-i\mathbf{R}_j \cdot \mathbf{p}_0}}{(\frac{p_0^2}{2} + I_p)} \Bigg\}. \end{aligned} \tag{197}$$

3.2.2 *Scattering waves and continuum-continuum transition matrix elements*

In order to get the rescattering states for the n-center molecular system, we are going to consider them as a plane wave plus corrections

(in a similar way as we have done for the rest of the studied cases), i.e.

$$\Psi_{\mathbf{p}_0}(\mathbf{p}) = \delta(\mathbf{p}-\mathbf{p}_0) + \sum_{j=1}^{n} \delta\Psi_{\mathbf{p}_0,j}(\mathbf{p}). \tag{198}$$

Starting from the Schrödinger equation and the SR potential proposed in Eq. (185) we have

$$\begin{aligned}\left(\frac{p^2}{2}-\frac{p_0^2}{2}\right)\delta\Psi_{\mathbf{p}_0}(\mathbf{p}) &= \gamma' \sum_{j=1}^{n} U(\mathbf{p})U(\mathbf{p}_0)e^{-i\mathbf{R}_j\cdot(\mathbf{p}-\mathbf{p}_0)} \\ &+ \gamma' \sum_{j=1}^{n} U(\mathbf{p}) \int U(\mathbf{p}')e^{-i\mathbf{R}_j\cdot(\mathbf{p}-\mathbf{p}')}\delta\Psi_{\mathbf{p}_0}(\mathbf{p}')d^3\mathbf{p}'.\end{aligned} \tag{199}$$

Using a change of variables as $\breve{\varphi}'_j = \int d^3\mathbf{p}'\delta\Psi_{\mathbf{p}_0}(\mathbf{p}')U(\mathbf{p}')e^{i\mathbf{R}_j\cdot\mathbf{p}'}$, and summing an infinitesimal quantity $i\epsilon$ to save the discontinuity when $p^2 = p_0^2$, we obtain after doing some algebra:

$$\begin{aligned}(p_0^2-p^2+i\epsilon)\delta\Psi_{\mathbf{p}_0}(\mathbf{p}) &= -2\gamma' \sum_{j=1}^{n} U(\mathbf{p})\, U(\mathbf{p}_0)\, e^{-i\mathbf{R}_j\cdot(\mathbf{p}-\mathbf{p}_0)} \\ &-2\gamma' \sum_{j=1}^{n} U(\mathbf{p})\, e^{-i\mathbf{R}_j\cdot\mathbf{p}}\, \breve{\varphi}'_j.\end{aligned} \tag{200}$$

Finally we have:

$$\delta\Psi_{\mathbf{p}_0}(\mathbf{p}) = -\frac{2\gamma'}{(p_0^2-p^2+i\epsilon)} \sum_{j=1}^{n} U(\mathbf{p})\, e^{-i\mathbf{R}_j\cdot\mathbf{p}} \left[U(\mathbf{p}_0)e^{i\mathbf{R}_j\cdot\mathbf{p}_0} + \breve{\varphi}'_j\right]. \tag{201}$$

To get $\breve{\varphi}'_j$, we use a similar procedure as before, completing the left-hand side of the Eq. (201), i.e.,

$$\begin{aligned}\breve{\varphi}'_j &= -\sum_{j'=1}^{n} \left[U(\mathbf{p}_0)\, e^{-i\mathbf{R}_{j'}\cdot\mathbf{p}_0} \int d^3\mathbf{p} \frac{2\gamma'}{(p_0^2-p^2+i\epsilon)}\, U^2(\mathbf{p})\, e^{i(\mathbf{R}_j-\mathbf{R}_{j'})\cdot\mathbf{p}}\right. \\ &\left. + \breve{\varphi}'_{j'} \int d^3\mathbf{p} \frac{2\gamma'}{(p_0^2-p^2+i\epsilon)}\, U^2(\mathbf{p})\; e^{i(\mathbf{R}_j-\mathbf{R}_{j'})\cdot\mathbf{p}}\right]\end{aligned} \tag{202}$$

where

$$\breve{\varphi}'_j = U(\mathbf{p}_0) \sum_{j'} e^{-i\mathbf{R}_{j'}\cdot\mathbf{p}_0}\, I'_{jj'} + \sum_{j'} \breve{\varphi}'_{j'}\, I'_{jj'}, \tag{203}$$

$$\breve{\varphi}'_j = \sum_{j'} K_{jj'} + \sum_{j'} \breve{\varphi}'_{j'}\, I'_{jj'}, \tag{204}$$

$$K_{jj'} = U(\mathbf{p}_0)\, e^{-i\mathbf{R}_{j'}\cdot\mathbf{p}_0}\, I'_{jj'}, \tag{205}$$

$$I'_{jj'} = -2\gamma' \int d^3\mathbf{p}\, \frac{U^2(\mathbf{p})\; e^{i(\mathbf{R}_j-\mathbf{R}_{j'})\cdot\mathbf{p}}}{(p_0^2-p^2+i\epsilon)}. \tag{206}$$

From here we have an eigenvalues problem that looks like:

$$\begin{pmatrix} \breve{\varphi}'_1 \\ \breve{\varphi}'_2 \\ \vdots \\ \breve{\varphi}'_n \end{pmatrix} = \begin{pmatrix} I'_{11} & I'_{12} & \cdots & I'_{1n} & \sum_{j'}^{n} K_{1j'} \\ I'_{21} & I'_{22} & \cdots & I'_{2n} & \sum_{j'}^{n} K_{2j'} \\ \vdots & \vdots & \ddots & \vdots & \vdots \\ I'_{n1} & I'_{n2} & \cdots & I'_{nn} & \sum_{j'}^{n} K_{nj'} \end{pmatrix} \times \begin{pmatrix} \breve{\varphi}'_1 \\ \breve{\varphi}'_2 \\ \vdots \\ \breve{\varphi}'_n \\ 1 \end{pmatrix} \tag{207}$$

The solution of this eigenvalues problem give us the values of $\breve{\varphi}'_j$ that fully determine the bound state. The correction depending on the atom position $\mathbf{R}_j$ can be written as $\delta\Psi_{\mathbf{p}_0}(\mathbf{p}) = \sum_{j=1}^{n} \delta\Psi_{\mathbf{p}_0,j}(\mathbf{p})$. The independent solution for each atom is,

$$\delta\Psi_{\mathbf{p}_0,j}(\mathbf{p}) = -\frac{2\gamma'}{(p_0^2 - p^2 + i\epsilon)}\, U(\mathbf{p})\, e^{-i\mathbf{R}_j\cdot\mathbf{p}} \left[U(\mathbf{p}_0) e^{i\mathbf{R}_j\cdot\mathbf{p}_0} + \breve{\varphi}'_j \right]. \tag{208}$$

3.2.2.1 *Continuum-continuum transition matrix element*

The continuum-continuum transition matrix element is defined as:

$$\mathbf{g}(\mathbf{p},\mathbf{p}') = \sum_{j=1}^{n} \langle \mathbf{v}_p | (\mathbf{r} - \mathbf{R}_j) | \delta\mathbf{v}' \rangle + \langle \delta\mathbf{v} | (\mathbf{r} - \mathbf{R}_j) | \mathbf{v}'_p \rangle \tag{209}$$

where, $\delta\mathbf{v} = \sum_{j=1}^{n} |\delta\mathbf{v}_j\rangle$ is the correction over all the centers. Working with Eq. (209) and applying some delta function properties we get:

$$\begin{aligned} \mathbf{g}(\mathbf{p}_1,\mathbf{p}_2) = & \sum_{j=1}^{n} \left[i\nabla_{\mathbf{p}} \delta\Psi_{\mathbf{p}_2,j}(\mathbf{p})|_{\mathbf{p}_1} - \mathbf{R}_j \delta\Psi_{\mathbf{p}_2,j}(\mathbf{p}) \right] \Big|_{\mathbf{p}_1} \\ & + \sum_{j=1}^{n} \left[i\nabla_{\mathbf{p}} \delta\Psi_{\mathbf{p}_1,j}(\mathbf{p}) - \mathbf{R}_j \delta\Psi_{\mathbf{p}_1,j}(\mathbf{p}) \right]^* \Big|_{\mathbf{p}_2} \end{aligned} \tag{210}$$

.labelEq : g(p1,p2)

Here, we have defined the direct and rescattering transition amplitudes for a general molecular system of n atoms. The same procedure is done with the matrix elements $\mathbf{d}(\mathbf{p}_0)$ and $\mathbf{g}(\mathbf{p}_1,\mathbf{p}_2)$.

To study a specific molecular system we need to fix the subscript j and use the Eqs. (193), (197), (208) and (**??**). Those equations are self-consistent with the diatomic and atomic cases as well. For a case of a three-center molecule, i.e., constituted by three atoms, the subscript j takes the values 1, 2 and 3, meaning $\mathcal{I}(\omega) = \sum_{j=1}^{3} \sum_{j'=1}^{3} \mathcal{I}_{jj'}(\omega)$ and $b(\mathbf{p},t) = \sum_{j=1}^{3} b_{0,j}(\mathbf{p},t) + \sum_{j=1}^{3} \sum_{j'=1}^{3} b_{1,jj'}(\mathbf{p},t)$. Notice that both the atomic and molecular HHG spectra depend directly on the time-dependent dipole moment. The latter, in turn, depends on the form of the bound-continuum matrix element and the continuum states transition amplitude, that are different for each of atomic, diatomic, or multiatomic system under study.

3.3 RESULTS AND DISCUSSION

Along this section, we compute HHG and ATI spectra generated from different molecular systems, with more than two atoms, using the theory presented above. We compare the HHG and ATI spectra computed using two different models, namely (i) *Model A* and (ii) *Model B* for four different molecular systems in order to establish similarities and differences. In the *Model A* we used a nonlocal SR potential to calculate the ground and scattering states, as well as the bound-continuum and rescattering matrix elements. In *Model B* we have a ground state approximated as a linear combination of atomic orbitals (LCAO) to calculate the bound-continuum matrix element.

We present calculations of HHG and ATI for three triatomic (CO_2, CS_2, H_2O) and one tetratomic (C_2H_2) molecular systems. Furthermore, the splitting of the contributions to the photoelectron spectra helps us to distinguish which of the direct and rescattering scenarios is relevant in the different energy/momentum regions.

In the Appendix 7 and 8 we develop the exact equations of the ground and scattering states for the three- and four-center systems, respectively. Those equations are obtained using the general equations presented in the sections before.

3.3.1 *HHG: Three-center molecular systems*

In order to study systems with more degrees of freedom and describe the different processes contributing to the total HHG spectra, as we have done for diatomics, we apply the model described before to both CO_2 and H_2O molecules.

3.3.1.1 *The carbon dioxide (CO_2) molecule*

The carbon dioxide molecule CO_2 is a linear system formed by three atoms, O=C=O, where the two oxygen atoms are separated by a distance $R = 4.38$ a.u (2.31 Å), when the system is in equilibrium. Here, to model the ground molecular state the parameters of the nonlocal SR potential are set to $\Gamma = 0.8$ and $\gamma = 0.11$ a.u. An ionization potential $I_p = 0.50$ a.u. (13.6 eV) is obtained. This value is in excellent agreement with the actual CO_2 ionization energy (13.77 eV) [64]. The incident laser electric field is defined in Eq. (1) and we use a laser wavelength and peak intensity of $\lambda = 800$ nm and $I_0 = 1 \times 10^{14}$ W $\cdot$ cm^{-2}, respectively. The laser pulse has 4 total cycles (11 fs of total duration) and the carrier-envelope phase (CEP) is set to zero [2].

We present HHG spectra, computed by using our quasiclassical SFA model, for the CO_2 molecule in Fig. 30. In the Fig. 30(a) we show the different contributions to the HHG spectra, i.e. the total $\mathcal{I}(\omega)$ (solid line with red circles), calculated from the time-dependent dipole moment presented in Eq. (182), the *local* $\mathcal{I}(\omega)$ (blue solid line),

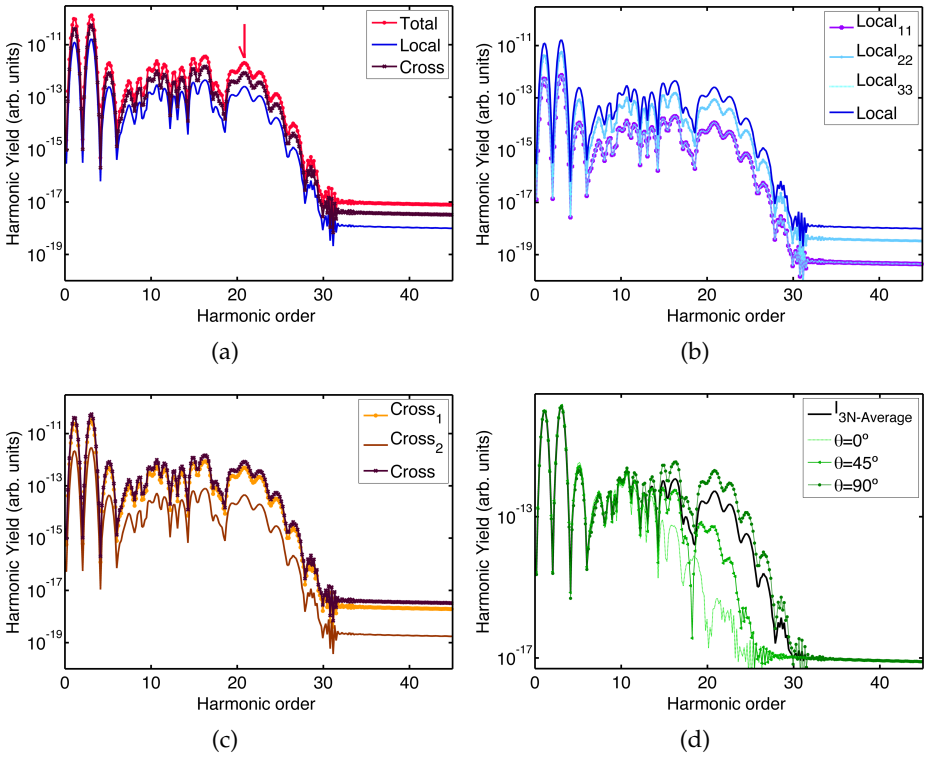

Figure 30: CO_2 molecular HHG spectra $\mathcal{I}(\omega)$ (in logarithmic scale) as a function of the harmonic order calculated by using our quasiclassical SFA. In panels (a)-(c) the CO_2 molecule is oriented perpendicular to the laser polarization, i.e., $\theta = 90°$ and with an internuclear distance of $R = 4.38$ a.u. The peak intensity was set to 1×10^{14} W $\cdot$ cm^{-2}

computed with Eq. (183), and the *cross* $\mathcal{I}(\omega)$ (dark brown line with asterisks), extracted from Eq. (184). These calculations show the well known HHG plateau that ends with a cutoff (marked with a red arrow) at around the 21th harmonic order (this last value is in perfect agreement with the one predicted by the semiclassical law, see Eq. (67)). Both *local* and *cross* contributions have almost the same yield over all the frequency range and only minor differences are visible.

In Fig. 30(b), we present a split of the *local* processes, namely, $\mathcal{I}_{11}(\omega)$ (solid line with purple circles), $\mathcal{I}_{22}(\omega)$ (solid line with light blue squares), and $\mathcal{I}_{33}(\omega)$ (dashed line). As we can see the contribution from the O atoms, placed at the end of the molecule, is equal in amplitude and shape and different in yield from the $\mathcal{I}_{22}(\omega)$ (corresponding to the C atom placed at the origin). This means that the O atoms contribute a slightly less than the C atom. We notice, however, that the shapes and positions of the minima are the same for the three contributions.

In Fig. 30(c), we present each of the contributions that build up the total *cross* processes. We have separated them depending on how long the laser-ionized electron travels in the continuum before recom-

bination. The $cross_1$ (solid line with orange circles), $\vec{\mu}_{12}(t) + \vec{\mu}_{21}(t) + \vec{\mu}_{23}(t) + \vec{\mu}_{32}(t)$,, and the $cross_2$ (solid brown line), $\vec{\mu}_{13}(t) + \vec{\mu}_{31}(t)$ contributions have similar yields. The main difference between these two HHG spectra is the yield: the $cross_1$ contribution has a higher yield than the $cross_2$ one. The position of the absolute minima around the 19^{th} harmonic order is present in both contributions - the same can be seen in the *local* term. For the calculations in Figs. 30(a)-30(c), we consider a CO_2 molecule aligned perpendicular to the incident laser pulse polarization, i.e., the internuclear axis vector is forming an angle $\theta = 90°$ with respect to the z axis, being this one the most favorable configuration [see Fig. 30(d)].

Finally, in Fig. 30(d) we present a set of total HHG spectra for different molecular orientations, namely, parallel ($\theta = 0°$), oblique ($\theta = 45°$), and perpendicular ($\theta = 90°$). In addition, we include an averaged HHG spectrum, obtained coherently adding four different orientations. We can observe a similar behavior as for the case of H_2 (see Fig. 16), i.e., the difference in the total spectra for different orientation angles is hardly to see for lower harmonic orders and starts to be visible in the mid-plateau and cutoff regions. Furthermore, the perpendicular orientation appears to be the dominant one. The comparable behavior between the CO_2 and H_2 molecules supports the fact that the former could be considered as a stretched diatomic O_2 molecule for interference minima calculations [58].

3.3.1.2 *The water (H_2O) molecule*

One of the most important three-center molecules is water (H_2O). It configures an essential part of the blocks that build biological life. In this section we theoretically investigate HHG spectra of the H_2O molecule using our semiclassical SFA approach.

The H_2O molecule is an angular molecule with two H atoms and one O atom. At equilibrium the internuclear distance of the bond H=O is about $R = 1.8$ a.u. (0.95 Å) and the angle between the two H atoms $\alpha = 104.5°$. For this configuration, and considering an ionization potential of $I_p = 0.46$ a.u. (12.52 eV) [65], we set the parameters of our nonlocal SR potential to $\Gamma = 0.8$ and $\gamma = 0.1$ a.u.

In Fig. 31 we show HHG spectra for a laser wavelength and peak intensity of $\lambda = 800$ nm and $I_0 = 1 \times 10^{14}$ W $\cdot$ cm^{-2}, respectively. The laser pulse has 4 total cycles (11 fs of total duration) and the CEP is set to 0 rad. In Fig. 31(a) we show HHG spectra both for five different molecular orientations, $\theta = 0°$, $\theta = 20°$, $\theta = 45°$, $\theta = 60°$, and $\theta = 90°$ and an averaged case. The molecular axis is fixed in space and forms an angle of $\alpha/2$ with respect to the vector position $\mathbf{R}_1$. Furthermore, θ defines the angle between this molecular axis and the laser electric field polarization (see Fig. 44 in the Appendix 7 for more details).

The dependency of the HHG spectra with respect to the molecular orientation is quite evident. For lower harmonic orders all the ori-

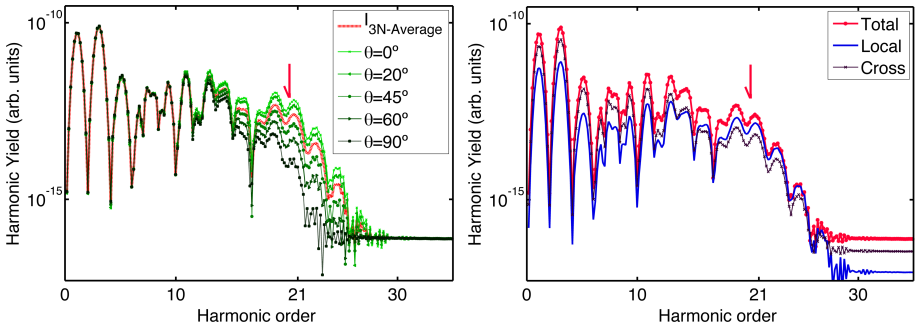

Figure 31: HHG spectra $\mathcal{I}(\omega)$ (in logarithmic scale) of an H_2O molecule, as a function of the harmonic order, computed using our quasi-classical MSFA model. (a) HHG spectra for $\theta = [0°, 20°, 45°, 60°, 90°]$ and averaged over eight orientations in the range $\theta = [0° - 360°]$; (b) different contributions to the averaged HHG spectra.

entations appear to be equivalent and the main differences start to materialize for harmonic orders $\gtrsim 12^{\text{th}}$. As we can see in Fig. 31(a) the HHG spectrum for $\theta = 0°$ (solid line with asterisks), 20° (solid line with left-pointing triangle) and 45° (dashed line) exhibit a similar structure. The other two orientations, 60° (right-pointing triangle line) and $\theta = 90°$ (square line), present an harmonic yield several orders of magnitude lower in this region. The total HHG spectra for all the molecular orientations show a slight minimum around the 17^{th} harmonic order that could be attributed to interference effects, although it is not an easy task to characterize it using a simple interference formula as in the case of diatomics.

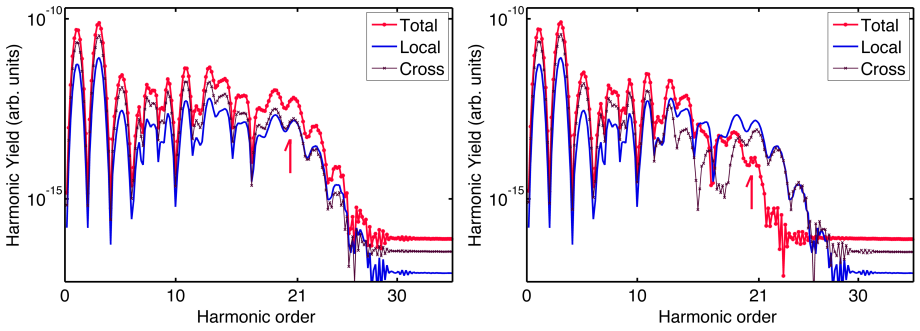

Figure 32: Different contributions total, local and cross to the H_2O molecular HHG spectra as a function of the harmonic order calculated by using our MSFA. (a) $\theta = 0°$ (parallel); (b) $\theta = 90°$ (perpendicular).

We have also included in Fig. 31(a) an averaged HHG spectrum over eight values of θ in the range $[0° - 360°]$ (dashed red line). As

we can see, the minimum survives the orientation average. Furthermore, for $\theta = 90°$ (square line) the total HHG spectrum rapidly decreases for harmonic orders $> 16^{th}$. This means that the interference between the *local* and *cross* processes is destructive and function of the molecular orientation. This behavior introduces a decrease of the total HHG yield. We note that for H_2O, contrarily to the CO_2 case, an enhancement of the total HHG spectrum is observed when the molecule is oriented parallel, $\theta = 0°$, to the laser electric field polarization. As we have done both for diatomics and CO_2 in Fig. 31 (b) we plot the different terms contributing to the total HHG averaged spectrum. Contrarily to the oriented case, here the *local* and *cross* processes appear to constructively contribute to the total HHG spectrum.

In order to study more deeply the underlying physics behind the enhancement and decrease of the total HHG spectrum for $0°$ and $90°$, we plot in Fig. 32 the different contributions for these two particular cases. For $\theta = 0°$ [Fig. 32(a)], the decrease of the HHG yield is evident for harmonic orders higher than the 15^{th}. Around this harmonic order, both contributions, the *local* and *cross*, have a similar yield and the coherent sum develops in a destructive interference decreasing the total HHG spectrum in about three orders of magnitude. On the other hand, for $\theta = 90°$ [Fig. 32(b)], we observe a steadily decrease of the *cross* processes, of about two orders of magnitude, in the whole spectral range. Consequently, we can argue that in this case the *cross* contributions are almost negligible (solid brown line with squares) and the total HHG spectrum is mainly dominated by the *local* processes (solid blue line).

3.3.2 *The role of the initial state in ATI: CO_2 and CS_2*

In this section we are going calculate the ATI spectra emitted for two prototypical three-center molecules. We start our analysis computing the ATI for the CO_2 molecule. We present the different contributions, direct and rescattering, to the total photoelectron spectra and discuss their differences and similarities. We use next the CS_2 molecule as another three-center prototypical system. For this case we also calculate the different processes contributing to the total spectra and make a similar study to the one done for CO_2. In this way we are able to highlight both the discrepancies and coincidences between these two comparable molecular systems (see the Appendix 7).

3.3.2.1 *The CO_2 molecule*

We consider a CO_2 molecule in equilibrium, i.e. the two oxygen atoms are separated a distance $R = 4.4$ a.u. (2.327 Å) with the carbon atom located in the mid point. The ionization potential of the outer electron predicted by GAMESS is $I_p = 0.39$ a.u. The corresponding parameters

of our nonlocal SR potential to obtain this I_p are $\Gamma = 0.8$ and $\gamma = 0.1$ a.u. [60].

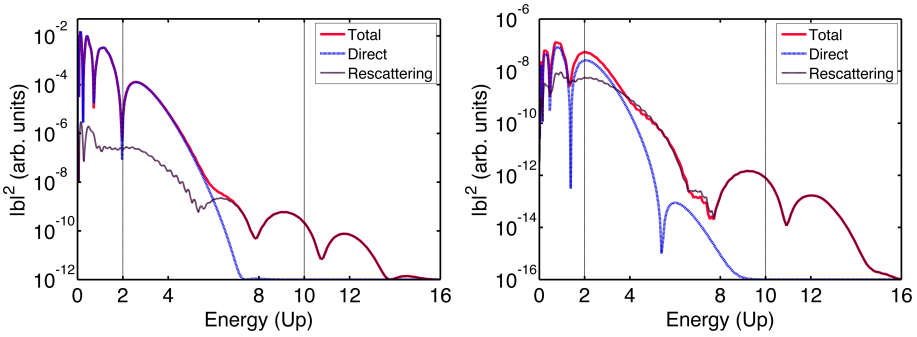

Figure 33: CO_2 molecular ATI spectra (in logarithmic scale) as a function of the electron energy in U_p units. (a) ATI spectra calculated using *Model A*; (b) ATI spectra computed using *Model B*. In both calculations the CO_2 molecule is oriented perpendicular to the laser polarization.

In Fig. 33 we present the ATI spectra, computed by using both the *Model A* [Fig. 33(a)] and *Model B* [Fig. 33(b)]. Here, we show the different contributions: the total $|b(\mathbf{p}, t)|^2$ (solid red line), the *direct* $|b_0(\mathbf{p}, t)|^2$ (blue solid line) and the *rescattering* $|b_1(\mathbf{p}, t)|^2$ (dark brown line) ones for each model. In both models we see that the direct processes contribute only in the low energy region of the spectra, $E_p \lesssim 6U_p$, being negligible at high energies, where the rescattering terms are dominant. In this case we also observe an overestimation of the direct terms and a difference of four orders of magnitude in the total yield between the *Model A* [Fig. 33(a)] and *Model B* [Fig. 33(b)]. Besides of this difference in amplitude, the shape of both spectra is quite similar: the change between direct and rescattering dominance is around the same energy ($\sim 5U_p$). On the other hand, we would like to attract the attention to the high energy part of the ATI spectra $E_p \gtrsim 4U_p$. As can be seen, the two models show the same number of minima at around the same positions $\approx 5U_p$, $\approx 8U_p$ and $\approx 11U_p$. In order to investigate if these minima are generated by the interference between the local and nonlocal+cross terms in Fig. 34 we split the different *rescattering* processes contributions.

As can be seen in Figs. 34(a) and 34(b), both *Local* and *NL+Cross* contributions have almost the same yield over all the electron energy range and only minor differences are visible. As a consequence the minima appear to be generated by the destructive interference between electrons tunnel-ionized and rescattered in the same ion core. In Figs. 34(c) and 34(d), we present a split of the *local* processes, namely, $|b_{1,11}(\mathbf{p}, t)|^2$ (solid yellow line with stars) and $|b_{1,33}(\mathbf{p}, t)|^2$ (solid purple line). We observe here that the contribution from the

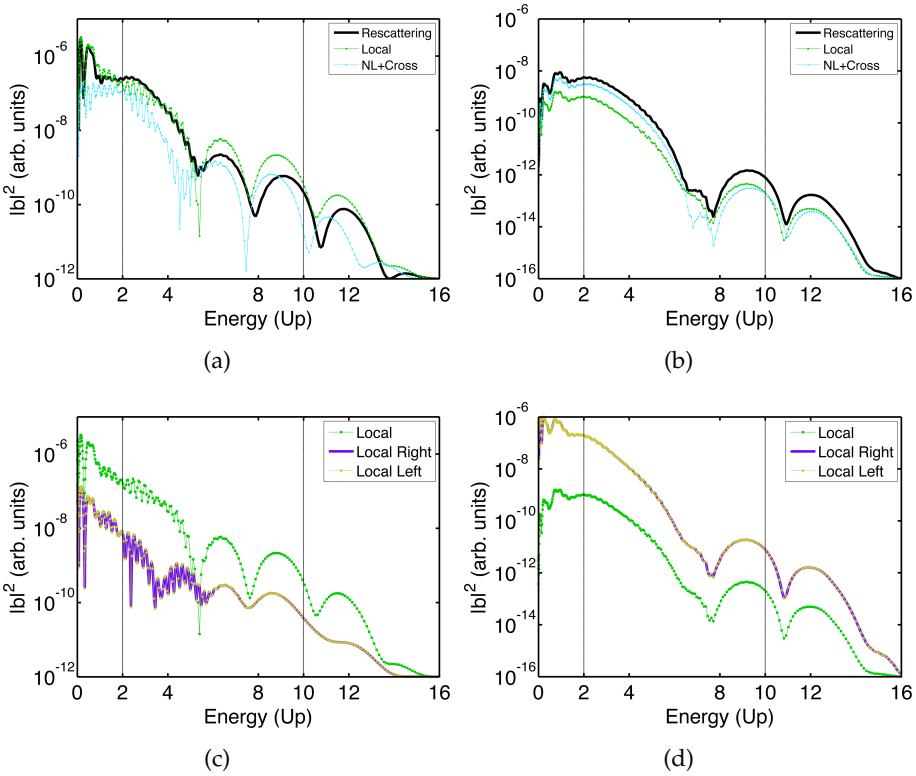

Figure 34: Different rescattering processes contributions to the CO_2 molecular ATI spectra (in logarithmic scale) as a function of the electron energy in U_p units. (a)-(c) Spectra calculated using *Model A*; (b)-(d) spectra computed using *Model B*. In both calculations the CO_2 molecule is oriented perpendicular to the laser polarization.

O atoms, placed at the end of the molecule, is equal in amplitude and shape in both models. On the contrary, the contribution of the C atom, placed at the origin, is almost negligible (not shown in the figure) in the case of *Model B*. In the contrary, for the calculations using the *Model A* we observed that the contribution from electrons ionized and rescattered on the C atom is higher than the contribution from the O atoms. This over estimation of $|b_{1,22}(\mathbf{p}, t)|^2$ in model *Model A* is directly related with the use of s-type orbital to describe the AO of the carbon atom in the molecule.

Regarding the deep minima, if we take a look at the Figs. 34(c) and 34(d), we see that the minima are present in the independent contribution $|b_{1,11}(\mathbf{p}, t)|^2$ and $|b_{1,33}(\mathbf{p}, t)|^2$. This reinforce the hypothesis that internal interferences, inside of the atoms, are the responsible of those minima. We can also observe that, in the case of the *Model A*, the local contributions (Right/Left) add up together to enhance the total local contribution. In the case of the *Model B*, those two local contributions interfere each other leading up a total contribution with lower amplitude and exactly the same shape. This is a direct consequence of both the bound state wave function and the HOMO shape.

Let us next analyze the effect of the molecular orientation on the ATI spectra. In order to do this we compute the final photoelectron spectra for the molecule oriented parallel and perpendicular with respect to the laser field polarization. In both cases we use the *Model B* and in Fig. 35 we show the results.

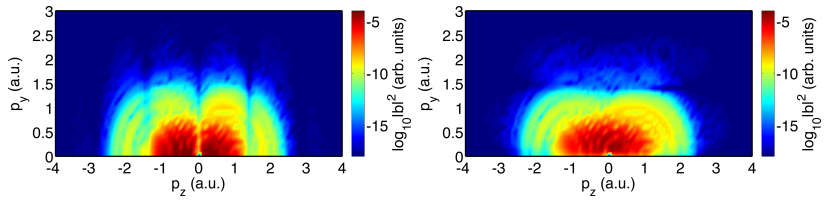

Figure 35: 2D-Total ATI photoelectron spectra (in logarithmic scale) for the CO_2 molecule as a function of the (p_z, p_y) electron momenta computed using the *Model B*. (a) The molecule is oriented parallel ($\theta = 0°$) to the laser field polarization, (b) the same as in (a), but the molecule is oriented perpendicular ($\theta = 90°$) to the laser field polarization.

In the parallel configuration, $\theta = 0°$ [Fig. 35(a)], we can see the typical interference pattern with deep minima located at around $p_z = \pm 1.4$ a.u. The position of these minima is in agreement with the second minimum predicted by the two slit interference formula [63] for two radiant points separated a distance $R = 2.2$ a.u, i.e. just the separation between the oxygen and the carbon atoms. On the contrary, in the perpendicular configuration, $\theta = 90°$ [Fig. 35(b)], there is no trace of two-center interferences.

3.3.2.2 *CS_2 molecule*

For the CS_2 molecule we focus our study in the dependency of the total photoelectron spectra with the molecular orientation. We perform calculations using both models for three different orientation angles. The parameters used in the nonlocal SR potential are $\Gamma = 0.71$ and $\gamma = 0.099$ a.u., respectively. With these values, we match the ionization potential $I_p = 0.32$ a.u of the CS_2 molecule obtained with GAMESS. Additionally, the CS_2 HOMO is modelled by the *Model B* as a combination of only 2p AOs.

We consider the molecule oriented at $\theta = 0°$, $\theta = 45°$ and $\theta = 90°$ with respect to the laser field polarization and we also include an averaged ATI spectra over these three orientations.

The calculations using the *Model A* [Fig. 36(a)] show only minor dissimilarities in shape and amplitude for the three different orientations. The main differences appear in the low energy part, where the spectra depict different yield and the position of the interference minima change. In this case the most favorable orientation, i.e. the one that gives the highest yield, is $\theta = 90°$, i.e. when the molecule is

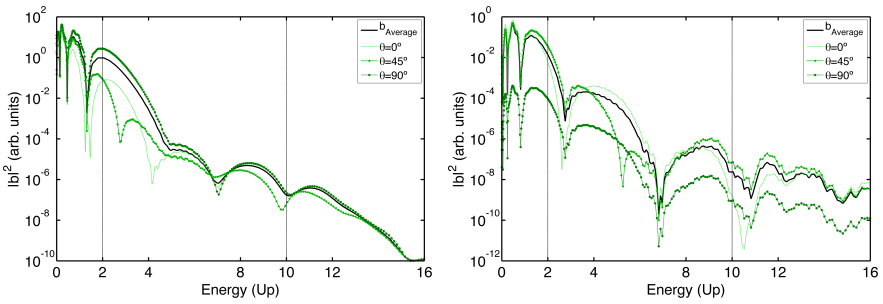

(a) nonlocal SR potential (b) LCAO

Figure 36: Total photoelectron spectra (in logarithmic scale) as a function the of the electron energy in U_p units for different orientations. (a) Calculated by using *Model A*; (b) calculated using *Model B*. In both models the CS_2 molecule is at equilibrium $R = 5.86$ a.u. (3.1 Å). The peak laser intensity used in this calculation is set to $I_0 = 1 \times 10^{14}$ W · cm^{-2}.

oriented perpendicular to the laser field polarization. This result is in agreement with our previous publication [63], where the HHG for a three-center molecule, CO_2, shows a similar behaviour.

For the ATI spectra obtained using the *Model B* [Fig. 36(b)], we observe that the behavior is completely the opposite: in the perpendicular case the total yield drops by more than three orders of magnitude and it is the parallel orientation the one that dominates. Additionally, the differences between the three orientations are now more visible. We could argue then that the *Model B* is not only more accurate in the molecular orbital (MO) description but also more sensitive to the molecular orientation.

In order to discuss differences and similarities with the CO_2 case, in Fig. 37 we present 2D-total photoelectron spectra for a CS_2 molecule oriented at $\theta = 0°$ [Fig. 37(a)] and $\theta = 90°$ [Fig. 37(b)], with respect to the laser field polarization.

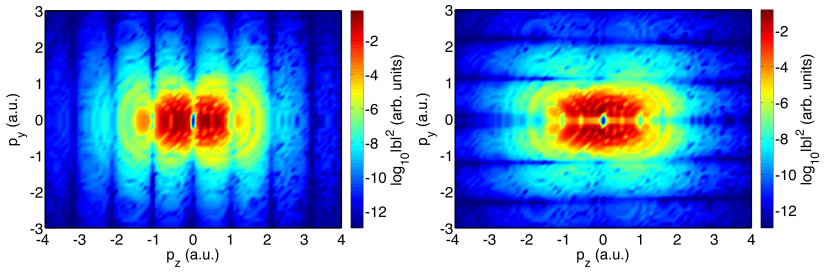

(a) (b)

Figure 37: 2D-Total ATI photoelectron spectra (in logarithmic scale) for the CS_2 molecule as a function of the (p_z, p_y) electron momenta computed using *Model B*. (a) The molecule is oriented parallel to the laser field polarization, (b) the same as in (a), but the molecule is oriented perpendicular to the laser field polarization.

The results obtained show the sensitivity of our model to the molecular orientation and the presence of interference minima now for the two orientations (this is in clear contrast to the CO_2 case, where for the perpendicular orientation, Fig. 35(b), there are not fingerprints of interferences). Furthermore, we observe that, for the parallel case, Fig. 37(a), the interference minima are placed for fixed p_z values, i.e. parallel to the p_y axis, meanwhile that for the case of $\theta = 90°$ these minima are for fixed p_y values, i.e. parallel to the p_z axis. These features are related with the shape of the CS_2 HOMO, that it is inherited in the molecular bound-free matrix element.

3.3.3 *Four-center molecular systems: HHG and ATI*

In this section we are going apply our MSFA model to a 4-center molecule. In here we calculate the HHG and ATI spectra for such a system within the nonlocal SR potential and the LCAO approximation to describe the MO. For this case we analyze the influence of the MO not only in the ATI but also in the HHG spectra. Specifically, we consider the acetylene molecule (C_2H_2) under the influence of a short and strong laser field.

3.3.3.1 C_2H_2

In this molecular system we use both *Model A* and *Model B*. In all the calculations we consider the molecule in equilibrium. It means that the two C atoms are separated a distance of $R_{CC} = 2.7$ a.u. (1.42 Å) meanwhile the bound distance of the C-H atoms is about $R_{HC} = 2.0$ a.u. (1.058 Å). The HOMO of the C_2H_2 molecule is constructed as a LCAO and it results as a composition of 2p states. The molecular orbital for acetylene is presented in Fig. 38.

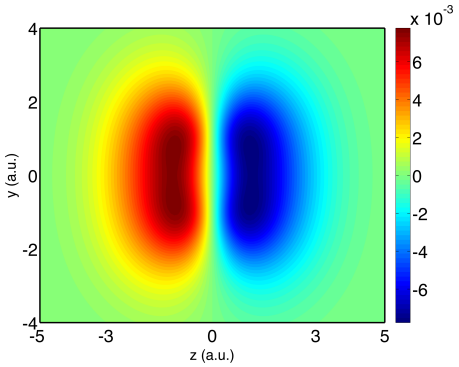

Figure 38: Coordinate space wavefunction for the C_2H_2 HOMO, presented in the $y - z$ plane, calculated using the LCAO method. The molecule is consider in equilibrium with internuclear distance of $R_{CC} = 2.7$ a.u. and $R_{HC} = 2.0$ a.u. respectively and the molecular axis is parallel to y-axis.

We can see that the MO is mainly a combination of $2p_z$ orbitals around the carbon atoms. The contribution of the hydrogen atoms to the HOMO is almost negligible, so we can then infer that hydrogens and carbons have different dynamics. This is just the opposite to the SR potential model, considering it is based in the combination of only s-type states, where all the atoms contribute in the same manner.

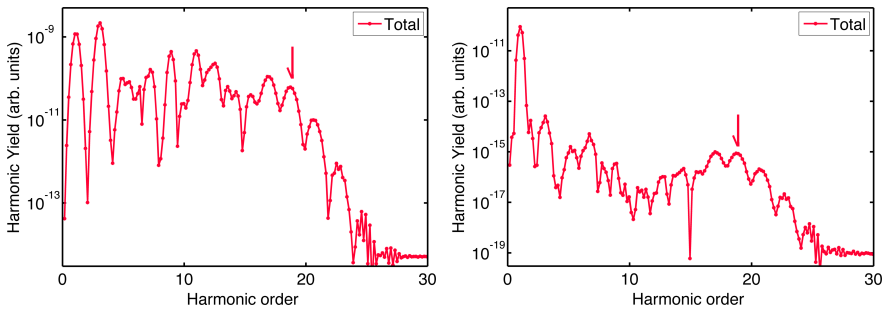

(a) *Model A*-SR potential (b) *Model B*-LCAO

Figure 39: HHG spectra (in logarithmic scale) of acetylene molecule, aligned 90° with respect to the laser field polarization, as a function of the harmonic order. The driven laser pulse have 800 nm of wavelength and intensity of $I_0 = 1 \times 10^{14}$ W · cm^{-2}. (a) Results obtained using the SR potential model: *Model A* and (b) results obtained the LCAO: *Model B*. The arrows in all the panels indicate the position of the classical HHG cutoff.

For the HHG and ATI spectra calculation we set the parameters of our nonlocal SR potential to $\Gamma = 0.8$ and $\gamma = 0.24$ a.u., respectively. Using these parameters the ionization potential results $I_p = 0.3629$ a.u., which is in agreement with the the one obtained using GAMESS. In Fig. 39 we present the results for the calculation of the HHG spectra using each of the models: *Model A* Fig. 39(a) and *Model B* Fig. 39(b) and for the molecule aligned perpendicular to the laser field polarization. The laser field intensity was set to $I_0 = 1 \times 10^{14}$ W · cm^{-2} with a total number of cycles is $N_c = 4$ and $\phi_0 = 0$ rad. The time step is set to $\delta t = 0.4$ a.u. and this corresponds to a total of $N_t = 1000$ points for the numerical integration.

As we can see in Fig. 39 the HHG spectra strongly depends on the MO shape. The amplitude and shape of the HHG spectra show stronger differences. The main ones, as in the previous calculations, is in the low energy part of the spectra where in Fig. 39(a) we can see a small increase of the harmonic yield whereas for the Fig. 39(b) we have a strong decrease of the yield. For the plateau region the behavior of both spectra is quite similar, developing a deep minimum around the harmonic 15^{th}. Likewise, both spectra end up abruptly at the cutoff.

In order to complete the analysis in the Fig. 40 we present the ATI calculation for this system. We use the MSFA presented before and a complete detail of the final equations is presented in the Appendix 8.

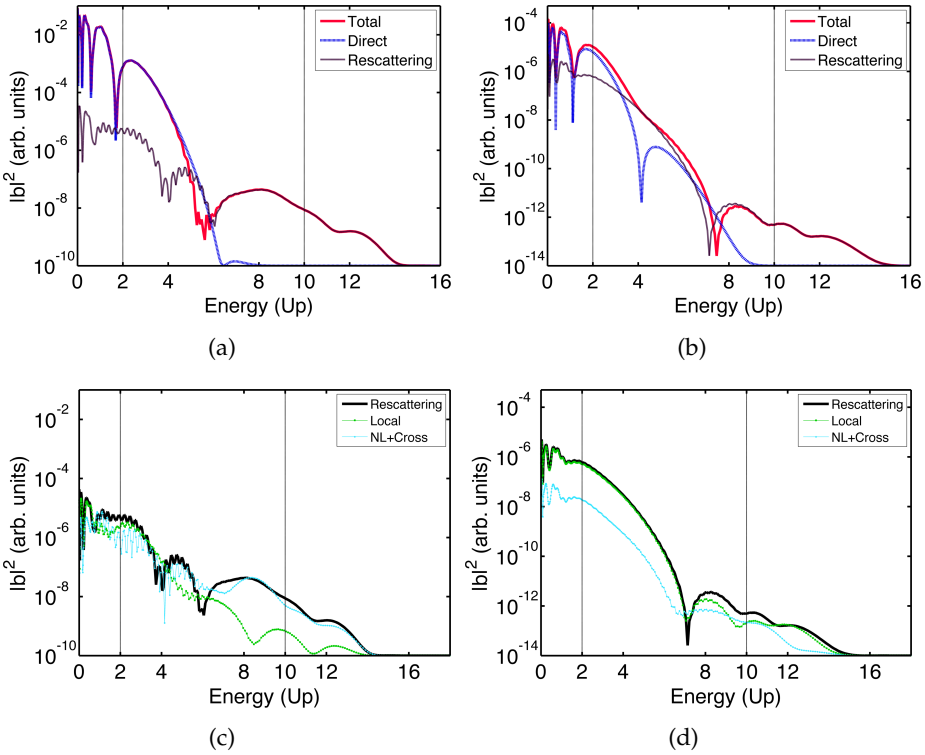

Figure 40: (a)-(b) Total, direct and rescattering contributions to the photoelectron spectra as a function of the final momentum, calculated using the *Model A*, and *Model B* respectively. (c)-(d) The split of the rescattering contributions using *Model A*-(c), and *Model B*-(d).

In the upper panels of Fig. 40 we can see the main contributions to the full final ATI photoelectron spectra: the total $|b(\mathbf{p},t)|^2$ [Eq. (35)], the direct $|b_0(\mathbf{p},t)|^2$ [Eq. (177)], and the rescattering $|b_1(\mathbf{p},t)|^2$ [Eq. (179)] terms, respectively. In the same way in the lower ones we plot the two main rescattering terms $|b_{Local}(\mathbf{p},t)|^2$ and $|b_{Nl+Cross}(\mathbf{p},t)|^2$.

These results, displayed in Figs. 40(a)-(b), present a some reasonable agreement between the *Model A* and *Model B*, particularly for the direct contribution (blue line), where the details of the molecular potential are not so relevant. Apart from the differences in amplitude, in both calculations we can observe that each term contributes to different regions of the photoelectron spectra, i.e. , for electron energies $E_p \lesssim 5U_p$ the direct term $|b_0(\mathbf{p},t)|^2$ dominates the spectrum and, on the contrary, it is the rescattering term $|b_1(\mathbf{p},t)|^2$ the one that wins in the high-energy electron region.

The terms that play an important role in the rescattering process $|b_{Local}(\mathbf{p},t)|^2$ (dotted green line) and $|b_{Nl+Cross}(\mathbf{p},t)|^2$ (cyan line) for the two models are displayed in Figs. 40(c)-(d). As we can infer

from the latter figure, the main contribution to the rescattering term is from the local processes. This is evident in the case of the calculation using *Model B*, Fig. 40(d), where the nonlocal and cross term differs in more than one order of magnitude. For the results obtained using model *Model A* we can see that the local and nonlocal and cross contribute in the same way for electron energies $E_p \lesssim 4U_p$, after which the nonlocal and cross processes are dominant. This rapid increasing of the nonlocal and cross term over the local one, for the high energy part, is directly related with the dipole matrix element. In the *Model A* the contribution of the all the atoms in the molecule is the same. This means that the nonlocal and cross terms related to the hydrogen atoms of the molecule are enhanced under the 'fictitious' action of the MO described with only *s*-type states.

To clarify this argument even more we proceed with the calculation of the nonlocal and cross term using *Model A* but now closing the nonlocal channels related to the hydrogen atoms located at $\mathbf{R}_1$ and $\mathbf{R}_4$. Thus, we define a new nonlocal term as $b_{NL+Cross(C-C)}(\mathbf{p},t) = b_{1,23}(\mathbf{p},t) + b_{1,32}(\mathbf{p},t)$. In Fig. 41 we plot the results; Fig. 41(a) is the same as Fig. 40(c) but in a new amplitude range and in Fig. 41(b) we present the local term (dotted green line), the new nonlocal term (magenta line), $|b_{NL+Cross(C-C)}(\mathbf{p},t)|^2$ and the coherent addition of this two contributions $|b_{Local}(\mathbf{p},t) + b_{NL+Cross(C-C)}(\mathbf{p},t)|^2$. The contribution of the hydrogen atoms to the total local term is low in comparison to contribution of the carbon ones. For this reason and for a better comparison we decided to plot the full local contribution of all the atoms instead of $|b_{Loca(C-C)}(\mathbf{p},t)|^2$.

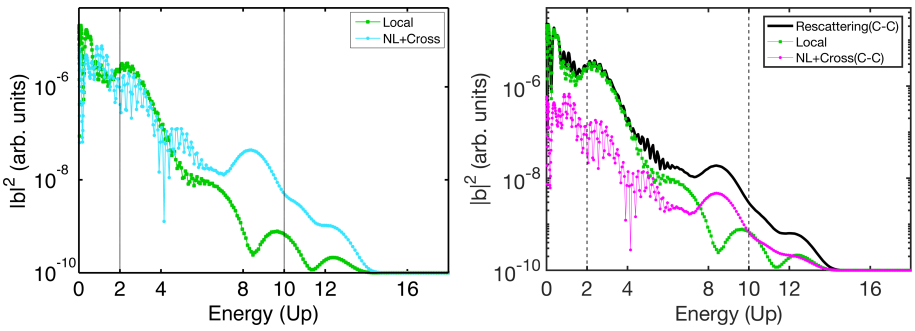

Figure 41: Local and nonlocal and cross contributions to the ATI spectra (in logarithmic scale) of acetylene molecule using *Model A*. (a) All the atoms contribution are considered on the total nonlocal and cross term; (b) only the contributions related to the carbon atoms on the total nonlocal and cross term are considered.

If we compare the result displayed in Fig. 40(b) with the one obtained with the model *Model B* we can find more similarities between the two models. In Fig. 40(b) we can see that the term

$|b_{NL+Cross(C-C)}(\mathbf{p}, t)|^2$ (magenta line) is about one order of magnitude lower than the local $|b_{Local}(\mathbf{p}, t)|^2$.

3.4 CONCLUSIONS AND OUTLOOK

We present a quasiclassical model, MSFA, for complex molecules with more than three centers. Our semi-analytical approach is a natural extension and generalization of the atomic and molecular model previously presented. This model go toward molecular HHG and ATI within the SAE.

We have applied the MSFA model to study the HHG and ATI spectra for different molecules of three and four centers: CO_2, CS_2, H_2O and C_2H_2.

First we calculated the total HHG spectra for both the carbon dioxide and water molecules. For the former we investigate the contribution of the different recombination processes to the total spectra. The HHG spectra showed that the cross processes are dominant over the local ones.

The split over the different cross contributions reveals that the most probably processes occur within the closest sites. In particular processes corresponding to different types of electronic trajectories where the electron tunnels and recombines in different atomic species. In the case of CO_2 there are two kind of cross processes: oxygen-carbon/carbon-oxygen and oxygen-oxygen. We show that the most frequent is the first one. In the case of the local processes, the contribution of the external atoms is lower; for CO_2 its mean the oxygen atoms.

Next, analyzing the molecular HHG spectra, we show the dependency of the cutoff energy on the molecular alignment. In the case of CO_2 we observe a dramatic decrease of the cutoff energy when the molecule is aligned parallel to the laser field polarization. This cutoff energy also depends on the molecular geometry. For example, in the CO_2 (linear) molecule the most favorable orientation is $\theta = 90°$ whereas for the water molecule it is the parallel one ($\theta = 0°$).

In the ATI section we use the *Model A* and *Model B* to understand how the p-type orbitals influence the rescattering picture. We calculate the ATI spectra using both models and, similarly to the diatomic case, we confirm that the shape of the molecular orbital imprints noticeable differences in the ATI spectra. The analysis of the 2D spectra reveals that the CS_2 molecule is more sensitive to the molecular orientation than the CO_2.

Finally, we applied our MSFA model to a 4-center molecule. We calculate both the HHG and ATI spectra for the acetylene system considering the two approaches: *Model A* and *Model B*. The comparison of the HHG spectra obtained with each of the models show the same trend: the well known HHG plateau that ends with an abrupt cutoff. There are, however, noticeable discrepancies, namely a clear

difference both in the HHG yield and the structure of the low-order harmonics region. For the ATI calculation we split the total and rescattering contributions, showing that they contribute in a similar way to different energy regions of the spectra.

Our model provides a simple framework for both the HHG and ATI understanding, which is in agreement with the available experimental observations and whose predictions are borne out by numerical calculations. The extension to more complex systems, with more than four centers, appears perfectible feasible.

Part II

CONCLUSIONS

4

GENERAL CONCLUSIONS AND OUTLOOK

To summarize, in this thesis we have presented a simple and analytical model to describe both the HHG and ATI processes in atoms and molecules. These phenomena configure the cornerstone in strong field physics. Our model follows a systematic pathway: we start from single center (atoms) systems and we extend it to multicenter ones. It is based on the analytical solution of the time-dependent Schrödinger equation by means of considering the bound and scattering states. These states are a composition of two parts depending on the relative position of the atoms inside of the molecule, within the framework of both the SFA and SAE approximations. Further, a systematic and analytical way of computing both the bound-free dipole, with respect to each center, and the rescattering transition matrix elements is developed. Additionally, we incorporate a more accurate description of the molecular ground state, employing information extracted from quantum chemistry software packages. This step forward allows us to include, in a detailed way, both the molecular symmetries and nodes present in the high-occupied molecular orbital. We are able then to, on the one hand, keep our formulation as analytical as in the case of simple molecules (diatomics), and, on the other hand, to still give a complete description of the underlying physics behind both the ATI and HHG processes.

The main advantages of our theoretical model, with respect to others used before, are:

(i) It gives solutions free of any artificial and nonphysical effects. In fact, a correct asymptotic behavior for $\mathbf{R} \to \infty$ and yet to $\mathbf{R} \to 0$ is obtained.

(ii) The time dependent dipole and the rescattering transition amplitude is written as a sum of components, obtained from equations which describe each recombination and rescattering processes, independently.

(iii) It is possible to disentangle the underlying contributions to the HHG and ATI spectra. In this way, we could isolate *direct* and *rescattering/recombination* processes and also treat both fixed and randomly oriented molecules.

(iv) We obtain explicitly different types of electronic trajectories: namely, *local* processes generated by tunneling and recombination of the active electron at the same site and *Nlocal+Cross* processes generated by tunneling followed by recombination at a different site.

(v) The low computational cost. By considering our approach involves only 1D and 2D time integrations, all the other quantities being analytical, it is clear that we compute molecular HHG/ATI spectra without too much computational effort.

(vi) The concrete feasibility to model more complex molecular ground states. For all the studied molecular cases we were able to model reasonably well the initial molecular ground state, both varying the parameters of our nonlocal SR potential and when modeled as a linear combination of molecular orbitals. With the latter we have set the foundations to model and tackle more complex systems, given the easy way to generate the HOMO, starting from the positions of the atoms in the molecule.

First, we have shown that our approach is able to capture the interference features, ubiquitously present in every molecular ATI and HHG processes. As is well known, both the molecular HHG and ATI spectra, as well as their dependence on the internuclear distance or the molecular orientation, contain interference patterns. These features result due to interference of the electronic wave emitted from the different atomic centers. These interference patterns can be correctly predicted by a simple two-slit interference formula and our model is able to reasonable follow it.

Second, we have studied how the ATI and HHG spectra can be maximized by using configurations that take fully advantage of a constructive interference. This will be achieved by choosing appropriate molecules and applying alignment techniques. Furthermore, information about the molecular structure can be obtained from both the HHG and ATI spectra. Hence, these observables may serve as a probe of nuclear dynamics.

As was already described, the core of our model are the saddle-point approximation and the linear combination of atomic orbitals. One of the main advantages of our approach is the possibility to disentangle, in an easy and direct way, the different contributions to the total ATI. This is particularly important for complex systems, where there exists a large amount of direct and rescattering 'scenarios' that otherwise would be impossible to extricate.

Next, we establish a comparison using two different ground states, one that uses a nonlocal SR potential, *Model A*, and the other based on the LCAO, *Model B*. Meanwhile both models allow us to formulate both the HHG and ATI in a semi-analytical way, the latter (*Model B*) gives a more accurate description of the MO. Nevertheless, we proved that, even when the former (*Model A*) predicts an overestimation of the direct processes, the shape and the spectra features are well reproduced. Additionally, *Model B* appears to be the adequate platform to investigate much more complex systems.

The focus of our study is on molecular systems, although the extension to more complex systems appears to be straightforward. For instance, the modeling of the DNA basis, formed by around a dozen of atoms, seems to be perfectly feasible. This will be object of future investigations.

One step beyond is to apply a strong laser field to a solid sample. Analogous to the three-step model in atoms, the HHG in a crystal solid via interband transitions can be described as follows: (i) electron (hole) tunneling excitation from the valence band to the conduction one, (ii) electron (hole) acceleration in the conduction (valence) band, and (iii) electron-hole recombination, resulting in an emission of a high harmonic that is a multiple of the frequency of the driving laser.

In this thesis, of course, we have only just begun to explore the capabilities of our MSFA model. Much of our work has focused on the scenario of an atom and a molecule ionized by a linearly polarized pulse. Not addressed in this work is the question about the role played by excited molecular electronic states and multielectron effects in the HHG and ATI spectra. Nevertheless, we are confident that our work will pave the way toward fascinating studies of structural information and charge migrations in the fragmentation processes in large molecules and other complex solid targets.

Part III

APPENDIX

5

REGULARIZATION AND TREATMENT OF SINGULARITIES

In many equations of this Thesis there appear expressions which involve an infinitesimal small ϵ, which can be viewed as a regularization parameter needed to avoid singularities, and even sometimes nonintegrable singularities. Quite generally, we treat all these terms in the sense of distribution theory, where the fundamental formula reads

$$\frac{1}{x_1 - x_0 - i\epsilon} = i\pi\,\delta(x_1 - x_0) + \mathcal{P}\frac{1}{x_1 - x_0}, \tag{211}$$

$\mathcal{P}$ being the (Cauchy's) *principal value* distribution. This is a clear example of an integrable singularity, since for any regular function $\phi(.)$, decaying sufficiently fast (formally for any infinitely differentiable probe function of finite support [5]), $\mathcal{P}$ is defined as

$$\begin{aligned}&\int_{-\infty}^{+\infty} \mathcal{P}\frac{1}{x_1 - x_0}\phi(x_0)\,dx_0 \\ &= \lim_{\epsilon\to 0}\left[\int_{-\infty}^{-\epsilon} + \int_{\epsilon}^{+\infty}\right]\frac{1}{x_1 - x_0}\phi(x_0)\,dx_0.\end{aligned} \tag{212}$$

In the following we concentrate on more complex cases, where we deal with the expressions of the form $1/(x_1 - x_0 - i\epsilon)^\alpha$, with $\alpha > 0$.

5.1 TREATMENT OF QUANTUM DIFFUSION

The singularity of the form $1/(t - t' - i\epsilon)^\alpha$, with $\alpha = d/2$,(d being the number of spatial dimensions), appears typically when we deal with the quantum diffusion (quantum ballistic expansion) of a free particle. A generic integral to calculate it has a form

$$I = \lim_{\epsilon\to 0}\int d^d\mathbf{p}\exp[-ip^2(t - t' - i\epsilon)]\phi(\mathbf{p}), \tag{213}$$

where $\phi(\mathbf{p})$ is a slowly varying function of $\mathbf{p}$. Such integrals, when are evaluated by means of the Laplace's saddle-point (steepest descent) method, give:

$$I \simeq \lim_{\epsilon\to 0}\left[\frac{2\pi}{i(t - t' - i\epsilon)}\right]^{d/2}\phi(\mathbf{0}). \tag{214}$$

In 1D the singularity is very weak and integrable with respect to, say, t'. Still, in numerical calculations it may cause problems and thus it makes sense to regularize it. In 2D the singularity is integrable in the sense of the Eq. (212), but numerically this once again causes

usually serious problems. Finally, in 3D and higher dimensions the singularity seems to be even nonintegrable. The remedy to this problem lies in appropriate corrections to the saddle-point approximation. This approach has already been discussed in detail in Ref. [1]. Typically, the function $\phi(\mathbf{p})$ is localized in the momentum space on some scale, let us say $1/\nu$. We can thus write:

$$\phi(\mathbf{p}) = \exp[-p^2/2\nu^2]\psi(\mathbf{p}),$$

defining in this way the Gaussian prefactor in the saddle-point calculation, so that:

$$\begin{aligned} I &\simeq \lim_{\epsilon\to 0}\left[\frac{2\pi}{i(t-t'-i\epsilon-i/\nu^2)}\right]^{d/2}\psi(\mathbf{o}) \\ &= \left[\frac{2\pi}{i(t-t'-i\epsilon')}\right]^{d/2}\psi(\mathbf{o}), \end{aligned} \tag{215}$$

where $\epsilon' = 1/\nu^2$. As we see, the singularity has vanished, or, better to say, has been smoothed on the characteristic momentum (time) scale ν ($1/\nu^2$). The wave packets that appear in our calculations have at least the size of the ground state, where the kinetic energy is of order of I_p; therefore, we can expect that $\nu^2/2 \simeq I_p$. Setting thus, let us say $\epsilon' = 0.1 \sim 0.2 \times 1/I_p$, we introduce maybe some errors of the order of 10%-20%, but it allows us to forget about the singularity. This is the strategy we adopt in the numerics.

5.2 TREATMENT OF RESCATTERING TERMS

Singularities appear also in the rescattering terms at the "energy conservation shell". Typically, we have to deal with two kinds of integrals. The firs kind can be written, in 3D, as

$$I_1(p_1^2) = \lim_{\epsilon\to 0}\int d^3\mathbf{p}_0 \frac{1}{p_1^2 - p_0^2 - i\epsilon}\phi(\mathbf{p}_0), \tag{216}$$

which is integrable in the sense of Eq. (212), but numerically may cause severe problems. The second kind seems to be even more serious,

$$I_2(p_1^2) = \lim_{\epsilon\to 0}\int d^3\mathbf{p}_0 \frac{1}{(p_1^2 - p_0^2 - i\epsilon)^2}\phi(\mathbf{p}_0), \tag{217}$$

since they do not seem to be integrable. Still, we observe that the above integrals, before taking the $\epsilon \to 0$ limit, should be understood as

$$I_2(p_1^2) = -\frac{\partial I_1(p_1^2)}{\partial p_1^2}, \tag{218}$$

so that if we learn how to regularize integrals of the form I_1, we shall get automatically prescription about how to deal with I_2.

The trick we propose and use throughout this Thesis is analogous to the one used in the analysis of the quantum diffusion above described. It is assumed that the function $\phi(\mathbf{p}_0)$ is localized on a certain scale; for simplicity, we take as example

$$\phi(\mathbf{p}_0) = \frac{1}{(p^2 + 2\nu^2)^2}\psi(p_0^2), \tag{219}$$

where $\psi(p_0^2)$ is slowly varying, so that we can replace its argument by a typical value, $\psi(p_0^2) \simeq \psi(\langle p_0^2 \rangle)$. This particular form is motivated by the momentum representation of the hydrogenlike ground-state wave function (cf. Ref. [1]). As a consequence we can write

$$\begin{aligned} I_1(p_1^2) &= i \lim_{\epsilon \to 0} \int d^3\mathbf{p}_0 \frac{1}{(p_1^2 - p_0^2 - i\epsilon)(p_0^2 + 2\nu^2)^2} \\ &\propto \lim_{\epsilon \to 0} \frac{p_1^2 - i\epsilon}{(p_1^2 + 2\nu^2 - i\epsilon)^2}. \end{aligned} \tag{220}$$

Of course, setting the value of ϵ to, let us say, $0.2 \times 2\nu^2$ will change the values of the integral, but not very significantly, keeping the qualitative character of the result essentially intact. The above analysis can be easily extended to the case when the integral includes trigonometric functions, such as $\sin(pA)$, $\cos(pA)$, or even Gaussian factors of the form $\exp[(-it - \mu)p_0^2/2]$ (which have then to be treated via a Fourier representation), etc. Note that going from I_1 to I_2 does not pose much problem; in the example above,

$$I_2(p_1^2) = -\frac{\partial I_1(p_1^2)}{\partial p_1^2} \propto \frac{1}{(p_1^2 + 2\nu^2)^3}. \tag{221}$$

6

SINGULARITIES IN THE SCATTERING THEORY

6.1 SINGULARITIES IN THE SCATTERING THEORY

One should note that the nonintegrable singularity at the "energy shell" is intrinsic in the scattering theory, where the scattering wave functions generically have an asymptotic (low momentum, large distance) form,

$$\Psi_{\mathbf{p}_0}(\mathbf{p}) = \delta(\mathbf{p}-\mathbf{p}_0) + \frac{\tilde{f}(\mathbf{p}_0)}{(p_0^2 - p^2 + i\epsilon)}, \tag{222}$$

or, in the position representation,

$$\Psi_{\mathbf{p}_0}(\mathbf{r}) = \exp(-i\mathbf{r}\cdot\mathbf{p}_0) + \frac{f(\mathbf{p}_0)\exp(-ip_0 r)}{p_0 r}. \tag{223}$$

We consider for simplicity scattering on a rotationally symmetric, i.e., a SR, potential. In Eq. (223) the coefficient $f(\mathbf{p}_0)$ is related to the scattering amplitude [6]. It is obvious that the matrix element $\mathbf{g}(\mathbf{p}_1, \mathbf{p}_2)$ has the same structural form as the one in Eq. (222), and exhibits, therefore, a nonintegrable singularity.

Note, however, that the relevant quantity is $\mathbf{E}(t)\cdot\mathbf{g}(\mathbf{p}_1, \mathbf{p}_2)$, or more precisely $\mathbf{E}(t)\cdot\langle\mathbf{p}_1|\mathbf{r}|\mathbf{p}_2\rangle$. Since the laser electric field $\mathbf{E}(t)$ is always focused on a finite region of transverse size (beam waist w_0) with dimensions of the order of the laser wavelength, and longitudinal size corresponding to confocal parameter $\tilde{b}$, the relevant matrix element for the problem thereby is

$$\mathbf{E}(t)\cdot\langle\mathbf{p}_1|\mathbf{r}\, w(\mathbf{r})|\mathbf{p}_2\rangle, \tag{224}$$

where $w(\mathbf{r})$ describes the laser beam shape. For Gaussian beams, and close to the focus, we can approximate $w(\mathbf{r}) \simeq \exp[-(x^2+y^2)/2w_0^2 - z^2/2\tilde{b}^2]$. It is clear that such finite size localization (spreading) in space implies a corresponding spreading (localization) in momentum space. The uncertainty of energy conservation is thus related to the typical kinetic energy associated with this localization. In 1D, for example, back-of-the-envelope estimate gives that the matrix element $\langle p_1|x\exp(-x^2/2w_0^2)|p_2\rangle$ has two contributions peaked at $\exp[-w_0^2(p_1 - p_2)^2/2]$ and $\exp[-w_0^2(p_1+p_2)^2/2]$. For the case of a broader focus the effect is obviously very small, but it proves that the singularity in Eq. (65) should be regarded as apparent, rather than real. If $w_0 = \lambda_0$, this corresponds to energies of the order of 0.05 a.u., or $0.1\cdot I_p$, not so far from the values used by us in our numerical calculations.

7

MSFA: THREE-CENTER MOLECULES

In this Appendix we find the explicit equations to calculate the ground and scattering states for the specific case of a three-center molecule. A sketch of the molecular system is shown in the Fig. 42. These equations are then used to obtain the transition matrix elements and finally to get the results presented in chapter 3.

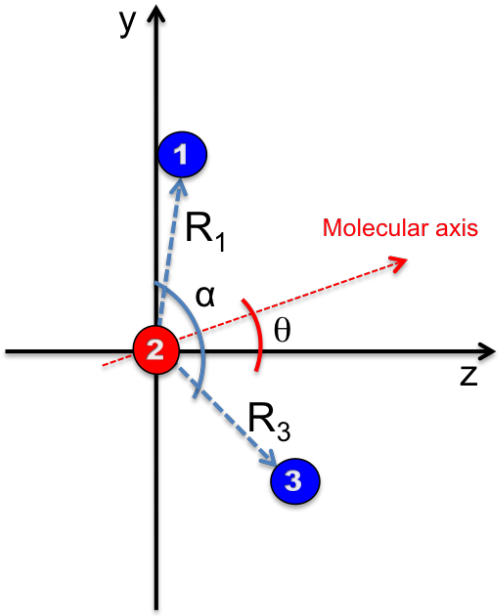

Figure 42: Three-center molecular system aligned a θ angle with respect to the laser electric field polarization. The red line represents the molecular axis that forms an angle of $\alpha/2$ between $\mathbf{R}_1 = [0, \frac{R}{2}\sin(\frac{\alpha}{2}+\theta), \frac{R}{2}\cos(\frac{\alpha}{2}+\theta)]$, $\mathbf{R}_2 = [0,0,0]$ and $\mathbf{R}_3 = [0, -\frac{R}{2}\sin(\frac{\alpha}{2}-\theta), \frac{R}{2}\cos(\frac{\alpha}{2}-\theta)]$.

7.1 GROUND STATE AND BOUND-CONTINUUM DIPOLE MATRIX ELEMENTS

Using the equations defined in Chapter 3 and setting $n = 3$ the ground state is defined as,

$$\Psi_0(\mathbf{p}) = \gamma' \sum_{j=1}^{3} \frac{\breve{\varphi}_j \, e^{-i\mathbf{R}_j\cdot\mathbf{p}}}{\sqrt{(p^2+\Gamma^2)}(\frac{p^2}{2}+I_p)}, \tag{225}$$

where the eigenvalues problem to solve is similar to the one defined in Eq. (192). The magnitudes in the eigenvalues problems are the integrals defined in Chapter 3, Eq. (191). These integrals depend explicitly

on the internuclear distance and $\mathbf{R}_1$, $\mathbf{R}_2$ or $\mathbf{R}_3$. If we look at those integrals is possible to detect some symmetries in the eigenvalue problem. For instance, we note that $I_{11} = I_{22} = I_{33}$ [these integrals have the same dependency as the one solved in the atomic Chapter (refch:01 in Eq. (121)]. In the same way we have that $I_{12} = I_{21} = I_{23} = I_{32}$ and $I_{13} = I_{31}$. So, it is possible to write the eigenvalue problem as,

$$\begin{pmatrix} \breve{\varphi}_1 \\ \breve{\varphi}_2 \\ \breve{\varphi}_3 \end{pmatrix} = \begin{pmatrix} I_{11} & I_{12} & I_{13} \\ I_{12} & I_{11} & I_{12} \\ I_{13} & I_{12} & I_{11} \end{pmatrix} \times \begin{pmatrix} \breve{\varphi}_1 \\ \breve{\varphi}_2 \\ \breve{\varphi}_3 \end{pmatrix}, \tag{226}$$

from where we have that,

$$I_{13} = \frac{(1 - I_{11})^2 - 2\, I_{12}^2}{1 - I_{11}}\,; \quad 1 - I_{11} \neq 0, \tag{227}$$

and

$$\breve{\varphi}_1 = \breve{\varphi}_3 = \frac{I_{12}}{1 - I_{11} - I_{13}}\, \breve{\varphi}_2, \tag{228}$$

where I_{11}, I_{12}, I_{13} can be solved in spherical coordinates as

$$I_{11} = \frac{4\pi^2 \gamma'}{\Gamma + \sqrt{2I_p}}, \tag{229}$$

$$I_{12} = \frac{8\pi^2 \gamma'}{R} \left\{ \frac{e^{-\frac{R\Gamma}{2}} - e^{-\frac{R\sqrt{2I_p}}{2}}}{2I_p - \Gamma^2} \right\}, \tag{230}$$

and

$$I_{13} = \frac{4\pi^2 \gamma'}{R \sin(\alpha/2)} \left\{ \frac{e^{-R\sin(\alpha/2)\Gamma} - e^{-R\sin(\alpha/2)\sqrt{2I_p}}}{2I_p - \Gamma^2} \right\}. \tag{231}$$

Finally, Eq. (225) reads as

$$\begin{aligned} \Psi_0(\mathbf{p}) = \frac{\mathcal{M}}{\sqrt{(p^2 + \Gamma^2)(\frac{p^2}{2} + I_p)}} \Bigg[\left(\frac{I_{12}}{1 - I_{11} - I_{13}} \right) e^{-i\mathbf{R}_1 \cdot \mathbf{p}} \\ + e^{-i\mathbf{R}_2 \cdot \mathbf{p}} + \left(\frac{I_{12}}{1 - I_{11} - I_{13}} \right) e^{-i\mathbf{R}_3 \cdot \mathbf{p}} \Bigg], \end{aligned} \tag{232}$$

where $\mathcal{M} = \gamma' \breve{\varphi}_1 = \frac{\gamma}{3} \breve{\varphi}_1$ is a normalization constant. It can be calculated using the usual normalization condition $\int d^3\mathbf{p}\, \Psi_0(\mathbf{p})^* \Psi_0(\mathbf{p}) = 1$, so,

$$\begin{aligned} 1 \;=\; \mathcal{M}^2 \int \frac{d^3\mathbf{p}}{(p^2 + \Gamma^2)(\frac{p^2}{2} + I_p)^2} \Bigg[\left(\frac{I_{12}}{1 - I_{11} - I_{13}} \right) e^{-i\mathbf{R}_1 \cdot \mathbf{p}} \\ + e^{-i\mathbf{R}_2 \cdot \mathbf{p}} + \left(\frac{I_{12}}{1 - I_{11} - I_{13}} \right) e^{-i\mathbf{R}_3 \cdot \mathbf{p}} \Bigg]^2. \end{aligned} \tag{233}$$

From the above equation we can define the normalization constant as,

$$\mathcal{M} = [1/I_{3N}]^{1/2}, \tag{234}$$

with I_{3N} defined as

$$\begin{aligned} I_{3N} &= \Big(\frac{I_{12}}{1-I_{11}-I_{13}}\Big)^2 \left\{I_{2R_1} + I_{2R_3} + 2I_{R_1+R_3}\right\} \\ &\quad + \frac{2\,I_{12}}{1-I_{11}-I_{13}} \left\{I_{R_1} + I_{R_3}\right\} + I_{1N}, \end{aligned} \tag{235}$$

where

$$\begin{aligned} I_{2R_1} &= \int_0^{2\pi} d\theta \int_0^{\infty} \frac{dp\, p^2}{(p^2+\Gamma^2)(\frac{p^2}{2}+I_p)^2} \int_0^{\pi} d\varphi\, \sin\varphi\, e^{-i\,2|R_1|\,p\cos\varphi} \\ &= \frac{4(2\pi^2)}{(2I_p-\Gamma^2)^2}\left\{\frac{e^{-2|R_1|\Gamma}}{2|R_1|} - \frac{e^{-2|R_1|\sqrt{2I_p}}}{2|R_1|} - \frac{e^{-2|R_1|\sqrt{2I_p}}(2I_p-\Gamma^2)}{2\sqrt{2I_p}}\right\}, \end{aligned} \tag{236}$$

$$\begin{aligned} I_{2R_3} &= \int_0^{2\pi} d\theta \int_0^{\infty} \frac{dp\, p^2}{(p^2+\Gamma^2)(\frac{p^2}{2}+I_p)^2} \int_0^{\pi} d\varphi\, \sin\varphi\, e^{-i\,2|R_3|\,p\cos\varphi} \\ &= \frac{4(2\pi^2)}{(2I_p-\Gamma^2)^2}\left\{\frac{e^{-1|R_3|\Gamma}}{2|R_3|} - \frac{e^{-1|R_3|\sqrt{2I_p}}}{2|R_3|} - \frac{e^{-2|R_3|\sqrt{2I_p}}(2I_p-\Gamma^2)}{2\sqrt{2I_p}}\right\}, \end{aligned} \tag{237}$$

and

$$\begin{aligned} I_{R_1+R_3} &= \int_0^{2\pi} d\theta \int_0^{\infty} \frac{dp\, p^2}{(p^2+\Gamma^2)(\frac{p^2}{2}+I_p)^2} \int_0^{\pi} d\varphi\, \sin\varphi\, e^{-i\,2|R_1+R_3|\,p\cos\varphi} \\ &= \frac{4(2\pi^2)}{(2I_p-\Gamma^2)^2}\left\{\frac{e^{-|R_1+R_3|\Gamma}}{|R_1+R_3|} - \frac{e^{-|R_1+R_3|\sqrt{2I_p}}}{|R_1+R_3|} - \frac{e^{-|R_1+R_3|\sqrt{2I_p}}(2I_p-\Gamma^2)}{2\sqrt{2I_p}}\right\}. \end{aligned} \tag{238}$$

Finally the normalization constant read as,

$$\begin{aligned} I_{3N} &= \Big(\frac{2\,I_{12}}{1-I_{11}-I_{13}}\Big)^2 \left\{\frac{4\pi^2}{R(2I_p-\Gamma^2)^2}\left[e^{-R\Gamma} - e^{-R\sqrt{2I_p}}\left(1\right.\right.\right. \\ &\quad \left.\left.\left. + \frac{R(2I_p-\Gamma^2)}{2\sqrt{2I_p}}\right)\right] + \frac{4\pi^2}{R\cos(\frac{\alpha}{2})(2I_p-\Gamma^2)^2}\left[e^{-R\cos(\frac{\alpha}{2})\Gamma}\right. \\ &\quad \left. - e^{-R\cos(\frac{\alpha}{2})\sqrt{2I_p}}\left(1 + \frac{R\cos(\frac{\alpha}{2})(2I_p-\Gamma^2)}{2\sqrt{2I_p}}\right)\right]\right\} \\ &\quad + \frac{8\,I_{12}}{1-I_{11}-I_{13}} \times \frac{4\pi^2}{\frac{R}{2}(2I_p-\Gamma^2)^2} \times \left[e^{-\frac{R}{2}\Gamma}\right. \\ &\quad \left. - e^{-\frac{R}{2}\sqrt{2I_p}}\left(1 + \frac{\frac{R}{2}(2I_p-\Gamma^2)}{2\sqrt{2I_p}}\right)\right] + \frac{4\pi^2(\sqrt{2I_p}-\Gamma)^2}{\sqrt{2I_p}(2I_p-\Gamma^2)^2}. \end{aligned} \tag{239}$$

With the exact knowledge of $\mathcal{M}$ we have now defined the ground state in our three-center molecular system [Eq. (232)]. Notice that the dependency of the system energy with the internuclear distance appears in the relation defined in Eq. (227).

7.1.1 *Bound-continuum matrix element*

The total bound-free matrix element for the three-center molecular system is defined as a sum:

$$\mathbf{d}(\mathbf{p}_0) = \sum_{j=1}^{3} \Big\{ -i\nabla_{\mathbf{p}} \Psi_{0,j}(\mathbf{p})\big|_{\mathbf{p}_0} + \mathbf{R}_j \Psi_{0,j}(\mathbf{p}_0) \Big\}, \tag{240}$$

where

$$\mathbf{d}(\mathbf{p}_0) \quad = \quad -2i\,\mathcal{M}\mathcal{A}(\mathbf{p}_0) \left[\frac{I_{12}}{1 - I_{11} - I_{13}} \left(e^{-i\mathbf{R}_1\cdot\mathbf{p}_0} + e^{-i\mathbf{R}_3\cdot\mathbf{p}_0} \right) + 1 \right]. \tag{241}$$

Finally notice that we could extract the contributions of each center from Eq. (241), i.e. ,

$$\mathbf{d}_1(\mathbf{p}_0) = -i\,\mathcal{M}\mathcal{A}(\mathbf{p}_0) \left(\frac{I_{12}}{1 - I_{11} - I_{13}} \right) e^{-i\mathbf{R}_1\cdot\mathbf{p}_0}, \tag{242}$$

$$\mathbf{d}_2(\mathbf{p}_0) = -i\,\mathcal{M}\mathcal{A}(\mathbf{p}_0), \tag{243}$$

and

$$\mathbf{d}_3(\mathbf{p}_0) = -i\,\mathcal{M}\mathcal{A}(\mathbf{p}_0) \left(\frac{I_{12}}{1 - I_{11} - I_{13}} \right) e^{-i\mathbf{R}_3\cdot\mathbf{p}_0}, \tag{244}$$

where $\mathcal{A}(\mathbf{p}_0)$ is the quantity defined in Sec. 1.3.1, Eq. (53).

7.2 SCATTERING WAVES AND CONTINUUM-CONTINUUM TRANSITION MATRIX ELEMENTS

To get the scattering states for this system, similarly to the ground state, we are going to use the Eq. (208),

$$\Psi_{\mathbf{p}_0}(\mathbf{p}) = \delta(\mathbf{p} - \mathbf{p}_0) - \frac{2\gamma' U(\mathbf{p})}{(p_0^2 - p^2 + i\epsilon)} \sum_{j=1}^{3} e^{-i\mathbf{R}_j\cdot\mathbf{p}} \left[U(\mathbf{p}_0) e^{i\mathbf{R}_j\cdot\mathbf{p}_0} + \breve{\varphi}'_j \right]. \tag{245}$$

From here we have an eigenvalues problem for the scattering states that maintains the same symmetries as before and looks like,

$$\begin{pmatrix} \breve{\varphi}'_1 \\ \breve{\varphi}'_2 \\ \breve{\varphi}'_3 \end{pmatrix} = \begin{pmatrix} I'_{11} & I'_{12} & I'_{13} & \sum_{j'}^{3} K_{1j'} \\ I'_{12} & I'_{11} & I'_{12} & \sum_{j'}^{3} K_{2j'} \\ I'_{13} & I'_{12} & I'_{11} & \sum_{j'}^{3} K_{3j'} \end{pmatrix} \times \begin{pmatrix} \breve{\varphi}'_1 \\ \breve{\varphi}'_2 \\ \breve{\varphi}'_3 \\ 1 \end{pmatrix}. \tag{246}$$

In this case the quantities I'_{11}, I'_{12}, $K_{3j'}$ and so on are the integrals defined in Eqs. (206) and (205) of Chapter 3. The solution of that problem leads,

$$\begin{aligned}
\breve{\varphi}'_1 &= \sum_{j'}^{3} \frac{K_{1j'}(1-I'_{11})^2 + K_{2j'}(1-I'_{11})I'_{12} + K_{3j'}(1-I'_{11})I'_{13}}{[(1-I'_{11})-I'_{13}][(1-I'_{11})^2+(1-I'_{11})I'_{13}-2{I'_{12}}^2]} \\
&\quad + \frac{-K_{1j'}{I'_{12}}^2 + K_{3j'}{I'_{12}}^2 + K_{2j'}I'_{12}I'_{13}}{[(1-I'_{11})-I'_{13}][(1-I'_{11})^2+(1-I'_{11})I'_{13}-2{I'_{12}}^2]}, \\
\breve{\varphi}'_2 &= \sum_{j'}^{3} \frac{K_{2j'}(1-I'_{11}) + K_{1j'}I'_{12} + K_{3j'}I'_{12} - K_{2j'}I'_{13}}{(1-I'_{11})^2+(1-I'_{11})I'_{13}-2{I'_{12}}^2}, \\
\breve{\varphi}'_3 &= \sum_{j'}^{3} \frac{K_{3j'}(1-I'_{11})^2 + K_{2j'}(1-I'_{11})I'_{12} + K_{1j'}(1-I'_{11})I'_{13}}{[(1-I'_{11})-I'_{13}][(1-I'_{11})^2+(1-I'_{11})I'_{13}-2{I'_{12}}^2]} \\
&\quad + \frac{K_{1j'}{I'_{12}}^2 + K_{3j'}{I'_{12}}^2 + K_{2j'}I'_{12}I'_{13}}{[(1-I'_{11})-I'_{13}][(1-I'_{11})^2+(1-I'_{11})I'_{13}-2{I'_{12}}^2]}.
\end{aligned} \tag{247}$$

The solution of I'_{11} is,

$$I'_{11} = \frac{-4\pi^2\,\gamma'}{\Gamma - i\sqrt{|p_0^2 + i\,\epsilon|}}. \tag{248}$$

Notice that the latter is the same integral defined in Eq. (145).

The others integrals are similar to the ones defined in the Sec. 2.4.1.3 but now referred to a three-center coordinates system, $I'_{12} \approx |\mathbf{R}_1 - \mathbf{R}_2|$ and $I'_{13} \approx |\mathbf{R}_1 - \mathbf{R}_3|$, i.e.

$$I'_{12} = \frac{-4\pi^2\,\gamma'}{\frac{R}{2}\,(p_0^2+\Gamma^2+i\epsilon)}\left[e^{i\frac{R}{2}\sqrt{p_0^2+i\epsilon}} - e^{-\frac{R}{2}\Gamma}\right], \tag{249}$$

and

$$I'_{13} = \frac{-4\pi^2\,\gamma'}{R\sin(\frac{\alpha}{2})\,(p_0^2+\Gamma^2+i\epsilon)}\left[e^{iR\sin(\frac{\alpha}{2})\sqrt{p_0^2+i\epsilon}} - e^{-R\sin(\frac{\alpha}{2})\Gamma}\right]. \tag{250}$$

Substituting the solutions of the scattering eigenvalues problem Eq. (247) into the scattering wave function and grouping the exponential factors we have,

$$\begin{aligned}
\delta\Psi_{\mathbf{p}_0,1}(\mathbf{p}) &= \frac{-\mathcal{D}_1(\mathbf{p}_0)\,e^{-i\mathbf{R}_1\cdot(\mathbf{p}-\mathbf{p}_0)}}{\sqrt{p^2+\Gamma^2}\,(p_0^2-p^2+i\epsilon)} - \frac{\mathcal{D}_3(\mathbf{p}_0)\,e^{-i\mathbf{R}_1\cdot\mathbf{p}+i\mathbf{R}_2\cdot\mathbf{p}_0}}{\sqrt{p^2+\Gamma^2}\,(p_0^2-p^2+i\epsilon)} \\
&\quad - \frac{\mathcal{D}_4(\mathbf{p}_0)\,e^{-i\mathbf{R}_1\cdot\mathbf{p}+i\mathbf{R}_3\cdot\mathbf{p}_0}}{\sqrt{p^2+\Gamma^2}\,(p_0^2-p^2+i\epsilon)},
\end{aligned} \tag{251}$$

$$\begin{aligned}
\delta\Psi_{\mathbf{p}_0,2}(\mathbf{p}) &= \frac{-\mathcal{D}_2(\mathbf{p}_0)\,e^{-i\mathbf{R}_2\cdot(\mathbf{p}-\mathbf{p}_0)}}{\sqrt{p^2+\Gamma^2}\,(p_0^2-p^2+i\epsilon)} - \frac{\mathcal{D}_5(\mathbf{p}_0)\,e^{-i\mathbf{R}_2\cdot\mathbf{p}+i\mathbf{R}_1\cdot\mathbf{p}_0}}{\sqrt{p^2+\Gamma^2}\,(p_0^2-p^2+i\epsilon)} \\
&\quad - \frac{\mathcal{D}_5(\mathbf{p}_0)\,e^{-i\mathbf{R}_2\cdot\mathbf{p}+i\mathbf{R}_3\cdot\mathbf{p}_0}}{\sqrt{p^2+\Gamma^2}\,(p_0^2-p^2+i\epsilon)},
\end{aligned} \tag{252}$$

and

$$\delta\Psi_{\mathbf{p}_0,3}(\mathbf{p}) = \frac{-\mathcal{D}_1(\mathbf{p}_0)\, e^{-i\mathbf{R}_3\cdot(\mathbf{p}-\mathbf{p}_0)}}{\sqrt{p^2+\Gamma^2}\,(p_0^2-p^2+i\epsilon)} - \frac{\mathcal{D}_3(\mathbf{p}_0)\, e^{-i\mathbf{R}_3\cdot\mathbf{p}+i\mathbf{R}_2\cdot\mathbf{p}_0}}{\sqrt{p^2+\Gamma^2}\,(p_0^2-p^2+i\epsilon)} - \frac{\mathcal{D}_4(\mathbf{p}_0)\, e^{-i\mathbf{R}_3\cdot\mathbf{p}+i\mathbf{R}_1\cdot\mathbf{p}_0}}{\sqrt{p^2+\Gamma^2}\,(p_0^2-p^2+i\epsilon)}. \tag{253}$$

Notice that we can write the total scattering wavefunction as a composition of the three contributions presented before, one from each atom located at $\mathbf{R}_1$, $\mathbf{R}_2$ and $\mathbf{R}_3$, respectively, as:

$$\Psi_{\mathbf{p}_0}(\mathbf{p}) = \delta(\mathbf{p}-\mathbf{p}_0) + \delta\Psi_{\mathbf{p}_0,1}(\mathbf{p}) + \delta\Psi_{\mathbf{p}_0,2}(\mathbf{p}) + \delta\Psi_{\mathbf{p}_0,3}(\mathbf{p}). \tag{254}$$

Now the constants are defined as,

$$\begin{aligned}
\mathcal{D}_1(\mathbf{p}_0) &= \frac{2\gamma'}{\sqrt{p_0^2+\Gamma^2}}\left(\frac{1+2I'_{11}+{I'_{11}}^2-{I'_{12}}^2}{(1+I'_{11}-I'_{13})([1+I'_{11}]^2+(1+I'_{11})I'_{13}-2{I'_{12}}^2)}\right);\\
\mathcal{D}_2(\mathbf{p}_0) &= \frac{2\gamma'}{\sqrt{p_0^2+\Gamma^2}}\left(\frac{1+I'_{11}+I'_{13}}{1+2I'_{11}+{I'_{11}}^2+I'_{13}+I'_{11}I'_{13}-2{I'_{12}}^2}\right);\\
\mathcal{D}_3(\mathbf{p}_0) &= \frac{2\gamma'}{\sqrt{p_0^2+\Gamma^2}}\left(\frac{-I'_{12}-I'_{12}I'_{11}+I'_{12}I'_{13}}{(1+I'_{11}-I'_{13})([1+I'_{11}]^2+(1+I'_{11})I'_{13}-2{I'_{12}}^2)}\right);\\
\mathcal{D}_4(\mathbf{p}_0) &= \frac{2\gamma'}{\sqrt{p_0^2+\Gamma^2}}\left(\frac{{I'_{12}}^2-I'_{13}-I'_{11}I'_{13}}{(1+I'_{11}-I'_{13})([1+I'_{11}]^2+(1+I'_{11})I'_{13}-2{I'_{12}}^2)}\right);
\end{aligned} \tag{255}$$

and

$$\mathcal{D}_5(\mathbf{p}_0) = \frac{2\gamma'}{\sqrt{p_0^2+\Gamma^2}}\left(\frac{-I'_{12}}{1+2I'_{11}+{I'_{11}}^2+I'_{13}+I'_{11}I'_{13}-2{I'_{12}}^2}\right). \tag{256}$$

Equation (251) represents electrons that have the probability of scatter with the core placed at the left in $\mathbf{R}_1$. In the same way, Eq. (252) [Eq. (253)] represents electrons that scatter with the nucleus placed at the center on $\mathbf{R}_2 = 0$ [at the right in $\mathbf{R}_3$].

7.2.1 *Continuum-continuum transition matrix element*

The continuum-continuum transition matrix element is defined in Eq. (209). It can be written as:

$$\begin{aligned}
\mathbf{g}(\mathbf{p}_1,\mathbf{p}_2) = &\sum_{j=1}^{3}\left[i\nabla_{\mathbf{p}}\delta\Psi_{\mathbf{p}_2,j}(\mathbf{p})|_{\mathbf{p}_1} - \mathbf{R}_j\delta\Psi_{\mathbf{p}_2,j}(\mathbf{p})\right]\Big|_{\mathbf{p}_1}\\
&+\sum_{j=1}^{3}\left[i\nabla_{\mathbf{p}}\delta\Psi_{\mathbf{p}_1,j}(\mathbf{p}) - \mathbf{R}_j\delta\Psi_{\mathbf{p}_1,j}(\mathbf{p})\right]^*\Big|_{\mathbf{p}_2}.
\end{aligned} \tag{257}$$

Inserting the wavefunctions defined in Eqs. (251), (252) and (253) on the previous equation it is possible to define three main matrix rescattering elements as (one for each of the atoms),

$$\begin{aligned}\mathbf{g}_1(\mathbf{p}_1,\mathbf{p}_2) &= \mathbf{g}_{11}(\mathbf{p}_1,\mathbf{p}_2)+\mathbf{g}_{12}(\mathbf{p}_1,\mathbf{p}_2)+\mathbf{g}_{13}(\mathbf{p}_1,\mathbf{p}_2),\\ &= \mathcal{Q}_1(\mathbf{p}_1,\mathbf{p}_2)\,e^{-i\mathbf{R}_1\cdot(\mathbf{p}_1-\mathbf{p}_2)}+\mathcal{Q}_5(\mathbf{p}_1,\mathbf{p}_2)\,e^{-i\mathbf{R}_2\cdot\mathbf{p}_1+i\mathbf{R}_1\cdot\mathbf{p}_2}\\ &\quad+\mathcal{Q}_4(\mathbf{p}_1,\mathbf{p}_2)\,e^{-i\mathbf{R}_3\cdot\mathbf{p}_1+i\mathbf{R}_1\cdot\mathbf{p}_2},\end{aligned}\tag{258}$$

In the same way for the atom on the center we have,

$$\begin{aligned}\mathbf{g}_2(\mathbf{p}_1,\mathbf{p}_2) &= \mathbf{g}_{21}(\mathbf{p}_1,\mathbf{p}_2)+\mathbf{g}_{22}(\mathbf{p}_1,\mathbf{p}_2)+\mathbf{g}_{23}(\mathbf{p}_1,\mathbf{p}_2),\\ &= \mathcal{Q}_3(\mathbf{p}_1,\mathbf{p}_2)\,e^{-i\mathbf{R}_1\cdot\mathbf{p}_1+i\mathbf{R}_2\cdot\mathbf{p}_2}+\mathcal{Q}_2(\mathbf{p}_1,\mathbf{p}_2)\,e^{-i\mathbf{R}_2\cdot(\mathbf{p}_1-\mathbf{p}_2)}\\ &\quad+\mathcal{Q}_3(\mathbf{p}_1,\mathbf{p}_2)\,e^{-i\mathbf{R}_3\cdot\mathbf{p}_1+i\mathbf{R}_2\cdot\mathbf{p}_2}\end{aligned}\tag{259}$$

and

$$\begin{aligned}\mathbf{g}_3(\mathbf{p}_1,\mathbf{p}_2) &= \mathbf{g}_{31}(\mathbf{p}_1,\mathbf{p}_2)+\mathbf{g}_{32}(\mathbf{p}_1,\mathbf{p}_2)+\mathbf{g}_{33}(\mathbf{p}_1,\mathbf{p}_2),\\ &= \mathcal{Q}_4(\mathbf{p}_1,\mathbf{p}_2)\,e^{-i\mathbf{R}_1\cdot\mathbf{p}_1+i\mathbf{R}_3\cdot\mathbf{p}_2}+\mathcal{Q}_5(\mathbf{p}_1,\mathbf{p}_2)\,e^{-i\mathbf{R}_2\cdot\mathbf{p}_1+i\mathbf{R}_3\cdot\mathbf{p}_2}\\ &\quad+\mathcal{Q}_1(\mathbf{p}_1,\mathbf{p}_2)\,e^{-i\mathbf{R}_3\cdot(\mathbf{p}_1-\mathbf{p}_2)},\end{aligned}\tag{260}$$

for the atom on the right. In here we have rewritten the constants as:

$$\begin{aligned}\mathcal{Q}_1(\mathbf{p}_1,\mathbf{p}_2) &= -\mathrm{i}\Big[\mathcal{D}_1(\mathbf{p}_2)\mathcal{C}_1(\mathbf{p}_1,\mathbf{p}_2)-\mathcal{D}_1^*(\mathbf{p}_1)\mathcal{C}_2(\mathbf{p}_1,\mathbf{p}_2)\Big],\\ \mathcal{Q}_2(\mathbf{p}_1,\mathbf{p}_2) &= -i\Big[\mathcal{D}_2(\mathbf{p}_2)\mathcal{C}_1(\mathbf{p}_1,\mathbf{p}_2)-\mathcal{D}_2^*(\mathbf{p}_1)\mathcal{C}_2(\mathbf{p}_1,\mathbf{p}_2)\Big],\\ \mathcal{Q}_3(\mathbf{p}_1,\mathbf{p}_2) &= -i\Big[\mathcal{D}_3(\mathbf{p}_2)\mathcal{C}_1(\mathbf{p}_1,\mathbf{p}_2)-\mathcal{D}_5^*(\mathbf{p}_1)\mathcal{C}_2(\mathbf{p}_1,\mathbf{p}_2)\Big],\\ \mathcal{Q}_4(\mathbf{p}_1,\mathbf{p}_2) &= -i\Big[\mathcal{D}_4(\mathbf{p}_2)\mathcal{C}_1(\mathbf{p}_1,\mathbf{p}_2)-\mathcal{D}_4^*(\mathbf{p}_1)\mathcal{C}_2(\mathbf{p}_1,\mathbf{p}_2)\Big],\\ \mathcal{Q}_5(\mathbf{p}_1,\mathbf{p}_2) &= -i\Big[\mathcal{D}_5(\mathbf{p}_2)\mathcal{C}_1(\mathbf{p}_1,\mathbf{p}_2)-\mathcal{D}_3^*(\mathbf{p}_1)\mathcal{C}_2(\mathbf{p}_1,\mathbf{p}_2)\Big],\end{aligned}\tag{261}$$

the magnitud $\mathcal{C}_1(\mathbf{p}_1,\mathbf{p}_2)$ and $\mathcal{C}_2(\mathbf{p}_1,\mathbf{p}_2)$ are defined in Eq. (66), Chapter 1.

The total rescattering matrix element for the whole three-center molecule reads thus as:

$$\begin{aligned}\mathbf{g}(\mathbf{p}_1,\mathbf{p}_2) &= \mathcal{Q}_1(\mathbf{p}_1,\mathbf{p}_2)\,e^{-i\mathbf{R}_1\cdot(\mathbf{p}_1-\mathbf{p}_2)}+\mathcal{Q}_5(\mathbf{p}_1,\mathbf{p}_2)\,e^{-i\mathbf{R}_2\cdot\mathbf{p}_1+i\mathbf{R}_1\cdot\mathbf{p}_2}\\ &\quad+\mathcal{Q}_4(\mathbf{p}_1,\mathbf{p}_2)\,e^{-i\mathbf{R}_3\cdot\mathbf{p}_1+i\mathbf{R}_1\cdot\mathbf{p}_2}+\mathcal{Q}_3(\mathbf{p}_1,\mathbf{p}_2)\,e^{-i\mathbf{R}_1\cdot\mathbf{p}_1+i\mathbf{R}_2\cdot\mathbf{p}_2}\\ &\quad+\mathcal{Q}_2(\mathbf{p}_1,\mathbf{p}_2)\,e^{-i\mathbf{R}_2\cdot(\mathbf{p}_1-\mathbf{p}_2)}+\mathcal{Q}_3(\mathbf{p}_1,\mathbf{p}_2)\,e^{-i\mathbf{R}_3\cdot\mathbf{p}_1+\mathrm{i}\mathbf{R}_2\cdot\mathbf{p}_2}\\ &\quad+\mathcal{Q}_4(\mathbf{p}_1,\mathbf{p}_2)\,e^{-i\mathbf{R}_1\cdot\mathbf{p}_1+i\mathbf{R}_3\cdot\mathbf{p}_2}+\mathcal{Q}_5(\mathbf{p}_1,\mathbf{p}_2)\,e^{-i\mathbf{R}_2\cdot\mathbf{p}_1+i\mathbf{R}_3\cdot\mathbf{p}_2}\\ &\quad+\mathcal{Q}_1(\mathbf{p}_1,\mathbf{p}_2)\,e^{-i\mathbf{R}_3\cdot(\mathbf{p}_1-\mathbf{p}_2)}.\end{aligned}\tag{262}$$

7.3 MOLECULAR ORBITAL AS LCAO: CO_2 AND CS_2 MOLECULES

In this section we obtain the ground state and bound-free dipole matrix element for the CO_2 and CS_2 molecules. We are going to follow the equations presented in Chapter 2 and Sec. 2.4.2.

7.3.1 *Ground states and bound-continuum dipole matrix elements: CO_2 molecule*

For the case of CO_2 the bound state can be written using the equation (158) as:

$$\Psi_{0-CO_2}(\mathbf{p}) = \sum_{j=1}^{3}\left[G_{j(2p_x)}\Phi_{j(2p_x)}(\mathbf{p}) + G_{j(2p_z)}\Phi_{j(2p_z)}(\mathbf{p})\right]. \quad (263)$$

A plot with the HOMO of this molecule is shown in Fig. 43(a). We consider the molecule in equilibrium - the C–O bond length is set to 2.2 a.u., and oriented perpendicular to the laser field polarization, i.e. along the y-axis.

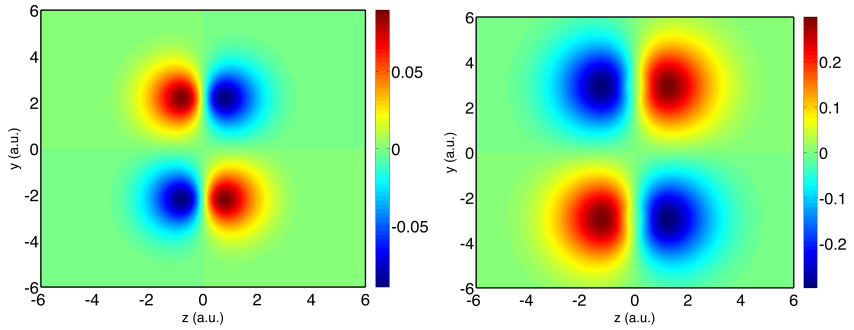

(a) CO_2 (b) CS_2

Figure 43: Coordinate space wavefunction for the CO_2 (a) and CS_2 (b) , presented in the $y-z$ planes, calculated using LCAO method. The molecules are aligned $\theta = 90°$ with the laser field polarization (z-axis).

With the bound state well defined in Eq. (263) it is then possible to obtain the dipole transition matrix element from Eq. (162). The bound-continuum matrix element reads as:

$$\begin{aligned}\mathbf{d}_{CO_2}(\mathbf{p}_0) = \sum_{j=1}^{3}\Bigg[&G_{j(2p_x)}\left\{i\,\mathbf{p}_0\frac{\Phi_{j(2p_x)}(\mathbf{p}_0)}{2\,\zeta_{n;j(2p_x)}} - \delta\Phi_{j(2p_x)}(\mathbf{p}_0)\,\hat{\mathbf{i}}\right\}\\ &+ G_{j(2p_z)}\left\{i\,\mathbf{p}_0\frac{\Phi_{j(2p_z)}(\mathbf{p}_0)}{2\,\zeta_{n;j(2p_z)}} - \delta\Phi_{j(2p_z)}(\mathbf{p}_0)\,\hat{\mathbf{k}}\right\}\Bigg].\end{aligned} \quad (264)$$

Remember that the quantities $\delta\Phi_{j(2p_z)}(\mathbf{p}_0)$ are defined in Eq. (166).

7.3.2 *Ground states and bound-continuum dipole matrix elements: CS_2 molecule*

The CS_2 bound state within the LCAO approach reads as:

$$\Psi_{0-CS_2}(\mathbf{p}) = \sum_{j=1}^{3}\Big[G_{j(2p_x)}\Phi_{j(2p_x)}(\mathbf{p}) + G_{j(2p_z)}\Phi_{j(2p_z)}(\mathbf{p}) + G_{j(3p_x)}\Phi_{j(3p_x)}(\mathbf{p}) + G_{j(3p_z)}\Phi_{j(3p_z)}(\mathbf{p})\Big]. \quad (265)$$

As in the previous case, we consider the CS_2 molecule in equilibrium - the C–S bond length is set to 2.92 a.u., and oriented parallel to the laser field polarization, i.e. along the z-axis. A plot of the CS_2 HOMO is depicted in Fig. 43 (b).

For the carbon dioxide molecule, CO_2, we use the equations presented in Chapter 2 and Sec. 2.4.2. In this way the bound-continuum matrix element for the CS_2 molecule is write as a combination of $2p_x$ and $2p_z$ orbitals as:

$$\begin{aligned}\mathbf{d}_{CS_2}(\mathbf{p}_0) = \sum_{j=1}^{3}\Bigg[& G_{j(2p_x)}\left\{i\,\mathbf{p}_0\frac{\Phi_{j(2p_x)}(\mathbf{p}_0)}{2\,\zeta_{j;n(2p_x)}} - \delta\Phi_{j(2p_x)}(\mathbf{p}_0)\,\hat{\mathbf{i}}\right\} \\ & + G_{j(2p_z)}\left\{i\,\mathbf{p}_0\frac{\Phi_{j(2p_z)}(\mathbf{p}_0)}{2\,\zeta_{j;n(2p_z)}} - \delta\Phi_{j(2p_z)}(\mathbf{p}_0)\,\hat{\mathbf{k}}\right\} \\ & + G_{j(3p_x)}\left\{i\,\mathbf{p}_0\frac{\Phi_{j(3p_x)}(\mathbf{p}_0)}{2\,\zeta_{j;n(3p_x)}} - \delta\Phi_{j(3p_x)}(\mathbf{p}_0)\,\hat{\mathbf{i}}\right\} \\ & + G_{j(3p_z)}\left\{i\,\mathbf{p}_0\frac{\Phi_{j(3p_z)}(\mathbf{p}_0)}{2\,\zeta_{j;n(3p_z)}} - \delta\Phi_{j(3p_z)}(\mathbf{p}_0)\,\hat{\mathbf{k}}\right\}\Bigg].\end{aligned} \quad (266)$$

Those equations are used to obtain the results presented in Chapter 3.

8

MSFA: FOUR-CENTER MOLECULES

In this section we present the equations for the ground and scattering states, needed to calculate the ATI and HHG spectra for four-center molecular systems. In here we use the model developed in Chapter 3 and consider a four-center molecular system with the symmetries shown in the Fig. 44.

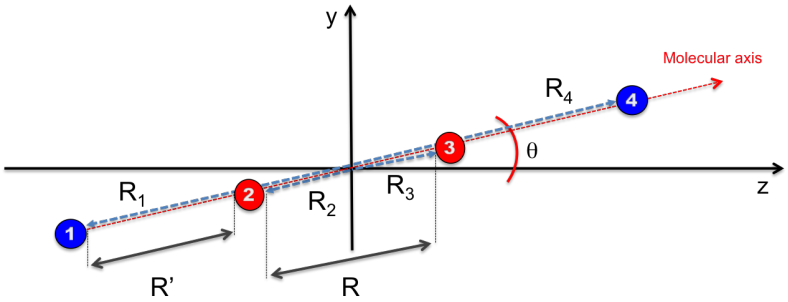

Figure 44: Four-center molecular system aligned a θ angle with respect to the laser electric field polarization. The red line represents the molecular axis. The vector positions are defined as $\mathbf{R}_1 = [0, -(R' + \frac{R}{2})\sin(\theta), -(R' + \frac{R}{2})\cos(\theta)]$, $\mathbf{R}_2 = [0, -\frac{R}{2}\sin(\theta), -\frac{R}{2}\cos(\theta)]$, $\mathbf{R}_3 = [0, \frac{R}{2}\sin(\theta), \frac{R}{2}\cos(\theta)]$ and $\mathbf{R}_4 = [0, (R' + \frac{R}{2})\sin(\theta), (R' + \frac{R}{2})\cos(\theta)]$.

8.1 GROUND STATE AND BOUND-CONTINUUM DIPOLE MATRIX ELEMENTS

For a molecule with four atoms, similar to the one presented in the Fig. 44, the eigenvalues problem, needed to obtain the bound state, defined in Eq. 192 looks like:

$$\begin{pmatrix} \breve{\varphi}_1 \\ \breve{\varphi}_2 \\ \breve{\varphi}_3 \\ \breve{\varphi}_4 \end{pmatrix} = \begin{pmatrix} I_{11} & I_{12} & I_{13} & I_{14} \\ I_{12} & I_{11} & I_{23} & I_{13} \\ I_{13} & I_{23} & I_{11} & I_{12} \\ I_{14} & I_{13} & I_{12} & I_{11} \end{pmatrix} \times \begin{pmatrix} \breve{\varphi}_1 \\ \breve{\varphi}_2 \\ \breve{\varphi}_3 \\ \breve{\varphi}_4 \end{pmatrix}. \tag{267}$$

Each of the integrals are directly related to the position of the atoms by the subindexes. This problem has the following solution:

$$\frac{I_{12} + I_{13}}{1 - I_{11} - I_{14}} = \frac{1 - I_{11} - I_{23}}{I_{12} + I_{13}}, \tag{268}$$

and

$$\breve{\varphi}_1 = \breve{\varphi}_4 = \breve{\varphi}_2 \left(\frac{I_{12} + I_{13}}{1 - I_{11} - I_{14}} \right) \; ; \; \breve{\varphi}_2 = \breve{\varphi}_3. \tag{269}$$

Finally, from Eq. (188) and setting $n = 4$ we have that the ground states reads as,

$$\Psi_0(\mathbf{p}) = \frac{\mathcal{M}}{\sqrt{(p^2+\Gamma^2)(\frac{p^2}{2}+I_p)}}\left[\left(\frac{I_{12}+I_{13}}{1-I_{11}-I_{14}}\right)e^{-i\mathbf{R}_1\cdot\mathbf{p}}\right.$$
$$\left.+e^{-i\mathbf{R}_2\cdot\mathbf{p}}+e^{-i\mathbf{R}_3\cdot\mathbf{p}}+\left(\frac{I_{12}+I_{13}}{1-I_{11}-I_{14}}\right)e^{-i\mathbf{R}_4\cdot\mathbf{p}}\right]. \quad (270)$$

The integrals $I_{11}, I_{12}, I_{13}, I_{23}, I_{14}$ are defined in Eq. (191) and are solved in a similar way as for the cases of two- and three-center molecular systems. In this way we can explicitly write:

$$I_{11} = \frac{4\pi^2\gamma'}{\Gamma+\sqrt{2I_p}}, \quad (271)$$

$$I_{12} = \frac{8\pi^2\gamma'}{R'}\left\{\frac{e^{-\frac{R'\Gamma}{2}}-e^{-\frac{R'\sqrt{2I_p}}{2}}}{2I_p-\Gamma^2}\right\}, \quad (272)$$

$$I_{13} = \frac{4\pi^2\gamma'}{(R+R')}\left\{\frac{e^{-(R+R')\Gamma}-e^{-(R+R')\sqrt{2I_p}}}{2I_p-\Gamma^2}\right\}, \quad (273)$$

$$I_{14} = \frac{4\pi^2\gamma'}{(R+2R')}\left\{\frac{e^{-(R+2R')\Gamma}-e^{-(R+2R')\sqrt{2I_p}}}{2I_p-\Gamma^2}\right\}, \quad (274)$$

and

$$I_{23} = \frac{4\pi^2\gamma'}{R}\left\{\frac{e^{-R\Gamma}-e^{-R\sqrt{2I_p}}}{2I_p-\Gamma^2}\right\}. \quad (275)$$

The normalization condition is $\mathcal{M} = \gamma'\,\breve{\varphi}_2 = \frac{\gamma}{4}\,\breve{\varphi}_1$; and is calculated using the usual normalization condition, i.e. ,

$$\int d^3\mathbf{p}\,\Psi_0(\mathbf{p})^*\,\Psi_0(\mathbf{p}) = 1, \quad (276)$$

so,

$$\mathcal{M}^2\int d^3\mathbf{p}\,\frac{1}{(p^2+\Gamma^2)(\frac{p^2}{2}+I_p)^2}\left[\left(\frac{I_{12}+I_{13}}{1-I_{11}-I_{14}}\right)e^{-i\mathbf{R}_1\cdot\mathbf{p}}\right.$$
$$\left.+e^{-i\mathbf{R}_2\cdot\mathbf{p}}+e^{-i\mathbf{R}_3\cdot\mathbf{p}}+\left(\frac{I_{12}+I_{13}}{1-I_{11}-I_{14}}\right)e^{-i\mathbf{R}_4\cdot\mathbf{p}}\right]^2 = 1, \quad (277)$$

where

$$\mathcal{M} = [1/I_{4N}]^{1/2}, \quad (278)$$

and

$$I_{4N} = \int d^3\mathbf{p}\,\frac{1}{(p^2+\Gamma^2)(\frac{p^2}{2}+I_p)^2}\left[\left(\frac{I_{12}+I_{13}}{1-I_{11}-I_{14}}\right)e^{-i\mathbf{R}_1\cdot\mathbf{p}}\right.$$
$$\left.+e^{-i\mathbf{R}_2\cdot\mathbf{p}}+e^{-i\mathbf{R}_3\cdot\mathbf{p}}+\left(\frac{I_{12}+I_{13}}{1-I_{11}-I_{14}}\right)e^{-i\mathbf{R}_4\cdot\mathbf{p}}\right]^2. \quad (279)$$

The normalization integral is then defined as,

$$\begin{aligned} I_{4N} &= \left(\frac{I_{12}+I_{13}}{1-I_{11}-I_{14}}\right)^2 \left\{I_{2R_1}+I_{2R_4}+2I_{R_1+R_4}\right\} \\ &+2\frac{I_{12}+I_{13}}{1-I_{11}-I_{14}} \left\{I_{R_1+R_2}+I_{R_1+R_3}+I_{R_4+R_2}+I_{R_4+R_3}\right\} \\ &+\left\{I_{2R_2}+2I_{R_2+R_3}+I_{2R_3}\right\}, \end{aligned} \tag{280}$$

where $I_{1N} = I_{R_1+R_4} = I_{R_2+R_3}$ and

$$\begin{aligned} I_{4N} &= \left(\frac{I_{12}+I_{13}}{1-I_{11}-I_{14}}\right)^2 \left\{I_{2R_1}+I_{2R_4}+2I_{1N}\right\} \\ &+2\frac{I_{12}+I_{13}}{1-I_{11}-I_{14}} \left\{I_{R_1+R_2}+I_{R_1+R_3}+I_{R_4+R_2}+I_{R_4+R_3}\right\} \\ &+\left\{I_{2R_2}+2I_{1N}+I_{2R_3}\right\}. \end{aligned} \tag{281}$$

Explicitly, the integrals above (I_{2R_1}, I_{2R_4}...) can be generalized using the subscript $\mathbf{X}$ to represent either $2R_1$, $2R_4$, R_1+R_4... successively. In this way the integrals presented before are solved as,

$$\begin{aligned} &I_X = \int \frac{d^3\mathbf{p}\, e^{-i\mathbf{X}\cdot\mathbf{p}}}{(p^2+\Gamma^2)(\frac{p^2}{2}+I_p)^2} = \\ &\frac{4(2\pi^2)}{(2I_p-\Gamma^2)^2}\left\{\frac{e^{-|X|\Gamma}}{|X|}-\frac{e^{-|X|\sqrt{2I_p}}}{|X|}-\frac{e^{-|X|\sqrt{2I_p}}(2I_p-\Gamma^2)}{2\sqrt{2I_p}}\right\}\int. \end{aligned} \tag{282}$$

With the exact knowledge of the normalization constant, $\mathcal{M}$, we have now defined the ground state in our four-center molecular system from Eq. (270). Notice that the dependency of the system energy with the internuclear distance appears in Eq. (268).

8.1.1 *Bound-continuum matrix element*

The total bound-continuum matrix element for the four-center molecular system is defined using Eq. (197), as a sum of 4 terms, i.e.

$$\mathbf{d}(\mathbf{v}) = -\sum_{j=1}^{4}\left(\langle\mathbf{v}_p|\mathbf{r}|0_j\rangle + \mathbf{R}_j\langle\mathbf{v}_p|0_j\rangle\right). \tag{283}$$

Considering the exact shape of the ground state and Eq. (197) we can explicitly write:

$$\begin{aligned} \mathbf{d}(\mathbf{p}_0) &= -i\,\mathcal{M}\mathcal{A}(\mathbf{p}_0)\left[\left(\frac{I_{12}+I_{13}}{1-I_{11}-I_{14}}\right)e^{-i\mathbf{R}_1\cdot\mathbf{p}}\right. \\ &\left.+e^{-i\mathbf{R}_2\cdot\mathbf{p}}+e^{-i\mathbf{R}_3\cdot\mathbf{p}}+\left(\frac{I_{12}+I_{13}}{1-I_{11}-I_{14}}\right)e^{-i\mathbf{R}_4\cdot\mathbf{p}}\right]. \end{aligned} \tag{284}$$

Finally notice that we could extract the contributions of each center from Eq. (284), i.e.,

$$\mathbf{d}_1(\mathbf{p}_0) = -i\,\mathcal{MA}(\mathbf{p}_0)\left(\frac{I_{12}+I_{13}}{1-I_{11}-I_{14}}\right)e^{-i\mathbf{R}_1\cdot\mathbf{p}_0}, \tag{285}$$

$$\mathbf{d}_2(\mathbf{p}_0) = -i\,\mathcal{MA}(\mathbf{p}_0)e^{-i\mathbf{R}_2\cdot\mathbf{p}_0}, \tag{286}$$

$$\mathbf{d}_3(\mathbf{p}_0) = -i\,\mathcal{MA}(\mathbf{p}_0)e^{-i\mathbf{R}_3\cdot\mathbf{p}_0}, \tag{287}$$

and

$$\mathbf{d}_4(\mathbf{p}_0) = -i\,\mathcal{MA}(\mathbf{p}_0)\left(\frac{I_{12}+I_{13}}{1-I_{11}-I_{14}}\right)e^{-i\mathbf{R}_4\cdot\mathbf{p}_0}, \tag{288}$$

where $\mathcal{A}(\mathbf{p}_0)$ is the quantity defined in Sec. 1.3.1, Eq. (53).

8.2 SCATTERING WAVES AND CONTINUUM-CONTINUUM TRANSITION MATRIX ELEMENTS

To get the scattering states for this system, similarly to the ground state, we are going to use the Eq. (208),

$$\begin{aligned}\Psi_{\mathbf{p}_0}(\mathbf{p}) &= \delta(\mathbf{p}-\mathbf{p}_0) - \frac{2\gamma' U(\mathbf{p})}{(p_0^2-p^2+i\epsilon)}\sum_{j=1}^{4} e^{-i\mathbf{R}_j\cdot\mathbf{p}}\left[U(\mathbf{p}_0)e^{i\mathbf{R}_j\cdot\mathbf{p}_0}+\breve{\varphi}'_j\right],\\ &= \delta(\mathbf{p}-\mathbf{p}_0)+\delta\Psi_{\mathbf{p}_0,1}(\mathbf{p})+\delta\Psi_{\mathbf{p}_0,2}(\mathbf{p})+\delta\Psi_{\mathbf{p}_0,3}(\mathbf{p})+\delta\Psi_{\mathbf{p}_0,4}(\mathbf{p}).\end{aligned} \tag{289}$$

For the four-center system the eigenvalues problem for the scattering states looks like,

$$\begin{pmatrix}\breve{\varphi}'_1\\ \breve{\varphi}'_2\\ \breve{\varphi}'_3\\ \breve{\varphi}'_4\end{pmatrix} = \begin{pmatrix} I'_{11} & I'_{12} & I'_{13} & I'_{14} & \sum_{j'}^{4} K_{1j'}\\ I'_{12} & I'_{11} & I'_{23} & I'_{13} & \sum_{j'}^{4} K_{2j'}\\ I'_{13} & I'_{23} & I'_{11} & I'_{12} & \sum_{j'}^{4} K_{3j'}\\ I'_{14} & I'_{13} & I'_{12} & I'_{11} & \sum_{j'}^{4} K_{4j'}\end{pmatrix}\times\begin{pmatrix}\breve{\varphi}'_1\\ \breve{\varphi}'_2\\ \breve{\varphi}'_3\\ \breve{\varphi}'_4\\ 1\end{pmatrix}. \tag{290}$$

The eigenvalues problem is solved as:

$$\breve{\varphi}'_1 = \frac{1}{\sqrt{p_0^2+\Gamma^2}}\times\frac{-1}{A_0}\left[e^{i\mathbf{R}_1\cdot\mathbf{p}_0}A_1+e^{i\mathbf{R}_2\cdot\mathbf{p}_0}A_3+e^{i\mathbf{R}_3\cdot\mathbf{p}_0}A_4+e^{i\mathbf{R}_4\cdot\mathbf{p}_0}A_5\right], \tag{291}$$

$$\breve{\varphi}'_2 = \frac{1}{\sqrt{p_0^2+\Gamma^2}}\times\frac{-1}{A_0}\left[e^{i\mathbf{R}_1\cdot\mathbf{p}_0}A_3+e^{i\mathbf{R}_2\cdot\mathbf{p}_0}A_2-e^{i\mathbf{R}_3\cdot\mathbf{p}_0}A_6+e^{i\mathbf{R}_4\cdot\mathbf{p}_0}A_4\right], \tag{292}$$

$$\breve{\varphi}'_3 = \frac{1}{\sqrt{p_0^2+\Gamma^2}}\times\frac{-1}{A_0}\left[e^{i\mathbf{R}_1\cdot\mathbf{p}_0}A_4-e^{i\mathbf{R}_2\cdot\mathbf{p}_0}A_6-e^{i\mathbf{R}_3\cdot\mathbf{p}_0}A_2+e^{i\mathbf{R}_4\cdot\mathbf{p}_0}A_3\right], \tag{293}$$

and

$$\breve{\varphi}'_4 = \frac{1}{\sqrt{p_0^2+\Gamma^2}} \times \frac{-1}{A_0}\Big[e^{i\mathbf{R}_1\cdot\mathbf{p}_0}A_5 + e^{i\mathbf{R}_2\cdot\mathbf{p}_0}A_4 + e^{i\mathbf{R}_3\cdot\mathbf{p}_0}A_3 + e^{i\mathbf{R}_4\cdot\mathbf{p}_0}A_1\Big]. \tag{294}$$

The constants $A_{i=0,1,\ldots,6}$ looks like,

$$\begin{aligned}
A_0 &= \Big[-1+(I'_{12}-I'_{13})^2 + I'_{23}(1+I'_{11}-I'_{14}) + I'_{14} \\
&\quad + I'_{11}(-2-I'_{11}+I'_{14})\Big] \times \Big[1-(I'_{12}+I'_{13})^2 + I'_{14} \\
&\quad + I'_{23}(1+I'_{11}+I'_{14}) + I'_{11}(2+I'_{11}+I'_{14})\Big]; \\
A_1 &= -3{I'_{11}}^3 - {I'_{11}}^4 - {I'_{12}}^4 + {I'_{13}}^2 - {I'_{13}}^4 + 2I'_{23}{I'_{13}}^2 I'_{14} \\
&\quad + {I'_{14}}^2 - {I'_{23}}^2{I'_{14}}^2 - 2I'_{12}I'_{13}(I'_{23}+2I'_{14}) + {I'_{12}}^2(1+2{I'_{13}}^2 \\
&\quad + 2I'_{23}I'_{14}) + {I'_{11}}^2(-3+{I'_{23}}^2+2{I'_{12}}^2+2{I'_{13}}^2+{I'_{14}}^2) \\
&\quad + I'_{11}(-1+{I'_{23}}^2+3{I'_{12}}^2-4I'_{23}I'_{12}I'_{13} \\
&\quad + 3{I'_{13}}^2 - 4I'_{12}I'_{13}I'_{14} + 2{I'_{14}}^2); \\
A_2 &= -3{I'_{11}}^3 - {I'_{11}}^4 + {I'_{12}}^2 - 4I'_{23}(1+I'_{11})I'_{12}I'_{13} + {I'_{13}}^2 \\
&\quad - ({I'_{12}}^2 - {I'_{13}}^2)^2 - 2I'_{12}I'_{13}I'_{14} + 2I'_{23} \times ({I'_{12}}^2 + {I'_{13}}^2)I'_{14} \\
&\quad + {I'_{23}}^2(1+I'_{11}-I'_{14})(1+I'_{11}+I'_{14}) + {I'_{11}}^2(-3+2{I'_{12}}^2 \\
&\quad + 2{I'_{13}}^2 + {I'_{14}}^2) + I'_{11}(-1+3{I'_{12}}^2 \\
&\quad + 3{I'_{13}}^2 - 4I'_{12}I'_{13}I'_{14} + {I'_{14}}^2); \\
A_3 &= {I'_{12}}^3 + (1+I'_{11})(I'_{23}+I'_{14})I'_{13} - I'_{12}[1+I'_{11}(2+I'_{11}) \\
&\quad + {I'_{13}}^2 + I'_{23}I'_{14}]; \\
A_4 &= -[(1+I'_{11})^2 + {I'_{11}}^2]I'_{13} + {I'_{13}}^3 + (1+I'_{11})I'_{12}I'_{14} \\
&\quad + I'_{23}(I'_{12} + I'_{11}I'_{12} - I'_{13}I'_{14}); \\
A_5 &= -I'_{23}({I'_{12}}^2 + {I'_{13}}^2) + {I'_{23}}^2 I'_{14} - (1+I'_{11}) \\
&\quad \times(-2I'_{12}I'_{13} + I'_{14} + I'_{11}I'_{14});
\end{aligned} \tag{295}$$

and

$$\begin{aligned}
A_6 &= -2(1+I'_{11})I'_{12}I'_{13} + ({I'_{12}}^2 + {I'_{13}}^2)I'_{14} \\
&\quad + I'_{23}(1+I'_{11}-I'_{14})(1+I'_{11}+I'_{14}).
\end{aligned} \tag{296}$$

The above integrals are defined within the Eq. (191) and can be solved to give:

$$I'_{11} = \frac{-4\gamma'\pi^2}{\Gamma - i\sqrt{|p_0^2 + i\,\epsilon|}}, \tag{297}$$

$$I'_{12} = \frac{-4\gamma'\pi^2}{R'\,(p_0^2+\Gamma^2+i\epsilon)}\left[e^{iR'\sqrt{p_0^2+i\epsilon}} - e^{-R'\Gamma}\right], \tag{298}$$

$$I'_{13} = \frac{-4\gamma'\pi^2}{(R'+R)\,(p_0^2+\Gamma^2+i\epsilon)}\left[e^{i(R'+R)\sqrt{p_0^2+i\epsilon}} - e^{-(R'+R)\Gamma}\right], \tag{299}$$

and

$$I'_{14} = \frac{-4\gamma'\pi^2}{(2R'+R)\,(p_0^2+\Gamma^2+i\epsilon)}\left[e^{i(2R'+R)\sqrt{p_0^2+i\epsilon}} - e^{-(2R'+R)\Gamma}\right], \tag{300}$$

and

$$I'_{23} = \frac{-4\gamma'\pi^2}{R\,(p_0^2+\Gamma^2+i\epsilon)}\left[e^{iR\sqrt{p_0^2+i\epsilon}} - e^{-R\Gamma}\right]. \tag{301}$$

With the exact dependency of $\breve{\varphi}'$ and working to separate all the exponential factors, the scattering wave function for each of the atoms reads as:

$$\begin{aligned}\delta\Psi_{\mathbf{p}_0,1}(\mathbf{p}) &= \frac{\mathcal{D}_1(\mathbf{p}_0)\,e^{-i\mathbf{R}_1\cdot(\mathbf{p}-\mathbf{p}_0)} + \mathcal{D}_3(\mathbf{p}_0)\,e^{-i\mathbf{R}_1\cdot\mathbf{p}+i\mathbf{R}_2\cdot\mathbf{p}_0}}{\sqrt{p^2+\Gamma^2}\,(p_0^2-p^2+\nu\epsilon)} \\ &\quad + \frac{\mathcal{D}_4(\mathbf{p}_0)\,e^{-i\mathbf{R}_1\cdot\mathbf{p}+i\mathbf{R}_3\cdot\mathbf{p}_0} + \mathcal{D}_5(\mathbf{p}_0)\,e^{-i\mathbf{R}_1\cdot\mathbf{p}+i\mathbf{R}_4\cdot\mathbf{p}_0}}{\sqrt{p^2+\Gamma^2}\,(p_0^2-p^2+i\epsilon)},\end{aligned} \tag{302}$$

$$\begin{aligned}\delta\Psi_{\mathbf{p}_0,2}(\mathbf{p}) &= \frac{\mathcal{D}_2(\mathbf{p}_0)\,e^{-i\mathbf{R}_2\cdot(\mathbf{p}-\mathbf{p}_0)} + \mathcal{D}_3(\mathbf{p}_0)\,e^{-i\mathbf{R}_2\cdot\mathbf{p}+i\mathbf{R}_1\cdot\mathbf{p}_0}}{\sqrt{p^2+\Gamma^2}\,(p_0^2-p^2+i\epsilon)} \\ &\quad - \frac{\mathcal{D}_6(\mathbf{p}_0)\,e^{-i\mathbf{R}_2\cdot\mathbf{p}+i\mathbf{R}_3\cdot\mathbf{p}_0} + \mathcal{D}_4(\mathbf{p}_0)\,e^{-i\mathbf{R}_2\cdot\mathbf{p}+i\mathbf{R}_4\cdot\mathbf{p}_0}}{\sqrt{p^2+\Gamma^2}\,(p_0^2-p^2+i\epsilon)},\end{aligned} \tag{303}$$

$$\begin{aligned}\delta\Psi_{\mathbf{p}_0,3}(\mathbf{p}) &= \frac{\mathcal{D}_2(\mathbf{p}_0)\,e^{-i\mathbf{R}_3\cdot(\mathbf{p}-\mathbf{p}_0)} + \mathcal{D}_3(\mathbf{p}_0)\,e^{-i\mathbf{R}_3\cdot\mathbf{p}+i\mathbf{R}_4\cdot\mathbf{p}_0}}{\sqrt{p^2+\Gamma^2}\,(p_0^2-p^2+i\epsilon)} \\ &\quad - \frac{\mathcal{D}_6(\mathbf{p}_0)\,e^{-i\mathbf{R}_3\cdot\mathbf{p}+i\mathbf{R}_2\cdot\mathbf{p}_0} + \mathcal{D}_4(\mathbf{p}_0)\,e^{-i\mathbf{R}_3\cdot\mathbf{p}+i\mathbf{R}_1\cdot\mathbf{p}_0}}{\sqrt{p^2+\Gamma^2}\,(p_0^2-p^2+i\epsilon)},\end{aligned} \tag{304}$$

and

$$\begin{aligned}\delta\Psi_{\mathbf{p}_0,4}(\mathbf{p}) &= \frac{\mathcal{D}_1(\mathbf{p}_0)\,e^{-i\mathbf{R}_4\cdot(\mathbf{p}-\mathbf{p}_0)} + \mathcal{D}_3(\mathbf{p}_0)\,e^{-i\mathbf{R}_4\cdot\mathbf{p}+i\mathbf{R}_3\cdot\mathbf{p}_0}}{\sqrt{p^2+\Gamma^2}\,(p_0^2-p^2+i\epsilon)} \\ &\quad + \frac{\mathcal{D}_4(\mathbf{p}_0)\,e^{-i\mathbf{R}_4\cdot\mathbf{p}+i\mathbf{R}_2\cdot\mathbf{p}_0} + \mathcal{D}_5(\mathbf{p}_0)\,e^{-i\mathbf{R}_4\cdot\mathbf{p}+i\mathbf{R}_1\cdot\mathbf{p}_0}}{\sqrt{p^2+\Gamma^2}\,(p_0^2-p^2+i\epsilon)},\end{aligned} \tag{305}$$

where,

$$\mathcal{D}_1(\mathbf{p}_0) = \frac{2\gamma'}{\sqrt{p_0^2+\Gamma^2}}\left(\frac{A_1-A_0}{A_0}\right);\ \mathcal{D}_2(\mathbf{p}_0) = \frac{2\gamma'}{\sqrt{p_0^2+\Gamma^2}}\left(\frac{A_2-A_0}{A_0}\right)$$

$$\mathcal{D}_3(\mathbf{p}_0) = \frac{2\gamma'}{\sqrt{p_0^2+\Gamma^2}}\left(\frac{A_3}{A_0}\right);\ \mathcal{D}_4(\mathbf{p}_0) = \frac{2\gamma'}{\sqrt{p_0^2+\Gamma^2}}\left(\frac{A_4}{A_0}\right);$$

$$\mathcal{D}_5(\mathbf{p}_0) = \frac{2\gamma'}{\sqrt{p_0^2+\Gamma^2}}\left(\frac{A_5}{A_0}\right);\ \mathcal{D}_6(\mathbf{p}_0) = \frac{2\gamma'}{\sqrt{p_0^2+\Gamma^2}}\left(\frac{A_6}{A_0}\right); \tag{306}$$

The Eq. (302) represents electrons that have the probability of scatter with the core placed at the left in $\mathbf{R}_1$. In the same way Eq. (303) represents electrons that scatter with the nucleus placed at $\mathbf{R}_2$ and Eq.(304) [305] that scatter with the nucleus placed at $\mathbf{R}_3$ [$\mathbf{R}_4$] respectively.

8.2.1 *Continuum-continuum transition matrix element*

To obtain the rescattering transition matrix element we are going to use the Eq. (**??**) defined in Chapter 3. Considering $n = 4$ the rescattering matrix element can be written as:

$$\begin{aligned}\mathbf{g}_1(\mathbf{p}_1,\mathbf{p}_2) &= \mathbf{g}_{11}(\mathbf{p}_1,\mathbf{p}_2)+\mathbf{g}_{12}(\mathbf{p}_1,\mathbf{p}_2)+\mathbf{g}_{13}(\mathbf{p}_1,\mathbf{p}_2)+\mathbf{g}_{14}(\mathbf{p}_1,\mathbf{p}_2),\\ &= \mathcal{Q}_1(\mathbf{p}_1,\mathbf{p}_2)\,e^{-i\mathbf{R}_1\cdot(\mathbf{p}_1-\mathbf{p}_2)}+\mathcal{Q}_3(\mathbf{p}_1,\mathbf{p}_2)\,e^{-i\mathbf{R}_2\cdot\mathbf{p}_1+i\mathbf{R}_1\cdot\mathbf{p}_2}\\ &\quad+\mathcal{Q}_4(\mathbf{p}_1,\mathbf{p}_2)\,e^{-i\mathbf{R}_3\cdot\mathbf{p}_1+i\mathbf{R}_1\cdot\mathbf{p}_2}+\mathcal{Q}_5(\mathbf{p}_1,\mathbf{p}_2)\,e^{-i\mathbf{R}_4\cdot\mathbf{p}_1+i\mathbf{R}_1\cdot\mathbf{p}_2},\end{aligned} \tag{307}$$

$$\begin{aligned}\mathbf{g}_2(\mathbf{p}_1,\mathbf{p}_2) &= \mathbf{g}_{22}(\mathbf{p}_1,\mathbf{p}_2)+\mathbf{g}_{21}(\mathbf{p}_1,\mathbf{p}_2)+\mathbf{g}_{23}(\mathbf{p}_1,\mathbf{p}_2)+\mathbf{g}_{24}(\mathbf{p}_1,\mathbf{p}_2),\\ &= \mathcal{Q}_2(\mathbf{p}_1,\mathbf{p}_2)\,e^{-i\mathbf{R}_2\cdot(\mathbf{p}_1-\mathbf{p}_2)}+\mathcal{Q}_3(\mathbf{p}_1,\mathbf{p}_2)\,e^{-i\mathbf{R}_1\cdot\mathbf{p}_1+i\mathbf{R}_2\cdot\mathbf{p}_2}\\ &\quad+\mathcal{Q}_6(\mathbf{p}_1,\mathbf{p}_2)\,e^{-i\mathbf{R}_3\cdot\mathbf{p}_1+i\mathbf{R}_2\cdot\mathbf{p}_2}+\mathcal{Q}_4(\mathbf{p}_1,\mathbf{p}_2)\,e^{-i\mathbf{R}_4\cdot\mathbf{p}_1+i\mathbf{R}_2\cdot\mathbf{p}_2},\end{aligned} \tag{308}$$

$$\begin{aligned}\mathbf{g}_3(\mathbf{p}_1,\mathbf{p}_2) &= \mathbf{g}_{33}(\mathbf{p}_1,\mathbf{p}_2)+\mathbf{g}_{34}(\mathbf{p}_1,\mathbf{p}_2)+\mathbf{g}_{32}(\mathbf{p}_1,\mathbf{p}_2)+\mathbf{g}_{31}(\mathbf{p}_1,\mathbf{p}_2),\\ &= \mathcal{Q}_2(\mathbf{p}_1,\mathbf{p}_2)\,e^{-i\mathbf{R}_3\cdot(\mathbf{p}_1-\mathbf{p}_2)}+\mathcal{Q}_3(\mathbf{p}_1,\mathbf{p}_2)\,e^{-i\mathbf{R}_4\cdot\mathbf{p}_1+i\mathbf{R}_3\cdot\mathbf{p}_2}\\ &\quad+\mathcal{Q}_6(\mathbf{p}_1,\mathbf{p}_2)\,e^{-i\mathbf{R}_2\cdot\mathbf{p}_1+i\mathbf{R}_3\cdot\mathbf{p}_2}+\mathcal{Q}_4(\mathbf{p}_1,\mathbf{p}_2)\,e^{-i\mathbf{R}_1\cdot\mathbf{p}_1+i\mathbf{R}_3\cdot\mathbf{p}_2}\end{aligned} \tag{309}$$

and

$$\begin{aligned}\mathbf{g}_4(\mathbf{p}_1,\mathbf{p}_2) &= \mathbf{g}_{44}(\mathbf{p}_1,\mathbf{p}_2)+\mathbf{g}_{43}(\mathbf{p}_1,\mathbf{p}_2)+\mathbf{g}_{42}(\mathbf{p}_1,\mathbf{p}_2)+\mathbf{g}_{41}(\mathbf{p}_1,\mathbf{p}_2),\\ &= \mathcal{Q}_1(\mathbf{p}_1,\mathbf{p}_2)\,e^{-i\mathbf{R}_4\cdot(\mathbf{p}_1-\mathbf{p}_2)}+\mathcal{Q}_3(\mathbf{p}_1,\mathbf{p}_2)\,e^{-i\mathbf{R}_3\cdot\mathbf{p}_1+i\mathbf{R}_4\cdot\mathbf{p}_2}\\ &\quad+\mathcal{Q}_4(\mathbf{p}_1,\mathbf{p}_2)\,e^{-i\mathbf{R}_2\cdot\mathbf{p}_1+i\mathbf{R}_4\cdot\mathbf{p}_2}+\mathcal{Q}_5(\mathbf{p}_1,\mathbf{p}_2)\,e^{-i\mathbf{R}_1\cdot\mathbf{p}_1+i\mathbf{R}_4\cdot\mathbf{p}_2},\end{aligned} \tag{310}$$

where we have rewritten the constants as:

$$\begin{aligned}
\mathcal{Q}_1(\mathbf{p}_1,\mathbf{p}_2) &= -i\Big[\mathcal{D}_1(\mathbf{p}_2)\mathcal{C}_1(\mathbf{p}_1,\mathbf{p}_2) - \mathcal{D}_1^*(\mathbf{p}_1)\mathcal{C}_2(\mathbf{p}_1,\mathbf{p}_2)\Big],\\
\mathcal{Q}_2(\mathbf{p}_1,\mathbf{p}_2) &= -i\Big[\mathcal{D}_2(\mathbf{p}_2)\mathcal{C}_1(\mathbf{p}_1,\mathbf{p}_2) - \mathcal{D}_2^*(\mathbf{p}_1)\mathcal{C}_2(\mathbf{p}_1,\mathbf{p}_2)\Big],\\
\mathcal{Q}_3(\mathbf{p}_1,\mathbf{p}_2) &= -i\Big[\mathcal{D}_3(\mathbf{p}_2)\mathcal{C}_1(\mathbf{p}_1,\mathbf{p}_2) - \mathcal{D}_3^*(\mathbf{p}_1)\mathcal{C}_2(\mathbf{p}_1,\mathbf{p}_2)\Big],\\
\mathcal{Q}_4(\mathbf{p}_1,\mathbf{p}_2) &= -i\Big[\mathcal{D}_4(\mathbf{p}_2)\mathcal{C}_1(\mathbf{p}_1,\mathbf{p}_2) - \mathcal{D}_4^*(\mathbf{p}_1)\mathcal{C}_2(\mathbf{p}_1,\mathbf{p}_2)\Big],\\
\mathcal{Q}_5(\mathbf{p}_1,\mathbf{p}_2) &= -i\Big[\mathcal{D}_5(\mathbf{p}_2)\mathcal{C}_1(\mathbf{p}_1,\mathbf{p}_2) - \mathcal{D}_5^*(\mathbf{p}_1)\mathcal{C}_2(\mathbf{p}_1,\mathbf{p}_2)\Big],\\
\mathcal{Q}_6(\mathbf{p}_1,\mathbf{p}_2) &= -i\Big[\mathcal{D}_6(\mathbf{p}_2)\mathcal{C}_1(\mathbf{p}_1,\mathbf{p}_2) - \mathcal{D}_6^*(\mathbf{p}_1)\mathcal{C}_2(\mathbf{p}_1,\mathbf{p}_2)\Big]. \qquad (311)
\end{aligned}$$

Notice that $\mathcal{C}_1(\mathbf{p}_1,\mathbf{p}_2)$ and $\mathcal{C}_2(\mathbf{p}_1,\mathbf{p}_2)$ are defined in Eq. (66), Chapter 1.

The total rescattering transition matrix element is then:

$$\begin{aligned}
\mathbf{g}(\mathbf{p}_1,\mathbf{p}_2) = {} & \mathcal{Q}_1(\mathbf{p}_1,\mathbf{p}_2)\, e^{-i\mathbf{R}_1\cdot(\mathbf{p}_1-\mathbf{p}_2)} + \mathcal{Q}_3(\mathbf{p}_1,\mathbf{p}_2)\, e^{-i\mathbf{R}_2\cdot\mathbf{p}_1+i\mathbf{R}_1\cdot\mathbf{p}_2}\\
& + \mathcal{Q}_4(\mathbf{p}_1,\mathbf{p}_2)\, e^{-i\mathbf{R}_3\cdot\mathbf{p}_1+i\mathbf{R}_1\cdot\mathbf{p}_2} + \mathcal{Q}_5(\mathbf{p}_1,\mathbf{p}_2)\, e^{-i\mathbf{R}_4\cdot\mathbf{p}_1+i\mathbf{R}_1\cdot\mathbf{p}_2},\\
& + \mathcal{Q}_2(\mathbf{p}_1,\mathbf{p}_2)\, e^{-i\mathbf{R}_2\cdot(\mathbf{p}_1-\mathbf{p}_2)} + \mathcal{Q}_3(\mathbf{p}_1,\mathbf{p}_2)\, e^{-i\mathbf{R}_1\cdot\mathbf{p}_1+i\mathbf{R}_2\cdot\mathbf{p}_2}\\
& + \mathcal{Q}_6(\mathbf{p}_1,\mathbf{p}_2)\, e^{-i\mathbf{R}_3\cdot\mathbf{p}_1+i\mathbf{R}_2\cdot\mathbf{p}_2} + \mathcal{Q}_4(\mathbf{p}_1,\mathbf{p}_2)\, e^{-i\mathbf{R}_4\cdot\mathbf{p}_1+i\mathbf{R}_2\cdot\mathbf{p}_2},\\
& + \mathcal{Q}_2(\mathbf{p}_1,\mathbf{p}_2)\, e^{-i\mathbf{R}_3\cdot(\mathbf{p}_1-\mathbf{p}_2)} + \mathcal{Q}_3(\mathbf{p}_1,\mathbf{p}_2)\, e^{-i\mathbf{R}_4\cdot\mathbf{p}_1+i\mathbf{R}_3\cdot\mathbf{p}_2}\\
& + \mathcal{Q}_6(\mathbf{p}_1,\mathbf{p}_2)\, e^{-i\mathbf{R}_2\cdot\mathbf{p}_1+i\mathbf{R}_3\cdot\mathbf{p}_2} + \mathcal{Q}_4(\mathbf{p}_1,\mathbf{p}_2)\, e^{-i\mathbf{R}_1\cdot\mathbf{p}_1+i\mathbf{R}_3\cdot\mathbf{p}_2}\\
& + \mathcal{Q}_1(\mathbf{p}_1,\mathbf{p}_2)\, e^{-i\mathbf{R}_4\cdot(\mathbf{p}_1-\mathbf{p}_2)} + \mathcal{Q}_3(\mathbf{p}_1,\mathbf{p}_2)\, e^{-i\mathbf{R}_3\cdot\mathbf{p}_1+i\mathbf{R}_4\cdot\mathbf{p}_2}\\
& + \mathcal{Q}_4(\mathbf{p}_1,\mathbf{p}_2)\, e^{-i\mathbf{R}_2\cdot\mathbf{p}_1+i\mathbf{R}_4\cdot\mathbf{p}_2} + \mathcal{Q}_5(\mathbf{p}_1,\mathbf{p}_2)\, e^{-i\mathbf{R}_1\cdot\mathbf{p}_1+i\mathbf{R}_4\cdot\mathbf{p}_2}. \qquad (312)
\end{aligned}$$

8.3 MOLECULAR ORBITAL AS LCAO: C_2H_2

In this section we obtain the ground state and bound-free dipole matrix element for the acetylene molecule . We are going to follow the equations presented in Chapter 2 and Sec. 2.4.2.

8.3.1 *Bound state and bound-continuum dipole matrix elements: C_2H_2 molecule*

For the case of C_2H_2 the bound state can be written using the Eq. (158) as:

$$\Psi_{0-C_2H_2}(\mathbf{r}) = \sum_{j=1}^{4} G_{j(2p_y)}\Phi_{j(2p_y)}(\mathbf{p}) + G_{j(2p_z)}\Phi_{j(2p_z)}(\mathbf{p}). \qquad (313)$$

The bound-free matrix element for the acetylene molecule is calculated using the definition in Eq. (162). Explicitly, the bound-continuum matrix element reads as:

$$\begin{aligned}\mathbf{d}_{C_2H_2}(\mathbf{p}_0) &= \sum_{j=1}^{4}\left[G_{j(2p_y)}\left\{i\,\mathbf{p}_0\,\frac{\Phi_{j(2p_y)}(\mathbf{p}_0)}{2\,\zeta_{j;n(2p_y)}} - \delta\Phi_{j(2p_y)}(\mathbf{p}_0)\,\hat{\mathbf{j}}\right\}\right. \\ &\left. + G_{j(2p_z)}\left\{i\,\mathbf{p}_0\,\frac{\Phi_{j(2p_z)}(\mathbf{p}_0)}{2\,\zeta_{j;n(2p_z)}} - \delta\Phi_{j(2p_z)}(\mathbf{p}_0)\,\hat{\mathbf{k}}\right\}\right].\end{aligned} \tag{314}$$

Those equations are used to obtain the results presented in Chapter 3, Section 3.3.3.

9

TREATMENT OF THE ASYMPTOTIC BEHAVIOR WHEN $\mathbf{R} \to 0$

In this Appendix we prove, analytically, that our model is capable to satisfy the asymptotic limit when the separation between the two atoms of the molecule is close to zero. For this condition, our model describes a single atom that satisfies the equations previously presented in Chapter 1 [4]. In this sense our theoretical formulation for a multiatomic molecule remains compatible with the atomic model.

In here and for a better understanding we will use superindexes to label the equations obtained for the two, three and four centers. For example in the diatomic case we rename the bound state wave function as, $\Psi_0^{\text{Two}}(\mathbf{p})$, and in the same way for the three and four center system. This is made in a way to distinguish the molecular formulation from the atomic one that will remain equal as presented in Chapter 1.

9.1 2-CENTER MOLECULES

9.1.1 *Ground state and bound-continuum transition matrix elements: 2-center*

When the internuclear distance is close to zero, the bound state of our diatomic molecule is equal to the bound state of an atom, $\lim_{\mathbf{R}\to 0} \Psi_0^{\text{Two}}(\mathbf{p}) = \Psi_0(\mathbf{p})$. The wavefunction describing the bound state for the atomic system is obtained in Chapter 1 Eq. (44). Explicitly we have:

$$\Psi_0(\mathbf{p}) = \frac{\mathcal{N}}{\sqrt{(p^2+\Gamma^2)}(\frac{p^2}{2}+I_p)}, \tag{315}$$

where,

$$\mathcal{N} = [1/I_{1N}]^{1/2} = \left(\frac{\sqrt{2I_p}\left(\Gamma+\sqrt{2I_p}\right)^2}{4\pi^2}\right)^{1/2}, \tag{316}$$

In order to perform the limit $\mathbf{R} \to 0$ for the molecular bound state $\Psi_0^{\text{Two}}(\mathbf{p})$, we are going to use Eq. (130) as,

$$\begin{aligned}\lim_{\mathbf{R}\to 0} \Psi_0^{\text{Two}}(\mathbf{p}) &= \lim_{\mathbf{R}\to 0}\left\{\frac{\mathcal{M}^{\text{Two}}\, e^{\frac{i\mathbf{R}}{2}\cdot\mathbf{p}}}{\sqrt{(p^2+\Gamma^2)}(\frac{p^2}{2}+I_p)} + \frac{\mathcal{M}^{\text{Two}}\, e^{-\frac{i\mathbf{R}}{2}\cdot\mathbf{p}}}{\sqrt{(p^2+\Gamma^2)}(\frac{p^2}{2}+I_p)}\right\}, \\ &= \frac{\lim_{\mathbf{R}\to 0} 2\mathcal{M}^{\text{Two}}}{\sqrt{(p^2+\Gamma^2)}(\frac{p^2}{2}+I_p)}.\end{aligned} \tag{317}$$

Now we need to probe that $\lim_{\mathbf{R}\to 0} 2\mathcal{M}^{\text{Two}} = \mathcal{N}$. Following Eq. (129) we have that $\mathcal{M}^{\text{Two}} = [1/I_{2N}]^{1/2}$ so,

$$\lim_{\mathbf{R}\to 0} 2[1/I_{2N}]^{1/2} = 2\Big[\frac{1}{2\lim_{\mathbf{R}\to 0}(I_R + I_{1N})}\Big]^{1/2}. \tag{318}$$

Taking the limit over the independent equations we have,

$$\lim_{\mathbf{R}\to 0} I_R = \frac{4\pi^2}{\sqrt{2I_p}(\sqrt{2I_p}+\Gamma)^2} = I_{1N}, \tag{319}$$

so the limit of the normalization constant is,

$$\lim_{\mathbf{R}\to 0} 2\mathcal{M}^{\text{Two}} = 2\Big[\frac{1}{4I_{1N}}\Big]^{1/2} = \frac{1}{\sqrt{I_{1N}}}, \tag{320}$$

that is exactly the normalization constant for the bound states in the atomic case. In this way we have demonstrated that,

$$\lim_{\mathbf{R}\to 0} 2\mathcal{M}^{\text{Two}} = \mathcal{N} \tag{321}$$

For the bound-continuum transition matrix element, Eq. (134), we follow the same analysis. By taking the asymptotic limit as

$$\begin{aligned}\lim_{\mathbf{R}\to 0} \mathbf{d}^{\text{Two}}(\mathbf{p}_0) &= \lim_{\mathbf{R}\to 0}\Big\{-i\,\mathcal{M}^{\text{Two}}\mathcal{A}(\mathbf{p}_0)\big[e^{\frac{i\mathbf{R}}{2}\cdot\mathbf{p}_0} + e^{-\frac{i\mathbf{R}}{2}\cdot\mathbf{p}_0}\big]\Big\},\\ &= -i\,\mathcal{A}(\mathbf{p}_0)\lim_{\mathbf{R}\to 0} 2\mathcal{M}^{\text{Two}},\end{aligned} \tag{322}$$

and using Eq. (321), we obtain

$$\lim_{\mathbf{R}\to 0} \mathbf{d}^{\text{Two}}(\mathbf{p}_0) = -i\mathcal{N}\,\mathcal{A}(\mathbf{p}_0), \tag{323}$$

which is exactly the bound-continuum transition matrix element for the atomic system, Eq. (52).

9.1.2 *Scattering waves and continuum-continuum transition matrix elements*

For the scattering states, we will prove that the diatomic case contains the atomic case for the limit when the two atoms in the molecule are close each other, i.e. $\lim_{\mathbf{R}\to 0} \Psi^{\text{Two}}_{\mathbf{p}_0}(\mathbf{p}) = \Psi_{\mathbf{p}_0}(\mathbf{p})$. For the atomic system, the scattering state can be written as:

$$\Psi^{\text{Two}}_{\mathbf{p}_0}(\mathbf{p}) = \delta(\mathbf{p}-\mathbf{p}_0) + \frac{\mathcal{B}(\mathbf{p}_0)}{\sqrt{p^2+\Gamma^2}\Big(p_0^2 - p^2 + i\epsilon\Big)}, \tag{324}$$

where $\mathcal{B}(\mathbf{p}_0) = \frac{-2\gamma}{(p_0^2+\Gamma^2)^{\frac{1}{2}}}\left(1 - \frac{4\pi^2 i\gamma}{|p_0|+i\Gamma}\right)^{-1}$ is the normalization constant.

On the other hand, from Eqs.(135) and (141), the asymptotic limit for the molecular system reads as

$$\begin{aligned}\lim_{\mathbf{R}\to 0}\Psi^{\mathrm{Two}}_{\mathbf{p}_0}(\mathbf{p}) &= \delta(\mathbf{p}-\mathbf{p}_0)+\lim_{\mathbf{R}\to 0}\left\{\frac{\mathcal{D}_1(\mathbf{p}_0)\left[e^{-\frac{i\mathbf{R}}{2}\cdot(\mathbf{p}-\mathbf{p}_0)}+e^{\frac{i\mathbf{R}}{2}\cdot(\mathbf{p}-\mathbf{p}_0)}\right]}{\sqrt{p^2+\Gamma^2}\,(p_0^2-p^2+i\epsilon)}\right.\\ &\left.-\frac{\mathcal{D}_2(\mathbf{p}_0)\left[e^{-\frac{i\mathbf{R}}{2}\cdot(\mathbf{p}+\mathbf{p}_0)}+e^{\frac{i\mathbf{R}}{2}\cdot(\mathbf{p}+\mathbf{p}_0)}\right]}{\sqrt{p^2+\Gamma^2}\,(p_0^2-p^2+i\epsilon)}\right\},\\ &= \delta(\mathbf{p}-\mathbf{p}_0)+\frac{2\,\lim_{\mathbf{R}\to 0}\left\{\mathcal{D}_1(\mathbf{p}_0)-\mathcal{D}_2(\mathbf{p}_0)\right\}}{\sqrt{p^2+\Gamma^2}\,(p_0^2-p^2+i\epsilon)}. \qquad (325)\end{aligned}$$

Working with the above equation we are going to prove that $\mathcal{B}(\mathbf{p}_0)=2\,\lim_{\mathbf{R}\to 0}\left\{\mathcal{D}_1(\mathbf{p}_0)-\mathcal{D}_2(\mathbf{p}_0)\right\}$. For this we need to work with the values of the constants; now we have:

$$\begin{aligned}&2\lim_{\mathbf{R}\to 0}\left\{\mathcal{D}_1(\mathbf{p}_0)-\mathcal{D}_2(\mathbf{p}_0)\right\}=\\ &\frac{2\gamma}{\sqrt{p_0^2+\Gamma^2}}\lim_{\mathbf{R}\to 0}\left\{\frac{1+I_1'}{I_2'^2-(1+I_1')^2}-\frac{I_2'}{I_2'^2-(1+I_1')^2}\right\}. \qquad (326)\end{aligned}$$

In the above equation we have two terms, the first one I_1' is constant in $\mathbf{R}$ and for the second I_2' the limit is calculated using Eq. (145) as,

$$\lim_{\mathbf{R}\to 0} I_2' = \frac{-2\pi^2\,\gamma}{R\,(p_0^2+\Gamma^2+i\epsilon)}\left[e^{iR\sqrt{p_0^2+i\epsilon}}-e^{-R\,\Gamma}\right]=\frac{-2\pi^2\,\gamma}{\Gamma-i\sqrt{|p_0^2+i\,\epsilon|}}, \qquad (327)$$

we find that $\lim_{\mathbf{R}\to 0} I_2' = I_1'$. From this last result we can then write

$$\begin{aligned}2\lim_{\mathbf{R}\to 0}\left\{\mathcal{D}_1(\mathbf{p}_0)-\mathcal{D}_2(\mathbf{p}_0)\right\} &= \frac{2\gamma}{\sqrt{p_0^2+\Gamma^2}}\left[\frac{1}{I_1'^2-(1+I_1')^2}\right],\\ &= \frac{-2\gamma}{\sqrt{p_0^2+\Gamma^2}}(1+2I_1')^{-1},\\ &= \frac{-2\gamma}{\sqrt{p_0^2+\Gamma^2}}\left(1-\frac{4\pi^2 i\gamma}{|p_0|+i\Gamma}\right)^{-1} \qquad (328)\end{aligned}$$

which is identical to Eq. (58) of Chapter 2 [4].

Concluding the analysis of the diatomic molecular system when $\mathbf{R}\to 0$ we proceed to demonstrate that the continuum-continuum molecular matrix element is equal to the continuum-continuum atomic

matrix element. The dipole matrix element for the atomic system can be written as

$$\begin{aligned}\mathbf{g}(\mathbf{p}_1,\mathbf{p}_2) &= i\mathcal{B}(\mathbf{p}_2)\mathbf{p}_1\left\{\frac{3p_1^2-p_2^2+2\Gamma^2}{(p_1^2+\Gamma^2)^{\frac{3}{2}}(p_2^2-p_1^2-i\epsilon)^2}\right\}\\ &\quad -i\mathcal{B}^*(\mathbf{p}_1)\mathbf{p}_2\left\{\frac{3p_2^2-p_1^2+2\Gamma^2}{(p_2^2+\Gamma^2)^{\frac{3}{2}}(p_1^2-p_2^2+i\epsilon)^2}\right\}.\end{aligned} \tag{329}$$

Taking the limit in Eq. (153) we write

$$\begin{aligned}&\lim_{\mathbf{R}\to 0}\mathbf{g}^{\text{Two}}(\mathbf{p}_1,\mathbf{p}_2) = 2\lim_{\mathbf{R}\to 0}\left[\mathcal{Q}_1(\mathbf{p}_1,\mathbf{p}_2)+\mathcal{Q}_2(\mathbf{p}_1,\mathbf{p}_2)\right],\\ &= i\mathcal{C}_1(\mathbf{p}_1,\mathbf{p}_2)\,2\lim_{\mathbf{R}\to 0}\left[\frac{1+I_1'}{I_2'^2-(1+I_1')^2}-\frac{I_2'}{I_2'^2-(1+I_1')^2}\right]_{p_2}\\ &-i\mathcal{C}_2(\mathbf{p}_1,\mathbf{p}_2)\,2\lim_{\mathbf{R}\to 0}\left[\frac{1+I_1'}{I_2'^2-(1+I_1')^2}-\frac{I_2'}{I_2'^2-(1+I_1')^2}\right]^*_{p_1},\end{aligned} \tag{330}$$

where more explicitly

$$\begin{aligned}\lim_{\mathbf{R}\to 0}\mathbf{g}^{\text{Two}}(\mathbf{p}_1,\mathbf{p}_2) &= i\,\mathcal{C}_1(\mathbf{p}_1,\mathbf{p}_2)\left\{\frac{2\gamma}{\sqrt{p_2^2+\Gamma^2}}\lim_{\mathbf{R}\to 0}\left[\frac{1}{I_1'^2-(1+I_1')^2}\right]_{p_2}\right\}\\ &-i\,\mathcal{C}_2(\mathbf{p}_1,\mathbf{p}_2)\left\{\frac{2\gamma}{\sqrt{p_1^2+\Gamma^2}}\lim_{\mathbf{R}\to 0}\left[\frac{1}{I_1'^2-(1+I_1')^2}\right]^*_{p_1}\right\}.\end{aligned} \tag{331}$$

By following the same procedure as in Eq. (328), we finally obtain that

$$\mathcal{B}(\mathbf{p}_2) = \left\{\frac{2\gamma}{\sqrt{p_2^2+\Gamma^2}}\lim_{\mathbf{R}\to 0}\left[\frac{1}{I_1'^2-(1+I_1')^2}\right]_{p_2}\right\} \tag{332}$$

and

$$\mathcal{B}^*(\mathbf{p}_1) = \left\{\frac{2\gamma}{\sqrt{p_1^2+\Gamma^2}}\lim_{\mathbf{R}\to 0}\left[\frac{1}{I_1'^2-(1+I_1')^2}\right]^*_{p_1}\right\}, \tag{333}$$

proving that,

$$\lim_{\mathbf{R}\to 0}\mathbf{g}^{\text{Two}}(\mathbf{p}_1,\mathbf{p}_2) = i\mathcal{B}(\mathbf{p}_2)\,\mathcal{C}_1(\mathbf{p}_1,\mathbf{p}_2) - i\mathcal{B}^*(\mathbf{p}_1)\,\mathcal{C}_2(\mathbf{p}_1,\mathbf{p}_2) \tag{334}$$

is nothing else than the atomic rescattering transition matrix element [see Eqs. (65) and (66) of Chapter 2 [4].

9.2 3-CENTER MOLECULAR SYSTEMS

9.2.1 *Ground state and bound-continuum transition matrix elements*

In order to perform the limit $\mathbf{R} \to 0$ for the three-center molecular bound state we are going to use Eq. (232), Writing it as an explicit function of $\mathbf{R}$ and taking the limit we have:

$$\begin{aligned}\lim_{\mathbf{R}\to 0} \Psi_0^{\text{Three}}(\mathbf{p}) &= \lim_{\mathbf{R}\to 0}\left\{\frac{\mathcal{M}^{\text{Three}}}{\sqrt{(p^2+\Gamma^2)}(\frac{p^2}{2}+I_p)}\left[\left(\frac{I_{12}}{1-I_{11}-I_{13}}\right)e^{-i\mathbf{R}_1\cdot\mathbf{p}}\right.\right.\\ &\quad \left.\left.+e^{-i\mathbf{R}_2\cdot\mathbf{p}}+\left(\frac{I_{12}}{1-I_{11}-I_{13}}\right)e^{-i\mathbf{R}_3\cdot\mathbf{p}}\right],\right\},\\ &= \lim_{\mathbf{R}\to 0}\left\{\frac{\mathcal{M}^{\text{Three}}}{\sqrt{(p^2+\Gamma^2)}(\frac{p^2}{2}+I_p)}\left(\frac{2I_{12}}{1-I_{11}-I_{13}}+1\right)\right\}.\end{aligned} \tag{335}$$

The integral $I_{11} = \frac{4\pi^2\gamma'}{\Gamma+\sqrt{2I_p}}$ do not have a dependency with $\mathbf{R}$, for the others the limit results:

$$\lim_{\mathbf{R}\to 0} I_{12} = \lim_{\mathbf{R}\to 0}\left\{\frac{8\pi^2\gamma'}{R}\left[\frac{e^{-\frac{R\Gamma}{2}}-e^{-\frac{R\sqrt{2I_p}}{2}}}{2I_p-\Gamma^2}\right]\right\} = \frac{4\pi^2\gamma'}{\Gamma+\sqrt{2I_p}}, \tag{336}$$

and

$$\begin{aligned}\lim_{\mathbf{R}\to 0} I_{13} &= \lim_{\mathbf{R}\to 0}\left\{\frac{4\pi^2\gamma'}{R\sin(\alpha/2)}\left[\frac{e^{-R\sin(\alpha/2)\Gamma}-e^{-R\sin(\alpha/2)\sqrt{2I_p}}}{2I_p-\Gamma^2}\right]\right\},\\ &= \frac{4\pi^2\gamma'}{\Gamma+\sqrt{2I_p}}.\end{aligned} \tag{337}$$

Notice that: $I_{11} = I_{12} = I_{13}$ and,

$$\begin{aligned}\lim_{\mathbf{R}\to 0} \Psi_0^{\text{Three}}(\mathbf{p}) &= \lim_{\mathbf{R}\to 0}\left\{\frac{\mathcal{M}^{\text{Three}}}{\sqrt{(p^2+\Gamma^2)}(\frac{p^2}{2}+I_p)}\left(\frac{2I_{11}}{1-2I_{11}}+1\right)\right\}\\ &= \lim_{\mathbf{R}\to 0}\left\{\frac{\mathcal{M}^{\text{Three}}}{\sqrt{(p^2+\Gamma^2)}(\frac{p^2}{2}+I_p)}\left(\frac{1}{1-2I_{11}}\right)\right\}.\end{aligned} \tag{338}$$

From the above equation is clear that $\lim_{\mathbf{R}\to 0}\Psi_0^{\text{Three}}(\mathbf{p}) = \Psi_0(\mathbf{p})$ if,

$$\lim_{\mathbf{R}\to 0}\left\{\mathcal{M}^{\text{Three}}\left(\frac{1}{1-2I_{11}}\right)\right\} = \frac{1}{\sqrt{I_{3N}}}(1-2I_{11})^{-1} = \mathcal{N}. \tag{339}$$

The normalization constant, I_{3N}, for the bound state in the three centers system is given by Eq. (235). Notice that if we take the limit of it we have that $\lim_{\mathbf{R}\to 0} I_{2R_1} = \lim_{\mathbf{R}\to 0} I_{2R_3} = \lim_{\mathbf{R}\to 0} I_{R_1+R_3} = I_{1N}$ and,

$$\begin{aligned}\lim_{\mathbf{R}\to 0} I_{3N} &= I_{1N}\left[4\left(\frac{I_{11}}{1-2I_{11}}\right)^2+4\frac{I_{11}}{1-2I_{11}}+1\right]\\ &= I_{1N}\left(2\frac{I_{11}}{1-2I_{11}}+1\right)^2 = I_{1N}(1-2I_{11})^{-2}.\end{aligned} \tag{340}$$

Finally

$$\begin{aligned}\lim_{\mathbf{R}\to 0}\left\{\mathcal{M}^{\text{Three}}\left(\frac{1}{1-2I_{11}}\right)\right\} &= \frac{1}{\sqrt{I_{1N}\left(1-2I_{11}\right)^{-2}}}\left(1-2I_{11}\right)^{-1},\\ &= \frac{1}{\sqrt{I_{1N}}\left(1-2I_{11}\right)^{-1}}\left(1-2I_{11}\right)^{-1},\\ &= \frac{1}{\sqrt{I_{1N}}}, \end{aligned} \tag{341}$$

so,

$$\lim_{\mathbf{R}\to 0}\left\{\mathcal{M}^{\text{Three}}\left(\frac{1}{1-2I_{11}}\right)\right\} = \mathcal{N}. \tag{342}$$

For the bound-continuum transition matrix element we follow the same analysis. By taking the asymptotic limit as:

$$\begin{aligned}\lim_{\mathbf{R}\to 0}\mathbf{d}^{\text{Three}}(\mathbf{p}_0) &= \lim_{\mathbf{R}\to 0}\left\{-i\,\mathcal{M}^{\text{Three}}\mathcal{A}(\mathbf{p}_0)\left[\frac{I_{11}}{1-2I_{11}}\left(e^{-i\mathbf{R}_1\cdot\mathbf{p}_0}+e^{-i\mathbf{R}_3\cdot\mathbf{p}_0}\right)+1\right]\right\},\\ &= -i\,\mathcal{A}(\mathbf{p}_0)\lim_{\mathbf{R}\to 0}\left\{\mathcal{M}^{\text{Three}}\left(\frac{1}{1-2I_{11}}\right)\right\}, \end{aligned} \tag{343}$$

and using Eq. (342), we obtain:

$$\lim_{\mathbf{R}\to 0}\mathbf{d}^{\text{Three}}(\mathbf{p}_0) = \mathbf{d}(\mathbf{p}_0). \tag{344}$$

9.2.2 *Scattering waves and continuum-continuum transition matrix elements*

For the scattering states we will proceed in the same way using Eq. (254), (251), (252) and (253). The asymptotic limit for the three-center molecular system reads as:

$$\lim_{\mathbf{R}\to 0}\Psi^{\text{Three}}_{\mathbf{p}_0}(\mathbf{p}) = \delta(\mathbf{p}-\mathbf{p}_0)+\lim_{\mathbf{R}\to 0}\delta\Psi^{\text{Three}}_{\mathbf{p}_0}(\mathbf{p}), \tag{345}$$

where

$$\begin{aligned}\lim_{\mathbf{R}\to 0}\delta\Psi^{\text{Three}}_{\mathbf{p}_0}(\mathbf{p}) = \lim_{\mathbf{R}\to 0}\Bigg\{&\frac{-2\mathcal{D}_1(\mathbf{p}_0)+2\mathcal{D}_3(\mathbf{p}_0)}{\sqrt{p^2+\Gamma^2}\,(p_0^2-p^2+i\epsilon)}\\ &+\frac{2\mathcal{D}_4(\mathbf{p}_0)+\mathcal{D}_2(\mathbf{p}_0)+2\mathcal{D}_5(\mathbf{p}_0)}{\sqrt{p^2+\Gamma^2}\,(p_0^2-p^2+i\epsilon)}\Bigg\}\end{aligned} \tag{346}$$

Working with the above equation we are going to prove that:

$$\mathcal{B}(\mathbf{p}_0) = -\lim_{\mathbf{R}\to 0}\left\{2\mathcal{D}_1(\mathbf{p}_0)+2\mathcal{D}_3(\mathbf{p}_0)+2\mathcal{D}_4(\mathbf{p}_0)+\mathcal{D}_2(\mathbf{p}_0)+2\mathcal{D}_5(\mathbf{p}_0)\right\}. \tag{347}$$

In here, similar to the previous cases, we are going to take the limits of the rescattering integrals defined in Eqs. (248), (249) and (250), where $\lim_{\mathbf{R}\to 0} I'_{12} = \lim_{\mathbf{R}\to 0} I'_{13} = I'_{11}$.

Substituting the values of the constants we have,

$$
\begin{aligned}
&-\lim_{\mathbf{R}\to 0}\Big\{2\mathcal{D}_1(\mathbf{p}_0)+2\mathcal{D}_3(\mathbf{p}_0)+2\mathcal{D}_4(\mathbf{p}_0)+\mathcal{D}_2(\mathbf{p}_0)+2\mathcal{D}_5(\mathbf{p}_0)\Big\}\\
&=\frac{-2\gamma'}{\sqrt{p_0^2+\Gamma^2}}\lim_{\mathbf{R}\to 0}\Big\{\frac{3(1+2I'_{11})}{1+3I'_{11}}-\frac{6I'_{11}}{1+3I'_{11}}\Big\},\\
&=\frac{-2\gamma'}{\sqrt{p_0^2+\Gamma^2}}\Big[\frac{3}{1+3I'_{11}}\Big]=\frac{-2\gamma'\,3}{\sqrt{p_0^2+\Gamma^2}}[1+3I'_{11}]^{-1},\\
=\quad&\frac{-2\gamma}{\sqrt{p_0^2+\Gamma^2}}\left(1-\frac{4\pi^2 i\gamma}{|p_0|+i\Gamma}\right)^{-1},
\end{aligned}
\tag{348}
$$

which is identical to Eq. (58) of Chapter 2 [4].

Concluding the analysis of the triatomic molecular system when $\mathbf{R}\to 0$ we proceed to demonstrate that the rescattering matrix element of the three centers system reach the atomic one. Taking the limit in Eq. (262):

$$
\begin{aligned}
\lim_{\mathbf{R}\to 0}\mathbf{g}^{\text{Three}}(\mathbf{p}_1,\mathbf{p}_2)\quad=\quad&\lim_{\mathbf{R}\to 0}\Big[2\mathcal{Q}_1(\mathbf{p}_1,\mathbf{p}_2)+\mathcal{Q}_2(\mathbf{p}_1,\mathbf{p}_2)+2\mathcal{Q}_3(\mathbf{p}_1,\mathbf{p}_2)\\
&+2\mathcal{Q}_4(\mathbf{p}_1,\mathbf{p}_2)+2\mathcal{Q}_5(\mathbf{p}_1,\mathbf{p}_2)\Big],
\end{aligned}
\tag{349}
$$

where,

$$
\begin{aligned}
&\lim_{\mathbf{R}\to 0}\mathbf{g}^{\text{Three}}(\mathbf{p}_1,\mathbf{p}_2)=-\mathcal{C}_1(\mathbf{p}_1,\mathbf{p}_2)\lim_{\mathbf{R}\to 0}\Big[2\mathcal{D}_1(\mathbf{p}_2)+\mathcal{D}_2(\mathbf{p}_2)+2\mathcal{D}_3(\mathbf{p}_2)\\
&+2\mathcal{D}_4(\mathbf{p}_2)+2\mathcal{D}_5(\mathbf{p}_2)\Big]+\mathcal{C}_2(\mathbf{p}_1,\mathbf{p}_2)\lim_{\mathbf{R}\to 0}\Big[2\mathcal{D}_1^*(\mathbf{p}_1)+\mathcal{D}_2^*(\mathbf{p}_2)\\
&+2\mathcal{D}_3^*(\mathbf{p}_2)+2\mathcal{D}_4^*(\mathbf{p}_2)+2\mathcal{D}*_5(\mathbf{p}_2)\Big].
\end{aligned}
\tag{350}
$$

The elements multiplying the term $\mathcal{C}_1(\mathbf{p}_1,\mathbf{p}_2)$ and $\mathcal{C}_2(\mathbf{p}_1,\mathbf{p}_2)$ are the same as defined in Eq. (348), so

$$
\lim_{\mathbf{R}\to 0}\mathbf{g}^{\text{Three}}(\mathbf{p}_1,\mathbf{p}_2)=\quad-\mathcal{C}_1(\mathbf{p}_1,\mathbf{p}_2)\left\{\frac{-2\gamma'}{\sqrt{p_2^2+\Gamma^2}}\Big[\frac{3}{1+3I'_{11}}\Big]_{p_2}\right\}\tag{351}
$$

$$
+\,\mathcal{C}_2(\mathbf{p}_1,\mathbf{p}_2)\left\{\frac{-2\gamma'}{\sqrt{p_1^2+\Gamma^2}}\Big[\frac{3}{1+3I'_{11}}\Big]^*_{p_1}\right\}.\tag{352}
$$

By following the same procedure as in Eq. (348), we finally obtain that:

$$
\mathcal{B}(\mathbf{p}_2)=\frac{-2\gamma'}{\sqrt{p_2^2+\Gamma^2}}\Big[\frac{3}{1+3I'_{11}}\Big]_{p_2}=\left\{\frac{-2\gamma}{\sqrt{p_2^2+\Gamma^2}}\left(1-\frac{4\pi^2 i\gamma}{|p_2|+i\Gamma}\right)^{-1}\right\},\tag{353}
$$

and

$$
\mathcal{B}^*(\mathbf{p}_1)=\frac{-2\gamma'}{\sqrt{p_1^2+\Gamma^2}}\Big[\frac{3}{1+3I'_{11}}\Big]^*_{p_1}=\left\{\frac{-2\gamma}{\sqrt{p_1^2+\Gamma^2}}\left(1-\frac{4\pi^2 i\gamma}{|p_1|-i\Gamma}\right)^{-1}\right\},\tag{354}
$$

which probe that for short distances we recover the atomic case in the rescattering matrix element [see Eqs. (65) and (66) of Chapter 2 [4]].

9.3 4-CENTER MOLECULAR SYSTEMS

To analytically probe the asymptotic limit for the four-center molecular system we use the equations previously obtained in Appx. 8. In this sense our theoretical formulation for the four-center molecule remains compatible with the atomic model.

9.3.1 *Ground state and bound-continuum transition matrix elements*

When the internuclear distance is close to zero, the bound state of the 4-center molecule is equal to the bound state of an atom, $\lim_{\mathbf{R}=\mathbf{R}'\to 0} \Psi_0^{\text{Four}}(\mathbf{p}) = \Psi_0(\mathbf{p})$.

In order to perform the limit $\mathbf{R} \to 0, \mathbf{R}' \to 0$ for the molecular bound-state we are going to use Eq. (270). If we write it as an explicit function of $\mathbf{R}, \mathbf{R}'$ and taking the limit we have:

$$\begin{aligned}
&\lim_{\mathbf{R}=\mathbf{R}'\to 0} \Psi_0^{\text{Four}}(\mathbf{p}) = \\
&\lim_{\mathbf{R}=\mathbf{R}'\to 0} \left\{ \frac{I_{12}+I_{13}}{1-I_{11}-I_{14}} \frac{\mathcal{M}^{\text{Four}}\, e^{-i\mathbf{R}_1\cdot\mathbf{p}}}{\sqrt{(p^2+\Gamma^2)}(\frac{p^2}{2}+I_p)} + \frac{\mathcal{M}^{\text{Four}}\, e^{-i\mathbf{R}_2\cdot\mathbf{p}}}{\sqrt{(p^2+\Gamma^2)}(\frac{p^2}{2}+I_p)} \right. \\
&\left. + \frac{\mathcal{M}^{\text{Four}}\, e^{-i\mathbf{R}_3\cdot\mathbf{p}}}{\sqrt{(p^2+\Gamma^2)}(\frac{p^2}{2}+I_p)} + \frac{I_{12}+I_{13}}{1-I_{11}-I_{14}} \frac{\mathcal{M}^{\text{Four}}\, e^{-i\mathbf{R}_4\cdot\mathbf{p}}}{\sqrt{(p^2+\Gamma^2)}(\frac{p^2}{2}+I_p)} \right\}, \\
= \quad & \frac{1}{\sqrt{(p^2+\Gamma^2)}(\frac{p^2}{2}+I_p)} \times \lim_{\mathbf{R}=\mathbf{R}'\to 0} \left\{ 2\,\mathcal{M}^{\text{Four}} \left(1 + \frac{I_{12}+I_{13}}{1-I_{11}-I_{14}}\right) \right\}. \qquad (355)
\end{aligned}$$

Taking the limit of the each of the individual integrals defined in Eqs. (271), (272), (273) and (274) we shows that $I_{11} = \lim_{\mathbf{R}=\mathbf{R}'\to 0} I_{12} = \lim_{\mathbf{R}=\mathbf{R}'\to 0} I_{13} = \lim_{\mathbf{R}=\mathbf{R}'\to 0} I_{14}$.

Then we need to probe that,

$$\begin{aligned}
&\lim_{\mathbf{R}=\mathbf{R}'\to 0} \left\{ 2\,\mathcal{M}^{\text{Four}} \left(1 + \frac{I_{12}+I_{13}}{1-I_{11}-I_{14}}\right) \right\} \\
&= \lim_{\mathbf{R}=\mathbf{R}'\to 0} \left\{ 2\,\mathcal{M}^{\text{Four}} \left(\frac{1}{1-2I_{11}}\right) \right\} = \mathcal{M}. \qquad (356)
\end{aligned}$$

The normalization constant for the molecular bound state is given by Eq. (278). As in the three centers system, we took the asymptotic limit of each of the integral inside ${}_4N$ (see section before). where,

$$\begin{aligned}
\lim_{\mathbf{R}=\mathbf{R}'\to 0} I_{4N} &= \left(\frac{2I_{11}}{1-2I_{11}}\right)^2 4I_{1N} + 2\left(\frac{2I_{11}}{1-2I_{11}}\right) 4I_{1N} + 4I_{1N}, \\
&= 4I_{1N}\left(\frac{2I_{11}}{1-2I_{11}} + 1\right)^2 = 4I_{1N}\left(1-2I_{11}\right)^{-2}. \qquad (357)
\end{aligned}$$

Working with the normalization constant equation and substituting Eq. (357) we get,

$$\begin{aligned}\lim_{\mathbf{R}=\mathbf{R}'\to 0}\left\{2\,\frac{1}{\sqrt{I_{4N}}}\Big(\frac{1}{1-2I_{11}}\Big)\right\} &= \lim_{\mathbf{R}=\mathbf{R}'\to 0}\left\{\frac{2}{\sqrt{I_{4N}}}(1-2I_{11})^{-1}\right\},\\ &= \frac{2}{2\sqrt{I_{1N}}(1-2I_{11})^{-1}}(1-2I_{11})^{-1},\\ &= \frac{1}{\sqrt{I_{1N}}}, \qquad (358)\end{aligned}$$

demonstrating that,

$$\lim_{\mathbf{R}=\mathbf{R}'\to 0}\left\{2\,\mathcal{M}^{\text{Four}}\Big(1+\frac{2I_{11}}{1-2I_{11}}\Big)\right\}=\mathcal{N}. \qquad (359)$$

For the bound-continuum transition matrix element we follow the same analysis. By taking the asymptotic limit as:

$$\begin{aligned}\lim_{\mathbf{R}=\mathbf{R}'\to 0}\mathbf{d}^{\text{Four}}(\mathbf{p}_0) &= \lim_{\mathbf{R}\to 0,\mathbf{R}'\to 0}\Big\{-i\,\mathcal{M}^{\text{Four}}\mathcal{A}(\mathbf{p}_0)\Big[\Big(\frac{I_{12}+I_{13}}{1-I_{11}-I_{14}}\Big)e^{-i\mathbf{R}_1\cdot\mathbf{p}}\\ &\quad +e^{-i\mathbf{R}_2\cdot\mathbf{p}}+e^{-i\mathbf{R}_3\cdot\mathbf{p}}+\Big(\frac{I_{12}+I_{13}}{1-I_{11}-I_{14}}\Big)e^{-i\mathbf{R}_4\cdot\mathbf{p}}\Big],\Big\}\\ &= -i\mathcal{A}(\mathbf{p}_0)\lim_{\mathbf{R}=\mathbf{R}'\to 0}\left\{2\,\mathcal{M}^{\text{Four}}\Big(1+\frac{2I_{11}}{1-2I_{11}}\Big)\right\}. \qquad (360)\end{aligned}$$

The above expression is nothing else but the bound-continuum transition matrix element for the atomic system.

9.3.2 *Scattering waves and continuum-continuum transition matrix elements*

For the scattering states we will prove that: $\lim_{\mathbf{R}=\mathbf{R}'\to 0}\Psi^{\text{Four}}_{\mathbf{p}_0}(\mathbf{p}) = \Psi_{\mathbf{p}_0}(\mathbf{p})$. From Eq. (289) the asymptotic limit for the four-center molecular system reads as:

$$\begin{aligned}\lim_{\mathbf{R}=\mathbf{R}'\to 0}\Psi^{\text{Four}}_{\mathbf{p}_0}(\mathbf{p}) &= \delta(\mathbf{p}-\mathbf{p}_0)+\lim_{\mathbf{R}=\mathbf{R}'\to 0}\frac{\Big\{2\mathcal{D}_1(\mathbf{p}_0)+4\mathcal{D}_3(\mathbf{p}_0)+4\mathcal{D}_4(\mathbf{p}_0)}{\sqrt{p^2+\Gamma^2}\,(p_0^2-p^2+i\epsilon)}\\ &\quad +\frac{2\mathcal{D}_5(\mathbf{p}_0)+2\mathcal{D}_2(\mathbf{p}_0)-2\mathcal{D}_6(\mathbf{p}_0)\Big\}}{\sqrt{p^2+\Gamma^2}\,(p_0^2-p^2+i\epsilon)}. \qquad (361)\end{aligned}$$

Working with the above equation we are going to prove that:

$$\begin{aligned}\mathcal{B}(\mathbf{p}_0) &= \lim_{\mathbf{R}=\mathbf{R}'\to 0}\Big\{2\mathcal{D}_1(\mathbf{p}_0)+4\mathcal{D}_3(\mathbf{p}_0)+4\mathcal{D}_4(\mathbf{p}_0)\\ &\quad +2\mathcal{D}_5(\mathbf{p}_0)+2\mathcal{D}_2(\mathbf{p}_0)-2\mathcal{D}_6(\mathbf{p}_0)\Big\}. \qquad (362)\end{aligned}$$

By taking the limit $\mathbf{R} = \mathbf{R}' \to 0$ in the constants and considering that $\gamma' = \frac{\gamma}{4}$ we have,

$$\begin{aligned}\mathcal{B}(\mathbf{p}_0) &= \frac{2\gamma'}{\sqrt{p_0^2+\Gamma^2}} \lim_{\mathbf{R}=\mathbf{R}'\to 0} \left\{4\Big[\frac{I'_{11}}{1+4I'_{11}} - 1\Big] + 12\Big[\frac{I'_{11}}{1+4I'_{11}}\Big]\right\}, \\ &= \frac{2\gamma'}{\sqrt{p_0^2+\Gamma^2}}\left\{\frac{-4}{1+4I'_{11}}\right\} = \frac{-2\gamma' 4}{\sqrt{p_0^2+\Gamma^2}}[1+4I'_{11}]^{-1}, \\ &= \frac{-2\gamma}{\sqrt{p_0^2+\Gamma^2}}\left(1 - \frac{4\pi^2 i\gamma}{|p_0|+i\Gamma}\right)^{-1}. \end{aligned} \tag{363}$$

Notice that here, similar to the cases presented before, the limit $\mathbf{R} = \mathbf{R}' \to 0$ of the integrals in the constants $\mathcal{D}_1, \mathcal{D}_2, \mathcal{D}_3, \mathcal{D}_4, \mathcal{D}_5$ and $\mathcal{D}_6$ is equal.

Concluding the analysis of the four-center molecular system when $\mathbf{R} \to 0$ we proceed to demonstrate that the rescattering molecular matrix element is equal to the atomic rescattering matrix element. Taking the limit in Eq. (312):

$$\begin{aligned}\lim_{\mathbf{R}=\mathbf{R}'\to 0} \mathbf{g}^{\text{Four}}(\mathbf{p}_1,\mathbf{p}_2) &= \lim_{\mathbf{R}=\mathbf{R}'\to 0}\Big[2\mathcal{Q}_1(\mathbf{p}_1,\mathbf{p}_2) + 4\mathcal{Q}_3(\mathbf{p}_1,\mathbf{p}_2) \\ &\quad + 4\mathcal{Q}_4(\mathbf{p}_1,\mathbf{p}_2) + 2\mathcal{Q}_5(\mathbf{p}_1,\mathbf{p}_2) \\ &\quad + 2\mathcal{Q}_2(\mathbf{p}_1,\mathbf{p}_2) + 2\mathcal{Q}_6(\mathbf{p}_1,\mathbf{p}_2)\Big], \end{aligned} \tag{364}$$

where,

$$\begin{aligned}\lim_{\mathbf{R}=\mathbf{R}'\to 0} \mathbf{g}^{\text{Four}}(\mathbf{p}_1,\mathbf{p}_2) &= -\mathcal{C}_1(\mathbf{p}_1,\mathbf{p}_2) \lim_{\mathbf{R}=\mathbf{R}'\to 0}\Big\{2\mathcal{D}_1(\mathbf{p}_2) + 4\mathcal{D}_3(\mathbf{p}_2) \\ &\quad + 4\mathcal{D}_4(\mathbf{p}_2) + 2\mathcal{D}_5(\mathbf{p}_2) + 2\mathcal{D}_2(\mathbf{p}_2) - 2\mathcal{D}_6(\mathbf{p}_2)\Big\}\Big|_{p_2} \\ &\quad + \mathcal{C}_2(\mathbf{p}_1,\mathbf{p}_2) \lim_{\mathbf{R}=\mathbf{R}'\to 0}\Big[\Big\{2\mathcal{D}_1(\mathbf{p}_1) + 4\mathcal{D}_3(\mathbf{p}_1) \\ &\quad + 4\mathcal{D}_4(\mathbf{p}_1) + 2\mathcal{D}_5(\mathbf{p}_1) + 2\mathcal{D}_2(\mathbf{p}_1) - 2\mathcal{D}_6(\mathbf{p}_1)\Big\}^*\Big|_{p_1}. \end{aligned} \tag{365}$$

Using the relations obtained for the normalization constant we have

$$\lim_{\mathbf{R}\to 0,\mathbf{R}'\to 0} \mathbf{g}^{\text{Four}}(\mathbf{p}_1,\mathbf{p}_2) = -\mathcal{C}_1(\mathbf{p}_1,\mathbf{p}_2)\left\{\frac{-2\gamma'}{\sqrt{p_0^2+\Gamma^2}}\left[\frac{4}{1+4I'_{11}}\right]_{p_2}\right\} \tag{366}$$

$$+ \mathcal{C}_2(\mathbf{p}_1,\mathbf{p}_2)\left\{\frac{-2\gamma'}{\sqrt{p_0^2+\Gamma^2}}\left[\frac{4}{1+4I'_{11}}\right]^*_{p_1}\right\}, \tag{367}$$

from where we get that

$$\lim_{\mathbf{R}\to 0,\mathbf{R}'\to 0} \mathbf{g}^{\text{Four}}(\mathbf{p}_1,\mathbf{p}_2) = \mathbf{g}(\mathbf{p}_1,\mathbf{p}_2). \tag{368}$$

We have indeed demonstrated, with the above analysis and relations, that the theoretical model presented in this thesis configures a general model which not only describes strong field processes in a n-center molecule, but is also able, when the appropriate limits are taken, to model their atomic counterparts.

BIBLIOGRAPHY

[1] M. Lewenstein, Ph. Balcou, M. Y. Ivanov, A. L'Huillier, and P. B. Corkum. "Theory of high-harmonic generation by low-frequency laser fields." In: *Phys. Rev. A* 49.3 (1994), pp. 2117–2132. DOI: 10.1103/PhysRevA.49.2117.

[2] N. Suárez, A. Chacón, J. A. Pérez-Hernández, J. Biegert, M. Lewenstein, and M. F. Ciappina. "High-order-harmonic generation in atomic and molecular systems." In: *Phys. Rev. A* 95.3 (2017), p. 033415. DOI: 10.1103/PhysRevA.95.033415.

[3] M. Lewenstein, K. C. Kulander, K. J. Schafer, and P. H. Bucksbaum. "Rings in above-threshold ionization: A quasiclassical analysis." In: *Phys. Rev. A* 51.2 (1995), pp. 1495–1507. DOI: 10.1103/PhysRevA.51.1495.

[4] N. Suárez, A. Chacón, M. F. Ciappina, J. Biegert, and M. Lewenstein. "Above-threshold ionization and photoelectron spectra in atomic systems driven by strong laser fields." In: *Phys. Rev. A* 92.6 (2015), p. 063421. DOI: 10.1103/PhysRevA.92.063421.

[5] L. Schwartz. "Thèorie des Distributions." In: NATO Advanced Studies Institute Series B: Physics (1950-1951). Ed. by B. Piraux, A. L'Huillier, and K. Rzążewski.

[6] R. G. Newton. "Scattering Theory of Waves and Particles." In: Text and Monographs in Physics (1982). Ed. by Wolf Beiglöck, Elliot H. Lieb, and Walter Thirring, p. 732.

[7] M. B. Gaarde, Ph. Antoine, A. L'Huillier, K. J. Schafer, and K. C. Kulander. "Macroscopic studies of short-pulse high-order harmonic generation using the time-dependent Schrödinger equation." In: *Phys. Rev. A* 57.6 (1998), pp. 4553–4560. DOI: 10.1103/PhysRevA.57.4553.

[8] J. Tate, T. Auguste, H. G. Muller, P. Salières, P. Agostini, and L. F. DiMauro. "Scaling of Wave-Packet Dynamics in an Intense Mid-infrared Field." In: *Phys. Rev. Lett.* 98.1 (2007), p. 013901. DOI: 10.1103/PhysRevLett.98.013901.

[9] M. F. Ciappina, J. Biegert, R. Quidant, and M. Lewenstein. "High-order-harmonic generation from inhomogeneous fields." In: *Phys. Rev. A* 85.3 (2012), p. 033828. DOI: 10.1103/PhysRevA.85.033828.

[10] K. C. Kulander. "Multiphoton ionization of hydrogen: A time-dependent theory." In: *Phys. Rev. A* 35.1 (1987), pp. 445–447. DOI: 10.1103/PhysRevA.35.445.

[11] H. G. Muller. "Numerical simulation of high-order above-threshold-ionization enhancement in argon." In: *Phys. Rev. A* 60.2 (1999), pp. 1341–1350. DOI: 10.1103/PhysRevA.60.1341.

[12] D. Bauer. "Emergence of Classical Orbits in Few-Cycle Above-Threshold Ionization of Atomic Hydrogen." In: *Phys. Rev. Lett.* 94.11 (2005), p. 113001. DOI: 10.1103/PhysRevLett.94.113001.

[13] C. I. Blaga, F. Catoire, P. Colosimo, G. G. Paulus, H. G. Muller, P. Agostini, and L. F. DiMauro. "Strong-field photoionization revisited." In: *Nature Phys.* 5.5 (2009), pp. 335–338. DOI: doi:10.1038/nphys1228.

[14] M. Ruf, H. Bauke, and C. H. Keitel. "A real space split operator method for the Klein-Gordon equation." In: *J. Comput. Phys.* 228.24 (2009), pp. 9092–9106. DOI: https://doi.org/10.1016/j.jcp.2009.09.012.

[15] L. V. Keldysh. "Ionization in the field of a strong electromagnetic wave." In: *Sov. Phys. JETP* 20.5 (1965), pp. 1307–1314. DOI: http://jetp.ac.ru/cgi-bin/dn/e_020_05_1307.pdf.

[16] M. V. Ammosov, N. B. Delone, and V. P. Krainov. "Tunnel ionization of complex atoms and of atomic ions in an alternating electromagnetic field." In: *Sov. Phys. JETP* 64 (1986), pp. 1191–1194. DOI: http://www.jetp.ac.ru/cgi-bin/dn/e_064_06_1191.pdf.

[17] F. H. M. Faisal. "Collision of electrons with laser photons in a background potential." In: *J. Phys. B* 6.11 (1973), pp. L312–L315. DOI: http://stacks.iop.org/0022-3700/6/i=11/a=003.

[18] H. R. Reiss. "Effect of an intense electromagnetic field on a weakly bound system." In: *Phys. Rev. A* 22.5 (1980), pp. 1786–1813. DOI: 10.1103/PhysRevA.22.1786.

[19] J. Grochmalicki, J. R. Kukliński, and M. Lewenstein. In: *J. Phys. B* 19.22 (1986), pp. 3649–3668. DOI: http://stacks.iop.org/0022-3700/19/i=22/a=010.

[20] F. Ehlotzky. "Harmonic generation in keldysh-type models." In: *Nuovo Cimento.* 14 (1992), pp. 517–525. DOI: https://doi.org/10.1007/BF02457041.

[21] M. Y. Kuchiev and V. N. Ostrovsky. "Quantum theory of high harmonic generation as a three-step process." In: *Phys. Rev. A* 60.4 (1999), pp. 3111–3124. DOI: 10.1103/PhysRevA.60.3111.

[22] P. B. Corkum. "Plasma perspective on strong field multiphoton ionization." In: *Phys. Rev. Lett.* 71.13 (1993), pp. 1994–1997. DOI: 10.1103/PhysRevLett.71.1994.

[23] J. L. Krause, K. J. Schafer, and K. C. Kulander. "High-order harmonic generation from atoms and ions in the high intensity regime." In: *Phys. Rev. Lett.* 68.24 (1992), pp. 3535–3538. DOI: 10.1103/PhysRevLett.68.3535.

[24] K. C. Kulander, K. J. Schafer, and K. L. Krause. "Super-Intense Laser Atom Physics." In: NATO Advanced Studies Institute Series B: Physics 316 (1993). Ed. by edited by B. Piraux, A. L'Huillier, and K. Rzążewski, p. 95.

[25] H. B. van Linden van den Heuvell and H. G. Muller. In: *Multiphoton Processes*. Ed. by S. J. Smith and P. L. Knight. Cambridge, UK: Cambridge University Press, 1998.

[26] See Ref. [88] where they give the name "Simpleman" theory to this classical description in which only the laser force is utilized. Such a theory is one in a class of theories of electrons in plane-wave radiation fields.

[27] O. Smirnova and M. Ivanov. "Attosecond and XUV Physics: Ultrafast Dynamics and Spectroscopy." In: (2014). Ed. by T. Schultz and M. Vrakking. DOI: 10.1002/9783527677689.ch7.

[28] M. Y. Kuchiev. "Atomic antenna." In: *Sov. Phys. JETP Lett.* 45.7 (1987), p. 404. DOI: http://www.jetpletters.ac.ru/ps/1241/article_18763.pdf.

[29] F. Brunel. "Not-so-resonant, resonant absorption." In: *Phys. Rev. Lett.* 59.1 (1987), pp. 52–55. DOI: 10.1103/PhysRevLett.59.52.

[30] F. Brunel. "Harmonic generation due to plasma effects in a gas undergoing multiphoton ionization in the high-intensity limit." In: *J. Opt. Soc. Am.* 7.4 (1990), pp. 521–526. DOI: https://doi.org/10.1364/JOSAB.7.000521.

[31] P. B. Corkum, N. H. Burnett, and F. Brunel. "Above-threshold ionization in the long-wavelength limit." In: *Phys. Rev. Lett.* 62.11 (1989), pp. 1259–1262. DOI: 10.1103/PhysRevLett.62.1259.

[32] L. Elsgoltz. *Differential Equations and the Calculus of Variations*. Miami, United States: University Press of the Pacific, 2003.

[33] H. Goldstein, C. Poole, and J. Safko. *Classical Mechanics*. 3rd edn. San Francisco, United States: Addison Wesley, 2002, p. 356.

[34] B. Chapman, G. Jost, and R. Van Der Pas. *Using **OpenMP**:Portable Shared Memory Parallel Programming*. Cambridge, MA, United States: The MIT Press, 2007.

[35] D. B. Milošević, G. G. Paulus, D. Bauer, and W. Becker. "Above-threshold ionization by few-cycle pulses." In: *J. Phys. B* 39.14 (2006), pp. 203–262. DOI: http://stacks.iop.org/0953-4075/39/i=14/a=R01.

[36] M. D. Feit, J. A. Fleck, and A. Steiger. In: *J. Comput. Phys.* 47.3 (1982), pp. 412–433. DOI: https://doi.org/10.1016/0021-9991(82)90091-2.

[37] M. Frigo and S. G. Johnson. *FFTW*. http://www.fftw.org/..

[38] G. G. Paulus, F. Grasbon, H. Walther, P. Villoresi, M. Nisoli, S. Stagira, E. Priori, and S. De Silvestri. "Absolute-phase phenomena in photoionization with few-cycle laser pulses." In: *Nature (London)* 414.6860 (2001), pp. 182–184. DOI: 10.1038/35102520.

[39] D. G. Arbó, S. Yoshida, E. Persson, K. I. Dimitriou, and J. Burgdörfer. "Interference Oscillations in the Angular Distribution of Laser-Ionized Electrons near Ionization Threshold." In: *Phys. Rev. Lett.* 96.14 (2006), p. 143003. DOI: 10.1103/PhysRevLett.96.143003.

[40] M. F. Kling, J. Rauschenberger, A. J. Verhoef, E. Hasović, T. Uphues, D. B. Milošević, H. G. Muller, and M. J. J. Vrakking. "Imaging of carrier-envelope phase effects in above-threshold ionization with intense few-cycle laser fields." In: *New J. Phys.* 10.2 (2008), p. 025024. DOI: http://stacks.iop.org/1367-2630/10/i=2/a=025024.

[41] T. Wittmann, B. Horvath, W. Helml, M. G. Schätzel, X. Gu, A. L. Cavalieri, G. G. Paulus, and R. Kienberger. "Single-shot carrier-envelope phase measurement of few-cycle laser pulses." In: *Nature Phys.* 5.5 (2009), pp. 357–362. DOI: 10.1038/nphys1250.

[42] J. Bauer. "Coulomb-corrected strong-field approximation for the two-electron atom." In: *Phys. Rev. A* 55.4 (1997), pp. 3261–3263. DOI: 10.1103/PhysRevA.55.3261.

[43] S. V. Popruzhenko, G. G. Paulus, and D. Bauer. "Coulomb-corrected quantum trajectories in strong-field ionization." In: *Phys. Rev. A* 77.5 (2008), p. 053409. DOI: 10.1103/PhysRevA.77.053409.

[44] C. J. Joachain, N. J. Kylstra, and R. M. Potvliege. *Atoms in Intense Laser Fields*. Cambridge Books Online. Cambridge University Press, 2011. ISBN: 9780511993459. DOI: http://dx.doi.org/10.1017/CBO9780511993459.

[45] H. Hetzheim, C. Figueira de Morisson Faria, and W. Becker. "Interference effects in above-threshold ionization from diatomic molecules: Determining the internuclear separation." In: *Phys. Rev. A* 76.2 (2007), p. 023418. DOI: 10.1103/PhysRevA.76.023418.

[46] C. C. Chirilă and M. Lein. "Strong-field approximation for harmonic generation in diatomic molecules." In: *Phys. Rev. A* 73.2 (2006), p. 023410. DOI: 10.1103/PhysRevA.73.023410.

[47] M. Busuladžić, A. Gazibegović-Busuladžić, Milošević, and W. Becker. "Angle-Resolved High-Order Above-Threshold Ionization of a Molecule: Sensitive Tool for Molecular Characterization." In: *Phys. Rev. Lett* 100.20 (2008), p. 203003. DOI: 10.1103/PhysRevLett.100.203003.

[48] W. Becker, S. Long, and J. K. Mclver. "Higher-harmonic production in a model atom with short-range potential." In: *Phys. Rev. A* 41.7 (1990), pp. 4112–4115. DOI: 10.1103/PhysRevA.41.4112.

[49] *NIST Standard Reference Data Program*. http://webbook.nist.gov/cgi/cbook.cgi?ID=C12184906&Units=SI. June 2016.

[50] M. W. Schmidt, K. K. Baldridge, J. A. Boatz, S. T. Elbert, M. S. Gordon, J. H. Jensen, S. Koseki, N. Matsunaga, K. A. Nguyen, S. J. Su, T. L. Windus, M. Dupuis, and J. A. Montgomery. "General Atomic and Molecular Electronic Structure System." In: *J. Comput. Chem.* 14.11 (1993), pp. 1347–1363. DOI: 10.1002/jcc.540141112.

[51] M. S. Gordon and M. W. Schmidt. "Advances in electronic structure theory: GAMESS a decade later." In: *Theory and Applications of Computational Chemistry, the first forty years*. Ed. by C. E. Dykstra, G. Frenking, K. S. Kim, and G. E. Scuseria. Amsterdam, Holland: Elsevier, 2005, pp. 1167–1189. DOI: 10.1016/B978-044451719-7/50084-6.

[52] M. Lein, N. Hay, R. Velotta, J. P. Marangos, and P. L. Knight. "Interference effects in high-order harmonic generation with molecules." In: *Phys. Rev. A* 66.2 (2002), p. 023805. DOI: 10.1103/PhysRevA.66.023805.

[53] M. F. Ciappina, C. C. Chirilă, and M. Lein. "Influence of Coulomb continuum wave functions in the description of high-order harmonic generation with H_2^+." In: *Phys. Rev. A* 75.4 (2007), p. 043405. DOI: 10.1103/PhysRevA.75.043405.

[54] M. Lein, P. P. Corso, J. P. Marangos, and P. L. Knight. "Orientation dependence of high-order harmonic generation in molecules." In: *Phys. Rev. A* 67.2 (2003), p. 023819. DOI: 10.1103/PhysRevA.67.023819.

[55] F. C. Figueira de Morisson. "High-order harmonic generation in diatomic molecules: A quantum-orbit analysis of the interference patterns." In: *Phys. Rev. A* 76 (4 2007), p. 043407. DOI: 10.1103/PhysRevA.76.043407. URL: https://link.aps.org/doi/10.1103/PhysRevA.76.043407.

[56] C. C. Chirilă, I. Dreissigacker, E. V. van der Zwan, and M. Lein. "Emission times in high-order harmonic generation." In: *Phys. Rev. A* 81.3 (2010), p. 033412. DOI: 10.1103/PhysRevA.81.033412.

[57] D. Gabor. "Theory of Communication." In: *J. Inst. Electr. Eng.* 93 (1946), p. 429. DOI: 10.1049/ji-1.1947.0015.

[58] M. Lein. "Molecular imaging using recolliding electrons." In: *J. Phys. B* 40.16 (2007), R135–R173. DOI: http://stacks.iop.org/0953-4075/40/i=16/a=R01.

[59] E. Gabriel, G. E. Fagg, G. Bosilca, T. Angskun, J. J. Dongarra, J. M. Squyres, V. Sahay, P. Kambadur, B. Barrett, A. Lumsdaine, R. H. Castain, D. J. Daniel, R. L. Graham, and T. S. Woodall. "Open MPI: Goals, Concept, and Design of a Next Generation MPI Implementation." In: *Proceedings, 11th European PVM/MPI Users' Group Meeting*. Budapest, Hungary, 2004, pp. 97–104.

[60] N. Suárez, A. Chacón, E. Pisanty, L. Ortmann, A. S. Landsman, A. Picón, J. Biegert, M. Lewenstein, and M. F. Ciappina. "Above-threshold ionization (ATI) in multicenter molecules: the role of the initial state." In: *Phys. Rev. A (Submitted)* (2017). DOI: arXiv:1709.04366.

[61] M. G. Pullen, B. Wolter, A. T. Le, M. Baudisch, M. Sclafani, H. Pires, C. D. Schroter, J. Ullrich, R. Moshammer, T. Pfeifer, C. D. Lin, and J. Biegert. "Influence of orbital symmetry on diffraction imaging with rescattering electron wave packets." In: *Nat. Comm.* 7 (2016), p. 11922. DOI: 10.1038/ncomms11922.

[62] M. Magrakvelidze, C. M. Aikens, and U. Thumm. "Dissociation dynamics of diatomic molecules in intense laser fields: A scheme for the selection of relevant adiabatic potential curves." In: *Phys. Rev. A* 86.2 (2012), p. 023402. DOI: 10.1103/PhysRevA.86.023402.

[63] N. Suárez, A. Chacón, M. F. Ciappina, B. Wolter, J. Biegert, and M. Lewenstein. "Above-Threshold Ionization and Laser-Induced Electron Diffraction in Diatomic Molecules." In: *Phys. Rev. A* 94.4 (2016), p. 043423. DOI: 10.1103/PhysRevA.94.043423.

[64] *NIST Standard Reference Data Program*. http://webbook.nist.gov/cgi/cbook.cgi?ID=124-38-9. June 2016.

[65] *NIST Standard Reference Data Program*. http://webbook.nist.gov/cgi/cbook.cgi?ID=C7732185. June 2016.